Progress in Materials Science 138 (2023) 101157

Contents lists available at ScienceDirect

Progress in Materials Science

journal homepage: www.elsevier.com/locate/pmatsci

A state-of-the-art review of experimental and computational studies of granular materials: Properties, advances, challenges, and future directions

Pejman Tahmasebi

Colorado School of Mines, Golden, CO 80401, USA

A B S T R A C T

Modeling of heterogeneous materials and media is a problem of fundamental importance to a wide class of phenomena and systems, ranging from condensed matter physics, soft materials, and composite media to porous media, biological systems, geosystems, ceramic engineering, pharmaceutical science and even in space discoveries. Among the most important materials are granular systems, which have received intense interest from the engineering, physics, and mathematics communities. In this review paper, the recent developments and new advances in experimental, and computational methods on a variety of scales and physics that extend understanding to a wide range of materials and phenomena are reviewed. Experimental advances include computed neutron and nanometer-scale tomography, magnetic resonance imaging, refractive index matching, digital image correlation, acoustic emission analysis, and the most recent 4D techniques. Furthermore, a tremendous shift has occurred from the continuum scale to micro-scale and developing multiscale approaches. As such, various computational methods, including, constitutive modeling, discrete modeling, and multiscale approaches, have been developed. Aside from all these evolutions, more complicated modeling called coupled, or multiphysics, systems representing a simultaneous presence of heat, fluid, chemical variation, and mechanical effect are also explored.

1. Introduction

There has been extensive interest in science and engineering fields in characterizing the complex behaviors of granular materials (GM). These ubiquitous materials can be found in a wide variety of arenas, such as materials science, geology, energy resource, geotechnical applications, ceramic, powder technology, agricultural science, additive manufacturing, batteries, mineral processing, pharmaceutical industry, chemical engineering, physics, environmental problems, etc.; see Fig. 1. Despite the recent advances in computational and experimental methods, a comprehensive understanding of such materials still remained obscure. For instance, it is estimated that 40% of the capacity in industrial operations is wasted due to our lack of understanding of the transport of GM [1]. Thus, even small progress in the understanding of GM can significantly reduce costs.

Generally, GM are composed of discrete particles, which can be found across various scales. For instance, polysilicon, sand, icebergs, and asteroid belts of the solar system are all examples of GM at different domains and scales ranging from nano- to mega-scale. Such materials, intrinsically, represent a multiscale nature such that the grain-grain interactions occur at the microscale, the force chain at the mesoscale, and finally the overall/bulk behaviors at the macroscale where all such scales are connected. For instance, particles' properties at the microscale along with the boundary conditions imposed at the macroscale affect the force chain in the mesoscale. Various methods have been developed to characterize GM at grain-scale, mesoscale, and also macro-scale. However, the connection between such scales is still vague and requires more research. These materials, depending on the energy of each individual particle, can appear as fluid, solid, or gas, which makes their characterization to be very complex as each phase's behavior can be

E-mail address: tahmasebi@mines.edu.

https://doi.org/10.1016/j.pmatsci.2023.101157
Received 27 March 2019; Received in revised form 31 May 2023; Accepted 24 June 2023
Available online 3 July 2023

completely unique and one must consider a multiscale and multiphysics framework; see Fig. 2. They can also exhibit vibration, which is another complex behavior. For example, they can take the morphology of the domain when they are passing through it. Such behaviors are described using physical properties, such as the morphology of particles, size, friction, stiffness, elasticity, etc. Furthermore, the behavior of GM becomes very complex when they are accompanied by fluid. Understanding their mechanical and morphological properties, while very complicated, is of great importance.

GM have undergone extensive research and development within both the experimental and computational fields. Coulomb (1773) probably has done one of the oldest studies in this field [2] where the relationship between yielding in GM and frictional forces was studied. Likewise, Faraday (1831) established convective instability in a vibrated system of GM. Reynolds (1885) also presented the dilatancy concept, which implies that GM tends to dilate (expand in volume) when they are sheared. In other words, the particles in GM tend to stay together in the equilibrium conditions, but they manifest expansion when the particles are moving under stress and it can be due to the reorganization of particles in a way that more void space is produced among them and, in turn, that can cause volume expansion. At the time of writing this review paper, describing the overall behavior of GM is still remained challenging due to their very unique and complex characteristics, and some also have suggested that such entities can also be considered as an additional state of matter [3,4]; see Fig. 3. For instance, a sand pile in its equilibrium condition (or a slope smaller than the angle of repose) appears solid, but it can flow if the pile is tilted. The intriguing complexities in GM, namely their heterogeneous flows, fragile, and self-organizing characteristics, have urged researchers from different fields, such as mathematics, materials science, physics, engineering, and even biology, to study such systems more closely. The latter characteristic has shown an extensive range of applications in other fields related to natural science and the discovered physics in GM, in turn, has been used widely in condensed matter. More precisely, the observed slow relaxation in GM is very similar to what is detected in glasses and flux lattices [5–8]. Similarly, fluid-like behavior is also widely observable in other fields [8–14], nonlinear dynamical behaviors as in semiconductors [15], grain-scale earthquakes at the gouge zones [16,17], and stick–slip friction can all be observed in GM [18,19].

GM has two unique characteristics: (*i*) due to static friction and an inelastic collision (i.e., kinetic energy is not conserved) the particles experience a dissipative collision, and (*ii*) temperature does not affect them as the energy scale is insignificant due to a negligible ration of energy scale to the gravity energy (mgd) of grain with a diameter of d and mass of m at room temperature [3]. It should be noted that due to the complexity of such systems and also considering this topic among researchers from different fields, several review papers on specific topics such as jammed GM [21–23] and physical properties and computational modeling [3,24–27], but each of such papers focuses on a particular part of GM. In this paper, however, most of the relevant topics have been reviewed and criticized. This review, therefore, aims to describe and discuss all the current and relevant methods on the recent trends and developments in GM. After describing the relevant theoretical, experimental, and computational aspects of these materials, many applications of GM are discussed. Furthermore, a comparison is made between such methods and the predictions for their properties and the existing data. A general overview of the materials included and reviewed in this paper is shown in Fig. 4.

Fig. 1. Some of the applications of GM in different fields.

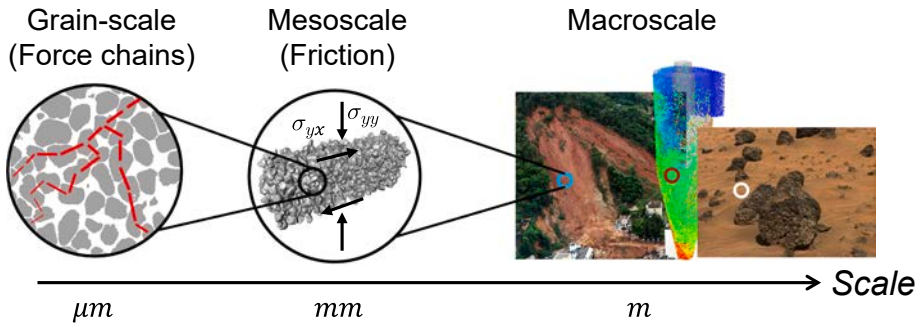

Fig. 2. Demonstration of the multiscale nature of GM and how such distinct scales are related.

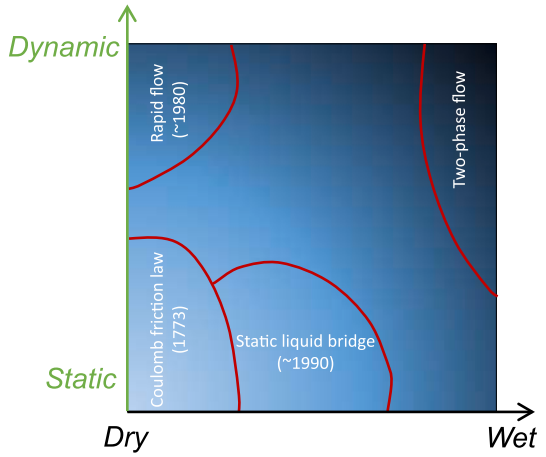

Fig. 3. Schematic diagram demonstrating the limits and existing capabilities in the current literature of GM (after [20]).

2. Particle characterization

2.1. Experimental methods

The behavior of GM is governed by complex interactions of particles. For example, some important macroscale events such as fractures and shear-band formation occur as a result of local instabilities at smaller (or grain) scales. Hence, full characterization of microstructures containing GM and their interactions must be achieved more realistically, which is required for the development of micromechanical constitutive models for GM. Microstructures have been difficult to quantify because of the limitations of equipment in obtaining microquantities such as micro-displacements, fabric quantities, and micro-strains [28]. The use of image acquisition and processing, however, has greatly enhanced the quantification of different material properties in GM. Experimental techniques such as imaging have emerged over the decades to help in the characterization of particle kinematics and examination of the material response at the scale of individual particles using advanced three-dimensional (3D) imaging techniques, e.g., X-ray computed tomography (CT) and synchrotron microcomputed tomography (SMT).

Generally speaking, experimental techniques can be either invasive or non-invasive (non-destructive). Examples of non-destructive techniques are X-ray tomography, neutron tomography, optical, magnetic resonance, and nuclear emission imaging. In this review paper, we briefly review all the above methods and illustrate their applications for GM. It should be mentioned that with the technology advancement, imaging can be conducted at very high resolution as well (i.e., 1 nm) using, for example, FIB-SEM (focused ion beam-scanning electron microscopy) and TEM (transmission electron microscopy) tomography which are rapidly developing. However, these techniques are not reviewed in this paper because they operate at a scale that is not well-suited for the investigation of GMs.

2.1.1. Non-Destructive methods

2.1.1.1. X-ray measurements. In earlier years of micromechanics, microstructural characterization was mainly based on 2D quantification to abstract 3D information [29,30]. Although such methods were able to provide a reasonable amount of information, the techniques were unable to provide sufficient accuracy, as well as quantify contact characteristics and branch vectors. Consequently, quantitative information such as deformation, strain localization, and the shear band would not be able to be quantified and, thus, the

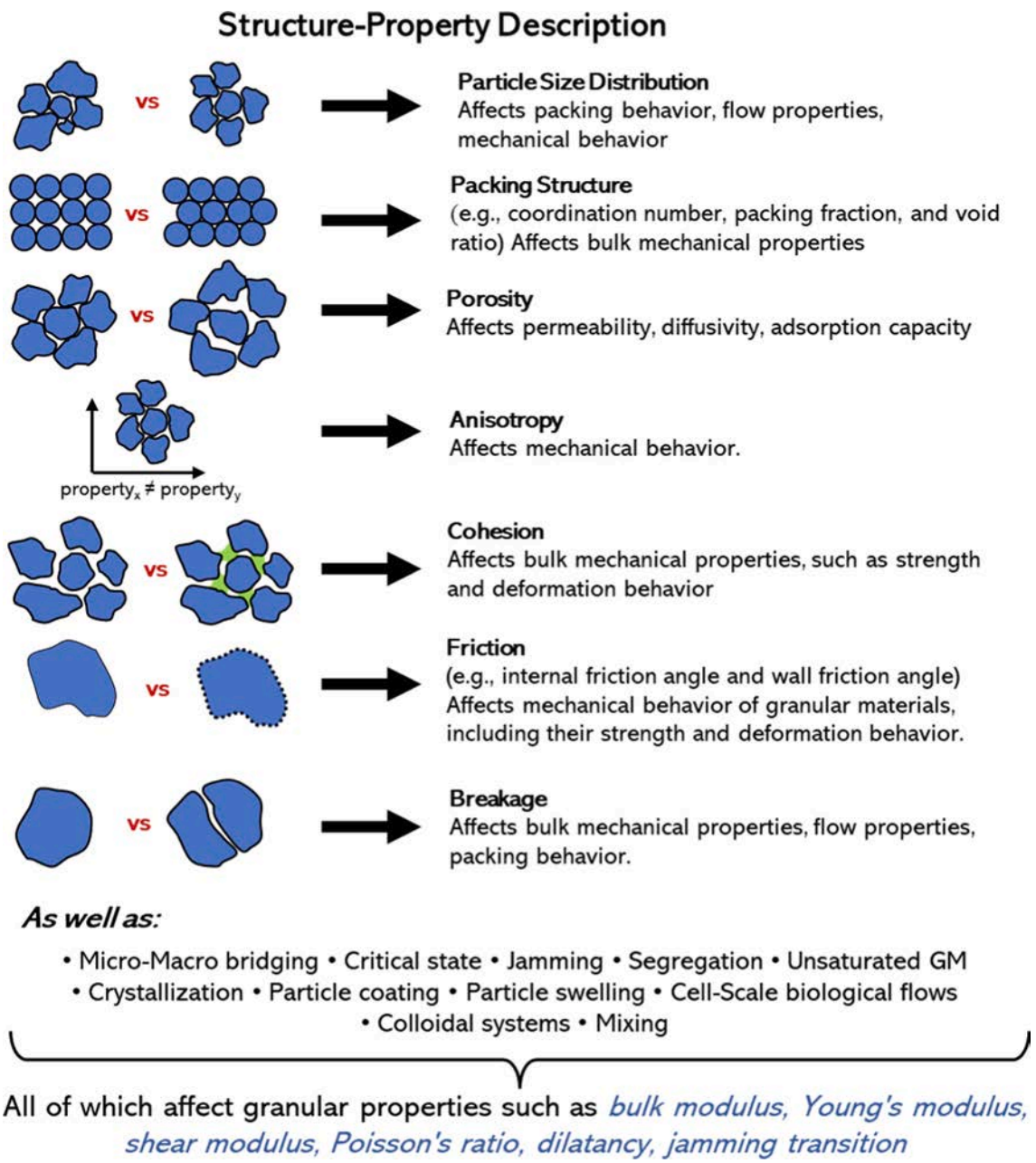

Fig. 4. The topics and features covered in this review paper in terms of structure–property relationships.

need for 3D imaging abilities is raised. Such imaging, indeed, can obtain multiple radiographs or radiograms at different angles while rotating the sample around an axis perpendicular to the beam direction.

3D X-ray tomography is regarded as one the most widely used experimental technique for characterizing GM and porous media which can also be used to study micromechanical information at that scale. It has a superior spatial resolution to other competing techniques and can be applied to a wide range of applications and materials. This is because it has a relatively short wavelength hence, it has a powerful penetrating ability and high sensitivity to material density. Moreover, due to its non-destructive nature, conventional X-ray imaging and synchrotron imaging, have been popularly applied to study GM and flow in granular systems. X-ray imaging can generate cross-sectional images by measuring the attenuation of the X-ray beam as it is rotated at increments within a plane with a rapidly increasing spatial and temporal resolution, and then collecting the attenuated X-ray using a detector system. It has the ability to collect stacks of 2D sectional images. The multiple images created can then be post-processed and reconstructed to generate a 3D volume rendering of the sample. Some examples of the X-ray images of complex GM can be found in Fig. 5.

The XCT scanning techniques based on resolution have been summarized by Ketcham and Carlson [33]. They grouped these

methods into four categories based on their spatial resolution and the size of objects. These are conventional with a resolution of 250 μm, high-resolution (100 μm), ultra-high resolution (10 μm), and microtomography or micro-CT with a resolution as high as 10—–1 μm. 3D imaging techniques are now becoming a well-known analysis methodology in numerous applications. Resolutions can reach below 1 μm in laboratory-based setups and well below 100 nm at synchrotron radiation facilities (nano-CT). For typical granular systems, resolutions of about 10 μm, can provide the resolution required to measure details at the individual particle level. Thus, XCT has been widely used to obtain the microstructure of a material and to investigate microscopic features within the material.

XCT imaging has been applied to the microstructural characterization of cement concrete, soil, asphalt concrete, and rock imaging. Submicron resolution has now recently been based in traditional fine-focus geometry with nano-focus X-ray source (better than 1 μm resolution (e.g., 50 nm), contact imaging, and magnifying X-ray optics. Nano-CT has been applied for imaging Lithium-ion batteries [34,35]; see Fig. 6; which can essentially be considered as GM. Such images can be used for measuring axial void distributions (AVD) and radial void distributions (RVD) more accurately. Other topological quantities, namely contact numbers, contact angle distributions, and contact surfaces, can be measured as well. Reimann et al [36] analyzed structural features of mono-sized sphere packings in cylindrical containers both with and without inner cylinders using void fraction distributions, sphere center positions, contact angle distributions, coordination numbers, radial distribution function, and Voronoi cell packing fractions to provide a comprehensive understanding of structural details. X-ray tomography-assisted was conducted by a phase inversion process in ceramic hollow fiber systems [37]. They were able to characterize, the micro-channels in 3D using XCT to determine micro-channel densities and diameters in the radial direction, as well as the 2D measurement of the pore size in the sponge-like layer. This could potentially help to realize

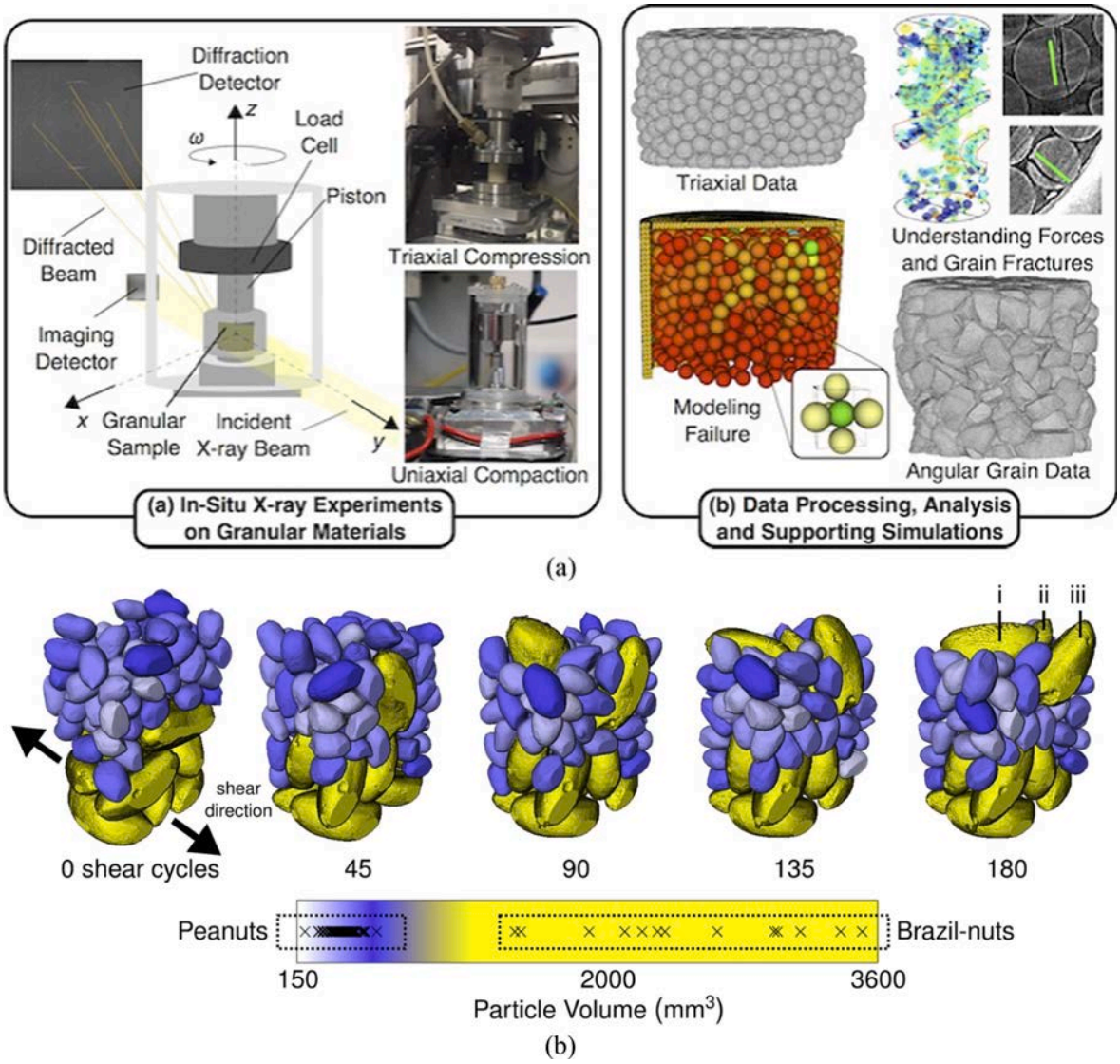

Fig. 5. (a) In situ X-ray imaging and diffraction for spherical and angular GM [31], (b) time-resolved 3D imaging for a complex GM (a nut mixture) where the evolution of particles' displacements can be seen [32].

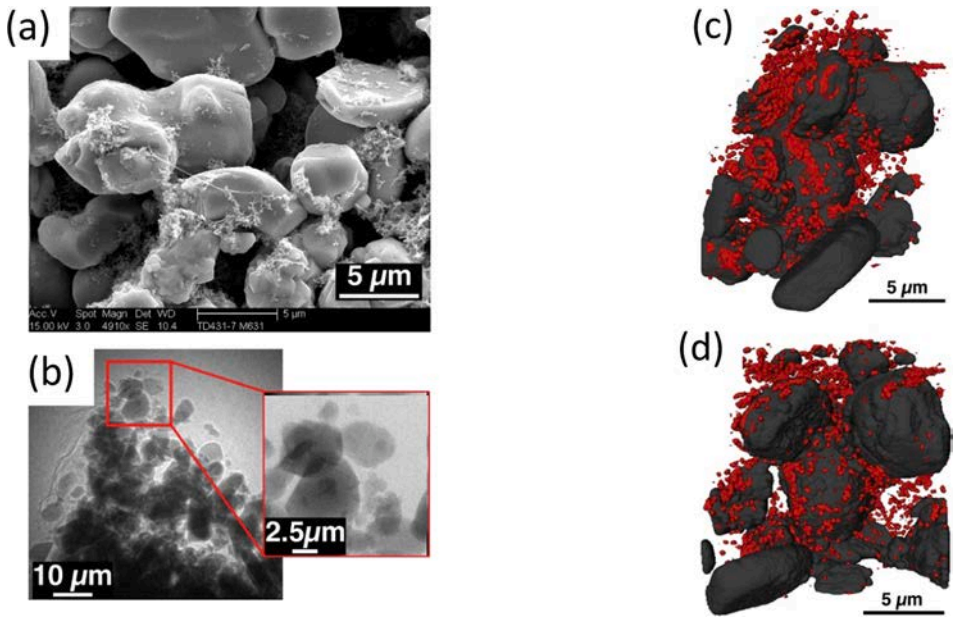

Fig. 6. SEM images and triangular sample. (a) Scanning electron microscope images of LiCoO2 cathode. (b) Large field of view radiograph of the LiCoO2 sample. (c-d) 3D reconstruction of the Li-ion cathode. (c) In-plane and (d) through-plane view of the reconstructed Li-ion cathode. The LiCoO2 particles (dark) and the additives (bright) are distinguished by combining absorption and Zernike phase contrast imaging modes [38].

practical morphology design and optimization.

Depending on the resolution of the target properties and the size, one can also take advantage of more advanced imaging, such as Scanning Electron Microscope (SEM) though which more details at a much finer scale can be revealed. An example is provided in Fig. 7 where the structure of an agglomerate structure with time is demonstrated [39]. As can be seen, a coater (Wurster) is added to the particle and makes it thicker. These images show the surface of a granular system and one can use X-ray imaging for seeing the internal structures. More images provided by the SEM are provided in Fig. 8 [40]. These images are limited in terms of their flied-of-view

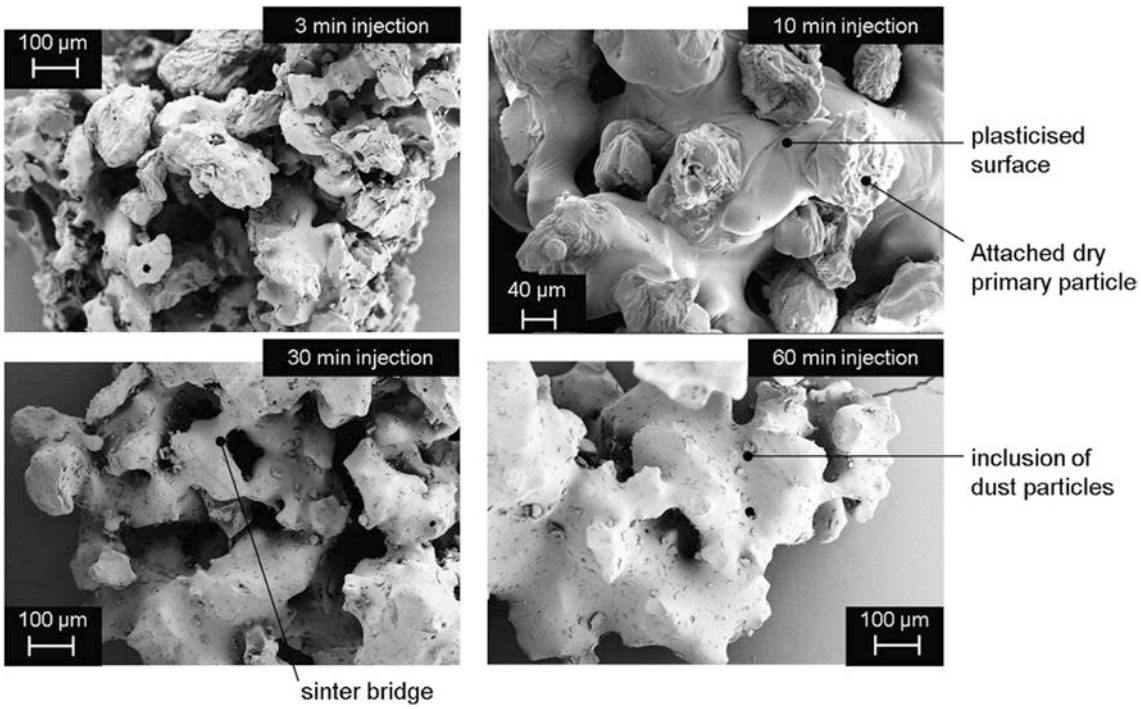

Fig. 7. SEM images of maltodextrin agglomerates produced in the Wurster-coater at 70 °C [39].

dictating a smaller region of the materials that can be scanned.

2.1.1.2. X-ray fluorescence (XRF) tomography. Although this paper is primarily devoted to reviewing GM assemblies, as mentioned earlier, an understanding of how components of a granular pack can be identified is equally important. One way of achieving this is by X-ray fluorescence (XRF). Most tomographic measurements are carried out using transmission or propagation-based tomography. However, these cannot be applied for chemical analysis, i.e., they provide little or no information regarding chemical element distribution. Methods such as XRF are useful techniques for obtaining missing information regarding chemical properties. This involves the use of "hard X-rays". These are X-rays with high energies typically in the range of 10——120 keV. They are able to penetrate deep into samples compared to *soft X-rays* because of their high energies. Absorption of these X-rays is followed by re-emission of the energy absorbed, leading to fluorescence. These interactions with matter can be used to gain information about the composition of a sample, including the type and location of individual atoms within it. The technique is a highly sensitive physicochemical method that enables quantitative element identification by collecting fluorescent X-ray photons emitted by the element of interest [41]. Typically, 10–15 elements are mapped simultaneously, leading to precise elemental colocalization maps [42]. XRF tomography can be applied for structural visualization, but technical challenges have limited the application to just 2D and low-definition studies. This is due to the fact that the technique can be very slow compared to transmission tomography. Thus, only a single voxel of data is collected at any one time [43].

XRF tomography also has analytical and technical challenges due to the misrepresentation of some images owing to the reabsorption of emitted XRF photons [42]. Application of XRF with synchrotron X-ray sources has outstanding capabilities such as the possibility of micrometer and submicron resolution, producing better signal-to-noise ratios and high brilliance, and hence can be used for the detection of trace elements in materials with high sensitivity. Very high submicron resolution e.g. sub-500-nm resolution XRF tomography, are now possible, providing a lot of details regarding elemental specificity [42]. Slow collection times have impeded its application to, for example, highly hydrated samples because of radiation damage and dehydration. These have been improved by the use of fast detectors [44] coupled with powerful data acquisition approaches, and the multi-pinhole method [41].

Micro-CT and XRF have also been integrated to be able to provide more concise (or clearer) information regarding spatial chemical distribution. These have been applied for GM to obtain important parameters such as grain-size distribution, void fraction, grain shape and orientation as well as chemical distribution. This method has been applied for visualizing the internal structure of natural building stones at the micro-scale as well as the chemical properties using XRF [45]. Balegem sandstone and the Massangis Roche Claire

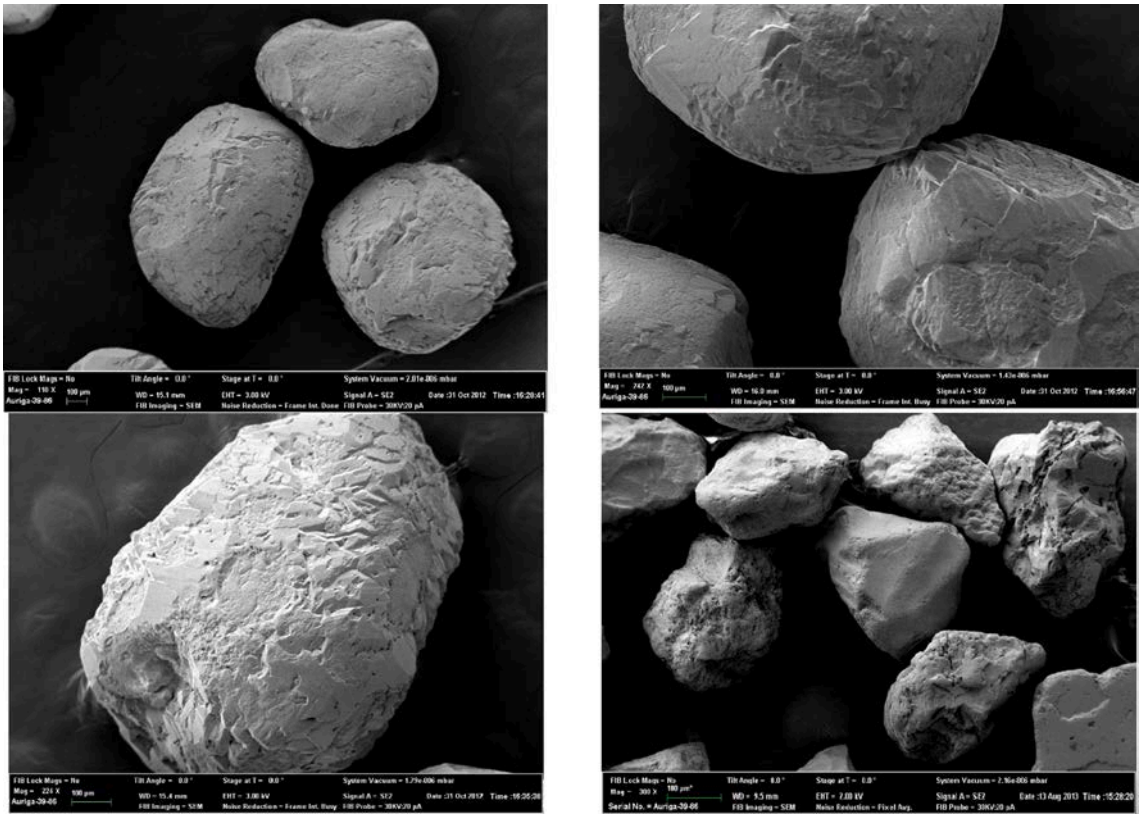

Fig. 8. SEM images of Ottawa sand. As can be seen, very irregular and rough surfaces exist on such particles, which is not possible to be observed using low-resolution imaging. These images can be used to provide insight into the roughness and the true morphology of GM at a small-scale [40].

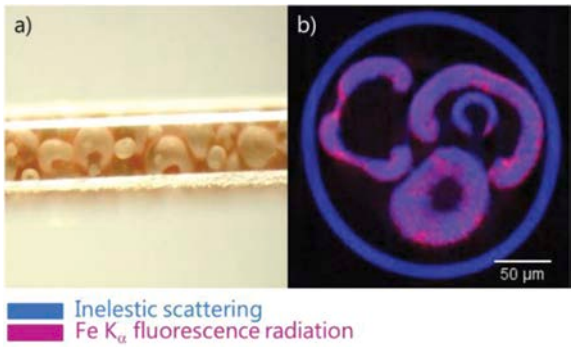

Fig. 9. XRF imaging of iron oxide in alumina granule [49].

limestone were visualized and quantified where iron-bearing minerals such as glauconite were identified. Laforce et al. [46] developed a novel 3D elemental and morphological analysis approach by combining XCT, XRF tomography, and confocal XRF analysis in a single laboratory instrument. They linked the (quantitative) spatial distribution of chemical elements within the investigated materials to their 3D internal morphology/structure down to a 1–10 µm resolution level. The distribution of iron atoms in the alumina granules of a certain powder combination was investigated using X-ray fluorescence tomography [47]. Tomography of several single slices for the capillary was carried out with a pencil X-ray beam with an energy of 7.9 keV. The optical microscopy image in Fig. 3(a) presents the sample preparation for the μXRF tomography measurements. The measurement was used to provide 3D information about the homogeneous distribution of iron oxide within the granules, shown in Fig. 9 (the Fe atoms are in pink color). Liu et al. [48] applied a direct, non-destructive, and single-particle analytical method, i.e., synchrotron radiation-induced X-ray fluorescence spectrometry (SR-XRF), to study the micro-scale characteristics of heavy metals in geomaterials. The forms of occurrence, spatial distribution, and associations of several concerning elements were visually inspected from μ-XRF maps as well as the size dependence characteristics of elemental composition, spatial distribution, and speciation in raw particles.

2.1.1.3. Synchrotron radiation. XCT imaging can be very slow and X-ray tomography often attains very high spatial resolution. Temporal resolution, on the other hand, is typically in the order of hours per scan. Various solutions have been proposed to enhance temporal resolutions of low-dose and fast micro-CT imaging methods based on EST (equally sloped tomography) [50] and CS (compressed sensing theory) [51] reconstruction algorithms, respectively, were developed in which one set of micro-CT projections could be collected in 1(s) or less time. Additionally, X-ray imaging methods such as local micro-CT were developed to improve temporal resolution within a short time range (ps-μs-ms).

Typically, the time needed to acquire an X-ray tomogram depends on the photon flux from the source. X-ray imaging sources can be classified into classical X-ray tubes or synchrotrons. X-ray tubes emit low photon flux and, as a result, require several minutes or hours for generating a single 3D image. Synchrotrons, however, produce an almost parallel beam and high photon flux (high brilliance), which allows for the acquisition of tomograms to occur in a few seconds. This also yields better image resolution and signal-to-noise ratio (SNR). High flux mono-chromaters can easily tune the beam to monochromatic radiation for the desired energy level to suit specimen size and attenuation level [52]. Other advantages of synchrotron tomography over X-ray imaging can be reviewed elsewhere [53–55]. The disadvantage of synchrotron tomography, however, is that they are expensive to set up, whereas X-ray tubes are comparatively low cost. Additionally, they have a field of view that is typically less than a cubic centimeter.

In GM, Synchrotron micro-computed tomography (SMT) was used by Hasan and Alshibli [56] to image a plane strain specimen, thereby quantifying particle orientation within the shear band. Druckrey and Alshibli [57] developed an algorithm to track the kinematics of ASTM 20–30 sand based on SMT images during triaxial testing. Druckrey et al [52] used SMT to image silica sands at the Bending Magnet Beamline 13D (13 BMD) at the Advanced Photon Source (APS), Argonne National Laboratory (ANL), Chicago, USA, by which they studied 3D characterization of sand particle morphology, orientation, and contact configuration.

Synchrotron imaging has also been a useful alternative for determining the porosity of GM. It was applied by Betson et al. [58] in examining porosity distributions in columns; see Fig. 10. Tomographic energy-dispersive diffraction imaging (TEDDI) [59] along with Tomographic X-ray fluorescence XRF were combined and used to highlight the porosity distribution of English Chalk; see Fig. 11.

2.1.1.4. Neutron imaging. X-ray imaging tends to suffer from a low attenuation coefficient in saturated media, such as GM filled with a liquid. For example, water, in general, does not show good contrast in the XCT for high-energy X-rays. A contrast agent is commonly included in water to improve the contrast [60]. This, however, could alter the contact angle in the system, depending on the type and amount of contrast agent being utilized. With Neutron imaging, however, water tends to show high contrast making it an excellent candidate for imaging saturated GM. A typical Neutron imaging setup is shown in Fig. 12. It has been applied in literature for

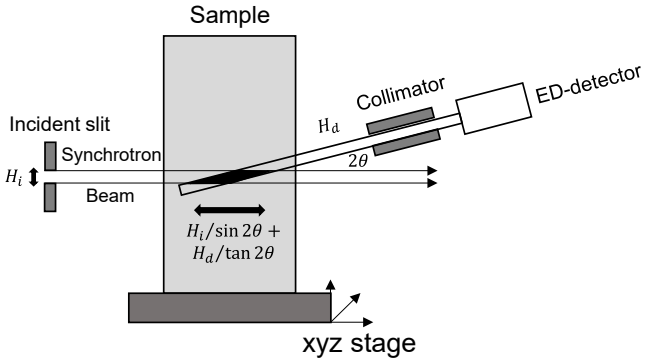

Fig. 10. TEDDI principle. .
Adapted from [58]

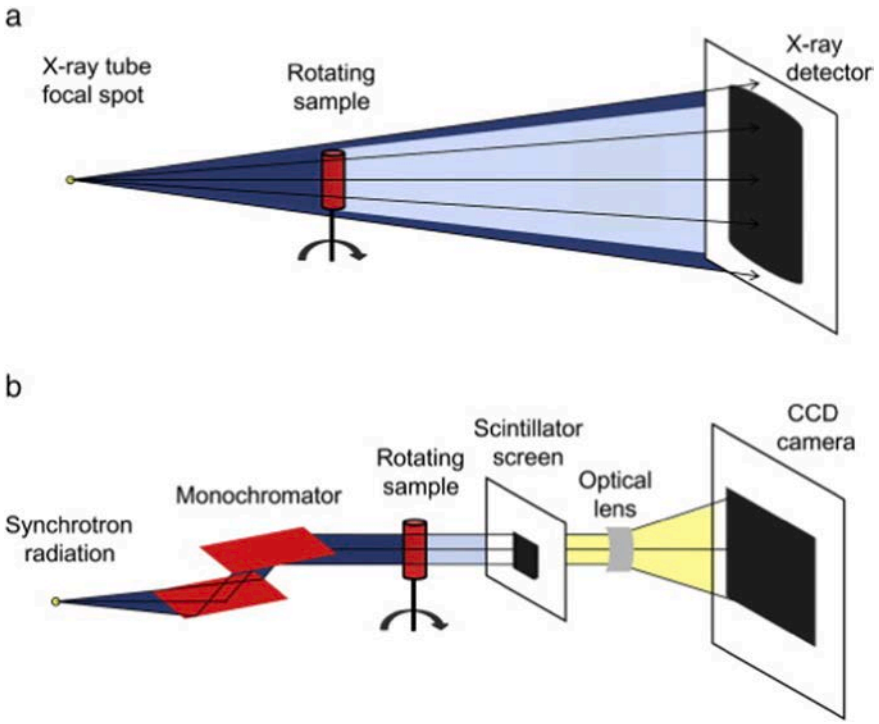

Fig. 11. (a): Schematic diagram of a typical lab-based micro-CT setup with a conical X-ray beam which allows geometrical magnification. (b). Schematic diagram of a typical synchrotron-based micro-CT setup. A white (polychromatic) X-ray beam is created in the synchrotron by means of a bending magnet, wiggler, or undulator. Figure .
adapted from [55]

visualizing and quantifying water distribution in partially saturated sand specimens [61]. The effect of particle morphology on water distribution in compacted granular columns was investigated using round and angular silica sand. This was done at a resolution of 127 mm/pixel. However, at such a coarse resolution, capillary bridges and fine features needed for defining the particle morphology were not observed.

In a similar work [62], higher resolution neutron imaging (13.7 mm/pixel) was applied on partially water-saturated compacted silica sand specimens with two different grain morphologies (round and angular). This was made possible by applying a very thin gadox scintillator with a high-resolution charged-coupled device (CCD) camera. Moreover, cold neutrons were employed instead of conventional thermal neutrons. This helped in the improvement of water contrast, and thus adequate detection of finer water capillary films was made possible. This was achieved in conjunction with microfocus X-ray imaging with a higher resolution of about 11.2 mm/pixel. Hence, gas and liquid phases were visualized using dual-modal contrast for different grain morphologies at the grain level and a precise location of the solid phase was also possible by this means. The visualizations of the images are shown in Fig. 13. Image reconstruction was achieved using filtered back propagation (FBP). The figures illustrate three compaction layers that are visible from

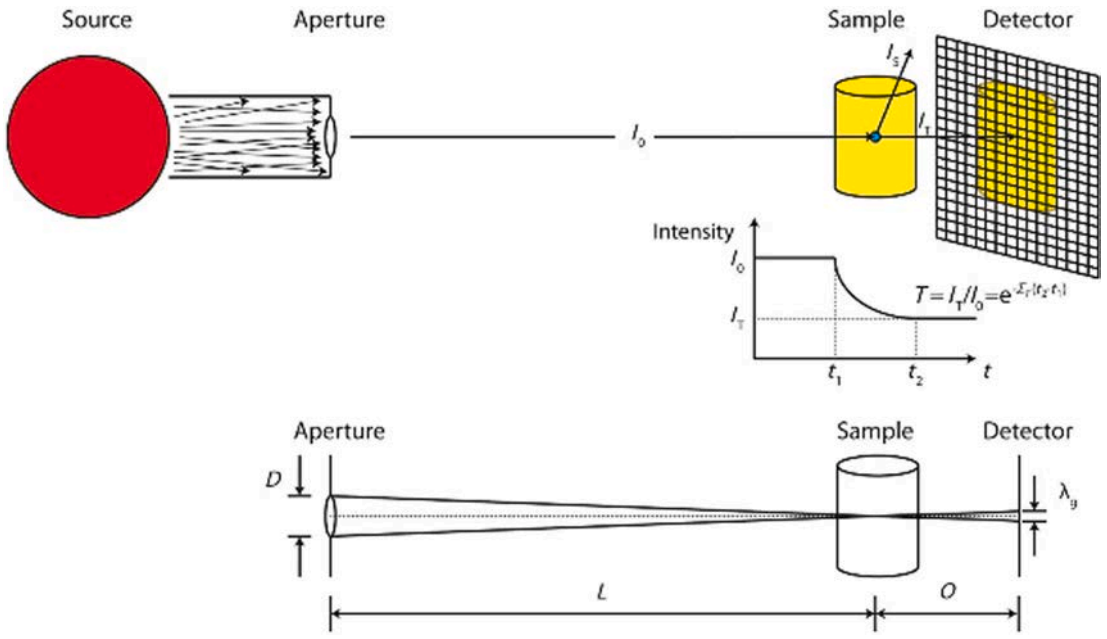

Fig. 12. Typical Neutron imaging setup. .
Adapted from [61]

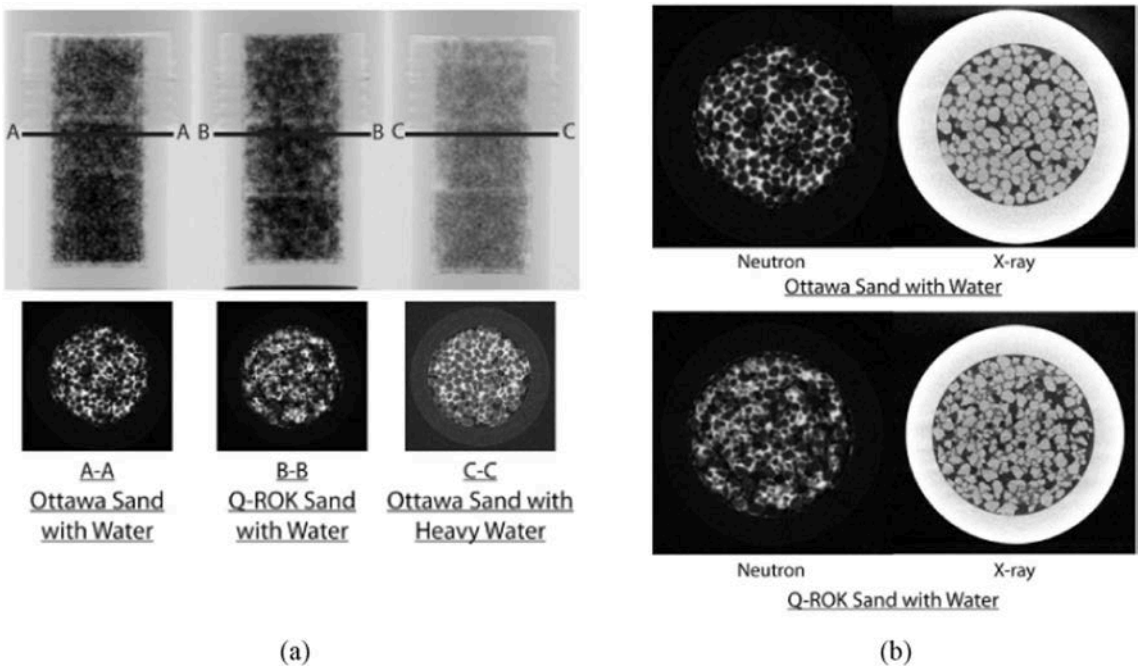

Fig. 13. Comparison of contrast of different specimens using neutron radiographs and X-ray tomography slices [62].

the radiographs because of the high attenuation of water to neutrons. The contrast difference between water and heavy water is shown as well as the grains from the X-ray tomography in Fig. 13(b).

It can be seen that microfocus X-ray is able to properly detect the silica solid grains in which water is well visualized with the high contrast Neutron imaging. Hence a dual-modal contrast has the potential to be able to provide a distinction for various problems in the field of saturated GM such as in soil mechanics and geotechnical engineering and can help to obtain other parameters, such as a spatially resolved void ratio and particle size distribution. Fig. 14 shows the 3D structure of the grains and water of the Ottawa Sand specimen.

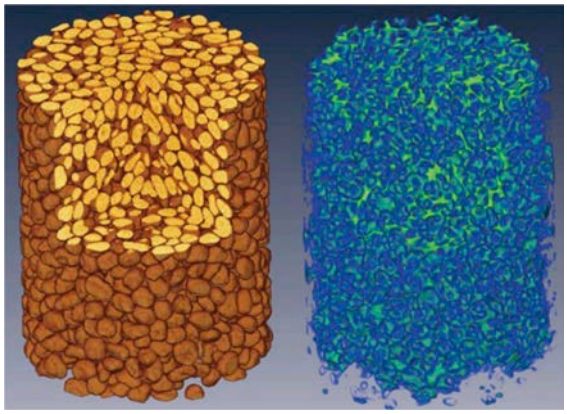

Fig. 14. X-ray imaging and neutron imaging, sand phase (left), and water phase (right) [62].

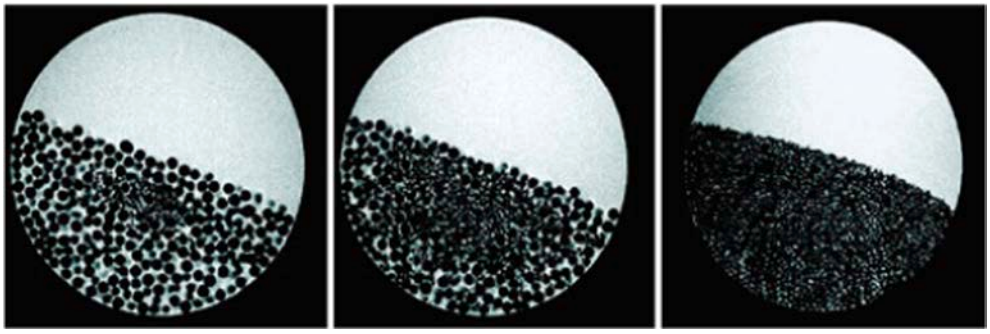

Fig. 15. An example of MRI imaging for demonstrating its ability for providing fast imaging on large GM samples without necessarily observing many details [72].

2.1.1.5. Magnetic resonance imaging (MRI). Magnetic Resonance Imaging (MRI) is also an important tool for imaging GM. It has a high potential for 3D imaging when the sample to be mapped contains some form of liquid. This applies to for example oil-containing seeds such as mustard seeds [63] or any form of solid that has been immersed in an NMR-active fluid [64]. There are a large number of NMR-active isotopes. However, most systems are programmed to detect hydrogen-containing fluids. X-ray tomography is usually the most preferred method for most applications; however, MRI has some qualities to offer over the XCT such as faster imaging of single slices with modern MRI techniques. MRI techniques have a sub-millimeter accuracy in macroscopic volumes, but only at a slow-scanning rate. They are limited to tracking materials that contain hydrogen atoms, such as organic materials [65]. The first demonstration of MRI was by Altobelli et al. [66] in fluid-embedded granulates. They showed that MRI techniques can be employed in the imaging of arbitrary planes within the bulk of fluid-filled GM noninvasively. It has been applied to a large range of problems in granular systems such as in the mixing and segregation of grains in an assembly that are under some form of mechanical agitation such as rotation, diffusion of grains, or interstitial fluids in a rotating cylinder, displacement of particles, and flow profiles of slurries or granular matter. Ehrichs et al. [63] used MRI to study the convection of GM in a vertically shaken cylinder. Radial and axial segregation which occurs when granular mixtures are rotated in horizontal cylinders has been also studied using MRI [67–70]. 3D MRI was used to study the mixing and segregation processes in a Turbula mixer (Turbula mixer is a special type of device used in chemical and pharmaceutical industries that can generate a good homogeneous mix of the granular samples) using binary mixtures of sugar beads [71]. A more detailed review of the applications of MRI for granular materials can be found elsewhere [72]. One example showing the quality of images and also the performance of MRI is shown in Fig. 15.

2.1.2. Quantitative analysis

All the imaging methods discussed above provide a 2D or 3D image of a granular sample for visualization and qualitative studies. A stack of 2D slices after reconstruction can be loaded into the computer memory to be visualized in three dimensions. Quantitative procedures, however, require more work from an imaging standpoint. The 3D analysis of such a volume typically starts with a segmentation step where connected regions are classified based on a voxel number, the separation of connected objects into sets of smaller objects, and the actual analysis of the separated objects to quantify parameters of interest.

In this section, we examine the quantitative analysis of static structures and the evolution of three-dimensional structures. The algorithmic analysis steps required to quantify particle properties from such images are in principle generic and can, in many cases, be applied to images of any imaging method. New techniques capable of examining the material response at the scale of individual

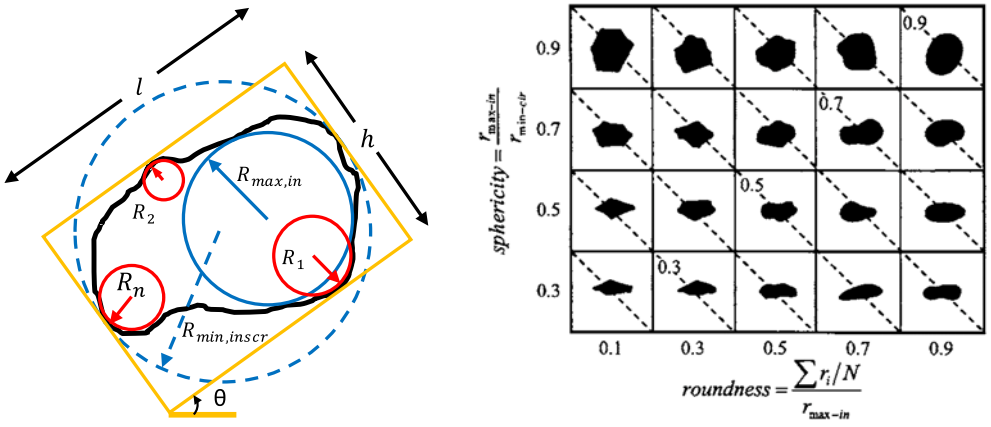

Fig. 16. (a) Schematic representation of morphological features for describing the shape of an angular particle [82], (b) relationship between particle shape descriptors (roundness and sphericity) [83].

particles have emerged in the last two decades. These measurements can be achieved using modeling techniques such as the discrete element method (DEM), or alternatively experimental techniques. In this section, we review how these measurements can be carried out experimentally and will discuss the computational methods in the next section. Significant progress has been made to characterize particle kinematic behavior using advanced 3D imaging techniques such as XCT and SMT. These techniques yield 3D images through which one can quantify individual particles with a resolution high enough for quantitative analysis. 2D and 3D XCT imaging has been used to quantify individual particle characteristics [73–76]. Some of such quantitative granular behavior include but are not limited to, particle kinematics (particle displacement and rotation), contact numbers, contact angle distributions, force transmission, and particle-to-particle interactions. As such, proper characterization is required to investigate the role of individual particles on overall behavior.

2.1.2.1. Shape characterization. Given the above descriptions, various methods have been developed to characterize the observed complex shapes in GM. The shape of particles is often characterized using some morphological features [77–79]. An angular particle is considered in Fig. 16. Given this example, one of the elementary measures for characterizing the morphology is *elongation E*, which is defined by:

$$E = h/l, \tag{1}$$

where h and l are the smallest and second relevant dimensions in the direction of θ, respectively. Note that the above equation is valid when θ is minimized. Furthermore, one can also define the *sphericity* using:

$$S = \sqrt{\frac{R_{max-in}}{R_{min-inscr}}}, \tag{2}$$

where R_{max-in} and $R_{max-inscr}$ are the largest inscribed and smallest circumscribed circles, respectively. This descriptor is called circularity in 2D. *Roundness* is also another important descriptor for estimating the corners/sharpness of particles and it is defined by:

$$Rd = \frac{\sum_i R_i}{N.R_{max-in}}, \tag{3}$$

where R_i is the radius of N circles in 2D using which the corners are estimated. All such descriptors vary with scale. For example, roughness can change by increasing the resolution of the particles/images. The morphology, in general, controls various important properties in GM and porous media, such as permeability, strength, tortuosity, … [80–82]. Particles with larger roughness and angularity, due to their higher degree of interlocking, can manifest more strength against mobilization [83]. Thus, it is very important to accurately describe the morphology of GM so that more representative models can be generated. We will come back to this point shortly.

2.1.2.2. Synthetic granular particles generation. As discussed earlier, experimental methods are widely used for acquiring images for GM using which a realistic representation of the morphology of particles can be obtained. Such images, then, can be used in computational methods to conduct the relevant modeling; see the next section. However, producing experimental images with acceptable accuracy is quite challenging, not only in the field of GM but also in any other related topics in which imaging of complex systems and samples is conducted. As such, producing stochastic porous media systems, and in particular, GM, is a general subject and various methods have been developed to date. These methods are studied elsewhere [84] and here we just put the focus on those exclusively related to GM.

2.1.2.2.1. Object-based methods. One of the earliest methods of creating sets of particles involved utilizing well-defined and ideal

shapes/objects. For example, objects such as spheres in 3D and circles in 2D [85–90], and cylinders [91] have been used widely to produce models of GM quickly. Since these objects may not represent the complexity one may observe in actual GM, more advanced morphologies have also been developed. For example, ellipsoids [92], polyhedrons [93], polyarcs [94], pentagons [95], rounded rectangles [96], and cubic particles [21,22] are some cases of such models. Using spherical and circular models is yet more dominant among the aforementioned morphologies. Since the process of building the GM packs is limited to some statistical information (e.g., void space/porosity, radius, the overlap between the particles, orientation, …), thus, more complex geometries and granular systems cannot be produced. Some examples of such models are shown in Fig. 17. The produced shapes, as demonstrated, are limited to those whose geometries can be defined mathematically. These shapes are yet to be enough for some manufactured particles and, thus, one does not need to add any further complexities.

2.1.2.2.2. Geometric packing methods. The previously discussed methods for building stochastic packs of particles are sufficient for manufactured materials in which particles often follow systematic and well-defined morphologies. For more complex and natural GM, however, such particles may not be adequate. One solution can be extracting important morphological information from the images produced by, for example, X-ray computed tomography and then using them in optimization algorithms to reproduce them on random particles. Producing more realistic particles, indeed, can help with computational modeling to result in a more accurate evaluation. Furthermore, investigating the behaviors of particles at this scale can better bridge the meso- and macro-scale phenomena [103–106].

The ultimate goal of the stochastic particle generation approaches is to generate realistic packings of particles with accurate

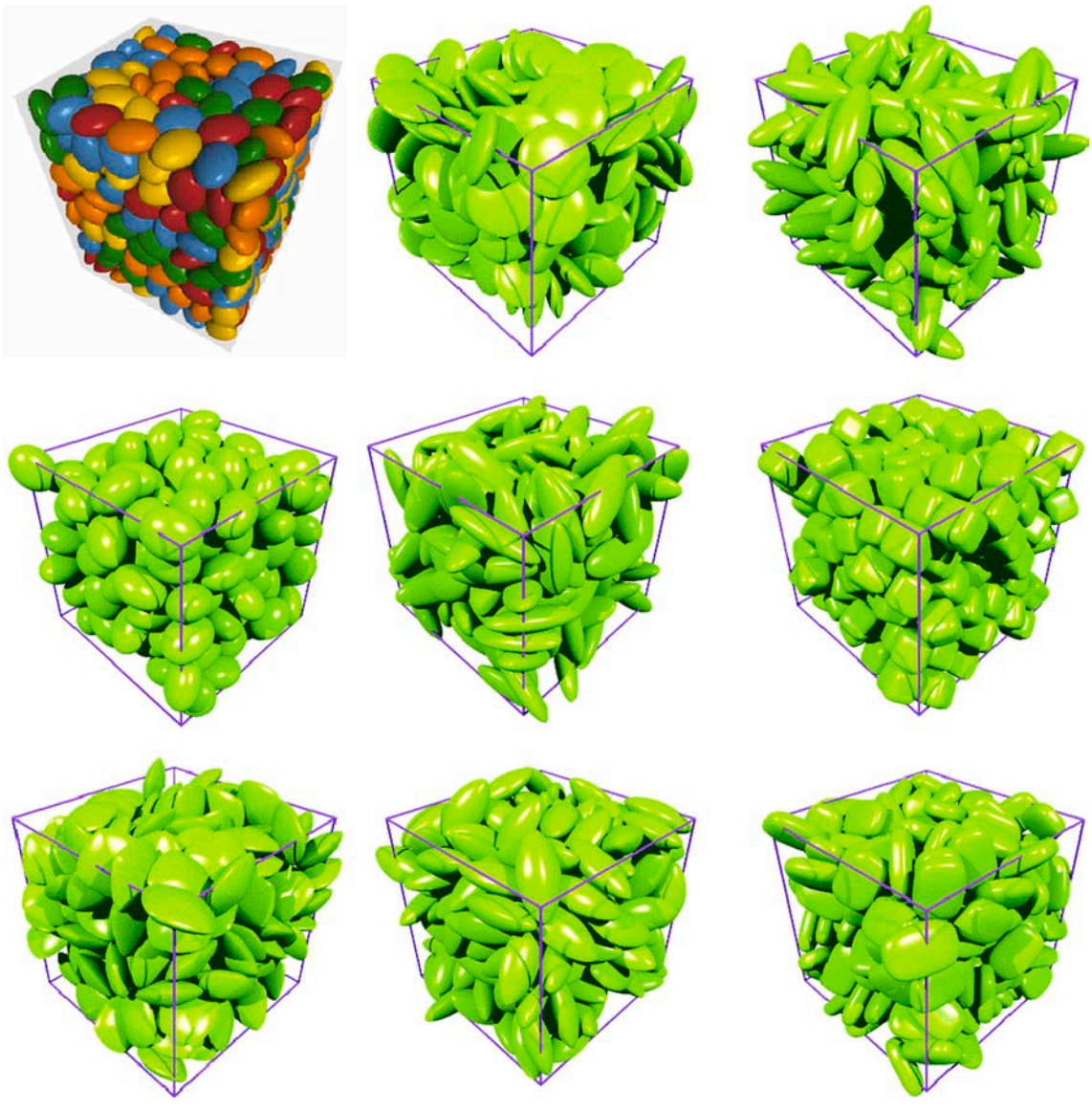

Fig. 17. Some of the packs generated using object-based modeling for representing GM [24,97–102].

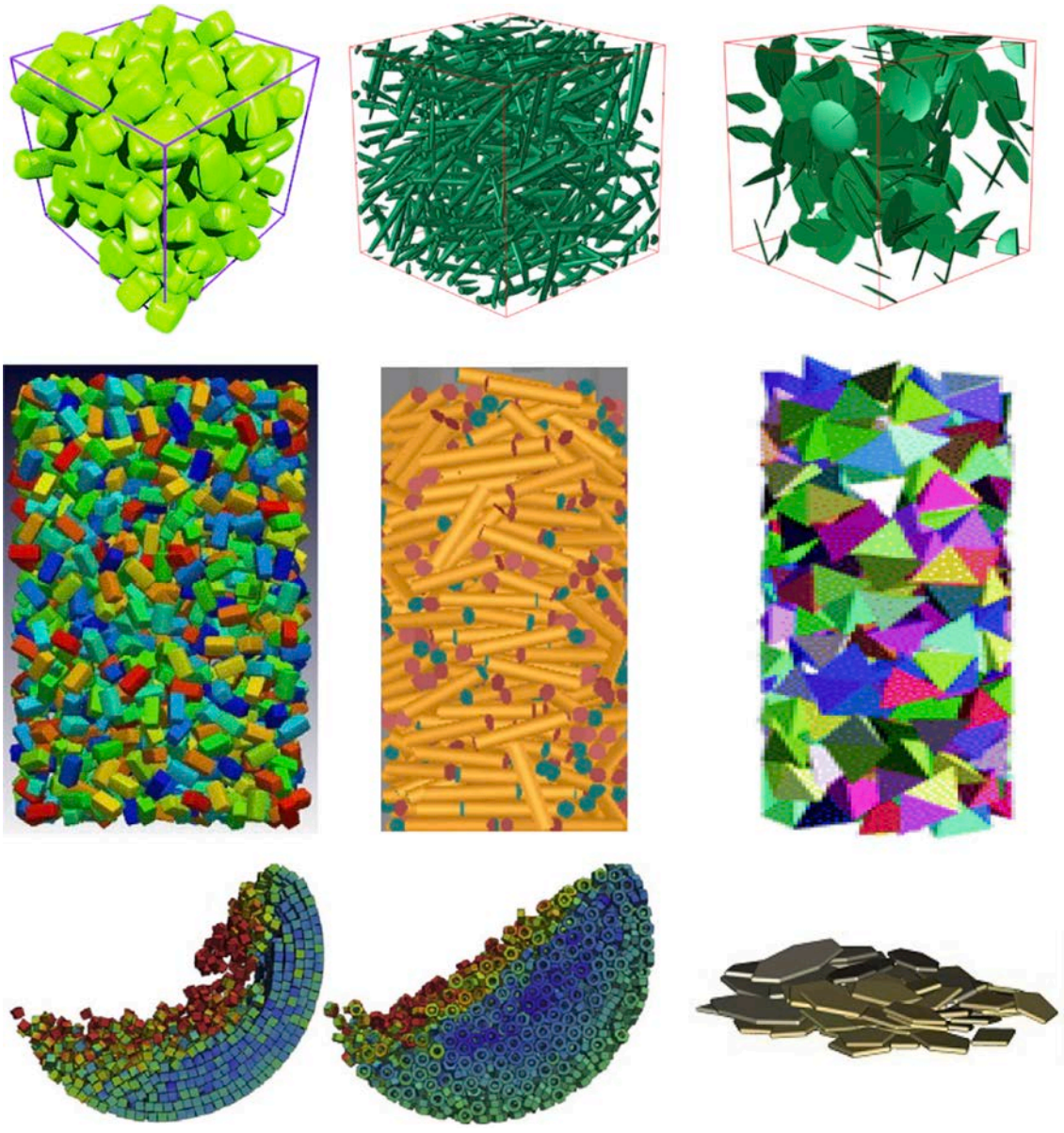

Fig. 17. (*continued*).

geometry by reproducing specific statistical and morphological properties (or shape descriptors) as expected to be seen in the final model [107–111]. For example, Mollon and Zhao [112] extracted the mean of the discrete Fourier transform from experimental images which are used on a Voronoi diagram representing the domain of each cell in the pack. Since each particle is represented by a cell, an inverse Monte-Carlo method can be used to match the sizes and orientations [113,114]. Then, given the boundary conditions (e.g., solid fraction), each cell is filled with a particle. In this method, 2D particles are represented by a set of contours each of which is composed of a certain number of points. Such points can be described by their angle and radial distance from the center of the particle and, thus, can be considered as a signal. Then, the fast Fourier transform (FFT) can be used to compute the discrete Fourier transform on the extracted signals after which spectrum computation can be done. This method assumes that the normalized amplitude (i.e., Fourier descriptors) of the calculated spectrum can reveal the shape of particles. Some of the results and specific features of this method are shown in Fig. 18.

The above-described method, in light of higher computational time, can include various shape descriptors. However, calibrating the Fourier spectrum and also the number of eigenmodes can be difficult and time-demanding. These parameters strongly affect the quality of particles. Furthermore, since this method works based on shape descriptors, accurate extraction of such statistics in the first place can also be problematic.

In a similar fashion, Monte-Carlo sampling has been used to extract the morphological descriptors from pre-computed shape

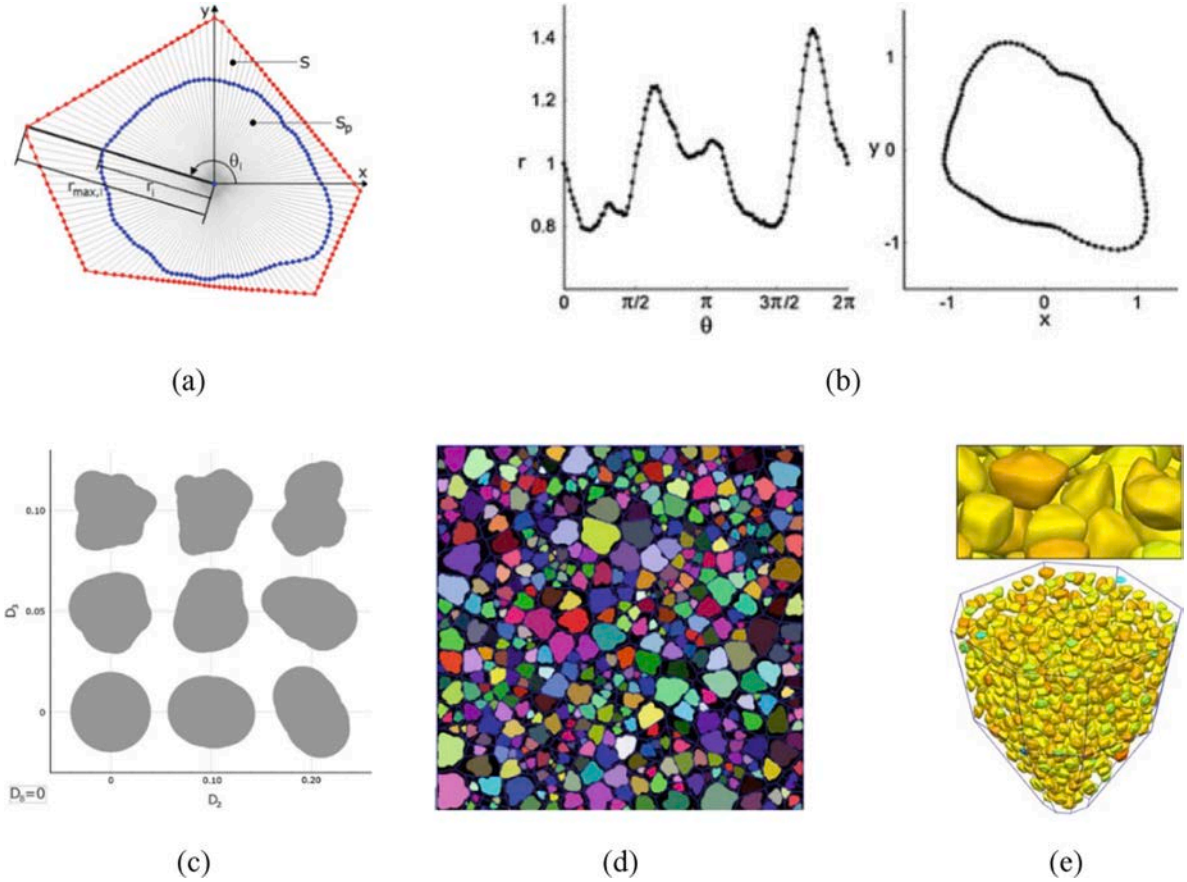

Fig. 18. Demonstration of the Fourier-based granular generation. (a) cell characterization along with a fitted particle, (b) a random signal and how it can be related to a particle, (c) the effect of two Fourier descriptors on the shape of particles, (d) a random 2D GM, and (e) a random 3D pack of GM [109,115].

distributions of a set of real grains [116]. This approach considers the shape descriptors in the final simulated grain in a step-by-step manner such that an initial ellipsoid particle with a random aspect ratio, which is sampled from the pre-defined distributions, is considered. It should be noted that the spherical radius distribution is calculated for all grains across all the points on the particles with different azimuthal and polar angles ($0 \leq \Phi \leq 2\pi, 0 \leq \Theta \leq \pi$). Then, given the calculated spherical radius distribution $f(R|\mu, \sigma^2)$, which is assumed to be Gaussian with the mean of μ and standard deviation of σ^2, a random radius value R^{**} is sampled from the newly conditional probably, namely $f(R|R^*, \sigma^2)$ where R^* is the radius value on a random point on the ellipsoid particle. This process is repeated for other shape distributions until they are matched. The described method is applied to individual particles without considering the existence of the neighboring ones. This algorithm, however, requires a large number of adjustments, such as the number of points on each particle, lack of control on sampling, etc.

2.1.2.2.3. Image-based modeling. The previously described methods are based on a set of shape descriptors through which new GM models can be produced. Such measures, however, even if all of them are considered, still cannot characterize complex GM, in particular, those that one often finds in nature. In most cases, the produced models do not agree with reality and a significant inconsistency is observed. Furthermore, some of the described descriptors have different definitions whose applications only depend on the user's choice [105,117]. Therefore, such uncertainty and diversity in the definitions and also lack of universality can result in producing unrealistic GM models.

One of the reliable sources for characterizing GM, as mentioned earlier, is the X-ray computed tomography images, which are often provided in 3D [118–120]. These images can be used directly in numerical modeling and calculate elastic strains, the void ratio in a shear band, flow properties and so many other physical properties, which all refer to digital computing [121,122]. These images offer a unique and excellent source as they manifest the true complexity of GM. Despite all the recent progress in this field, however, providing various images of GM to represent any alternatives in terms of morphology and grain packing is not feasible and, thus, it can jeopardize the reliability of the evaluations. To address this issue, one should extract many samples from the target GM and conduct imaging over all of them, which is not viable both financially and temporally. Thus, developing methods that can use such images directly and produce other scenarios is very crucial. This question has been partially addressed in the field of porous media and materials science [119,123–132], and such methods are not fully reviewed but an interested reader can refer to a recently published paper on these

methods [84]. For example, some of such methods use an input image through which useful information is extracted via correlation functions. Then, stochastic models are generated by iteratively matching the extracted correlation functions in an optimization process. But, of particular interest are the image-based methods, which are briefly reviewed here as they are in direct use in GM.

Image-based techniques aim to use the available images of GM directly without considering any shape descriptors. These methods can use the manifested complexity of GM in the provided X-ray images directly. Therefore, the common simplifications introduced in the previously described shape descriptors, or in the lower-order statistics, are no longer used, but the morphological properties of particles are extracted directly from such images and used in the final pack without sacrificing the convolution in GM. One of the successful image-based modeling techniques is the cross-correlation-based simulation (CCSIM) which can produce realistic packings of particles in 2D and 3D [133]. This method in essence is a Markovian technique where the previously simulated points/cells are used to estimate the current cells.

The CCSIM algorithm is used on a computational grid **G** which can be equal to the size of the target GM models. Note that the size of the input digital image can be different from the **G**, meaning that, for example, very larger models can be produced using a representative input digital image (**DI**). Both models are considered 2D/3D matrices on a Cartesian grid. Each cell on **G** will get a value z and, thus, it can be shown using $\mathbf{G} = \{z_1, z_2, \cdots, z_N\}$, in which N is the number of cells in **G**. To begin the modeling process, **G** is divided into small blocks **T** ($T_x \times T_y$) with a certain overlap **OL** ($D_x \times D_y$) between them. As will be discussed shortly, the **OL** region is considered to produce granular models with a seamless transition between the blocks. Then, the following probability is calculated for each cell:

$$p(\mathbf{Z}) = p(z_1)p(z_2|z_1)\cdots p(z_N|z_{N-1}, z_{N-2}, \cdots, z_2, z_1). \tag{4}$$

Evaluating the above chain of equations can be computationally expensive when one deals with large models. Alternatively, this

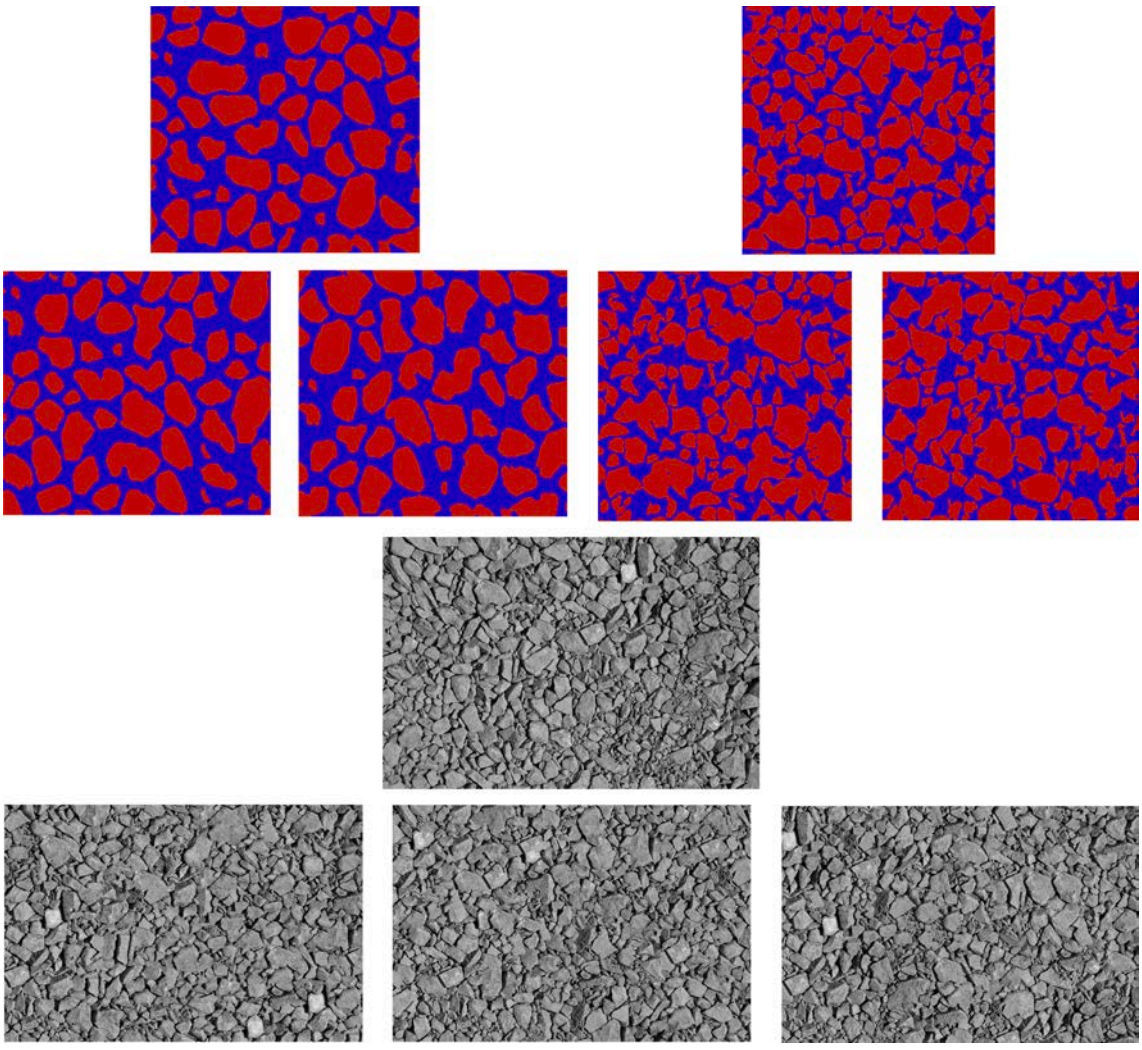

Fig. 19. Produced models using an image-based simulation for an angular sand sample (upper left), silica sample (upper right), and also a granite-type continuous image (lower two rows) [81].

equation can be estimated using a Gaussian kernel, or here Euclidean distance, which calculates the distance between the current **OL** regions and the entire patterns in the **DI**:

$$d^2 = \sum_{x=0}^{D_x-1} \sum_{y=0}^{D_y-1} \{\boldsymbol{DI}(x+i, y+j) - \boldsymbol{OL}(x,y)\}^2, \tag{5}$$

where $i \in [0T_x + D_x - 1)$ and $j \in [0T_y + D_y - 1)$ and $i,j \in \mathbf{Z}$. Due to using a raster path in this algorithm, the above equation can be decomposed and calculate $\mathbf{DI}(x+i, y+j)^2$ and $\mathbf{OL}(x,y)^2$ only once [82,132]. Thus, this equation can be summarized as:

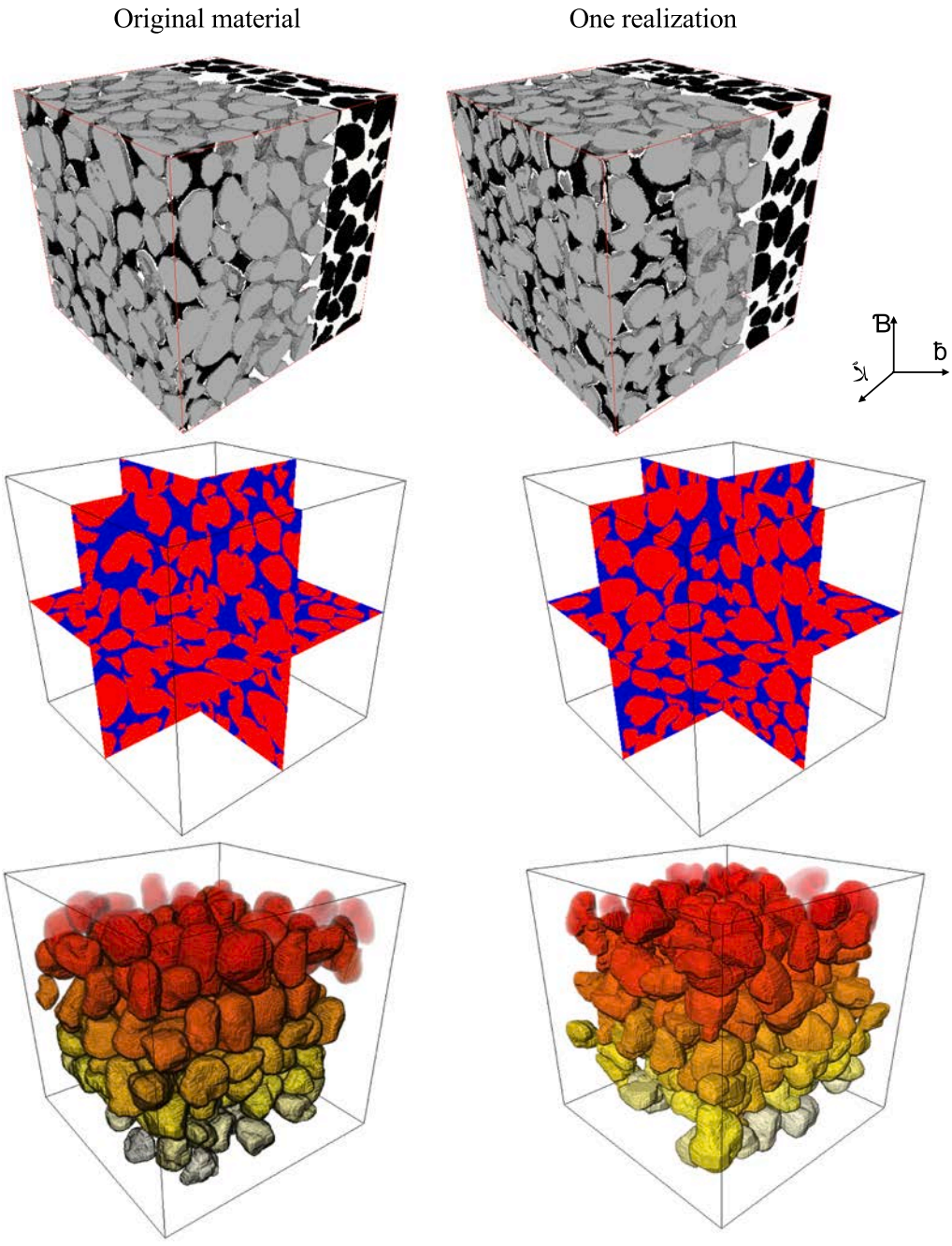

Fig. 20. One realization produced using image-based modeling for a complex 3D sandstone sample. For the sake of comparison, the original image based on which the synthetic sample is produced is also shown here. The results can be compared from different angles [81].

$$\mathscr{C}(i,j;x,y) = \sum_{x=0}^{OL_x-1} \sum_{y=0}^{OL_y-1} \mathbf{DI}(x+i,y+j)\mathbf{D}_T(x,y). \tag{6}$$

This equation was further accelerated by conducting the computations in the Fourier domain [134]. After defining the corresponding equations, the described algorithm selects the first pattern randomly from the **DI** and inserts it in a corner in **G**. Then, based on the defined **OL**, the next block is simulated by taking the **OL** region and calculating its similarity with the entire **DI**, which results in a similarity map using which the patterns can be sorted. A certain number of similar patterns are then selected and one of them is randomly chosen and inserted in the visiting area. This procedure is continued on the raster path and only the **OL** region(s) is changed. It should be noted that this algorithm also takes advantage of various other features for addressing the patchiness issue and also producing conditional models. Furthermore, this method can be used with non-stationary systems, those whose statistical properties vary with space and time, as well as continuous images [135]. Some of the results using this method for 2D and 3D systems are shown

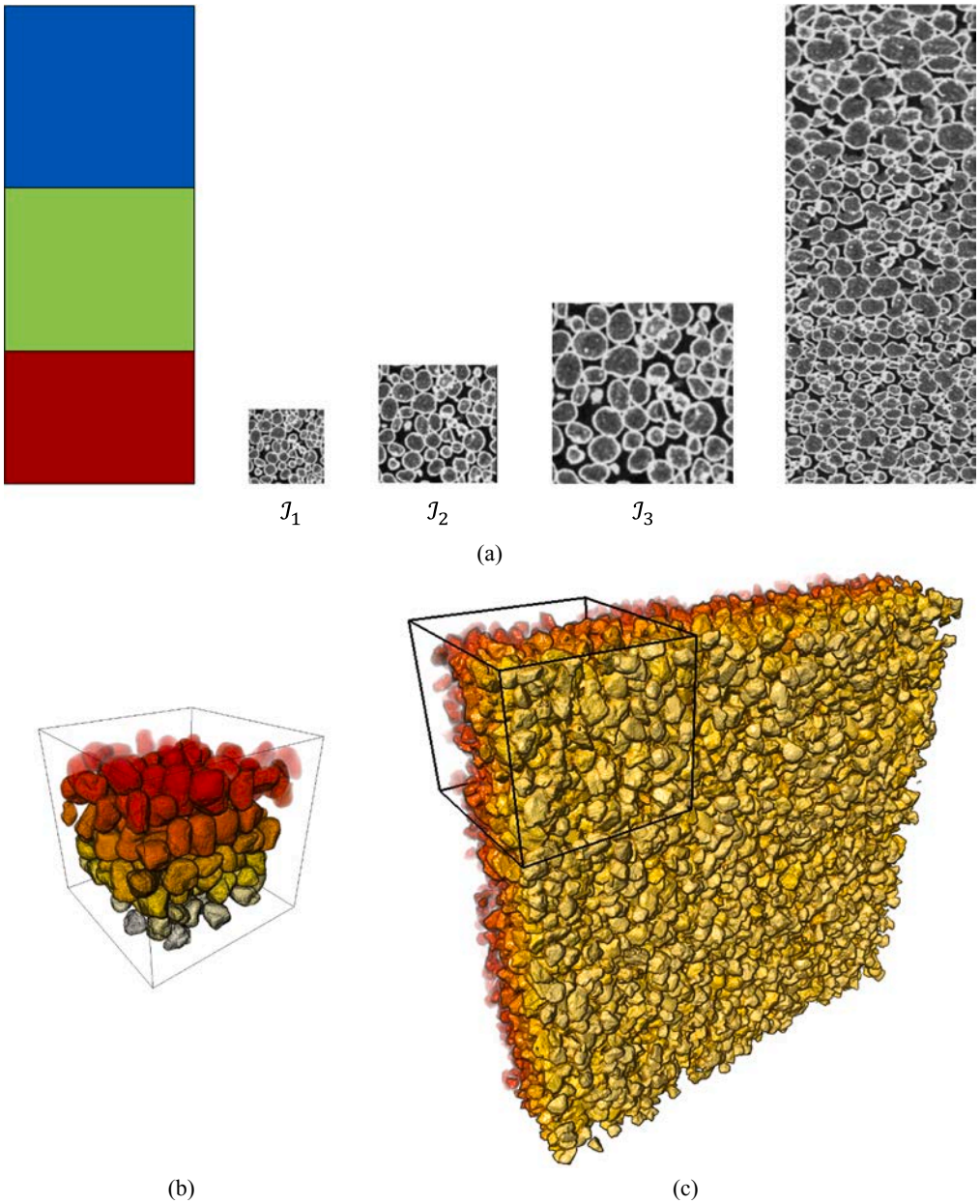

Fig. 21. (a) producing conditional models, here scale-dependent heterogeneity, using three auxiliary regions. Each region has a specific degree of compaction, and all these three features are shown in the produced model where a seamless transition can be observed between such regions. (b) a small input image and its corresponding large pack of particles in (c) [82].

in Fig. 19 and Fig. 20, respectively.

As mentioned, image-based modeling can be easily used to produce more realistic models. For instance, the size of grains can be controlled within a conditional framework such that one single input can be used while models with different properties are produced. Furthermore, these methods can use images of any size while much larger models are produced. Two examples are shown in Fig. 21.

2.1.2.3. Position and orientation. All the following quantitative analyses can be conducted on either the original or produced stochastic models described above. One such analysis is characterizing the position and orientation of particles. Quantitative analysis, however, requires post-processing of the acquired images to detect the location of the particle's surface [136,137]. After extracting the detailed shape information, further analysis of the experimental data can be achieved. Obtaining such properties is important for accurate characterizations. Depending on what type of imaging technique is used, a 3D reconstruction of the 2D slices is produced and then the particle positions, orientation, and shape can be tracked by computerized post-processing of the data. In some situations, recording a single 2D slice of the sample might be adequate to track the dynamics. In such cases, Refractive Index Matched Scanning (RIMS) and MRI can provide single slices at a very fast data-collection rate [138].

2.1.2.4. Displacement and velocities. Imaging techniques can also be used for measuring displacements and velocities. To achieve such, some form of imaging is taken before and after some agitation of the material, such as shearing or mixing. Displacement measurements can be obtained by obtaining the position of the object. This must be carried out with precision. Particle velocities are obtained from the particle displacements which occur within a time interval. From these measurements, a velocity field can be obtained based on the accumulated measurements as the particle moves. An easier approach is, however, to obtain a Lagrangian particle trajectory in which high-precision particle position measurements have been made from which the corresponding times are recorded simultaneously. Thus, the velocities can be deduced. Translational motion by tracking the centers of the particles can also be recorded. Tracking individual particles can be achieved by tagging a small number of tracers. The rotational or sliding motion requires information such as form, intensity distribution, tracking marks, or patterns on the particles. Tracer particles (single radioactively labeled in the case of PEPT, high dielectric constant for radar tracking, steel spheres for X-ray radiography, or NMR-active nuclei for MRI) can be embedded inside the material (or spin-labeled in MRI) and the system is imaged while subjected to some excitation or loading. Velocities can be measured without the identification step. One of the relevant techniques is MRI. This technique could use a time-varying magnetic field as a probe and then allow the velocities of the MRI-active particles to be deconvolved from the response signals.

The above-described goal can be achieved in GM by labeling the grains [72]. For example, Cheng et al. [139] applied MRI to describe the evolution of granular shear flow as a function of height in a split-bottom Couette cell, as well as the 3D flow profile with MRI of tracers. NMR-labeled grains or NMR-active nuclei i.e., poppy seeds, in this case, served as markers to a system composed mainly of amaranth seeds. Both seeds had comparable diameters and densities. The images were recorded while the system was subjected to some excitation or loading and thus the flow profile could be reconstructed from the cross-correlations of these images. Börzsönyi et al. [140] used BioSpec 47/20 MRI scanner to map out displacement and the width of the shear zone at the surface with color-marked grains non-invasively. Poppy seeds were used as markers in low concentration to the MRI-invisible glass beads and corundum grains. The images were recorded at slider displacements in 2.5 mm steps, and the tracer positions were extracted. From the displacements of all tracers, a shear zone profile was reconstructed in each slice. Other methods for detecting displacements using MRI scans are by labeling spins or spin tag approach in certain regions of the sample using an appropriate tool to detect rearrangements of particles. Ehrichset et al. [63] studied the displacement of particles in a container after one single shake. The authors studied the detection of the convection flow based on the cylindrical container (16.5 mm) filled with poppy seeds.

Another solution to obtain flow profiles of NMR-active grains or of interstitial fluids in a granular bed is gradient-echo experiments from which the velocity along the gradient (field gradients of the opposite sign of magnets refocuses the magnetization in the absence of translational motion) can be obtained. Both methods can be combined to obtain a more comprehensive view of flow in complex geometries. Such a strategy was chosen, e.g., in a study of the flow of a fluid (water) through a cylindrical tube (19 mm) filled with randomly packed glass beads (4 mm) and different catalyst pellets [141].

2.1.2.5. Lattice strain. Obtaining particle strains is important since some measurements such as force distributions cannot be attained directly and hence are inferred from strains [142]. Lattice strain tensors can be obtained experimentally and subsequently employed to compute the corresponding stress tensor assuming an elastic stress–strain relationship. Computed average lattice stresses within particles will eventually be related to interparticle contact forces and force chains using 3D finite-element analysis [143]. X-ray and synchrotron imaging methods have been applied in a large number of tasks involving particle kinematics. It has also been used for strain measurements. The first application of X-ray radiography for strain measurements was for 2D strain fields in the sand [144]. 3D measurements based on localization patterning in the sand followed [145–148]. These studies demonstrate the potential that X-ray tomography could exhibit as a quantitative tool. Other measurements with synchrotron, which provides a much finer spatial resolution, were performed later [149], after in-situ testing [150,151].

Despite the tremendous improvements over the years in the above techniques, they still fall short in their ability to measure interparticle forces and strain within particles. Neutron diffraction techniques, however, have been applied. Neutrons have a power of penetration much higher for most materials than that of X-ray's. Thus, using Neutron diffraction techniques, it is possible to measure strain and stresses because it can go beyond the surface level because of high penetrating power making it a suitable tool for probing strains and stresses in the interior of bulk materials in a non-destructive way, as opposed to X-rays which are limited to the surface region due to the significant attenuation. The lattice strain in terms of d-spacing change can be defined as:

$$\varepsilon = \frac{d - d_0}{d_0}, \tag{7}$$

where d_0 is the interplanar d-spacing under stress-free conditions between planes that randomly align with the measurement geometry, d is the interplanar d-spacing for a given external loading between planes that randomly align with the measurement geometry, and ε is the lattice strain. Neutron diffraction measurements have been used [152,153], leading to small gauge volumes or elastic strain measurements of each particle being defined. 3D X-ray diffraction (3DXRD) microscopy, an extension of classical X-ray diffraction, has also emerged as a reliable non-destructive technique that can characterize the position and orientation as well as the volume-averaged lattice strain of hundreds of individual grains and sub-grains inside bulk materials. Hall et al. [142] carried out one-dimensional compression tests for Ottawa sand using 3DXRD measurements on quartz-glass odometers. Furthermore, several other studies such as Alshibli [154], within individual silica sand particles, Cil et al. [155], and Hall and Wright [156] have also conducted similar experiments. Full-grain kinematics characterization has also become possible using X-ray tomography plus particle tracking.

X-ray micro tomography imaging along with 3D volumetric digital image correlation (V-DIC) techniques was applied to view details of grain-scale details of a deforming sand specimen, as well as the 3D displacement and strain fields evolution throughout the loading process [120,157]. Mehmet et al. [143] presented an integrated technique of applying both 3D X-ray diffraction (3DXRD) and SMT acting to examine the lattice strain evolution in natural Ottawa sand particles; see Fig. 22. They addressed the need for the measurement of particle kinematics while also investigating the elastic and plastic deformations simultaneously. They examined the evolution of particle fracture and deformation characteristics of the sand assembly using high-resolution 3D SMT images while the average particle-averaged lattice strain within each sand particle was measured using 3DXRD and then used to calculate the corresponding lattice stress tensor. Hence, the ability to track particles while calculating the volume-averaged strain tensors at different load stages in 3DXRD data analysis was made possible. More recently, in situ X-ray tomography and 3DXRD analysis have been studied by Pagan and co-workers for investigating the mechanical behavior of non-cemented and lightly cemented quartz particles under quasi-static confined uniaxial compaction [158] and in situ fracture evolution during compaction [159,160].

2.1.2.6. Force chains. Quantification of interparticle forces has been a very important subject over the years. Mapping out of these forces in GM requires a high level of complexity based on the particle shape, anisotropy, and loading condition. When loads are applied on such a granular assembly, the in-contact particles form a complex network to resist the applied load. These particles, based on their initial configuration, tend to first self-organize by translating and rotating and eventually form a heterogeneous structure or force chain [161–163]. In other words, such structures are capable of linking up with neighboring particles and eventually readjusting to handle the loading requirement of the bulk system. These regions are primarily characterized as having high contact stress while other regions possess lower contact stresses to act as a cushion for the force chain particles [164]. Two examples of force chains are shown in Fig. 23.

One of the routes through which a force chain can be characterized is using the coordinate number Z, which describes how many contacts a particle has with its neighboring ones. This number can provide insight into the stability of GM and also pertain to the microstructure and its network. As such, various studies have tried to formulate this important parameter using experimental

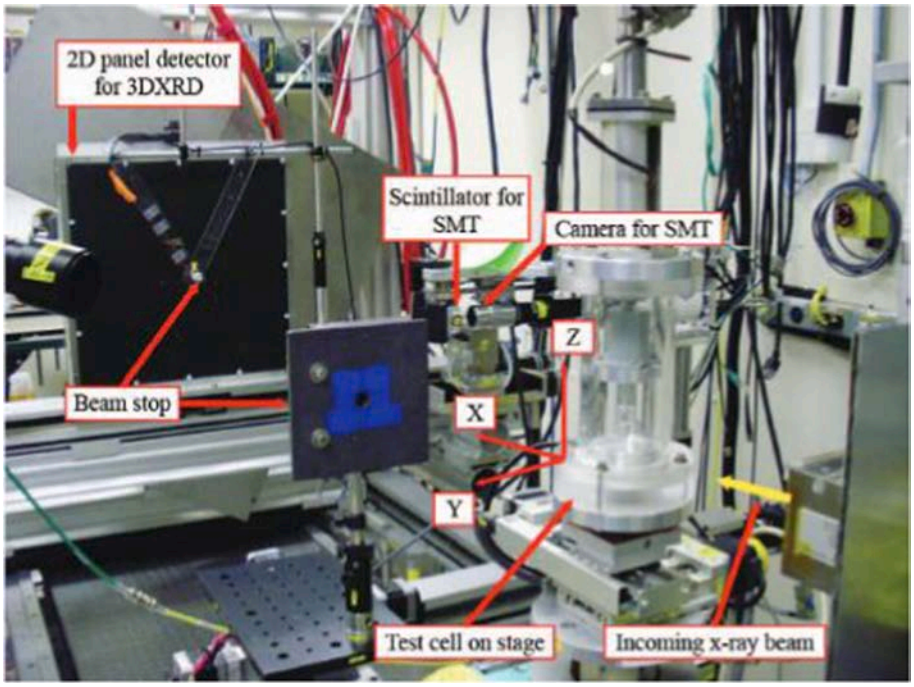

Fig. 22. Combined 3DXRD and SMT [143].

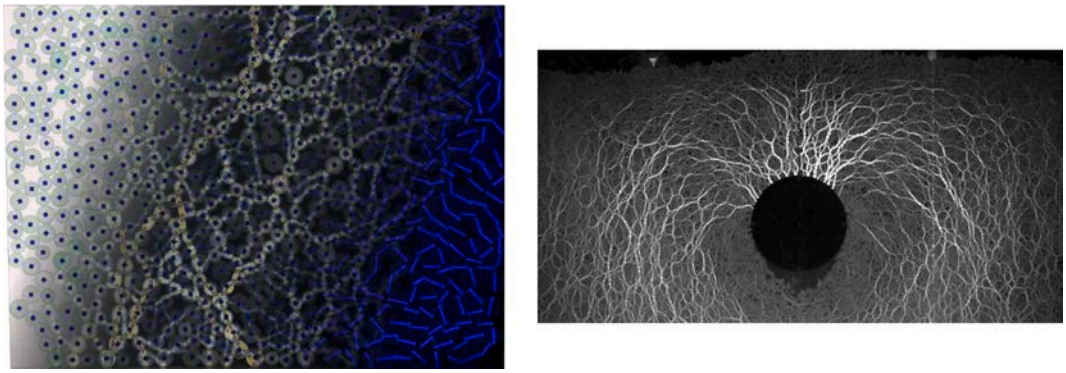

Fig. 23. (left) an integrative image showing actual particle on the left side, force chains in the middle, and rotation of particles in the right, (right) force chains in GM when an intruder – the black circle - is pulled out from the system [165–167].

[168–170] and numerical tests [171–174]. For example, this number is found to be 2 for 2D circular disks and also 6 for very dense hexagonal packing. In 3D models, a power-law equation is also derived based on the porosity/void-space ϕ of the pack and that is $\phi = Z/(z+2\times\sqrt{3})$. Due to such a strong relationship between the particles in GM, it is believed that force chains go beyond the individual particles, and they can act like a wave. Furthermore, force chain has been shown to be more important than the contact network which only demonstrates how particles are connected. In fact, the contact network only shows the structure using which the forces *may be* transmitted and are often distributed consistently as they are mostly controlled by the porosity and particle size distribution. The force chains, on the other hand, manifest both the structure and also the magnitude of forces transmitted using particle–particle contact.

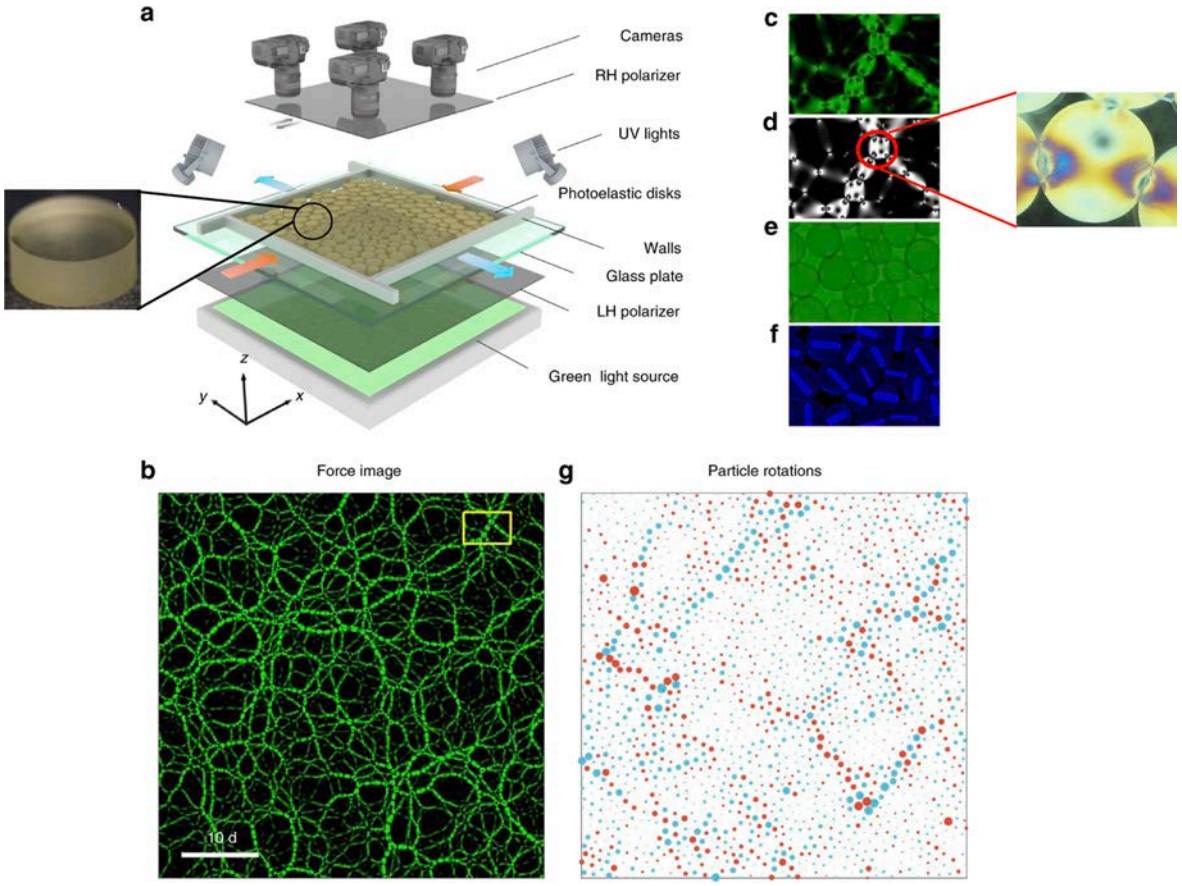

Fig. 24. (a) A workflow for conducting force chains experiment, (b) force chains in a random time-step, the yellow area in (b) is further demonstrated in (c-f) where (d) is the same region after completing a cleaning process, (e) the actual particles, (d) a UV image for showing the rotations, and (g) the global distribution of orientations [166,208].

Besides, force chains are more responsive than the GM's structure [2]. As such, the GM's system can experience a significant change in force chains while the particles remain in the same position. Thus, force chains can be counted as the main cause in studying the stability, flowability, elasticity, and mechanical behaviors of GM. The study of force chains can, in fact, provide a clear link between the mechanism of the formation of shear bands, internal failure of granular bodies and the buckling of force chains. The investigation of such contact forces has been carried out by experimental and numerical techniques. In this section, we will discuss the experimental techniques and the numerical methods will be examined in the next part.

Photoelasticity is perhaps the most common method for quantifying the internal stresses within solid bodies [161–163]. This technique is based on light polarization and the medium's refractive index. As shown in Fig. 23, this method produces visible and colorful patterns based on the force exerted on the particles which eventually allows one to quantify the stress in GM using the stress-optic law [175]. One of the advantages of this technique is that it can be used to make both qualitative and quantitative measurements of the existing forces. It is capable of generating high-quality images of stress within the GM which can be used to quantitatively determine the vector contact forces for each of many circular particles in the granular system [163]. It was first applied to GM by Wakabayashi [176] who used epoxy tracer particles. Since then, this method has been used on other systems [177–181]. Some of such applications are the characterization of erratic stress variability in shear GM [182–184], the response of a granular material to local perturbations [185], shear jamming [186–189], impact in GM [179,190,191], the effect of particle morphology on stress distribution and contacts [192,193], sound propagation [194–196], dilatancy softening [197], the sensitivity of granular force chain orientation to disorder-induced metastable relaxation [198], and the effect of fluid flow [199], as well as other related fields such as the effect of stress caused by plant roots [200–202] and faulting in earthquakes [203–206].

Fundamentally, photoelasticity is defined based on the change of optical properties when a material experiences deformation, in particular the dielectric media. This method can provide an easy way of observing internal stress in GM. In other words, certain transparent materials show birefringence behavior in which the passing light through the material experiences two reflective indices. Using this specific characteristic, photoelastic materials manifest double refraction when they are under stress and the magnitude of reflection can be related to the amount of stress at that point. This unique feature is not available in all materials. However, one can replicate the photoelastic properties by using various linear polarizers and quarter-wave plates around the target materials. The easiest way is, probably, cutting sheets/particles from materials that already exhibit photoelastic properties, such as Plexglas or polyurethane. Alternatively, one can also use 3D printing for more complex shapes. Some examples of this solution are Durus White [207] and VeroClear. After preparing the GM and depending on the magnitude of the photoelastic response as well as the level of accuracy, the imaging method must be selected, which is discussed extensively elsewhere [166].

Once the imaging technique is selected, recorded images can be analyzed to produce quantitative results (e.g., orientation, position, and force), which all depends on the quality of images, the sensitivity of photoelastic particles, and also some boundary conditions, such as the magnitude of the external load. One of the popular workflows is shown in Fig. 24. As can be seen, the initial step starts with taking images from the GM when it goes under stress. At a larger scale, the force chains can be seen. For instance, a small region of the force chains is selected and presented separately. Using this small and simple example, the particles should be segmented so that they can be tracked easily. Furthermore, a channel, usually a UV ink bar, is often placed on each particle to make the tracking easier using which the orientation of particles can be followed.

The final step is calculating the forces on each particle. This can be accomplished using two methods, namely, a light intensity-based method [209], which is very quick, and also solving an inverse problem to get vector contact forces. The former method assumes that the intensity of particles increases with the exerted force linearly. This concept is shown in Fig. 25 where the initial linear section is often used for setting a threshold force above the image intensity reaches a plateau. Using this threshold the forces can be calculated by the gradient of the intensities [163,167,179,182,183,185,188,189,191,197,210–212]. The second method, namely considering the problem as an inverse problem, aims to consider a known stress field using the contact forces and calculate the corresponding intensity field, which can be achieved using an optimization method.

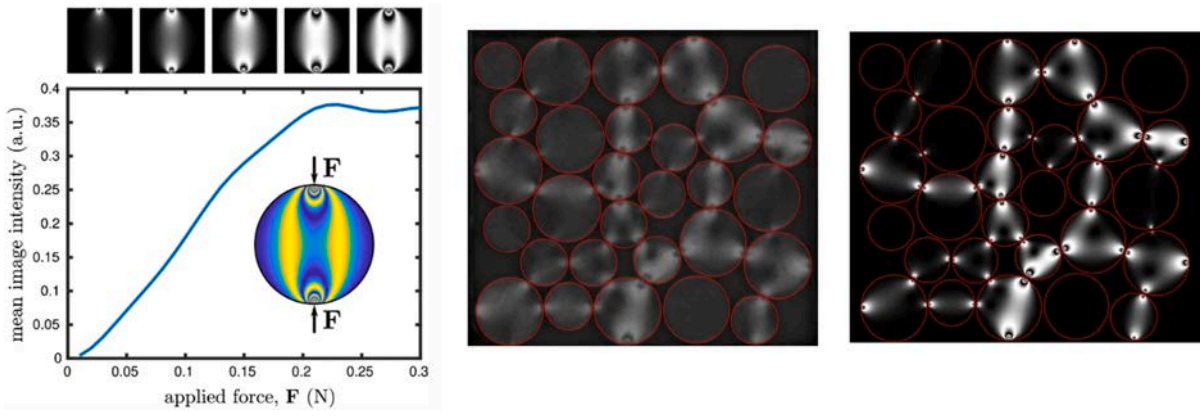

Fig. 25. (left) Demonstration of relating mean image intensity to force in photoelastic particles for a single disk. Comparison between experimental (middle) and an inverse problem method (right) for calculating the contact force [166].

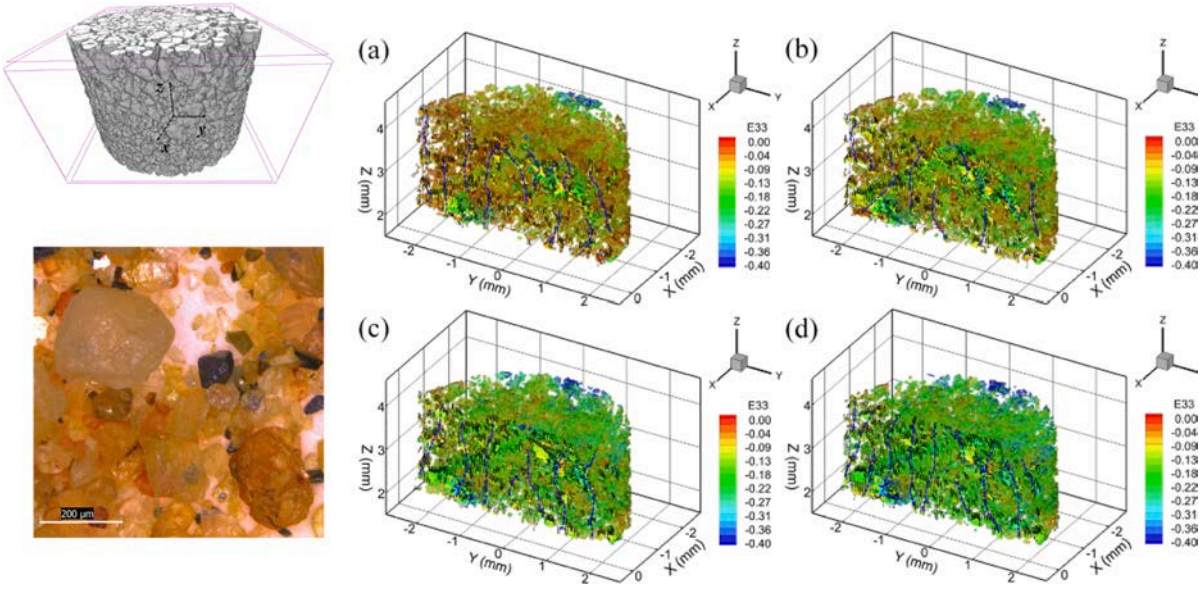

Fig. 26. (a) Optical micrograph of Mason and segmented image. (b) Force chains formed using DVC [216].

Despite the capabilities of photoelasticity for clear visualization of force chains, they involve the use of idealized shapes such as spheres and ellipses although more complex shapes with lower accuracy can be produced using 3D printing. Therefore, in order to carry out particle kinematics studies for more complex GM, X-ray tomography is a valuable tool. Extracting of interparticle forces was achieved by using experimental data from XCT and 3DXRD in tandem with an equilibrium averaged force constraint model to compute the force chain [213,214]; see Fig. 26. Refractive index matching tomography has also been applied for measuring 3D force information for deformable hydrogel particles that are compressed and decompressed uniaxially. As described in the earlier section, a combination of high-resolution diffraction techniques plus particle tracking can help in obtaining interparticle stress/strains. Averaged grain strains can be estimated and used to infer forces transmitted between contacting grains [142]. Hurley et al. [215] combined 3D X-ray diffraction, X-ray tomography, and a numerical force inference technique to quantify interparticle forces and their heterogeneity in an assembly of quartz grains undergoing a one-dimensional compression cycle. Most of these studies, however, have been performed on 2D disks or 3D spherical particles. Hence, there is still a need for studies that investigate force chains of the real 3D shape of GM. Imseeh and Alshibli [164] presented a technique for direct quantification of 3D force chains in a physical GM using a careful combination of neutron tomographic imaging and diffraction-based strain measurement. Hu et al. [216] investigated the mesoscale behavior of Mason sand through X-ray tomography of a sample in compression. The mesoscale deformations were determined by incremental digital volume correlation (DVC) [217] which enables measurement of the 3D internal deformation from the volumetric images acquired from 3D imaging. The force chains were then analyzed using the approach given by Peters et al. [218].

2.1.2.7. Rose diagrams. Since GM appear in 2D and 3D, it is important to demonstrate the distribution of some of other their properties as they might vary on the surface of particles in different directions. One of the solutions is using the rose diagrams which are well-suited for showing the distribution of directional data on a circle/sphere. This plot contains all directions from 0 to 360°where its length represents the magnitude of the target variable in that specific direction. This diagram is very applicable in problems related to GM as it can briefly show force directions and connect them to the structures. This plot provides an efficient way of analyzing large contact networks [219–221].

One of the common analyses in GM is studying the contact normal vectors and their distributions. This parameter can be related to the void space, stiffness, and strength if analyzed in different directions. In 3D samples, one can provide this quantity with three elements representing X, Y, and Z directions. But, for the sake of simplicity, one can consider only the 2D direction by projecting the contacts on a 2D plane, which makes it more suitable for the rose diagrams. An example of such analyses is shown in Fig. 27 for different strains ε_a. In this test, a granular sample is under an axisymmetric triaxial compression with confining pressure. As can be seen, the rose diagram initially shows a preferential orientation in the horizontal direction, which is due to the natural orientation of particles as they are deposited in the domain. As the strain increases, the contact normal distribution deforms into a vertical orientation after $\varepsilon_a = 6.9\%$. Thus, the rose diagram can be used to briefly analyze the contact normal forces in different directions under variable boundary conditions and provide some insights on how such conditions can change the directional properties (e.g., contact force) [222]. The images in Fig. 27(a) indicate how the initial anisotropic force distributions are evolving with strain. Furthermore, an example of the 3D rose diagram is also provided in Fig. 27(b). These plots are more informative since they represent the variabilities in all three directions.

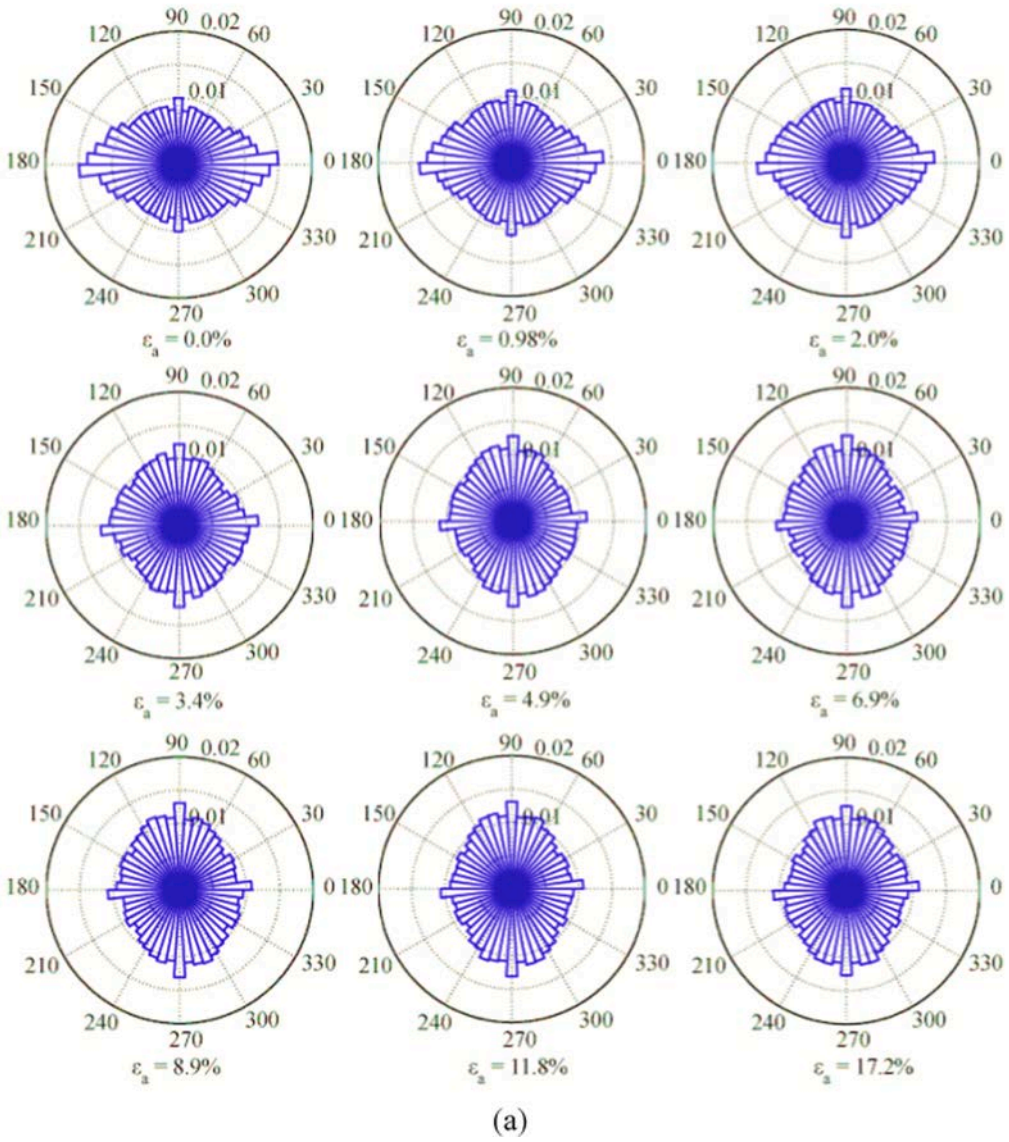

Fig. 27. (a) evaluation of global contact normal distribution for a GM sample under different strains [223], (b) anisotropy evolution for different variables in a granular system under a shear tress [224].

2.1.2.8. Particle-to-Particle contact. Another subject that is important is the detection of particle contact and orientation. An accurate 3D description of the particle contact configuration for GM is fundamental for the development of micromechanical constitutive models. Particle-to-particle contact and evolution of contact are hence non-trivial components in fabric evolution and force transmission in GM [52]. Several techniques have been applied for characterizing particle–particle contacts from XCT and SMT images including Hasan and Alshibli [56], Hall et al. [120] Andò et al.[122]. These works identified contacts and spatial locations but did not define the location as well as the orientation of contact with neighboring particles which is required to investigate how particles interact with neighboring particles; see also the orientation of contact based on CT images [137,225]. Druckery [52] developed a code to analyze 3D images of GM and calculate particle contact location and orientation based on SMT imaging as well as to measure particle lengths, volume, surface area, and global centroid location. They assessed the fabric evolution of F-35 sand undergoing axisymmetric triaxial compression during in-situ SMT imaging using fabric tensor techniques. The techniques list above, however, require high-resolution images. Such images are, in fact, needed to provide more accurate particle boundaries as opposed to low-resolution images which produce blurry particle contacts.

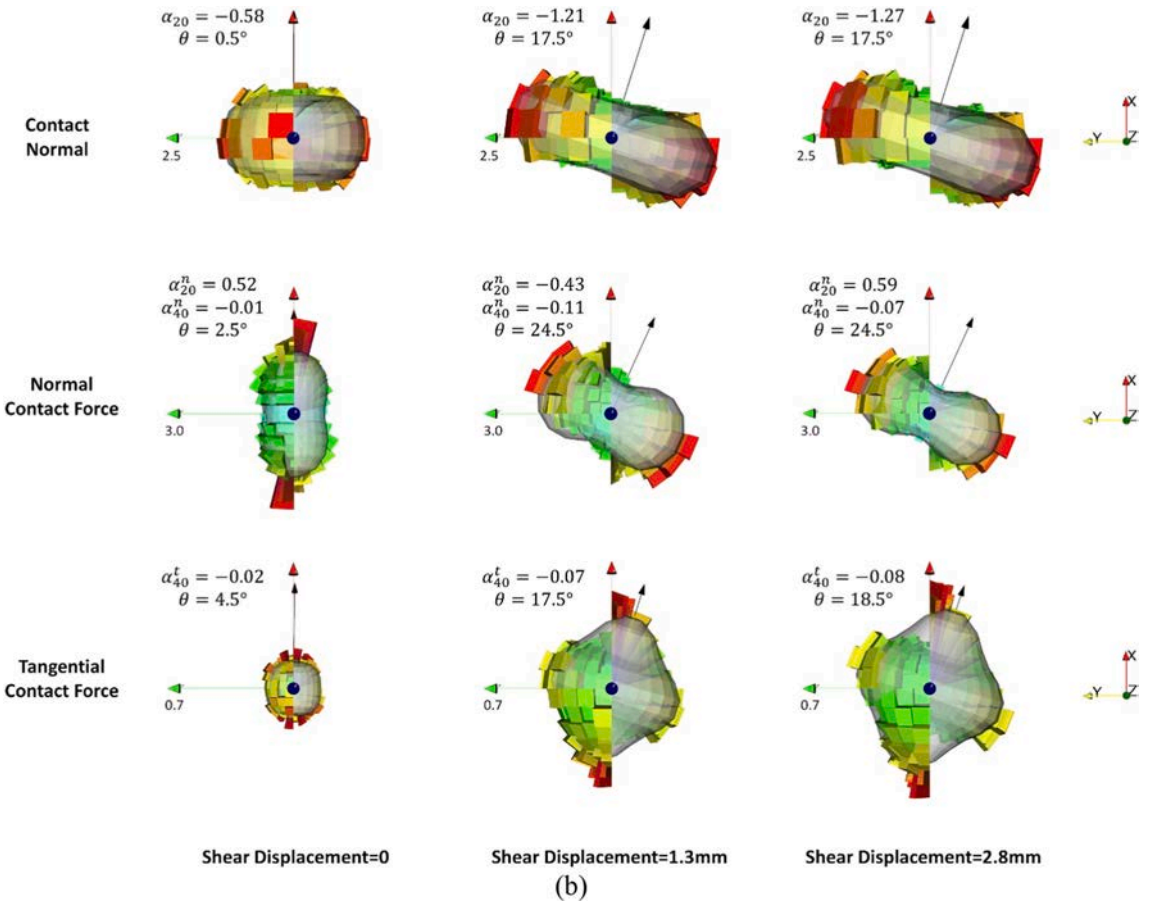

Fig. 27. (*continued*).

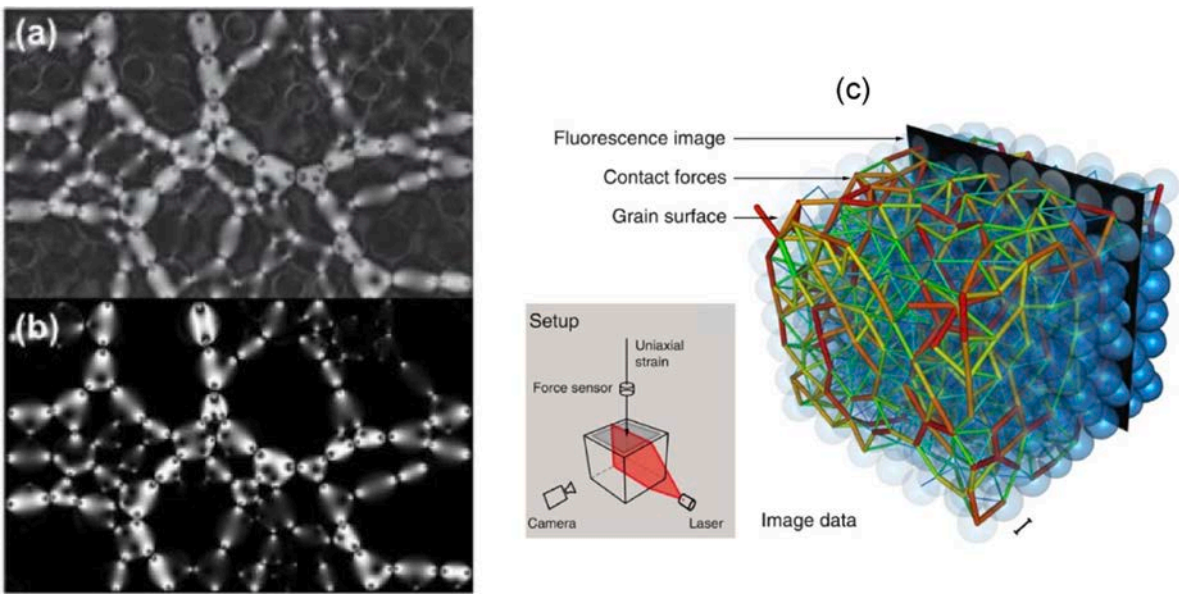

Fig. 28. Force chains obtained from photoelasticity. (a) Image of force chains obtained using darkfield photoelastic measurements. The bright areas indicate the regions where contact forces modulate the photoelastic response of the disks. (b) A computer-generated fit to the data is shown in (a). (c) Image of 3D interparticle forces obtained on frictionless hydrogel particles [226].

2.1.2.9. 4D imaging. As already discussed, X-ray's penetrative ability into samples makes it an attractive method for scanning 3D samples. Most scanning procedures have been used for static scenarios where 3D packing structures are imaged to provide precise microscopic structural information about the packings. Granular packings under external activity, however, pose a different level of intricacy such that they manifest a dynamic behavior and require special imaging techniques to carefully observe the structural evolvement under various excitations. Conventional X-ray tomography imaging techniques lack this capability due to the long data-acquisition time. However, newer techniques such as fast synchrotron X-ray micro-tomography have allowed for such measurements to be possible due to faster data acquisition times hence leading to the prospect of 4D imaging; see Fig. 28. Recent works using 4D digital image analysis have provided quantitative characterization of deformation and structural evolution (e.g., grain contacts, strain fields, and grain kinematics) in granular assemblies.

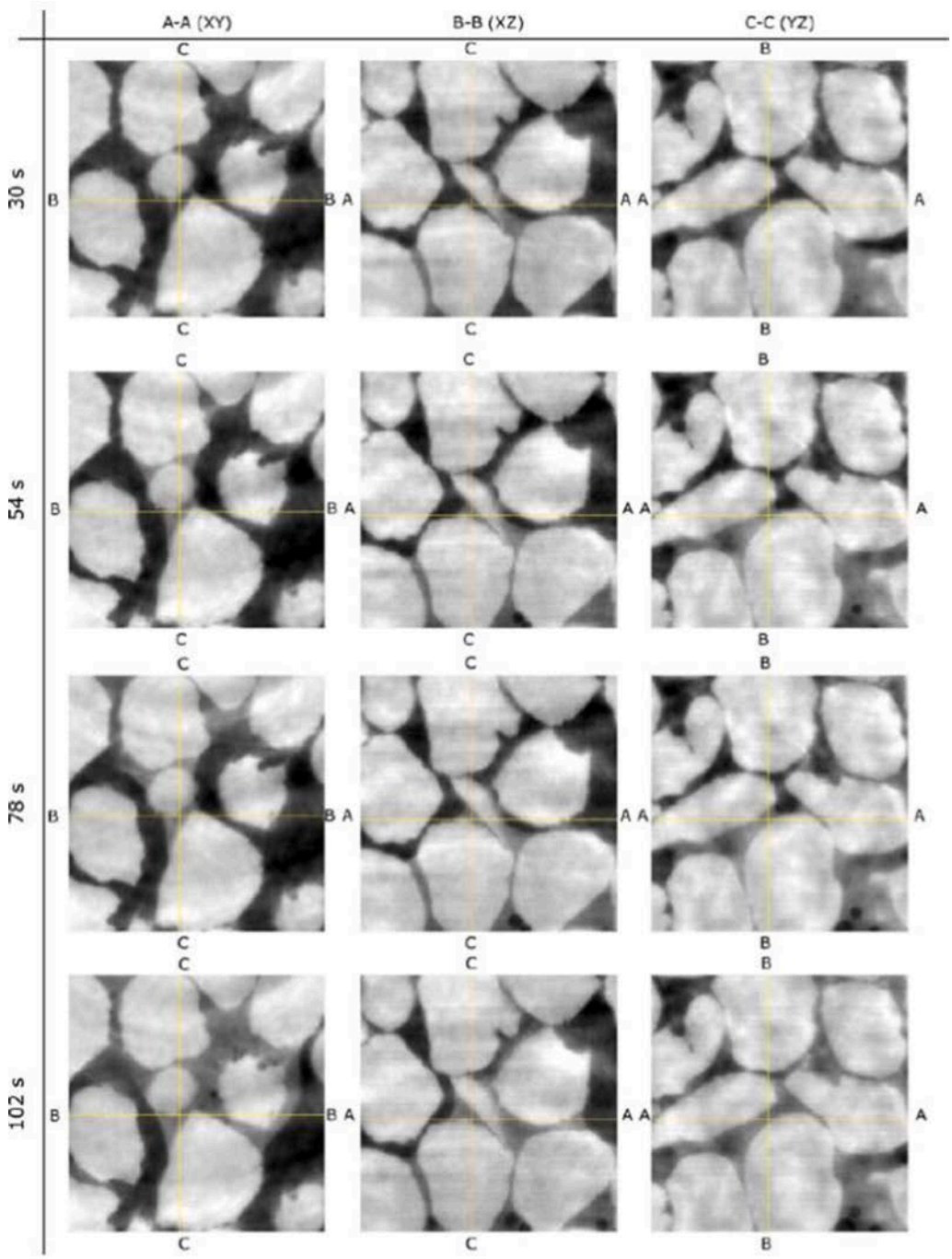

Fig. 29. Time-lapsed CT images at orthogonal orientations [229].

Wang et al. [227] utilized the dynamic synchrotron X-ray micro-tomography to image the evolution of a 3D packing of glass beads under vertical tapping. They tracked each particle's trajectory and mapped out the flow field of the whole packing under tapping. 4D imaging has especially been applied for agricultural purposes. Time-resolved, microfocus XCT imaging in 3D was applied by [228] to visualize, quantify and assess root/fertilizer interactions of wheat plants in agricultural soil during the entire plant life cycle. In-situ root/soil/fertilizer interactions were observed over 14 weeks to investigate the interaction of wheat roots with discrete granules of two contrasting fertilizers. Visualization of complex two-phase fluid flow in Ottawa sand column using 4D imaging was demonstrated by Kim et al. [229] at Argonne National Laboratory. Advancing fluid fronts through tortuous flow paths and their interactions with sand grains were captured, and formations of air bubbles and capillary bridges were visualized. Synchrotron 4D imaging allowed for the capturing of the dynamic evolution of both solid and fluid phases. Computed Tomography (CT) scans were collected every 12 (s) with a pixel size of 3.25 μm. Grain shape and fluid flow evolution are shown in Fig. 29 from 30 s to 102 s with scans collected at every 12(s). As fluid flow evolved, majority of the pore space was filled with fluid with formation of air bubbles also visible at the bottom of the volume from slices B-B and C–C.

2.2. Computational methods

Acquiring measurements within a particulate system could be a challenging task using conventional experimental techniques (i.e., XCT and SMT). The use of computational methods to quantify particle kinematics alternatively can be a faster approach particularly now with the advent of high computational power for systems with a large number of particles. Experimental techniques also still have difficulties in their temporal resolution and hence find it challenging. On the other hand, computational methods are used widely, and they can describe complex behaviors in GM with any needed resolution. Such methods, based on the way they represent the GM, are often categorized into two groups: the continuum and discrete states. Representing the GM in discrete form allows one to explore the complexity of GM more closely and accurately while such results can also be verified using analytical solutions. At the same time, continuum approaches (e.g., finite element/difference methods) are also used extensively for modeling systems with large deformation and for more practical applications. Another set of continuum methods, such as Smooth Particle Hydrodynamics (SPH), Particle-in-Cell (PIC), … (see the methods in this section), represent meshless techniques and they have been shown promising in dealing with different problems. However, these methods might not be very practical for those materials/cases where fracturing, fragmentation, and intense mass transfer occur. Therefore, the particle-based methods are reviewed to tackle such problems, which can be used for various scales, starting from atomic- to particle-scale. Aside from the above topics, other methods such lattice-Boltzmann method (LBM), which is used widely to simulate complex particulate and fluid flows in GM applications, will also be reviewed. All such methods aim to model the rheology of GM and determine how such systems move in both small- and large-scale domains.

Before going over the aforementioned methods, let us discuss the importance of rheology. The rheology of GM is, indeed, governed by momentum between the particles and also energy dissipation (friction and inelastic collision) when particles are in contact with each other. This event can be described using a dimensionless measure called the inertial number I:

$$I = \dot{\tau}\overline{d}\sqrt{\rho_p/\sigma_c}, \tag{8}$$

where $\dot{\tau}$ is the shear rate, $\overline{d}$ is the mean diameter of particles with a density of ρ_p, and σ_c is the confining pressure. This equation can be interpreted as the ratio between the inertial time $\left(\rho_p/\sigma_c\right)^{1/2}/\overline{d}$ and the shear time $1/\dot{\tau}$, respectively. A simple shear flow can be produced when the GM is sheared by applying a constant velocity while a constant σ_c is applied, which results in increasing the μ as ϕ reduces. Alternatively, one can keep ϕ constant while σ_c and $\dot{\tau}$ are variable such that σ_c increases when the shear is applied. The rheology of granular flows can be described using μ, ϕ, coordinate number Z, and contact anisotropy a_c, which all are controlled by I. Using this measure, the GM can be fully characterized. For instance, the granular flow is called *collisional* when I is very large. The granular flow is also called *quasi-static* when I is small (e.g., $I < 10^{-3}$). If I is something between the above limits, then, the flow regime is called *granular liquid* and it represents a dense flow.

In general, two classes of methods are developed for dealing with particle collision, namely deterministic and stochastic techniques. In the former approach, the collision between two particles occurs when their trajectories meet. These methods are mesh-free and very accurate for particles but can be computationally expensive. On the other hand, stochastic methods are very fast but not as accurate as deterministic techniques. These methods calculate the collision probability of a particle with a radius of r_i with other ones in a mesh cell using:

$$p_{ij} = \frac{\pi\left(r_i + r_j\right)^2\left|\boldsymbol{v}_{ij}\right|\Delta t}{V_{\text{cell}}} = \beta\frac{\Delta t}{V_{\text{cell}}}, \tag{9}$$

$$\beta = \pi\left(r_i + r_j\right)^2\left|\boldsymbol{v}_{ij}\right|, \tag{10}$$

where $\boldsymbol{v}_{ij}$ is the relative velocity between two particles i and j, Δt is the timestep, V_{cell} is the volume of the cell, and β is the collision kernel. If p_{ij} follows a Poisson distribution, then:

$$P(N) = e^{-\overline{\mu}}\frac{\overline{\mu}^N}{N!}, \tag{11}$$

where $\overline{\mu}$ equal to p_{ij}. Therefore, a collision occurs only if a uniform number $RN \in [0, 1)$ satisfies the following condition:

$$RN > e^{-\bar{\mu}}. \tag{12}$$

These methods have, however, several shortcomings. First, β is defined as in molecular kinetic theory while it should reflect materials properties and the existing fluid in the system. Second, the utilized Poisson equation is not physically realistic and thus adds more ambiguity to the collision's calculations. Third, Δt, which is considered as the time a particle moves between two collision locations does not have any limit and it makes this parameter to be very sensitive. Given the above issues, these methods have not received much attention for the understanding of GM and are not discussed largely in this review paper. However, it should be noted that it has been implemented for large-scale simulations in various commercial codes.

2.2.1. Particle-Finite element method

Small-scale computational modeling always provides invaluable insight into the main phenomena involved in complex systems. Many large-scale modeling formulations are developed based on such observations. Thus, using such methods is crucial. However, simulating large-scale systems using the complexity considered in fine-scale techniques is not feasible currently. It is, therefore, necessary to develop methods that can mimic the fine-scale features as much as possible. This problem even becomes more complicated when one aims to develop multiphysics modeling. One of the most practical and primary methods for achieving this goal is probably the finite element method (FEM) which is used on a mesh.

FEM is quite an effective way of modeling deformation, which itself can be divided into several groups depending on the particular application. One such classification is based on the considered framework, which includes Eulerian and Lagrangian approaches. In the Eulerian approach, the field is defined as a function of location $\boldsymbol{x}$ and time t; e.g., flow velocity $\mathbf{u}(\boldsymbol{x}, t)$. On the other hand, particles are tracked in the Lagrangian approaches with time while they are labeled by, for instance, a time-independent vector property $\boldsymbol{x}_0$ (usually the center of the particle at time t_0). Thus, flow can be characterized by $\mathbf{X}(\boldsymbol{x}_0, t)$. These two approaches can be linked using:

$$\mathbf{u}(\mathbf{X}(\boldsymbol{x}_0, t), t) = \frac{\partial \mathbf{X}}{\partial t}(\boldsymbol{x}_0, t), \tag{13}$$

where $\boldsymbol{x}$ and $\boldsymbol{x}_0$ are called Eulerian and Lagrangian coordinates.

Translating the above definition for a Eulerian approach in the FEM framework represents a system where the FE mesh is fixed while the material is moving in the grid. Therefore, since the material and grid are detached, convection is considered in the relevant equations. Eulerian methods are often used for systems with large deformations but tracking the interface in such a method is difficult and one can add more advanced methods such as level-set [230] or volume-of-fluid methods [231]. In contrast, the FE mesh moves

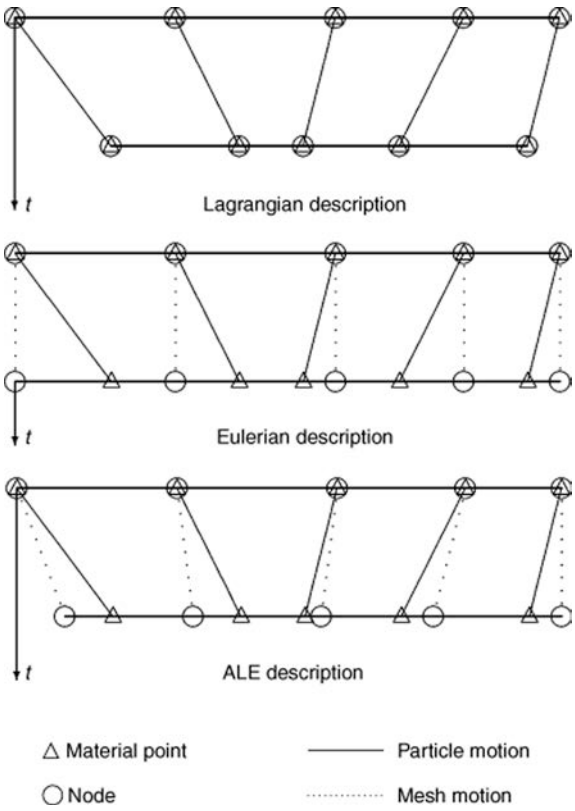

Fig. 30. A simple and 1D representation of Eulerian, Lagrangian, and ALE for particle [239].

with the material in the Lagrangian approach in which the interfaces are tracked, and no convection is considered as well. This approach, however, can introduce substantial distortion for large deformations.

A middle-ground approach is the Arbitrary Lagrangian-Eulerian (ALE) method in which the computational framework is neither attached to the material as in the Lagrangian method nor fixed in the domain as in Eulerian techniques. This approach can resolve many of the issues in the above two formulations such that the computational grid can move arbitrarily in the domain to adjust the shape of elements whereas the interfaces' mesh can also move with the material which allows tracking the interfaces and boundaries. This feature is schematically shown in Fig. 30. As can be seen, the computational mesh in the Lagrangian method follows the particle during the motion. On the other hand, the mesh is fixed in the Eulerian algorithm. However, the ALE method can move the mesh with particles, or adjust it in an arbitrary way to enhance the capability of the simulation. This flexibility, compared to the purely Lagrangian and Eulerian methods, allows the ALE method to address the previous issues. This approach still can produce unrealistic results for large deformations [232].

In the context of GM, the idea behind Lagrangian mesh-based methods is more relevant when such systems undergo displacements. As such, various attempts have been made to address the issues mentioned above regarding mesh deterioration: conducting a remeshing [233–237], or not using a mesh by applying mesh-less techniques. The latter approach has been used widely in GM as one can represent the system and its physical properties as a collection of particles. These particles can be displaced based on their assigned physical properties (e.g., weight) and also their interactions with the surrounding particles [238]. We will come back to these methods shortly.

One of the effective methods in dealing with the issues in the Lagrangian methods is considering the Particle Finite Element Method (PFEM) wherein the capabilities of mesh-based methods are integrated with the particle-based techniques [232,240,241]. More specifically, a fast-remeshing approach can be used within a Lagrangian FEM method. This method considers a set of particles that overlap with the mesh nodes, and they are displaced in a Lagrangian fashion given their velocity and physical properties (e.g., viscosity and density). Therefore, the updated velocity, or in general the differential governing equations, is calculated using FEM because they are located on the nodes. Since the nodes are moving, thus, the mesh should be regenerated, in particular when the mesh experiences a significant displacement, which can be achieved using a Delaunay triangulation [242].

PFEM has been used on a variety of problems, including free-surface dynamics (e.g., dam break) [240,243–249], fluid–structure interaction [241,245,246,250–252], multiphase fluid flow [253–255], thermal coupling [253,256–258], hydraulic [249], landslides [259–261], and manufacturing [262–264]. In this review paper, however, we have put an emphasis on granular flow. GM have been considered using PFEM for their solid- and fluid-like behaviors where the quasi-static and dynamic behaviors of GM are reproduced [265]. This model is also extended for large deformations and plasticity [266], which eventually is extended to large-scale problems, such as tumbling mills [267]. The accuracy of this method has also been verified by comparing it to several experimental tests for collapsing [268] and large deformations [269]. The fluid-like behaviors of GM are also considered in this method [260,270]. An example of the PFEM method for the collapse of a cylindrical column of GM is shown in Fig. 31. This method is, however, not able to capture the fine-scale behaviors as one expects to observe at the grain level in GM. On the other hand, this method can be considered a solution for large-scale problems when significant deformation is anticipated.

2.2.2. *Smoothed-Particle Hydrodynamics*

SPH is a powerful particle-based method that is appropriate for complex multiphysics flow and deformation problems. It is a meshless Lagrangian technique that is well suited for scenarios such as interaction with dynamic moving bodies and discrete particles where flow or material history is important. SPH is a useful method for micromechanical simulations as it can naturally account for

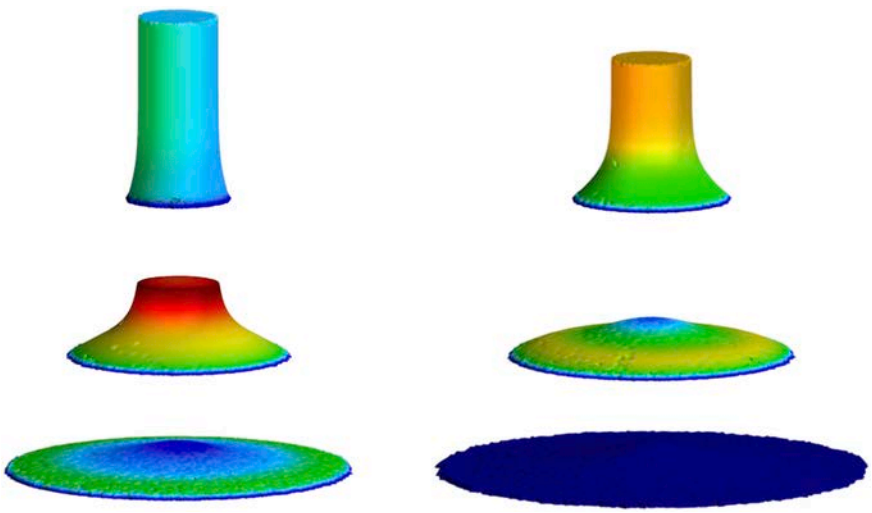

Fig. 31. The performance of PFEM for the collapse of a column of GM [270].

extremely large deformations. The method was initially applied to simulate non-axisymmetric phenomena in astrophysics [271–273]. It was then later applied to incompressible flows by Monaghan [274]. The rationale behind SPH is using kernel interpolants through which fluid dynamics problems can be simulated by representing them as particles. As such, it does not require tracking the interfaces since it is a particle-based, or a Lagrangian, method [275,276].

As a particle method, it involves fluid mass being advected with each particle and that is why this method is well-suited for studying

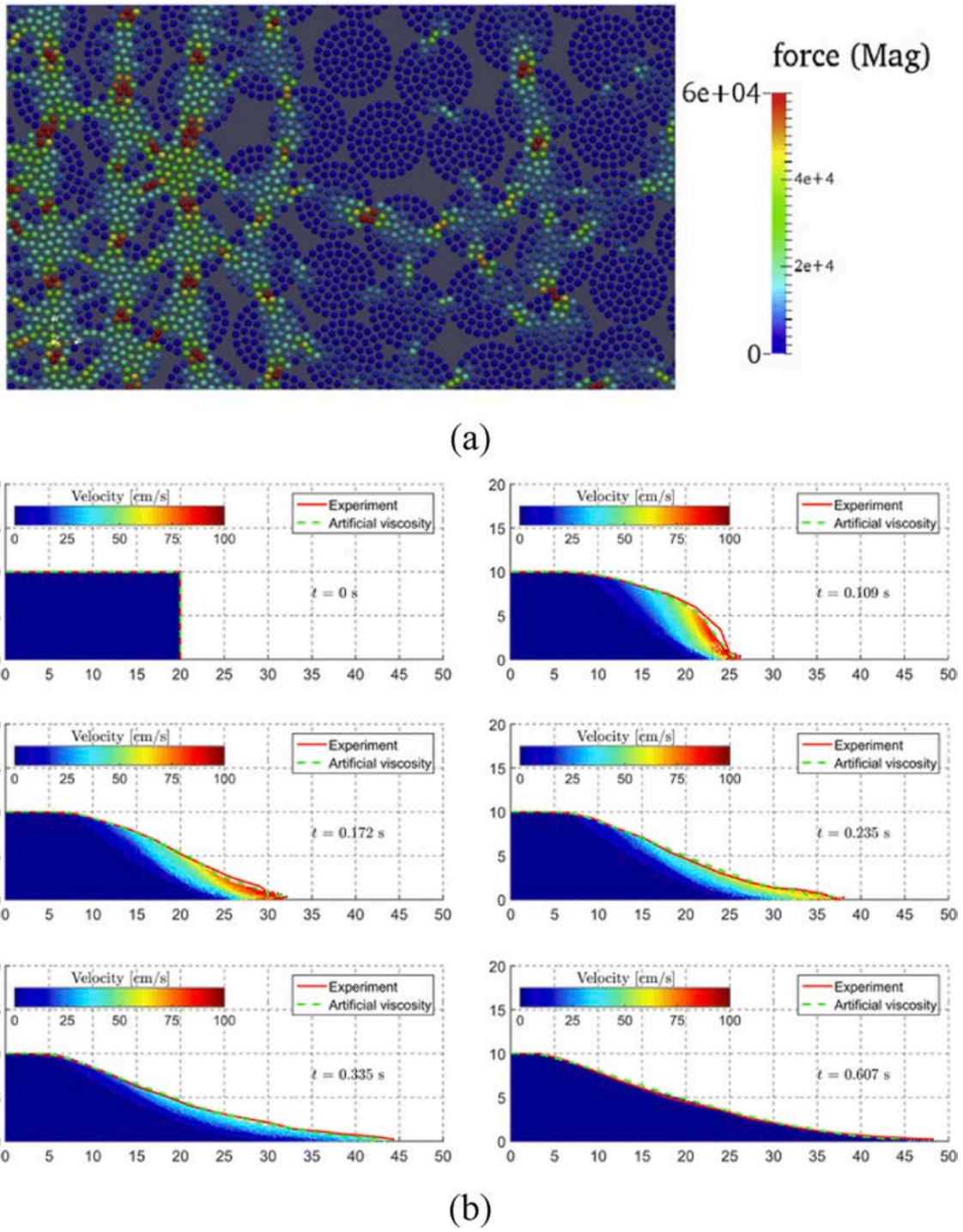

Fig. 32. (a) Force chains prediction using SPH where each disk consists of 61 SPH particles [280], (b) Comparison between SPH and experiment in a failure of a column of GM [286].

GM [277–281]. The SPH is generally capable of being expanded to incorporate several physical phenomena such as multiphase flow, solute transport problems, precipitation, thermal problems, and electrical/magnetic field problems which makes it an approach for flow simulations in general. Although the approach is relatively easier to implement than other tools, SPH traditionally has posed problems with parallelization compared to its mesh-based alternatives. However, this challenge has been addressed over the years [282]. SPH is also prone to consistency and stability issues and is usually more expensive than other techniques such as the FEM. However, it is argued that this expense can be justified by the versatility with which such a variety of multi-physics phenomena can be included [282].

The SPH equations are simply an approximation of the solutions for the general equations of fluid dynamics. SPH replaces the fluid with a set of points. These points, which represent a certain volume, are called particles and move in the system in a Lagrangian manner. Using a kernel function, these points can be employed to discretize partial differential equations without any underlying mesh. In SPH, the interpolation formula for a quantity $A(\boldsymbol{r})$ is an approximation to an integral interpolant of the form [275]:

$$A(\boldsymbol{r}) = \sum_b m_b \frac{A_b}{\rho_b} W(\boldsymbol{r} - \boldsymbol{r}_b, h) \mathbf{d}\boldsymbol{r}_b, \tag{14}$$

where m_b is the mass and $\boldsymbol{r}_b$ is the position, b denotes a particle label. $W(\boldsymbol{r} - \boldsymbol{r}_b, h)$ is a C^2 spline interpolation or smoothening kernel with radius 2 h which provides an approximation of a Gaussian function. A_b is the value of any quantity A at $\boldsymbol{r}_b$.

The continuity equation written in SPH form is given as:

$$\frac{d\rho_a}{dt} = \sum_b m_b (\mathbf{v}_a - \mathbf{v}_b) \cdot \nabla W_{ab}, \tag{15}$$

where ρ_a is the density of particle a which has a velocity of $\mathbf{v}_a$ and particle of mass m_b has a velocity of $\mathbf{v}_b$. W_{ab} is the interpolation kernel with smoothing length h. Likewise, the momentum equation is written in SPH form as:

$$\frac{d\mathbf{v}_a}{dt} = -\sum_b m_b \left(\frac{P_b}{\rho_b^2} + \frac{P_a}{\rho_a^2} \right) \nabla W_{ab}, \tag{16}$$

where P_a and P_b are the contribution of the pressure on particle a from particle b. More details of the SPH theory and its expansion

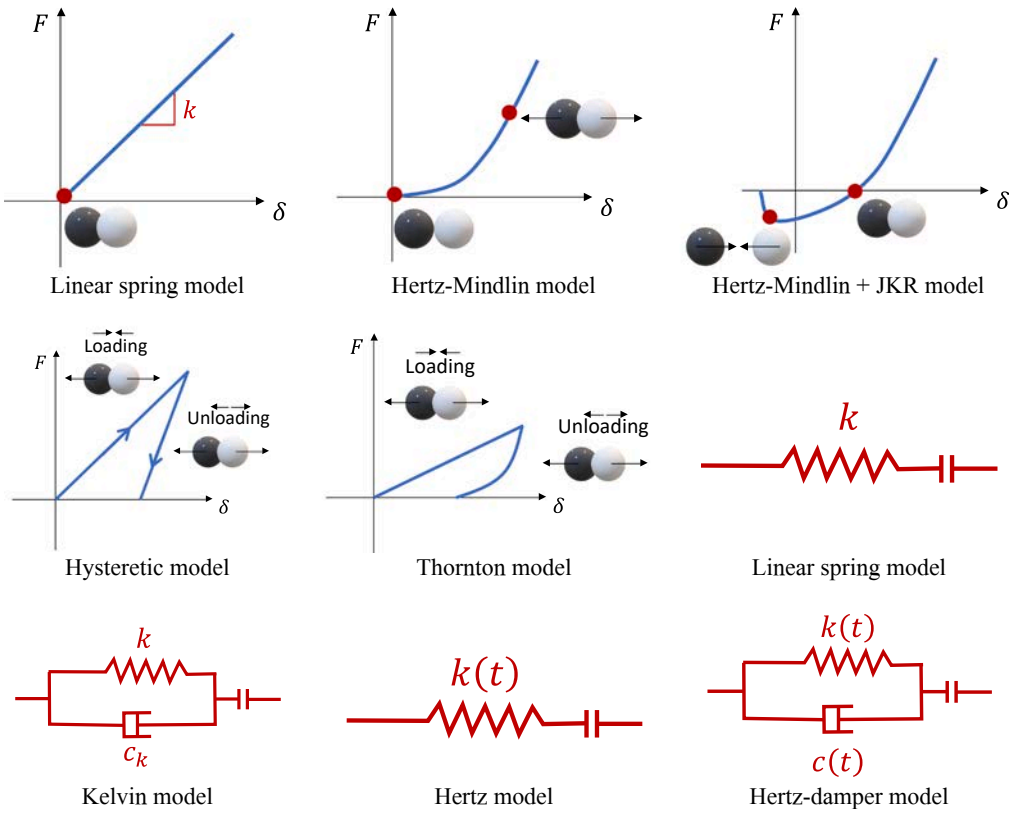

Fig. 33. Various contact models in DEM [289,290].

for other physical phenomena can be found elsewhere [273].

SPH has been used for studying GM when they undergo large deformations. In this model, the Drucker-Prager model plastic flow is added to the SPH formulation to characterize the elastic–plastic behaviors [283,284]. However, the authors reported considerable tensile instability such that unrealistic particle clustering occurred. This issue was later addressed by introducing a diffusion term that depends on stress and strain [285–287]. Some of the results produced using this method are shown in Fig. 32. As can be seen, SPH can produce the force chain with some degree of accuracy, but it is quite successful in reproducing the experimental data for large deformations.

2.2.3. Discrete element method

The discrete element method (DEM) is a numerical model for simulating the dynamics of discrete and interacting particles. DEM was pioneered by Cundall and Strack, who simulated the mechanical behavior of assemblies of discs and spheres [288]. The nature of the DEM is to consider contact forces between particles, and the motion of particles is simulated consequently. The method allows particles to deform or overlap which results in contact forces, such as elastic or frictional forces, and the translational/rotational motion and trajectory of individual particles are updated by Newton's equations of motion. The basic steps in the DEM are to first calculate the forces and torques acting on particles and then calculate the velocities and trajectories of particles. When it comes to the calculation of forces/torques, there are various approaches [289,290]. The linear spring–dashpot model was proposed by Cundall and Strack, which is a simple linear and most popular model; see Fig. 33. The spring in the model plays the role of calculating the elastic deformation while the dashpot is used for the viscous dissipations. In addition to the linear force calculation, there are more complex models, such as the non-linear elastic Hertz theory [291]. Hertz's theory depends on elastic deformation to solve the problem of stress being infinite when contact occurs in form of a point or on a line. Mindlin and Deresiewicz proposed another different force-contact model in which loading history and instantaneous rate of change of the normal/tangential force/displacement contributes to the development of force/displacement [292]. More descriptions of the force-contact theory can be found elsewhere [293–295]. It is reasonable that the non-linear force-contact models are computationally time-consuming, which makes them much less popular than the force calculation used by Cundall and Strack. With the development of DEM, its applications have been growing in various fields involved with GM. Particularly, the discrete nature of DEM makes it attractive for studying the mechanics of GM.

The Newton-Euler equation for describing the motion of a particle with any arbitrary shape and mass of m_p are:

$$m_p \boldsymbol{a} = \boldsymbol{F}, \tag{17}$$

$$\boldsymbol{I\alpha} + \boldsymbol{\omega} \times L = \boldsymbol{M}, \tag{18}$$

where $\boldsymbol{I}$ is the inertia tensor, $\boldsymbol{a}$ and $\boldsymbol{\alpha}$ are, respectively, the translational and angular acceleration, $\boldsymbol{F}$ and $\boldsymbol{M}$ are the external forces and moments exerted on the particle, and $\boldsymbol{\omega}$ is the angular velocity (vector). It should be noted that several forms of force and moments can be found in a granular system and they all should be included in the above equations (e.g., gravity, moments, external forces, damping, contact forces). Damping is used to present the energy dissipation in GM, which is known as global damping. Another form of damping, namely local damping, can be used to describe the energy dissipation due to particle interactions, which is achieved by using a dash-pot force model.

The DEM computations are conducted on a Lagrangian domain through which all the available forces and torques on each single particle p, as demonstrated in Fig. 34, can be computed via:

$$m_p \ddot{x}_p = \sum \mathbf{F}_p = \mathbf{F}_{p,n} + \mathbf{F}_{p,t} + \mathbf{F}_{p,f} + \mathbf{F}_{p,p} + \mathbf{F}_{p,v} + \mathbf{F}_{p,etc}, \tag{19}$$

and

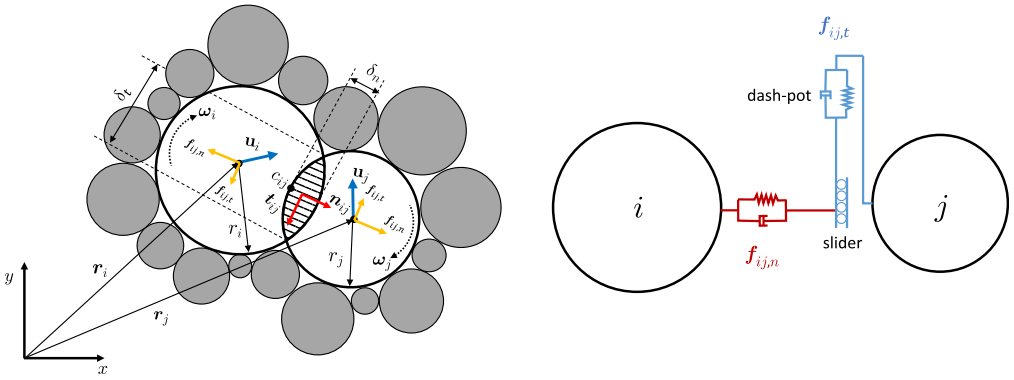

Fig. 34. Collision between two spherical particles i and j [296].

$$I_p\frac{d\omega_p}{dt}=\mathbf{r}_{p,c}\times\mathbf{F}_{p,c}+\mathbf{T}_{p,r}, \tag{20}$$

where $\mathbf{F}_{p,n}$ is the normal force, $\mathbf{F}_{p,t}$ is the tangential force and $\mathbf{F}_{p,f}$ can be the force from a fluid. $\mathbf{F}_{p,p}$ and $\mathbf{F}_{p,v}$, respectively, represent the pressure and viscous force on the particles. Any extra forces (e.g., gravity and magnetic forces $\mathbf{F}_{p,etc}$) can also be included in this equation. A list of the possible forces is provided in Table 1.

As mentioned, particles are allowed to have a small overlap $\boldsymbol{\delta}_p=\{\boldsymbol{\delta}_n,\boldsymbol{\delta}_t\}$ based on which the normal and tangential forces, velocities, and momentums are produced at the contact point c: $\mathbf{F}_{ij,c}=\{\mathbf{F}_{ij,n},\mathbf{F}_{ij,t}\}$ and $\Delta\mathbf{u}_{ij,n}$, and $\mathbf{M}_{ij,c}=\{\mathbf{M}_{ij,n},\mathbf{M}_{ij,t}\}$. Thus, the contact force can be written as:

$$\mathbf{F}_{ij,n}=k_n\boldsymbol{\delta}_{ij,n}-\lambda_n m_{eff}\mathbf{u}_{ij,n},$$

$$\mathbf{F}_{ij,t}=k_t\boldsymbol{\delta}_{ij,t}-\lambda_t m_{eff}\mathbf{u}_{ij,t}, \tag{22}$$

where $m_{eff}=(m_i m_j)/(m_i+m_j)$, k is the spring coefficient, λ is the damping coefficient, and $\boldsymbol{\delta}$ represents the elastic displacement. Thus, the perpendicular overlap between two particles can be expressed by:

$$\boldsymbol{\delta}_n=\left[(r_i+r_j)-r_{ij}\right]\mathbf{n}_{ij,t}, \tag{23}$$

where

$$\mathbf{r}_{ij}=\mathbf{r}_i+\mathbf{r}_j, \tag{24}$$

$$r_{ij}=\left|\mathbf{r}_{ij}\right|. \tag{25}$$

Similarly, the tangential displacement can be written as:

$$\boldsymbol{\delta}_t=\mathbf{u}_{ij,t}\min\left(\frac{|\boldsymbol{\delta}_n|}{\mathbf{u}_{ij}.\eta_{ij}},\Delta t\right), \tag{26}$$

where η_{ij} represents the unit normal vector from particle i to particle j and is defined by:

$$\eta_{ij}=\frac{\mathbf{r}_{ij}}{r_{ij}}. \tag{27}$$

Finally, the tangential contact force can be expressed by:

$$\mathbf{F}_{p,t}=\min\left\{\left|k_t\int_{t_{c,0}}^{t}\Delta\mathbf{u}_{p,t}dt+c_{p,t}\Delta\mathbf{u}_{p,t}\right|,\mu_{p,c}\mathbf{F}_{p,n}\right\}, \tag{28}$$

where the first term represents the spring and the tangential motion. The second part represents energy dissipation.

One of the primary methods of dealing with small and surface non-sphericity is considering rolling friction [297]. This, in turn, adds an extra torque to the previous equations, which can be quantified by:

$$\mathbf{T}_{p,r}=\mathbf{R}_{p,\mu}k_{p,n}\Delta x_p\frac{\omega_{p,rel}}{\left|\omega_{p,rel}\right|}r_p, \tag{29}$$

where $\omega_{p,rel}$, as the relative angular velocity, is defined by:

$$\omega_{p,rel}=\frac{r_{p,ci}\omega_{p,i}+r_{p,cj}\omega_{p,j}}{r_{p,ci}+r_{p,cj}}. \tag{30}$$

The relative velocity of the colliding particle can be computed by:

Table 1
Various forms of forces and torques available exist in the DEM modeling.

$\mathbf{F}_{p,n}$	$-k_{p,n}\Delta\boldsymbol{\delta}_p+c_{p,n}\Delta\mathbf{u}_{p,n}$
$\mathbf{F}_{p,t}$	$\min\left\{\left\|k_{p,t}\int_{t_{c,0}}^{t}\Delta\mathbf{u}_{p,t}dt+c_{p,t}\Delta\mathbf{u}_{p,t}\right\|,\mu_{p,c}\mathbf{F}_{p,n}\right\}$
$\mathbf{F}_{p,p}$	$-V_p\nabla P=\left(\frac{1}{2\rho_f\nabla\mathbf{u}_f^2}\right)V_p+\rho_f\mathbf{g}V_p$
$\mathbf{F}_{p,v}$	$-\nabla.(\tau_f)V_p$
$\mathbf{F}_{p,etc}$	$m_p\mathbf{g}$
$\mathbf{T}_{p,r}$	$\mathbf{R}_{p,\mu}k_{p,n}\Delta x_p\frac{\omega_{p,rel}}{\left\|\omega_{p,rel}\right\|}r_p$

$$\mathbf{u}_{ij} = \mathbf{u}_i - \mathbf{u}_j + \left(r_i\boldsymbol{\omega}_i + r_j\boldsymbol{\omega}_j\right) \times \mathbf{n}_{ij}, \tag{31}$$

$$\mathbf{u}_{ij,n} = \left(\mathbf{u}_{ij}.\mathbf{n}_{ij}\right)\mathbf{n}_{ij} \tag{32}$$

$$\mathbf{u}_{ij,t} = \mathbf{u}_{ij} - \mathbf{u}_{ij,n} \tag{33}$$

The Moment $\mathbf{M}_{i,n}$ and $\mathbf{M}_{j,n}$ corresponding to normal contact forces are defined as:

$$\mathbf{M}_{i,n} = \left(c_{ij} - \boldsymbol{r}_i\right) \times \mathbf{F}_{i,n}, \tag{34}$$

$$\mathbf{M}_{j,t} = \left(c_{ij} - \boldsymbol{r}_j\right) \times \mathbf{F}_{j,t}, \tag{35}$$

where the contact point between i and j is signified by c_{ij}.

The above equations can be used when the medium does not contain any other physical elements that vary the forces. In the latter sections, the coupling of such equations with fluid and other physical properties will be discussed.

The second-order velocity Verlet method [298] is commonly used to calculate the above properties in the next timestep, which is known as time integration. First, one can calculate the translational and angular velocity at time $t + \Delta t/2$:

$$\boldsymbol{v}^{t+\Delta t/2} = \boldsymbol{v}^t + \boldsymbol{\alpha}^t \Delta t/2, \tag{36}$$

$$\boldsymbol{\omega}^{t+\Delta t/2} = \boldsymbol{\omega}^t + \boldsymbol{\alpha}^t \Delta t/2. \tag{37}$$

Then, the position and orientation can be updated using:

$$\boldsymbol{x}^{t+\Delta t} = \boldsymbol{x}^t + \boldsymbol{v}^{t+\Delta t/2}\Delta t, \tag{38}$$

$$[\mathbf{03B8}]^{t+\Delta t} = [\mathbf{03B8}]^t + \boldsymbol{\omega}^{t+\Delta t/2}\Delta t. \tag{39}$$

Similarly, the velocities can also be computed using:

$$\boldsymbol{v}^{t+\Delta t} = \boldsymbol{v}^{t+\Delta t/2} + \boldsymbol{\alpha}^{t+\Delta t/2}\Delta t/2, \tag{40}$$

$$\boldsymbol{\omega}^{t+\Delta t} = \boldsymbol{\omega}^{t+\Delta t/2} + \boldsymbol{\alpha}^{t+\Delta t/2}\Delta t/2. \tag{41}$$

Given the above procedure, one cycle of DEM can be described as follows:

1. Based on the current state of particles (velocities and positions), identify the particles that are in contact with each other,
2. Compute the forces and moments for all particles based on the contact information and existing forces,
3. Compute the motion of all particles,
4. Update the velocities and locations of all particles using the described time-integration approach.

One of the useful features of DEM is its flexibility in taking the morphology of complex particles into account. One can either use a single-particle method using which well-defined and yet non-spherical shapes can be used in DEM. Some of these objects/particles are shown and discussed in Section 2.2.6 (Morphology). One other approach, which is also explained in the previously mentioned section, is using a composition of simple particles, such as spheres, for representing complex geometries.

One of the important elements in DEM is deciding on the appropriate contact model, and several of them are available. These models are often comprised of dash-pots, springs, and sliders using which the motion of particles and their interactions can be simulated; see Fig. 33. Here, the normal and tangential forces can be simulated using the springs while the dash-pots are in charge of local damping. Furthermore, the sliders represent shear failure.

- Most simply, one can use a **linear elastic model** wherein two elastic springs, two dash-pots, and one slider are used, and the contact force can be written as:

$$\boldsymbol{F} = \boldsymbol{F}_n + \boldsymbol{F}_t = F_n\boldsymbol{n}_n + F_t\boldsymbol{n}_t. \tag{42}$$

If the magnitude of displacement in both directions $(\Delta\delta_n, \Delta\delta_t)$ for timestep Δt, then:

$$\boldsymbol{F}_n = F_n^0 + k_n\Delta\delta_n - \lambda_n\sqrt{\overline{m}k_n}\dot{\delta}_n, \tag{43}$$

$$\boldsymbol{F}_t = \min\left(F_t^0 + k_t\Delta\delta_t - \lambda_t\sqrt{\overline{m}k_t}\,\dot{\delta}_t, \mu_c F_t\right), \tag{44}$$

where F_n^0 is the normal force at the beginning, $\dot{\delta}_n$ is the relative normal velocity, μ_c is the friction coefficient, and $\overline{m} = m_i m_j/(m_i + m_j)$.

- **Rolling resistance model**

This model is similar to the linear elastic model while it represents the rolling resistance moment to the contact moment [299,300]:

$$\boldsymbol{M} = \min\left(\boldsymbol{M}^0 + k_r \Delta\theta_b, \mu_r \overline{R} F_n\right), \tag{45}$$

where $\boldsymbol{M}^0$ is the initial contact moment, $\Delta\theta_b$ is the relative bending-rotation increment, μ_r is the rolling resistance coefficient, $\overline{R} = R_i R_j/(R_i + R_j)$ is the contact effective radius and k_r is the rolling resistance stiffness and can be written as:

$$k_r = k_t \overline{R}^2 \tag{46}$$

- **Hertz-Mindlin model**

This model is a combination of Hertz and Mindlin's models for contact normal and tangential forces, respectively. It also considers the stiffness variation as a result of the change of contact overlapping distance between two particles. This model considers a similar composition to the elastic model. Furthermore, this model considers the normal contact force as a cumulative overlapping distance. Thus,

$$\boldsymbol{F}_n = k_n \Delta\delta_n - \lambda_n \sqrt{\overline{m} k_n}\, \dot{\delta}_n, \tag{47}$$

$$\boldsymbol{F}_t = \min\left(F_t^0 + k_t \Delta\delta_t - \lambda_t \sqrt{\overline{m} k_t}\, \dot{\delta}_t, \mu_c F_t\right), \tag{48}$$

where,

$$k_n = \frac{4}{3}\overline{E}\sqrt{\overline{R}\delta_n}, \tag{49}$$

$$k_t = 8\overline{G}\sqrt{\overline{R}\delta_n}. \tag{50}$$

Here,

$$\frac{1}{\overline{E}} = \frac{(1-\nu_i^2)}{E_i} + \frac{\left(1-\nu_j^2\right)}{E_j} \tag{51}$$

$$\frac{1}{\overline{G}} = \frac{2(2-\nu_i)(1+\nu_i)}{E_i} + \frac{2(2-\nu_i)(1+\nu_i)}{E_j}, \tag{52}$$

where $\overline{G}$ and $\overline{E}$ are shear modulus and effective Young's modulus of the in-contact particles, and ν_i and E_i are the Poisson's ratio and Young's modulus of the ith particle.

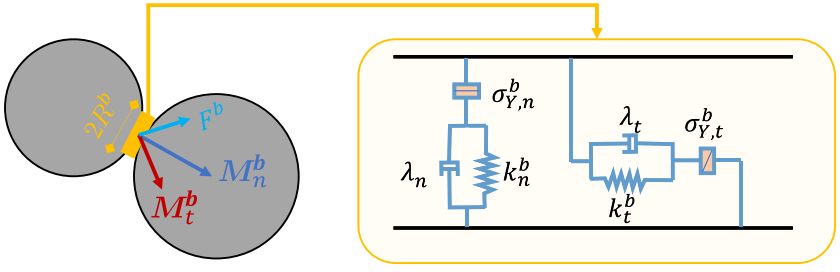

Fig. 35. Linear parallel bond model.

- **Linear parallel bond model**

This model is used to describe the contact behaviors of two bonded particles and is shown graphically in Fig. 35. In its linear state, the bond is considered to be a cylinder with a small radius and thickness where the pints on the bond are connected using two linear elastic springs to demonstrate the normal F_n^b and shear forces F_t^b. Thus, the total bonding force and moment (normal M_n^b and tangential M_t^b) can be calculated using the integral of all such stresses in the bonding location (b) with an area of A:

$$\Delta F_n^b = k_n^b A \Delta\delta_n, \tag{53}$$

$$\Delta F_t^b = k_t^b A \Delta\delta_t, \tag{54}$$

$$\Delta M_n^b = k_t^b J \Delta\theta_n, \tag{55}$$

$$\Delta M_t^b = k_n^b I \Delta\theta_s, \tag{56}$$

where I and J are the moment of inertia and polar moment of inertia of the bond, respectively. This model can be used for modeling breakage in particles. For example, the bond can be broken if shear or normal stresses exceed the shear/normal strength. Here, both the normal force and swinging moment control the normal stress. Similarly, both the shear force and twisting moment control the shear stress. Thus, one may write bond breakage as:

$$\sigma_{\max}^b = \frac{F_n^b}{A} + \frac{M_t^b R^b}{I} < \sigma_{Y,n}^b, \tag{57}$$

$$\tau_{\max}^b = \frac{F_t^b}{A} + \frac{M_n^b R^b}{J} < \sigma_{Y,t}^b, \tag{58}$$

where $\sigma_{Y,n}^b$ and $\sigma_{Y,t}^b$ are the normal and shear strengths, respectively.

Generally, GM are composed of macroscopic discrete particles with sizes ranging from micrometer in pharmaceutical, e.g., medicine powder, to decimeter size in geological environments, e.g., rocks in debris flows. The dynamic behavior of GM can often be observed in nature, such as landslides, collapse, debris flows, and displacement of deformation of porous media, in modern industries, referred chemical, pharmaceutics, mining, food processing, and cosmetics, as well as the materials used for building small and large batteries [301–306]. Mishra and Rajamani applied the DEM for the simulation of ball mills. They carefully determined the material properties, such as the stiffness, damping as well as friction coefficient of particles, based on experimental operations. With a particular model for the coefficient of friction, they found the simulation results for the system of a 55 cm ball mill consisting of 42 walls and filled with 148 balls agreed well with the experiments [307]. Tsuji et al. carried out DEM on pneumatic conveying with cohesionless, spherical particles conveyed in a horizontal pipe. They calculated the motion of individual particles by a modified Cundall model and applied the Hertzian contact theory for the interactions between particles. Moreover, they considered the fluid force acting on particles with the Ergun Equation. The simulation results showed that the flow patterns and the wave-like motion of the flow boundary were in good agreement with relevant reported research [308]. Later, Tsuji et al. simulated the motion of individual particles in a two-dimensional gas-fluidized bed by the DEM. The particle motion in the gas-fluidized bed was mainly determined by fluid drag force. In turn, the flow behavior of the inviscid gas was also greatly affected by the motion of particles. With the consideration of all forces, that is contact force between particles and fluid drag force between particles and fluid, the formation of bubbles and slugs as well as the particle mixing process were clearly shown by the simulation results [309]. Iwashita and Oda modified the classic DEM by considering the effect of rolling resistance and then simulated the microstructure developed in shear bands. It was found that the relative rotation between two particles was contributed by rolling movement with a common contact, which can make the conservation law of angular momentum available for more general cases. With the rolling resistance, the DEM simulation successfully generated the large voids inside a shear band and the high gradient of particle rotation along shear band boundaries [310]. Thornton demonstrated the quasi-static shear deformation of granular media by the numerical simulation of polydisperse systems consisting of elastic spheres. The results showed that the mechanical properties in the triaxial compression, such as deviator stress, void ratio, degree of structural anisotropy, percentage of sliding contacts, and critical mechanical coordination number, were all constant and independent of the initial packing density when the particle system deformed at constant volume. With the increase in interparticle friction, it was found that both the percentage of sliding contacts and critical mechanical coordination number decreased while there was an increase in the critical void ratio [311]. Lu and McDowell used the DEM to simulate the motion of particles of railway ballast by using both spheres and clumps of spheres. They generated the clumps of spheres, which were much more similar to real ballast particles than spheres, based on sphericity, angularity and surface roughness. With the comparisons between spheres and clumps, it was found that the particle rotations and displacements were smaller in the system of three-dimensional clumps due to the interlocking. When it comes to spheres, the deformation concentrates on the corners and sides of the sleeper. While the deformation is concentrated directly under the sleeper in the system of clumps. Overall, the load-deformation response of the clumps resembles the response of real ballast particles much more [89]. Scholtès and Donzé proposed an enhanced 3D DEM to model progressive failure in fractured rock masses. Pre-existing fractures or discontinuities are explicitly included into the discrete representation of the intact medium. The typical mechanisms involved in the progressive failure, such as deformation along pre-existing discontinuities, stress concentration at discontinuity tips, and the development and propagation of new fractures, are successfully modelled. Moreover, the method can accurately

determine the critical failure surface without assumptions relevant to its location because the zones where material strength is insufficient for loading are the main area for the stress induced fractures. With the potential of a better understanding of slope failure mechanisms, the method can provide useful information for the design and maintenance of both natural and engineered slopes [312]. Lim and Andrade improved the classical DEM focusing on regular disks or spheres to the granular element method (GEM) with the ability to accurately represent complex grain geometries by using Non-Uniform Rational B-Splines (NURBS). The shape capture depends on the seamless transition from binary images of real grain shapes to NURBS representation. The contact detection and force calculation are also adjusted based on the characters of NURBS. With higher computational time than conventional DEM, the GEM results showed that the accuracy of particle kinematics and contact topology has been improved [313]. Kawamoto et al. proposed the level set discrete element method (LS-DEM), which has the ability to capture the arbitrary morphology of 3D particles by using level set functions as a geometric basis. Compared with the GEM which also has the ability to describe the irregular particle shape, LS-DEM is more efficient in contact calculations. With the LS-DEM simulations on two virtual triaxial specimens generated from XRCT images of experiments, they proved that the LS-DEM can accurately capture and predict stress–strain and volume–strain behavior observed in the relevant triaxial compression experiments [314]. Suchorzewski et al. operated the uniaxial compression tests on concrete cubic specimens both experimentally and numerically. In the DEM simulation, aggregate particles, cement matrix, interfacial transitional zones, and macrovoids formed a random heterogeneous four-phase material which is the virtual representation of real concrete cubic specimens. The DEM model accurately simulated the occurrence, formation, and propagation of cracks, and provided the satisfactory stress–strain responses observed in the corresponding experiments [315]. Zhao et al. used DEM to understand the varying discharge rates of lognormal particle size distributions (PSDs) in a 3D conical hopper with the same arithmetic mean of the particle diameter but different PSD widths. The simulation results provided some worthy information: (a) the lack of adequate understanding of the effect of PSD width caused the mis-predicts discharge rate trends; (b) bulk density has a small influence on the discharge rate. (c) increase in the PSD width results in an increase in collision forces, radial particle velocity, radial, and vertical particle angular velocities. (d) the increase in the particle velocity and collision forces decreases the hopper discharge rate because of the impediment to particle flow out of the hopper orifice [316].

Despite the popularity of DEM, compared to all other described methods, it has many shortcomings. For example, DEM's formulation considers the interactions among the particles to be binary and additive. Besides, it is assumed that such effective interactions can be summarized by a contact force instead of considering a distribution for the forces, which can affect evaluating the torque. Each pair of particles are also in contact with each other at only-and-only one contact point (the convexity assumption for particles). Furthermore, other physical effects, such as breaking in particles, are often not considered when GM are studied in general. Aside from the above issues, DEM also considers the particles to be respected as rigid body than soft.

2.2.4. *Material point method*

As mentioned earlier, FEM is one of the most popular methods for solving engineering problems. This method, however, shows a deficiency in dealing with large strains when it is used in the Lagrangian framework. The main drawback is mesh distortion which can significantly affect the accuracy of calculations. Thus, remeshing techniques were introduced to rebuild the mesh when the aforementioned issue arises. This transition is, however, not always straightforward and efficient and can introduce an error. On the other hand, FEM methods in Eulerian format are also not suitable when one deals with free materials. Some of the solutions were discussed in the section of PFEM.

Another group of methods is described as meshless techniques in which a group of points/particles are used to manifest large strains. Here, thus, the problem of mesh distortion in FEM does not occur. These methods are generally categorized into four classes: moving weighted least square [317–320], kernel methods [271,321–326], partition of unity [327–329], and material point method.

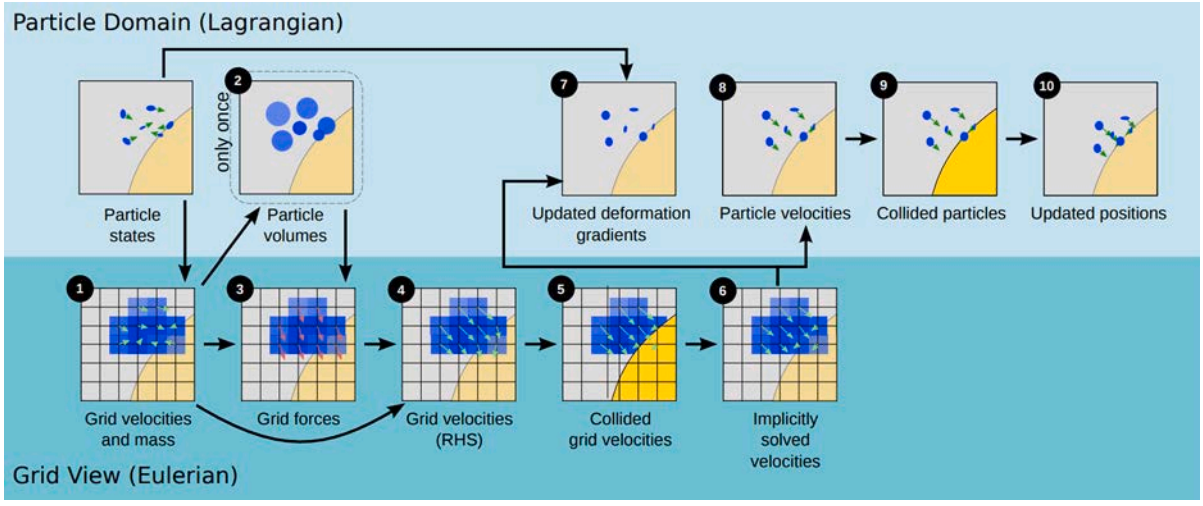

Fig. 36. Overview of the steps taken in the MPM method [346].

Among these methods, Material Point Method (MPM) offers an alternative to the Lagrangian-based techniques [330–333], which originally was proposed and known as particle-in-cell (PIC). Since then, this method has been used on various problems where additional components are also added [333–345]. This method, briefly, can be interpreted as a FEM devised in an ALE framework. In other words, the state variables are followed at the material points, which are separately specified for a Eulerian mesh, and unlike the FEM method, the MPM technique does not need to conduct a periodical remeshing and reprojecting of the state variables. The application of this mesh is for solving the motion of materials. Thus, since the computational mesh is designated separately, the common issues in Lagrangian FEM can be prevented. Therefore, equilibrium calculations are conducted in a background mesh, which is based on the information provided in the points inside the material. This allows the material points to move separately from the mesh and makes them suitable for problems with large deformations. Furthermore, dealing with history-dependent models is easier in MPM, and in general particle-based methods.

Generally, the conservation of mass and momentum can be expressed by:

$$\frac{\partial \rho}{\partial t} + \nabla.(\rho \mathbf{v}) = 0, \tag{59}$$

$$\rho \frac{D\mathbf{v}}{Dt} = \nabla.\sigma + \mathbf{f}, \tag{60}$$

respectively. Here, t is the time and $\rho(\boldsymbol{x}, t)$ is the density. Besides, $\sigma(\boldsymbol{x}, t)$ is the Cauchy stress tensor (pressure and shear) and $\mathbf{f}(\boldsymbol{x}, t)$ is the body force. $\mathbf{v}(\boldsymbol{x}, t)$ is also the velocity. Due to the Lagrangian nature of MPM, the conservation of mass can be simplified. Similarly, the discretization of the left side of the conservation of momentum's equation can also be streamlined. At the same time, the Eulerian side of MPM can help stress evaluation and discretization of $\nabla.\sigma$ as one does in FEM.

Since MPM uses two overlaid systems, namely particles and grid nodes/mesh, we use m_i^n to denote the mass of node $\boldsymbol{i}$ at time n, while m_p represent the mass of particle p. The background mesh is equally spread out and their corresponding properties are stored at the centers. As mentioned, various versions of MPM have been presented, but here we only discuss one of them, which contains the following steps [346], which are also shown graphically in Fig. 36.

1) Data transfer from particle to the grid: This step includes transferring the mass of particles to the grid, which can be accomplished using $m_i^n = \sum_p m_p w_{ip}^n$, where w_{ip} is the interpolated weight. Similarly, velocity should be transferred using a normalized form to preserve momentum conservation $v_i^n = \sum_p v_p m_p w_{ip}^n / m_i^n$. This particular implementation uses dyadic products of 1D cubic B-splines for the grid basis function [347]: $N_i^h(x_p) = N\left(\frac{1}{h}(x_p - ih)\right) N\left(\frac{1}{h}\left(y_p - jh\right)\right) N\left(\frac{1}{h}(z_p - kh)\right); \boldsymbol{i} = (i,j,k), \boldsymbol{x}_p = \left(x_p, y_p, z_p\right)$, where $\boldsymbol{i}$ and $\boldsymbol{x}_p$ are the grid index and the position, respectively. $N(x)$ is also defined as:

$$N(x) = \begin{cases} \frac{1}{2}|x|^3 - x^2 + \frac{2}{3}, & 0 \le |x| < 1 \\ -\frac{1}{6}|x|^3 + x^2 - 2|x| + \frac{4}{3}, & 1 \le |x| < 2 \\ 0, & \text{otherwise} \end{cases}. \tag{61}$$

Thus, the weight can be calculated using $w_{ip} = N_i^h(\boldsymbol{x}_p)$.

2) Calculate the densities and volumes of particles: This step is considered only once and in the first timestep. This information is needed for force calculation. The density of a cell is estimated via m_i^0/h^3, where h is the grid spacing. This quantity can be related to the particle as $\rho_p^0 = \sum_i m_i^0 w_{ip}^0 / h^3$. Thus, the particle volume can be estimated by $V_p^0 = m_p/\rho_p^0$.

3) Grid force calculations: As mentioned above, the Cauchy stress σ_p must be calculated for computing the grid forces. This property depends on the constitutive model $\Psi\left(F_{E_p}, F_{P_p}\right)$ and also the deformation gradient $\boldsymbol{F}_p^n$, which can be set to $\boldsymbol{I}$ for the initial timestep. As indicated, Ψ can be defined using the elasto-plastic energy density function. One can get the first Piola-Kirchhoff stress using:

$$\sigma_p^{PK1} = \frac{\partial \Psi}{\partial \boldsymbol{F}_p}. \tag{62}$$

The above equation signifies that:

$$\sigma_p = \frac{1}{\det\left(\boldsymbol{F}_{E_p}^n\right)} \frac{\partial \Psi}{\partial \boldsymbol{F}_p} \left(\boldsymbol{F}_{E_p}^n\right)^T = \frac{1}{J_{E_p}} \frac{\partial \Psi}{\partial \boldsymbol{F}_p} \left(\boldsymbol{F}_{E_p}^n\right)^T. \tag{63}$$

Finally, the force can be computed using:

$$\boldsymbol{f}_i = -\sum_p V_p^n \sigma_p \nabla w_{ip}^n. \tag{64}$$

4) Updating the velocity on the grid: The velocity on the grid can be updated using:

$$\boldsymbol{v}_i^* = \boldsymbol{v}_i^n + \frac{\Delta t}{m_i^n} \boldsymbol{f}_i^n. \tag{65}$$

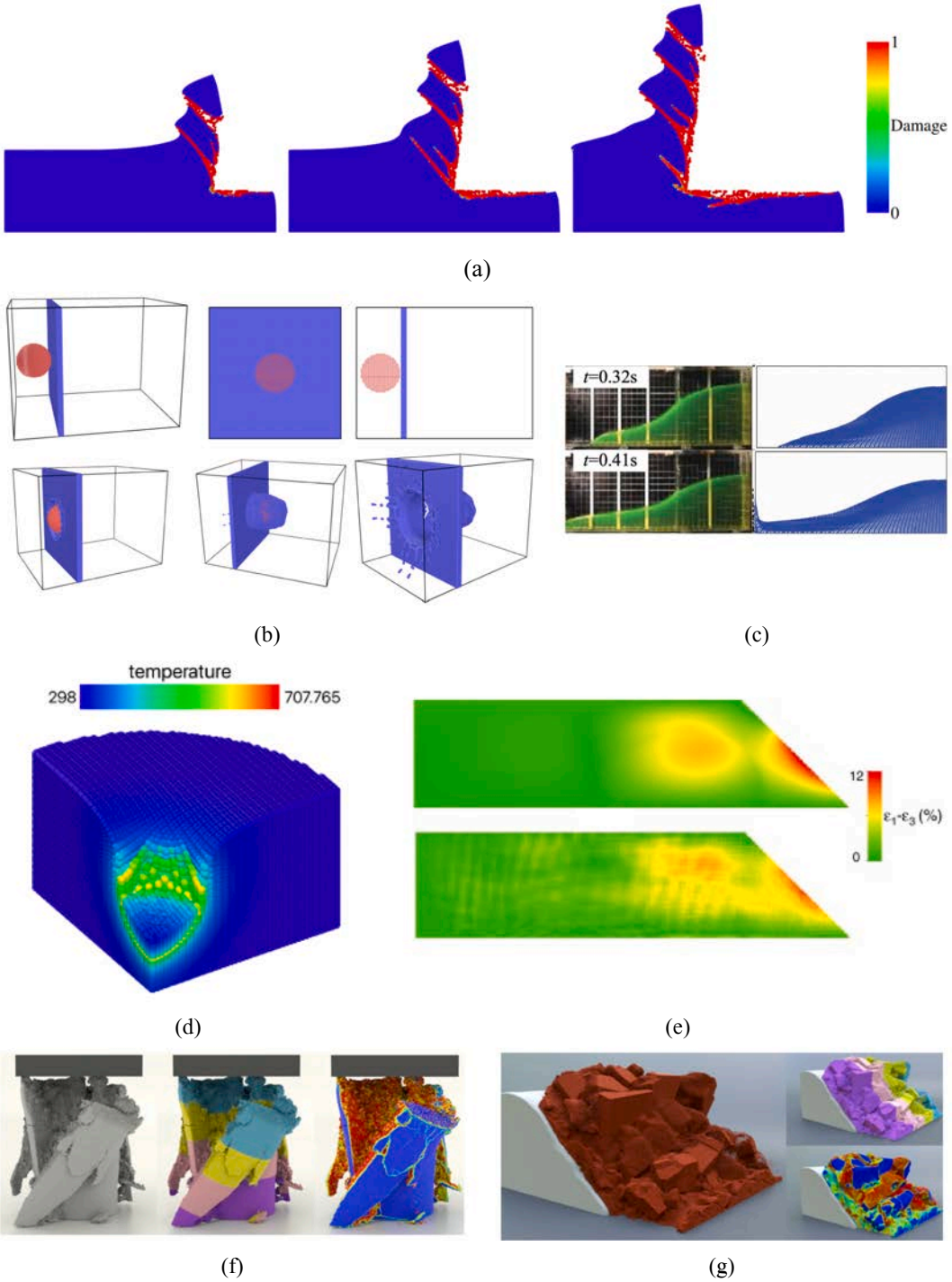

Fig. 37. Representative examples showing the performance of the MPM method in dealing with complex and large deformation problems for a variety of applications, such as (a) the cutting process of high-strength steel [356], (b) steel plate penetration [356], (c) dam break [356], (d) cold spraying accompanied with an impact [356], (e) large-scale deformations in geo-GM (upper image show the FEM results while the lower one represents the MPM results) [357], (f) concrete crushing wherein the colors represent plastic volumetric strain [358], (g) soil failing [358], (h) fracture modeling [359], and (i) simulating of a Newtonian viscosity material (toothpaste) [360].

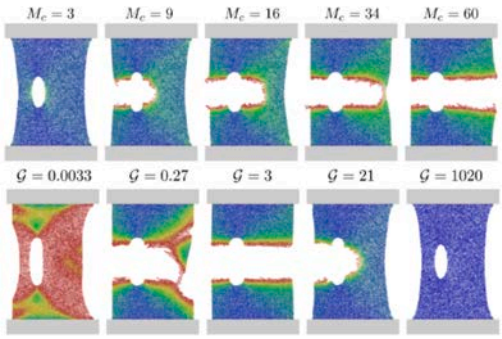

(h)

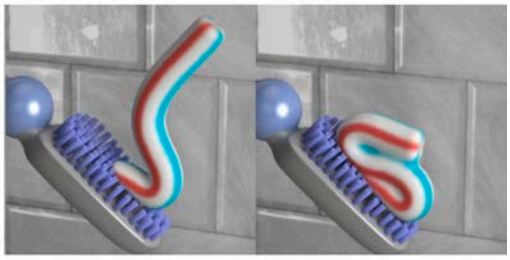

(i)

Fig. 37. (*continued*).

5) Grid-based body collisions: The velocity can be updated in both one- and two-way schemes in MPM on the grid nodes based on the locations $\boldsymbol{x}_i$. The collision between particles can be detected as one does in DEM. Relative velocity $\boldsymbol{v}_{\text{rel}} = \boldsymbol{v} - \boldsymbol{v}_{\text{co}}$ can be calculated using the collision velocity. Besides, $\boldsymbol{v}_{\text{rel}}$ can determine if particles are moving away from each other ($v_{\text{n}} = \boldsymbol{v}_{\text{rel}}.\boldsymbol{n} \geq 0$) or getting closer. The latter scenario requires calculating the relative tangential velocity $\boldsymbol{v}_t = \boldsymbol{v}_{\text{rel}} - \boldsymbol{n}v_{\text{n}}$. It should be noted that $\boldsymbol{v}'_{\text{rel}} = 0$ if $\|\boldsymbol{v}_t\| \leq -\mu_f v_n$, where μ_f is the coefficient of friction. Otherwise, the new velocity should be calculated accordingly using $\boldsymbol{v}'_{\text{rel}} = \boldsymbol{v}_t + \mu_f v_n \frac{\boldsymbol{v}_t}{\|\boldsymbol{v}_t\|}$. Finally, $\boldsymbol{v}' = \boldsymbol{v}'_{\text{rel}} + \boldsymbol{v}_{\text{co}}$.

6) Time integration: If explicit time integration is used, then one can use $\boldsymbol{v}_i^{n+1} = \boldsymbol{v}_i^*$. Otherwise, an implicit backward Euler scheme can be used and build a mass symmetric linear system, which eventually can be used in Conjugate Residual or MINRES to solve it. It should be noted that the implicit time integration can help with the stability of the solver for large timesteps, while the explicit time integration is very faster and easy to implement.

7) Update deformation gradient: The deformation gradient consists of both elastic and plastic ($\widehat{\boldsymbol{F}}_{P_p}^{n+1} = \boldsymbol{F}_{P_p}^n$) portions, which should be calculated for the next timestep $\boldsymbol{F}_p^{n+1} = \widehat{\boldsymbol{F}}_{E_p}^{n+1} \widehat{\boldsymbol{F}}_{P_p}^{n+1}$. The elastic deformation at the next time step can be calculated using:

$$\widehat{\boldsymbol{F}}_{E_p}^{n+1} = \left(\boldsymbol{I} + \Delta t \nabla \boldsymbol{v}_p^{n+1}\right) \boldsymbol{F}_{E_p}^n, \tag{66}$$

$$\nabla \boldsymbol{v}_p^{n+1} = \sum_i \widehat{\boldsymbol{v}}_i^{n+1} \left(\nabla w_{ip}^n\right)^T.$$

8) Update particle states: This step involves updating the velocity and location as below:

$$\boldsymbol{v}_p^{n+1} = (1-\alpha) \sum_i \boldsymbol{v}_i^{n+1} w_{ip}^n + \alpha \left(\boldsymbol{v}_i^n + \sum_i \left(\boldsymbol{v}_i^{n+1} + \boldsymbol{v}_i^n\right) w_{ip}^n \right), \tag{67}$$

$$\boldsymbol{x}_p^{n+1} = \boldsymbol{x}_p^n + \Delta t \sum_i \boldsymbol{v}_i^{n+1} w_{ip}^n, \tag{68}$$

where one can use $\alpha = 0.95$.

MPM has been used on a variety of problems, ranging from fluid dynamics to solid mechanics wherein some assumptions of GM are used. For the former problem, MPM/PIC has been used extensively to simulate a broad range of problems such as biological tissues [348], particle flows in a sedimentation column [349], fluid-membrane interactions [350], coupling atomic-scale modeling with continuum-scale simulations [351]. A more comprehensive review of the application of MPM for this group of problems can be found elsewhere [352]. In a more interesting work, this method has been used for making more realistic animations developed by Walt Disney [346,353]. This method is also used for problems in solid GM for a variety of purposes, such as collision, penetration, and also fracture modeling. In particular, its application of geo-GM has rapidly increased and extended to landslides and soil-GM [354,355]. Some of the results produced using the method on a diverse group of problems are shown in Fig. 37.

Aside from all the above advantages, MPM requires more storage compared to other methods since both particles and mesh are used. Furthermore, MPM entails more computations compared with FEM owing to the fact that the grid is reset after each MPM iteration. Due to using a mesh in this method, thus, its size and orientation can influence the results.

2.2.5. Morphology

Although the basic equations for describing GM are developed for ideal shapes such as spherical particles, actual GM are often found in complex shapes. Such particles can be found widely in various fields of research in science and engineering; e.g. pharmaceutics, agriculture, energy, mining, environment, and geological engineering. Some of such examples are shown in Fig. 38.

Fig. 38. Some examples indicating the widespread occurrence of non-spherical particles.

Characterizing GM systems with irregular particles can tremendously help with an accurate description, and design, and reduce the risk as they directly control the mechanical behaviors. One of the longstanding problems in modeling such particles is including the morphology while the contact between them is accurately identified, which has been studied extensively within the framework of the DEM method [361–364].

Most of the aforementioned techniques are developed for dealing with spherical particles, except the FEM which can be applied to GM with any shape at a small scale and a very small number of particles. However, as indicated before, the goal of this paper is not to review the capability of such general methods, but to be more focused on those techniques exclusively developed for GM. In that sense, the overall behavior of GM can be divided into two groups, the properties of the materials (e.g., particle size distribution, morphology, …) and state characteristics which refer to the properties that change with the boundary conditions (e.g., porosity, …). Although significant progress has been made in the modeling of GM, our current modeling techniques are still immature when it comes to dealing with actual GM with complex morphologies. Most of the existing methods consider the shape of particles as disks (in 2D) or spheres (in 3D) as it tremendously reduces the computations and very straightforward procedure of contact detection and force calculation. Making such assumptions can, however, result in a considerable over/underestimation of the micro and macro responses. For example, it is *impossible* to produce torque when the particles are considered in form of a disk/sphere. As such, researchers have

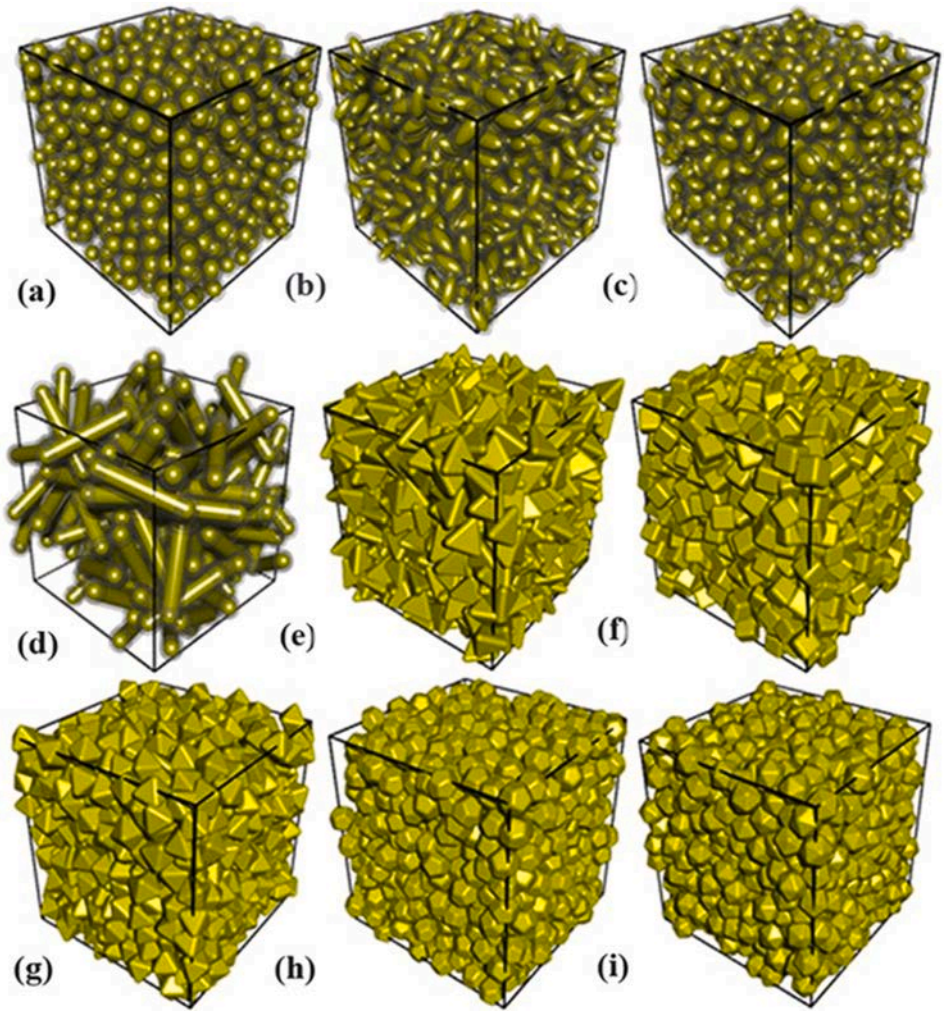

Fig. 39. Demonstration of various possible objects/particles that can be used within the DEM formulations [365].

tried to better represent the shape of particles in GM while they keep the computations feasible. Some of such more complex, yet idealized, shapes were discussed previously (e.g., ellipsoids, spheres, pentagons, polyhedrons, …) and some additional models are also provided in Fig. 39.

Including the morphology of particles within the current GM modeling requires representing the shape of the objects as accurately as possible to minimize the discrepancy between the actual computational model and reality. Furthermore, contact identification between complex particles is another daunting problem that remained the main reason for having a large computational burden in the relevant mechanical methods [366]. In fact, unlike the spherical particles where the overlap between them is well-defined, finding the true distance for irregular particles requires extra assumptions and calculations. This problem becomes more complex when the system is considered in a multiphysics environment (e.g., fluid) where the external forces and interactions exerted by other physical agents should be considered realistically. For example, the presence of fluid requires integrating the mechanical equations such that they manifest the drag force, which can be complicated when the particles are irregular. The effect of the shape of particles on the behavior of GM is demonstrated in Fig. 40 using computational modeling and similar results are obtained based on experimental tests conducted using photoelastic particles [367].

A more practical way of showing the shape of particles in GM is using overlapped/clumped particles [369–371] in which several disks/spheres are fit to show the morphology of particles. Using such objects for capturing complex morphologies allows a simple extension of the current methods developed for spherical particles. This goal can be achieved using three approaches, which are shown in Fig. 41.

Among the above-mentioned methods, domain overlapping filling is the common technique as it requires a much smaller number of spheres and, thus, lower computations. Increasing the number of disks/spheres can help to capture the morphology better, but it can result in a higher computation. Therefore, it is very important to keep the number of fitted disks/spheres low while the results are not affected substantially. This issue is one of the current challenges [369,370,373,374]. Most of the current methods of building complex

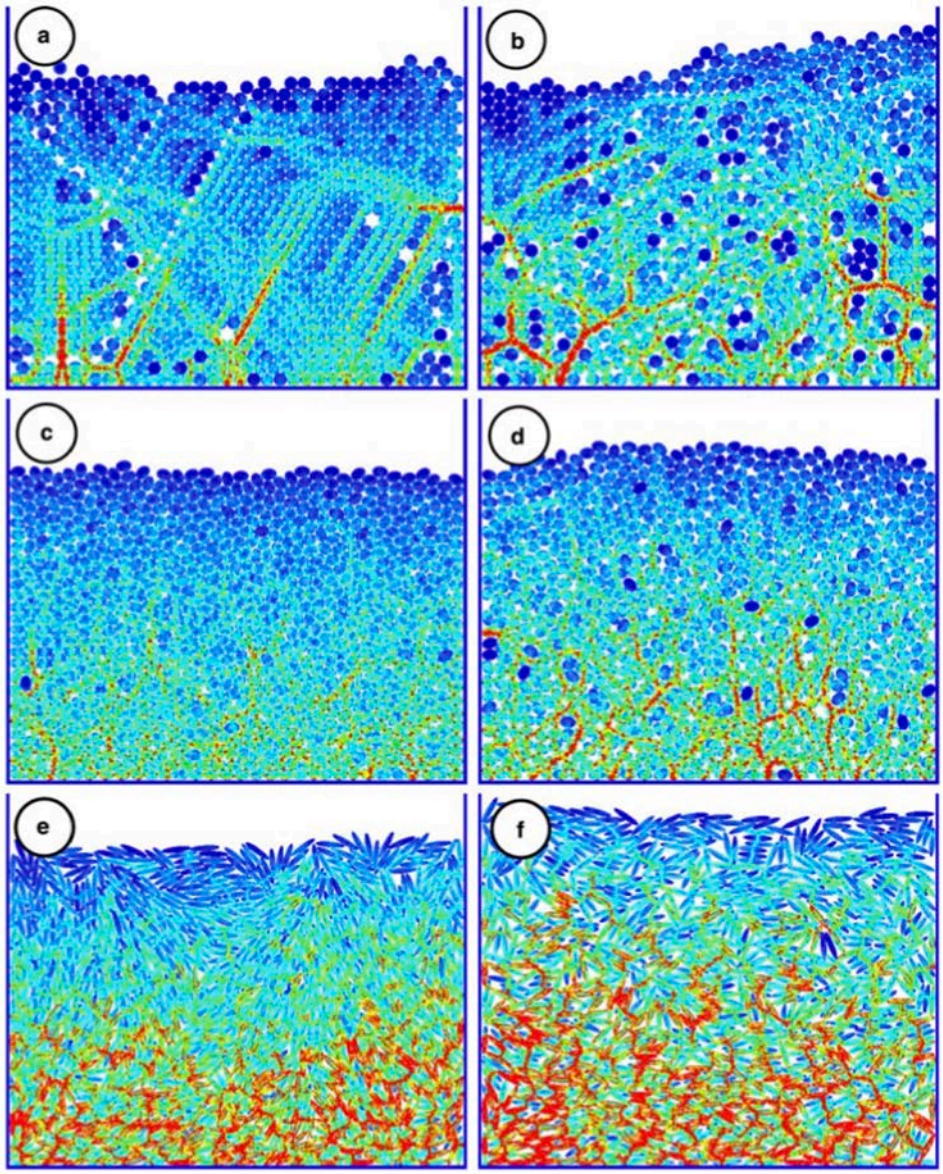

Fig. 40. A combined effect of shape and friction on the behaviors of GM. Each pack contains 900 particles where (a), (c), (e) are frictionless, and (b), (d), (f) include friction. The color represents the magnitude of the stress [368].

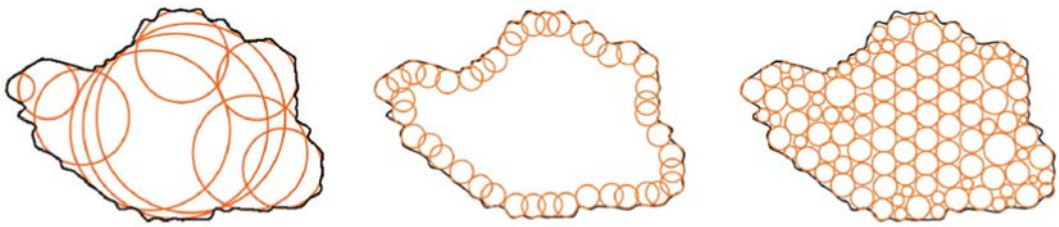

Fig. 41. Demonstration of three methods for representing complex particles using a set of circles in 2D and spheres in 3D. (left) overlapping filling, (middle) boundary filling, and (right) non-overlapping filling [372].

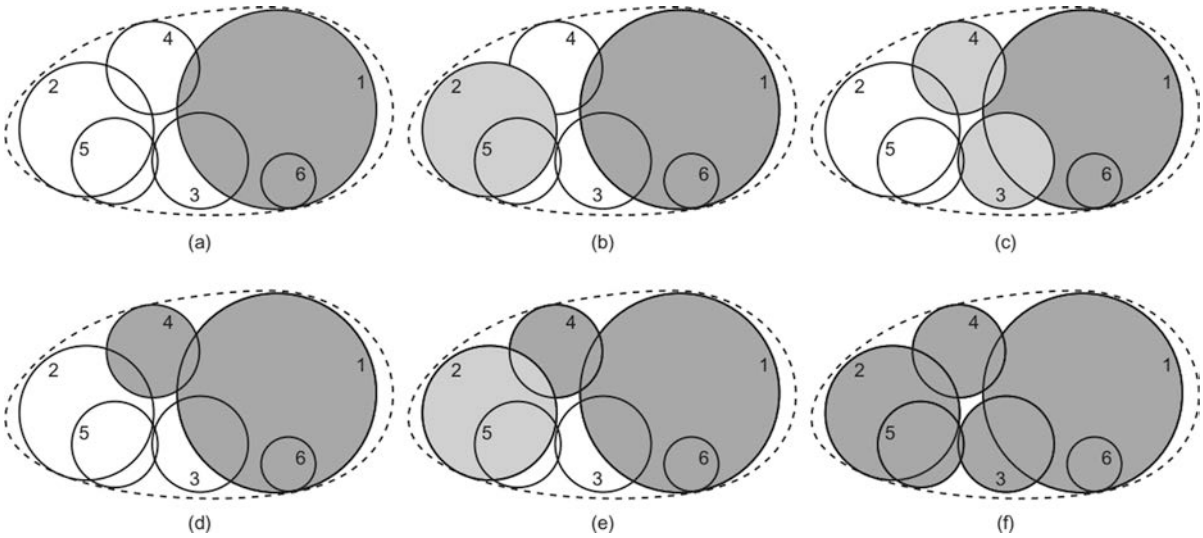

Fig. 42. Schematic representation of the steps for capturing the morphology of an angular particle using the multisphere/clumped approach [375].

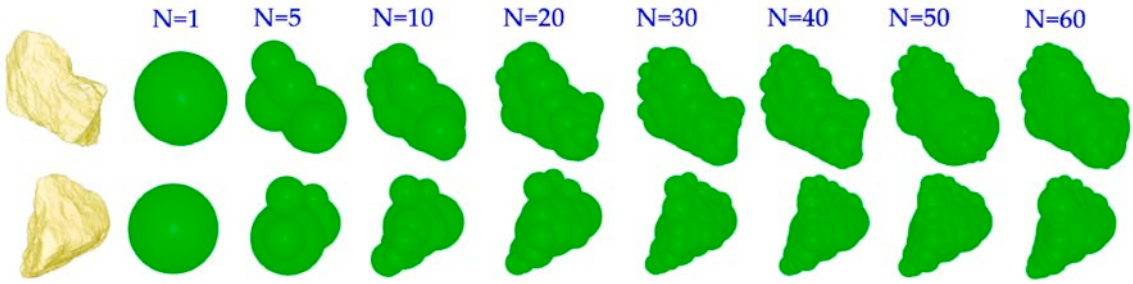

Fig. 43. Comparison between the number of spheres used in clumped modeling for two complex particles [377]. As can be seen, the shape can be presented better when the number of spheres increases.

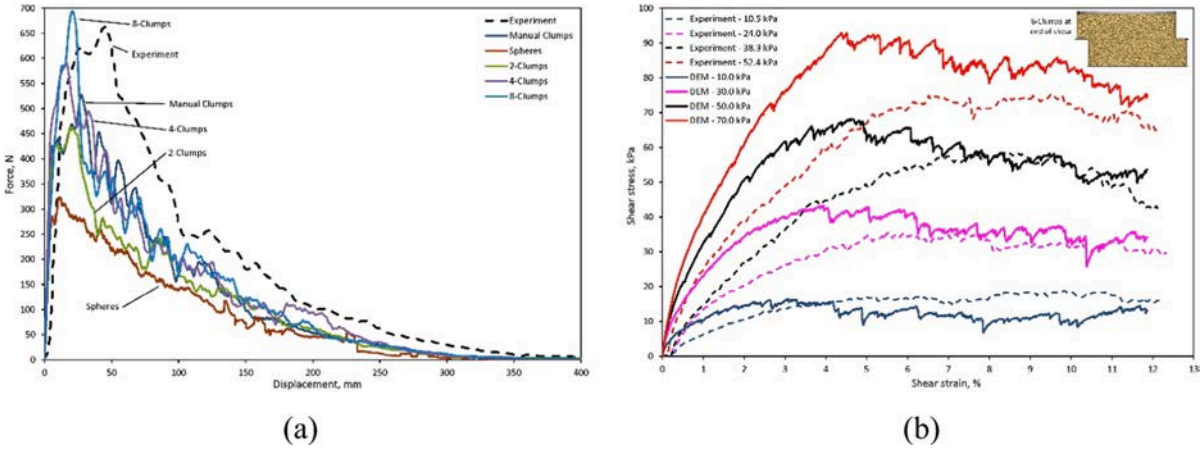

Fig. 44. Comparison between experimental results and those obtained using DEM with a different number of spheres in the produced clumps, for (a) anchor pull-out test using four clump models (1/spherical, 2, 4, 8) (b) shear stress–strain test under different normal forces for 2-clumps (2, 4, 8) [378].

particles start with sequentially adding spheres to a pack of overlapping particles with the hope of representing the shape. This approach itself can be divided into two groups, namely non-overlapping spheres and overlapping spheres, where the latter is more popular. One such algorithm is shown in Fig. 42 schematically. Some of the utilized criteria in this algorithm are volume and inertia.

There is a tradeoff between the number of spheres and capturing the complexity such that selecting the correct number of them and also their locations are still under investigation [376], which eventually can result in raising a critical question: which morphological features of complex particles are more important and must be preserved? Without considering a simplification, one may have to deal with thousands of spheres to reproduce an angular particle. Among the morphological properties, sphericity and roundness are the most crucial ones. Despite all such progress, showing the actual shape of particles is still a daunting challenge; see Fig. 43.

After deciding on the number of spheres for showing the morphology of angular particles, the produced particles can undergo any relevant modeling, in particular the DEM. Although promising results were obtained using this approach for simple angular particles, the application of this method for complex systems and particles with sharp edges is still challenging. A comparison between the experimental results and those obtained from DEM under different normal forces and clump specifications is provided in Fig. 44. As can be seen, a significant difference still appears between such results, though clumped particles have made a considerable improvement over the spherical particles.

2.2.6. *Movable cellular automaton*

Movable cellular automation (MCA) was first introduced for studying the mechanical properties of GM in the mesoscale [379]. The philosophy behind this method is that complex materials systems cannot be described on one single scale (e.g., micro or macro). MCA proposes a new way of looking at such models by using many-body-forces, which is similar to DEM. Here, the deformation is not controlled strictly by the relationship between strain and stress, but it considers the structure as a whole. This method has been applied to a variety of problems related to crack modeling, fragmentation, … [380–383].

One of the distinct features of MCA, compared to DEM, is addressing the issue of pair-wise potential interaction in DEM, which can result in unrealistic responses. For example, there is a strong dependency between the macroscopic behaviors and packing properties (e.g., porosity, shape, randomness, …). Furthermore, adjusting the free parameters, such as elastic properties (e.g., Young modulus, Poisson ratio, …), can be time-demanding. Aside from these limitations, simulating materials with irreversible strains in ductile GM is also controversial since plasticity is defined in the crystal lattice scale. It also should be noted that some of these limitations are partially addressed, but the pair-wise approximation for characterizing the interaction is still an open question. This problem can, however, be addressed using many-body interaction forces [384,385], but they are limited to elastic-brittle materials. Another alternative is combining the capabilities of DEM with some concepts of cellular automata.

The MCA considers the medium as a set of finite-size objects and automata while they interact with each other and can move based on the calculations conducted using Newton's equations. The interactions can cover a wide range of cases, such as chemically bonded (linked, cohesion/adhesion) and fractured (unlinked) systems. The connected automata can have normal and tangential interactions. Thus, the relationship between discrete automate can be described by these two spatial properties expressed as Δr_{ij}^{n} and Δr_{ij}^{t}. Consequently, the force and momentum are also computed using these properties when are integrated in time. Therefore, the linked elements can be discontinued to simulate damage and crack. Mathematically speaking, the translation of the pair automata *ij* with:

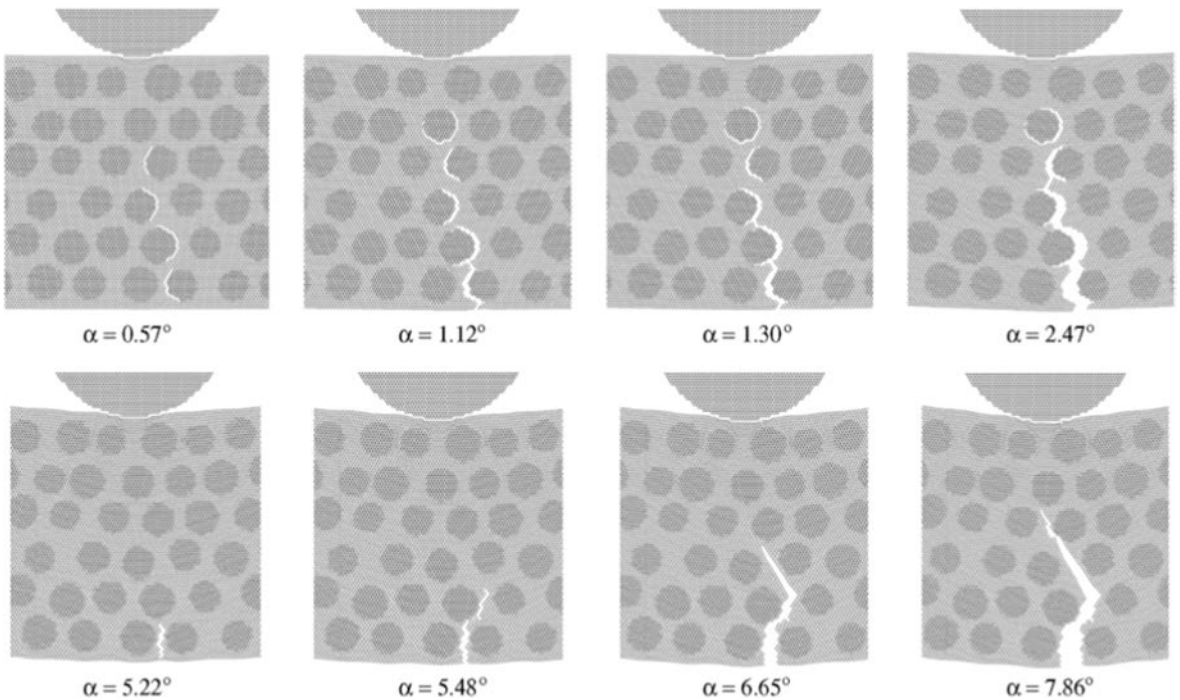

Fig. 45. Fracture propagation in a metal-ceramic sample. α is the bending angle [386].

$$\varepsilon^{ij} = \frac{h^{ij}}{r_0^{ij}} = \frac{(q^{ij} + q^{ji}) - \left(d^i + d^j\right)/2}{\left(d^i + d^j\right)/2}, \tag{69}$$

where $h^{ij} = r^{ij} - \left(d^i + d^j\right)/2$ is the overlap size between i and j with the radii of d^i and d^j, respectively, and q^{ij} is the distance from the contact point of automaton j to the center of i. Thus,

$$\left(\Delta\varepsilon^{i(j)} + \Delta\varepsilon^{j(i)}\right)\frac{\left(d^i + d^j\right)}{2} = V_n^{ij}\Delta t, \tag{70}$$

where Δt is the timestep and V_n^{ij} is the relative velocity.
The equation of motion of translation is given by:

$$\frac{d^2h^{ij}}{dt^2} = \left(\frac{1}{m^i} + \frac{1}{m^j}\right)p^{ij} + \sum_{k\neq j} C(ij,ik)\psi\left(\alpha_{ij,ik}\right)\frac{1}{m^i}p^{ik} + \sum_{l\neq i} C(ij,jl)\psi\left(\alpha_{ij,jl}\right)\frac{1}{m^j}p^{jl}, \tag{71}$$

where p^{ij} is the central force between automata i and j, $C(ij,ik)$ is a coefficient between pairs ij and ik, $\psi\left(\alpha_{ij,jl}\right)$ is the angle between directions ij and jl. The above equation can be revised to include the effect of rotation:

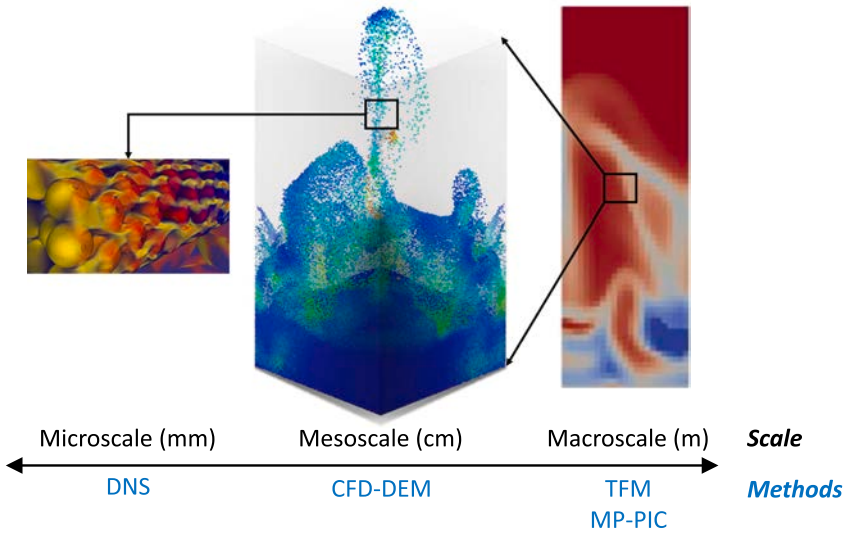

(a)

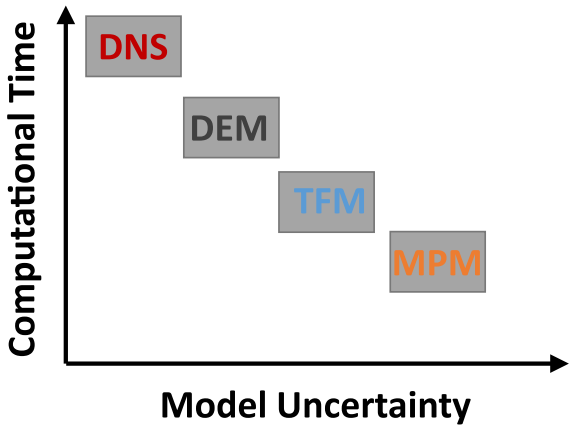

(b)

Fig. 46. (a) Demonstration of the multiscale nature of GM across different scales and their relevant methods. (b) Comparison between some of the described methods in terms of their uncertainties and computational times.

$$\frac{d^2\theta^{ij}}{dt^2} = \left(\frac{q^{ij}}{J^i} + \frac{q^{ji}}{J^j}\right)\tau^{ij} + \sum_{k\neq j} S(ij,ik)\frac{q^{ik}}{J^i}\tau^{ik} + \sum_{l\neq j} S(ij,jl)\frac{q^{jl}}{J^j}\tau^{jl}, \tag{72}$$

where θ^{ij} is the angle of rotation, $S(ij,jl)$ is also similar to the definition of $C(ij,ik)$ but for rotation, τ^{ij} is the pair tangential interaction, and J^i is the moment of inertia of automaton i. These equations closely follow those for the many-particle method.

As mentioned, MCA is used extensively for studying irreversible deformations. The deformation of automaton i in the presence of automaton j can be expressed by ε^{ij}. One of the deformation results, which has caused fracturing, is shown in Fig. 45.

2.2.7. Hybrid modeling

There are several reasons why multiscale modeling is necessary. First, most of the phenomena around us have a multiscale nature and one cannot understand them without considering such systems at both small- and large-scale. Second, no single numerical technique can handle the mentioned complexity across all scales. This problem even becomes more complicated when one deals with a dynamic system. Thus, several methods across different scales have been developed to address this crucial aspect. Models with higher resolutions are advantageous since they do not need to borrow constitutive equations since they themselves are the source of uncertainty. This concept is shown in Fig. 46.

Multiscale methods are not limited to problems with various physics, but they can be generalized to single-physics problems as well. For instance, modeling of large deformations can be accomplished using fast computational modeling wherein some locations might be simulated using fine-scale techniques. On the other hand, one of the preliminary methods for studying GM coupled with fluid is using the DNS. This method tracks the particles in a Lagrangian manner and the interactions between particles are addressed using hard- or soft-sphere contact models. These numerical simulations are good for building and discovering constitutive models. As such, they come with considerable computational time and are recommended for systems with a couple of thousands of particles. A faster method, Eulerian-Lagrangian, where a locally averaged version of fluid equations is used in a Eulerian framework, can provide a more feasible solution. These methods, however, still need some input data on the interaction forces and effective stress. Alternatively, Eulerian-Eulerian methods can be used in which both the solid and fluid parts undergo a locally averaging scheme and are often known as two-fluid-model (TFM). In this set of methods, the same parameters as in the Eulerian-Lagrangian methods are required to be used as input. Therefore, as can be seen, each individual method has an issue that limits its generalization capacity. On the other hand, these methods, in a lot of cases, can aid each other and fill the gaps. In this section, thus, such methods are briefly reviewed.

Without considering the effect of other important physics, FEM and DEM are two of the popular methods for mechanical modeling. FEM, on one hand, is based on constitutive models and cannot manifest the discrete properties of GM, which requires various insights from experimental results to calibrate the modeling. On the other hand, the DEM can consider the GM in their discrete form and can elegantly represent such characteristics, but they may not be suitable for large-scale modeling. Besides, current DEM methods are also designed to deal with well-defined and unrealistic shapes and the user-dependent parameters are, therefore, changed until a desirable outcome is produced. One solution is to use the power of DEM as a mesoscale technique with what FEM can offer for continuum-scale modeling [387–393]. One of the primary multiscale FEM-DEM methods was developed based on the Taylor hypothesis where the motion of particles is limited. Although it can provide results with smaller computations, it may produce unrealistic stiffness and thus physically unrealistic reactions among the particles. Later, an upscaling method based on the information provided by plasticity models was developed which can be used in continuum models. To be more specific, the Drucker-Prager model and an averaged version of the Mohr-Coulomb model guided by the Matsuoka-Nakai model are extracted from the granular-scale DEM modeling and upscaled to the continuum-scale methods. In another study, FEM was used to mesh the macroscopic domain on which DEM was implemented with the memory of loading history and received information from FEM for its boundary condition [394]. Then, DEM is solved to extract the constitutive models in each point which are feedback to FEM. In this method, DEM can capture the nonlinear dissipative behaviors of GM. This idea was later extended to crushable GM where particle breakage was modeled using DEM by replacing larger particles with smaller ones [395]. There are several other studies on how macro- and mesoscale modeling can be linked [396] and also more efficient numerical FEM-DEM modeling [397–401].

Generally, a set of finite-element meshes are used to discretize the region and DEM is used to provide the material constitutive model necessary for mesh integral points wherein the stresses and tangent moduli are calculated. Such properties, namely the stress increment and stiffness matrix, are derived based on the constitutive hypothesis in FEM. This assumption is relaxed in multiscale FEM-DEM as DEM will provide such information from the grain-scale modeling.

To conduct a hierarchical multiscale simulation, the domain should be discretized into appropriate FEM mesh. A weak form of the governing equation for a quasi-static condition can be written as:

$$\int_{\Omega} \boldsymbol{\sigma} : \nabla \mathscr{T} dV = \int_{\partial\Omega_t} t . \mathscr{T} dA, \tag{73}$$

where t is the boundary traction on the surface $\partial\Omega_t$ and $\mathscr{T}$ is the test function (e.g., displacement). This equation can be rewritten in FEM format as follow:

$$\boldsymbol{K}\boldsymbol{u} = \boldsymbol{f}, \tag{74}$$

where $\boldsymbol{K}$ is the stiffness matrix, and the displacement is shown by $\boldsymbol{u}$. $\boldsymbol{f}$ is also the nodal force vector. Since this equation is integrated with DEM and $\boldsymbol{K}$ depends on the loading history and state parameters, this parameter is replaced with the tangent matrix $\boldsymbol{K}_t$:

$$\boldsymbol{K}_t = \int_{\Omega} \boldsymbol{B}^T \boldsymbol{D} \boldsymbol{B} dV, \tag{75}$$

where $\boldsymbol{B}$ is the deformation matrix. One can use the Newton-Raphson method and update $\boldsymbol{K}_t$ and $\boldsymbol{\sigma}$ by minimizing the residual force $\boldsymbol{R}$:

$$\boldsymbol{R} = \int_{\Omega} \boldsymbol{B}^T \boldsymbol{\sigma} dV - \boldsymbol{f}. \tag{76}$$

By implementing the DEM, the mesoscale stress can be obtained using Love's formula for homogenized Cauchy stress from a set of particles:

$$\boldsymbol{\sigma} = \frac{1}{V} \sum_{N_c} \boldsymbol{f}^c \otimes \ell^c, \tag{77}$$

where the contact force, the branch vector connecting the centers of the two contacted particles, and the total volume of the system are presented by $\boldsymbol{f}^c$, ℓ^c, and V, respectively. Here, N_c represents the number of contacts within the volume. Consequently, the mean effective stress p and deviatoric stress q can be computed by:

$$p = \frac{1}{2} \mathrm{tr}(\boldsymbol{\sigma}), \tag{78}$$

$$q = \sqrt{\frac{1}{2} \boldsymbol{s} : \boldsymbol{s}}, \tag{79}$$

where the deviatoric stress tensor is shown by $\boldsymbol{s} = \boldsymbol{\sigma} - p\boldsymbol{\delta}$ with $\boldsymbol{\delta}$ defined as the Kronecker delta. In the multiscale approaches, the tangent operator is often derived from a homogenized bulk elastic module provided by DEM as [391]:

$$\boldsymbol{D} = \frac{1}{V} \sum_{N_c} (k_n \boldsymbol{n}^c \otimes \ell^c \otimes \boldsymbol{n}^c \otimes \ell^c + k_s \boldsymbol{t}^c \otimes \ell^c \otimes \boldsymbol{t}^c \otimes \ell^c), \tag{80}$$

where,

$$k_n := \frac{df_n^c}{du_n^c}, \tag{81}$$

$$k_t := \frac{df_t^c}{du_t^c}, \tag{82}$$

with u_n^c being the relative normal displacement of two particles. If, for example, the Hertz-Mindlin contact model is used, the stiffnesses can be calculated using:

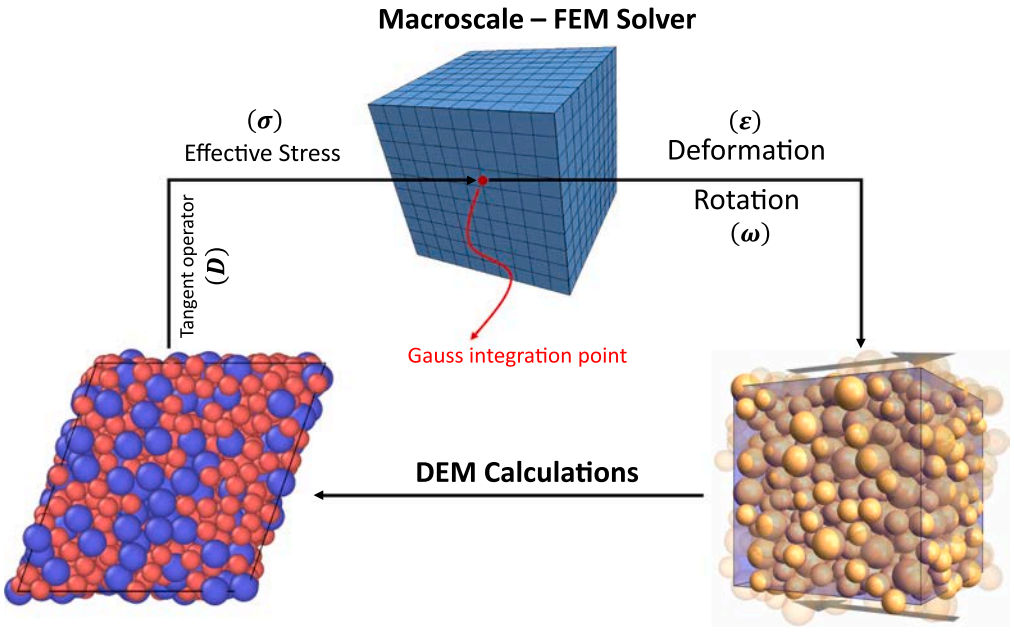

Fig. 47. The workflow for multiscale modeling (after [394]).

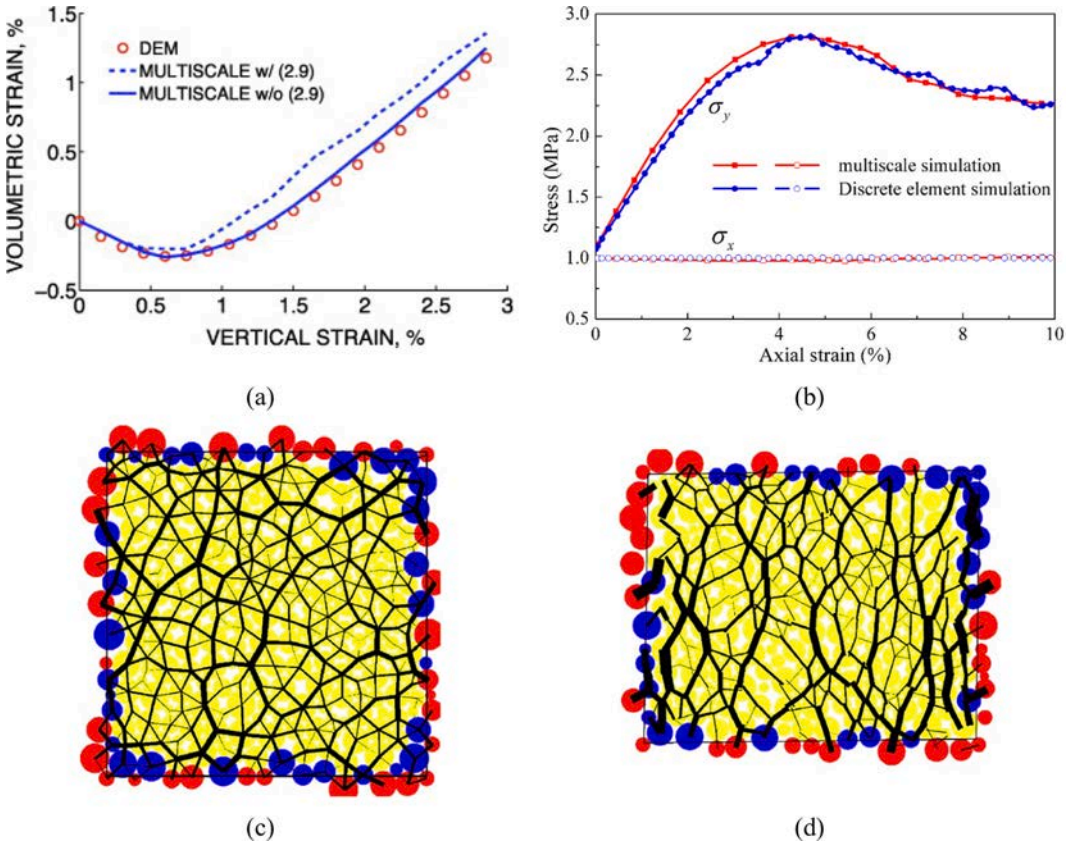

Fig. 48. (a) Illustration of the capability of multiscale modeling in reproducing similar results as of DEM's [403], (b) comparison between multiscale and DEM results [404], (c) the initial state of contact force distribution, (d) the final distribution of contact force after the loading on the GM shown in (d). (c) and (d) show how the fine-scale GM varies with loading.

$$k_n = \frac{G}{1-\nu}\sqrt{2r^* u_n^c}, \tag{83}$$

$$k_t = \frac{2G}{2-\nu}\sqrt{2r^* u_n^c}, \tag{84}$$

where r^* is the common radius of the contacted particles with the radii of r_1 and r_2, and follows $r^* = \frac{2r_1 r_2}{r_1+r_2}$.

One procedure that can be followed for establishing a hierarchical multiscale FEM-DEM modeling may follow these steps (see Fig. 47 as well):

1. Discretize the domain into finite sub-elements and select Gauss points on the inter-element boundaries or inside the elements. Each Gauss point must be connected to a DEM assembly.
2. Initiate the external loop corresponding to the FEM on the entire simulation domain
   i. Calculate the tangent operator ***D***
   ii. Find the displacement u

Several experiments have been conducted and promising results are obtained; see Fig. 48. Most of the available studies compare the multiscale results with those provided by the DEM to demonstrate how the multiscale method is capable of reproducing the main deformation features while the results, to some extent, agree with fine-scale modeling. This framework is further developed to deal with heat transfer by combining the discrete and continuum approaches [402].

2.2.8. *Multiphysics modeling*

In many problems of GM, it is not adequate to only consider the mechanical or flow behaviors, but considering them with other physics is necessary, which is called coupling. In this process, one can use momentum, mass, and energy in order to describe a multiphysics system. In GM, when accompanied by fluid, the system can be characterized using the position of particles, their velocity, size, concentration, and also temperature. This problem, clearly, becomes more complicated when additional physics is included.

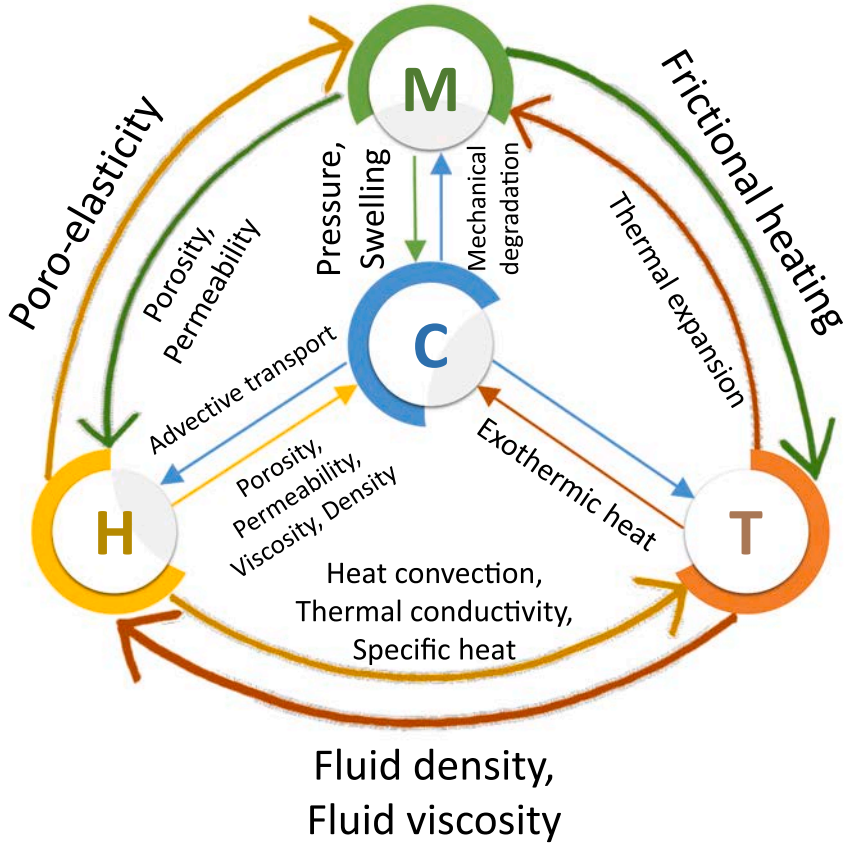

Fig. 49. The connections between the THMC processes in GM. Here, T, H, M, and C represent thermal, hydromechanical (fluid), mechanical, and chemical elements, respectively.

The chemical reactions can affect the final responses significantly and likewise, the amount of fluid (saturated/unsaturated) is also important. This problem in multiphysics literature is called thermo-hydro-mechanical-chemical (THMC) coupling and has witnessed tremendous progress. For example, the physical interactions in granular battery systems can be very variable, depending on the scale and conditions. In such a system, heat is produced due to cell inefficiencies, and it can affect the performance of the battery, both its mechanical properties and functionality. Likewise, chemical interactions of fluid and solid can cause mechanical and thermal reactions. Furthermore, all such changes can result in pressure build-up and significant deformation. Some GM also manifests swelling/shrinkage when they are in contact with a fluid, or when they experience a thermal variation. A similar condition may also be taken place when liquid interactions can cause cementation. The above phenomena can also be found in geo-GM where the in-situ/injected fluid can produce large deformations. Two such examples can be found in carbon storage and geothermal applications [296]. A schematic diagram showing the multi-connections between different physics is presented in Fig. 49.

The THMC problem has been investigated in large-scale geo-systems wherein understanding a simultaneous effect of different physics is important when one aims to quantify the deformation and distribution of risky elements/fluids or natural hazards systems. This topic is not, however, well studied in GM at a fine-scale due to the complexity of coupling. Nevertheless, a lot of work has been done on the effect of fluid, mechanical forces, and also temperature. We still need to conduct more research to better connect these physics in a more realistic and precise framework.

2.2.8.1. Fluid coupling. Coupling solid and fluid was probably one of the first multiphysics simulations conducted in the field of GM. In this modeling, Computational Fluid Dynamics (CFD) is often incorporated with DEM and is known as CFD-DEM. DEM oversees tracking the particles/solids while fluid motion is described using CFD. DEM is based on Newton's second law whereas CFD-DEM is based on Newton's third law indicating that all forces between the particles and fluid(s) exist in equal size and opposite directions. The coupling of fluid and particles, in general, can be achieved using both Eulerian-Eulerian and Eulerian-Lagrangian approaches. The former one is sometimes called the two-fluid-model (TFM) and considers both the fluid and solid as continuous and fully interpenetrating continua [405]. Thus, the solid is described by fluid-like properties, such as pressure, viscosity, and temperature. This type of modeling is constructed based on the kinetic theory of granular flow (KTGF) [406,407]. The Eulerian-Eulerian method is well-suited for modeling large systems. On the other hand, the Eulerian-Lagrangian method still considers the fluid as a continuum, but the solid is taken into account as particles (or parcels where a group of particles is considered together). In this approach, the particles are tracked

based on the forces exerted on them by the other particles and fluid. Through this review paper, we have provided an overview of the above two popular approaches for coupling GM and fluid. Overall, computational modeling methods have been found to be very useful and they can help to reduce the cost and also test various configurations and boundary conditions using which more reliable designs and deeper understanding can be achieved.

The Eulerian-Eulerian method comes with its simplicity in terms of using similar governing equations for each phase (GM and fluid). At the same time, it also imposes complex closure equations. The continuity and momentum equations for the fluid phase are:

$$\frac{\partial(\alpha_f\rho_f)}{\partial t}+\nabla.(\alpha_f\rho_f\mathbf{u})=0, \tag{85}$$

$$\frac{\partial(\alpha_f\rho_f\mathbf{u})}{\partial t}+\nabla.(\alpha_f\rho_f\mathbf{uu})=\alpha_f\nabla p_f-\nabla.\alpha_f\boldsymbol{\tau}_f-\mathbf{f}_d+\alpha_f\rho_f\mathbf{g}-\mathscr{T}, \tag{86}$$

where $\mathbf{f}_d$ and $\boldsymbol{\tau}_f$ are the Eulerian force between particles and fluid and viscous stress tensor, respectively. $\mathscr{T}$ is the total interfacial force, which includes the drag force and the lift force. For the solid phase, here particles p, similar equations can be used:

$$\frac{\partial([1-\alpha_f]\rho_p)}{\partial t}+\nabla.([1-\alpha_f]\rho_p\mathbf{v})=0, \tag{86}$$

$$\frac{\partial([1-\alpha_f]\rho_p\mathbf{v})}{\partial t}+\nabla.([1-\alpha_f]\rho_p\mathbf{vv})=-[1-\alpha_f]\nabla p_f-\nabla p_p-\nabla.[1-\alpha_f]\boldsymbol{\tau}_p-\mathbf{f}_d-[1-\alpha_f]\rho_p\mathbf{g}+\mathscr{T}, \tag{87}$$

where the velocity of the solid is shown by $\mathbf{v}$ and other particle properties are denoted by subscription p. p_p represents the particle normal forces of particle–particle interactions. In the above equations, the stress tensors for fluid and particle phases can be defined by:

$$\boldsymbol{\tau}_f=\mu_f[\nabla\mathbf{u}+(\nabla\mathbf{u})^T]+\frac{2}{3}\mu_f(\nabla.\mathbf{u})\boldsymbol{I}, \tag{88}$$

$$\boldsymbol{\tau}_p=(-p_p+\zeta_p\mathbf{v})\boldsymbol{I}+\mu_p\left\{[\nabla\mathbf{v}+(\nabla\mathbf{v})^T]-\frac{2}{3}\mu_f(\nabla.\mathbf{v})\boldsymbol{I}\right\}, \tag{89}$$

where μ_f is shear fluid viscosity, ζ_p is the bulk particle viscosity. The latter parameters account for the resistance of the solid phase to deform and can be expressed as:

$$\zeta_p=\frac{4}{3}[1-\alpha_f]^2\rho_p d_p g_0(1+e)\sqrt{\Theta/\pi}, \tag{90}$$

where $g_0=\frac{1}{2(1+\alpha_f)}/\alpha_f{}^3$ is defined as particle radial distribution, e is particle collision restitution coefficient and $\Theta=\langle\mathbf{C}_p.\mathbf{C}_p\rangle/3$ is the granular temperature wherein $\mathbf{C}_p$ implies the particle fluctuation velocity.

The particle–particle force is defined as follows, which accounts for velocity fluctuations (left term) and collisions (right term):

$$p_p=\rho_p[1-\alpha_f]\Theta_p+2\rho_p[1-\alpha_f]^2\Theta_p g_0(1+e). \tag{91}$$

Thus, the particle shear viscosity can be expressed as:

$$\mu_p=\mu_{p,Collisional}+\mu_{p,Kinetic}, \tag{92}$$

each of which is defined as:

$$\mu_{p,Collisional}=\frac{4}{5}[1-\alpha_f]^2\rho_p d_p g_0(1+e)\sqrt{\Theta/\pi}, \tag{93}$$

$$\mu_{p,Kinetic}=\frac{5\sqrt{\pi}}{48}\frac{\rho_p d_p}{(1+e)g_0}\left(1+\frac{4}{5}\eta(1+e)g_0[1-\alpha_f]\right)^2\sqrt{\Theta}, \tag{94}$$

$$\eta=\frac{1}{2}(1+e)$$

Since the role of particles is not considered directly, thus, one must consider the interactions between particles in terms of the pressure of particles p_p, bulk particle viscosity ζ_p, and particle shear viscosity λ_p [408].

For calculating $\mathscr{T}$ in the above equations, the drag force, and lift force must be included. The drag force per unit volume for spherical particles is defined as:

$$\mathscr{T}_d=\frac{3C_D}{4d_p}[1-\alpha_f]\rho_f|\mathbf{v}-\mathbf{u}|(\mathbf{v}-\mathbf{u}), \tag{95}$$

where C_D is drag coefficient and can be defined using the following equation for closely distributed particles (i.e., $\alpha_f<0.2$):

$$C_D = \alpha_f^{-1.65}\max\left\{\frac{24}{N'_{Re_p}}\left(1+0.15N'^{\,0.687}_{Re_p}\right), 0.44\right\}, \tag{96}$$

where $N'_{Re_p} = \alpha_f N_{Re_p}$ and $N_{Re_p} = \rho_f|\mathbf{u}-\mathbf{v}|d_p/\mu_f$. For $\alpha_f > 0.2$, the Gidaspow model can be used, which is defined as [406]:

$$\mathscr{F}_d = \frac{150(1-\alpha_f)^2\mu_f}{\alpha_f d_p^2} + \frac{7}{4}\frac{(1-\rho_f)\rho_f|\mathbf{u}-\mathbf{v}|}{d_p}. \tag{97}$$

For the lift force, one can use the Saffman and Mei model [409].

In this method, however, prescribing a particle size distribution can increase the computational cost since several phases are required to model several particle sizes. At the same time, because the fluid-particle interactions are interpreted in a continuum domain, no specific information is available for every single particle if one aims to get such data.

Unlike the above-described Eulerian-Eulerian framework, Eulerian-Lagrangian methods offer more flexibility and detailed information about the nature of interactions in granular systems. One such method is the CFD-DEM method wherein the motion of each particle is traced individually. Thus, more complex particle shapes with a diverse size distribution can be used. Furthermore, adhesive/cohesive GM can be also simulated. The same flexibility also exists for heat transfer. Depending on the resolution/scale of modeling, CFD-DEM can be used with two schemes, namely resolved and unresolved methods. In other words, CFD-DEM can be a balance between the required computations for direct numerical simulations (DNS) and also two-phase-fluid modeling.

In the resolved CFD-DEM, the CFD mesh is considerably smaller than the particle size, which is suitable for modeling a small number of particles and can be thought of as a group of DNS methods. In contrast, the fluid mesh is much larger than the particle size in unresolved methods. Thus, a mesh cell can encompass several particles and the computational cost of CFD is reduced compared to the resolved methods. This type of modeling is well-suited for systems with a large number of particles. As mentioned earlier, however, one can clump a group of particles together and consider them as a single particle to accelerate the CFD-DEM simulation [410–412].

CFD-DEM as a Eulerian-Lagrangian method is an excellent option for studying GM in the presence of fluid such that high accuracy can be achieved if a small mesh is used. This approach allows acceptable descriptions of the fluid and GM. To make such methods more practical, the fictitious domain approach can reformulate this problem as a moving boundary problem where the fluid and solid/particle domains are considered separately and the forces are exchanged between them [413]. The exchange of information can, however, result in inaccuracy and instability for numerical modeling. To prevent this issue, a continuous indicator function was introduced through which the CFD cells get a number. This number does not show the solid ratio but a smooth representation provided by a Heaviside function [414]. One such approach is the immersed boundary method. Later, the idea of fictitious domain method with Lagrangian multiplier improved the integration of body force with the Navier-Stokes equations [415–418]. This revised algorithm takes three steps. First, the entire domain is considered fluid and the movement of the solid is enforced and relaxed subsequently. More specifically, the Navier-Stokes equations are used on the entire domain and the produced information by DEM about the solid is added as a body force and the velocity field will eventually be updated given the conservation equation. Finally, the pressure will also be adjusted as well.

The above descriptions and procedures are now depicted mathematically. As of the computational domain, which encompasses both GM (Ω_p) and fluid (Ω_f), the governing equations can be written as:

$$\nabla.\mathbf{u} = 0 \text{in} \Omega_f, \tag{98}$$

$$\rho\left(\frac{\partial \mathbf{u}}{\partial t} + (\mathbf{u}.\nabla)\mathbf{u}\right) = \nabla.\boldsymbol{\sigma} + \rho g \nabla z \text{in} \Omega_f, \tag{99}$$

$$\mathbf{u} = \mathbf{u}_i \text{on} \Gamma_p, \tag{100}$$

$$\boldsymbol{\sigma}.\boldsymbol{n} = \boldsymbol{t}_{\Gamma_p} \text{on} \Gamma_p, \tag{101}$$

$$\mathbf{u}(t) = \mathbf{u}_0 \text{in} \Omega_f, \tag{102}$$

$$m_p\frac{d\mathrm{u}_p}{dt} = m_p g + f_{p,f} + \sum_{N_p} F_{p,p} + \sum_{N_w} F_{w,p}, \tag{103}$$

where Γ_p is the interface of fluid and particle, $\boldsymbol{t}_{\Gamma_p}$ is the traction vector excreted on the particle surface by the fluid, and a no-slip boundary condition is considered for the fluid-wall interface.

To use the above equations, a temporary velocity field $\widehat{\mathbf{u}}$ is first calculated using the NS equations for the entire domain, which can be accomplished using a finite volume CFD method. Then, $\widehat{\mathbf{u}}$ is corrected in Ω_p by enforcing the particle velocity produced by DEM, which results in a new velocity filed $\widetilde{\mathbf{u}}$. This can be achieved by adding the body force to the NS equations:

$$f = \rho\frac{\partial}{\partial t}(\widetilde{\mathbf{u}} - \widehat{\mathbf{u}}). \tag{104}$$

The new velocity should also satisfy the continuity equation, thus:

$$\nabla.\underbrace{\overline{\boldsymbol{u}}}_{(\tilde{\boldsymbol{u}}-\nabla\phi)}=0, \tag{105}$$

where $\nabla\phi$ is the correction factor and can be calculated using:

$$\nabla\phi=\nabla.\tilde{\mathbf{u}}. \tag{106}$$

Using the corrected terms, the above equations can be revised as follows [416,419]:

$$\rho\frac{\partial\widehat{\mathbf{u}}}{\partial t}=\rho\frac{\partial\overline{\mathbf{u}}}{\partial t}+\rho\frac{\partial(\nabla\phi)}{\partial t}-f, \tag{107}$$

$$\rho\frac{\partial\overline{\mathbf{u}}}{\partial t}+\nabla.(\rho\widehat{\mathbf{u}}\widehat{\mathbf{u}})=-\left(\nabla p+\rho\frac{\partial(\nabla\phi)}{\partial t}\right)+\mu\Delta\widehat{\mathbf{u}}+f. \tag{108}$$

The above procedure allows updating the CFD equations, but the DEM must also be connected to update the motion of particles given the extra force excreted by the fluid. Calculating the trajectory of particles can be achieved using Verlet integration [298]. For doing such, one can start with the body's boundary which fluid exerts a force on. Thus, Eq. (101) is integrated over Γ_p:

$$\int_{\Gamma_p}\boldsymbol{\sigma}.\boldsymbol{n}d\Gamma_p=\int_{\Gamma_p}\boldsymbol{t}_{\Gamma_p}d\Gamma_p. \tag{109}$$

By applying divergence to the above equation, we get:

$$\int_{\Gamma_p}\nabla.\boldsymbol{\sigma}d\Omega_p=\int_{\Gamma_p}\boldsymbol{t}_{\Gamma_p}d\Gamma_p. \tag{110}$$

By assuming dealing with an incompressible fluid (i.e., $\boldsymbol{\sigma}=-p\boldsymbol{I}+\boldsymbol{\tau}$), the above equation can be rewritten as:

$$\int_{\Gamma_p}-\nabla p+\nabla.\boldsymbol{\tau}d\Omega_p=\int_{\Gamma_p}\boldsymbol{t}_{\Gamma_p}d\Gamma_p. \tag{111}$$

Besides, the shear stress in a Newtonian fluid is defined as:

$$\boldsymbol{\tau}=2\mu D(\mathbf{u})=\mu\left(\nabla\mathbf{u}+(\nabla\mathbf{u})^T\right). \tag{112}$$

Thus,

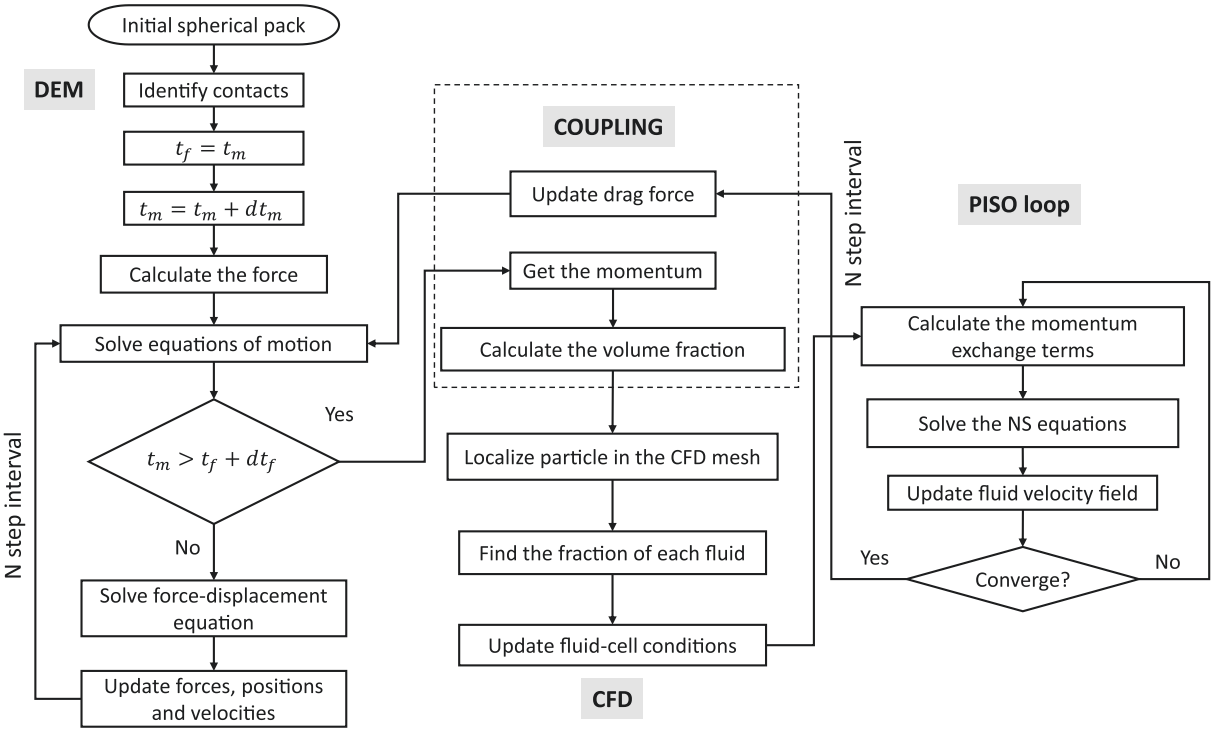

Fig. 50. The diagram of CFD-DEM coupling.

$$\int_{\Omega_p} -\nabla p + \nabla.\mu\left(\nabla\mathbf{u} + (\nabla\mathbf{u})^T\right)d\Omega_p = \int_{\Gamma_p} \boldsymbol{t}_{\Gamma_p} d\Gamma_p, \tag{113}$$

which can be expressed as:

$$\int_{\Omega_p} -\nabla p + \nu\rho\Delta\mathbf{u}d\Omega_p = \int_{\Gamma_p} \boldsymbol{t}_{\Gamma_p} d\Gamma_p. \tag{114}$$

The above equation contains a pressure and a viscous term, which come from the *discrete fluid domain*. Therefore, this requires discretizing the above equation. First, this equation should be extended to the entire domain Ω as what we have for the fluid:

$$\int_{\Omega_p} -\nabla p + \nu\rho\Delta\mathbf{u}d\Omega_p = \int_{\Omega} (-\nabla p + \nu\rho\Delta\mathbf{u})\xi_\Omega d\Omega, \tag{115}$$

where $\xi_\Omega = 1$ if the node is in the particle domain and $\xi_\Omega = 0$ otherwise. Thus, the whole domain Ω can be decomposed (T_h) into cells c using which the equation can be rewritten as:

$$\int_{\Omega} (-\nabla p + \nu\rho\Delta\mathbf{u})\xi_\Omega d\Omega = \sum_{c\in T_h}\int_{\mathrm{V}(c)} (-\nabla p + \nu\rho\Delta\mathbf{u})\xi_\Omega d\mathrm{V}(c), \tag{116}$$

where $\mathrm{V}(c)$ is the volume of cell c. Finally, the force between fluid and particles for all cells within the solid domain $\overline{T}_h$ can be expressed by:

$$f_{p,f} = \sum_{c\in\overline{T}_h} (-\nabla p + \nu\rho\Delta\mathbf{u})(c)\mathrm{V}(c). \tag{117}$$

The above-described procedures are summarized in Fig. 50.

The above-described method is well-suited for studying GM systems with a small number of particles. To deal with models with many particles, as mentioned earlier, one can use the TFM method. Here, we describe an alternative that considers the particles as discrete elements while an analogy of what is decided in TFM for fluid, namely locally averaged NS equations, is still considered for fluid. Thus, the new method is still based on CFD-DEM with a slight modification for the fluid part and the force exchange procedure. To do so, the fluid–solid interaction force can be defined by:

$$\mathbf{f}_d = K_d(\mathbf{u} - \mathbf{v}), \tag{118}$$

where

$$K_d = \frac{1}{\Delta V}\sum \mathscr{F}_{d,i}. \tag{119}$$

The governing equations for particles, which are based on DEM, almost remain as described before with an extra element representing the fluid-particle interactions $f_{p,f}$. Thus, we will have:

$$m_p\frac{du_p}{dt} = m_p g + f_{p,f} + \sum_{N_p} f_{p,p} + \sum_{N_w} f_{w,p}, \tag{120}$$

where all the forces between fluid and particle $f_{p,f}$ is shown using:

$$f_{p,f} = \mathscr{F}_d + f_{\nabla p} + f_{\nabla.\tau} + f_{vm} + f_B + f_{Saff} + f_{Mag}. \tag{121}$$

In this equation, $\mathscr{F}_d$, as defined before, is the drag force, $f_{\nabla p}$ the pressure gradient force, $f_{\nabla.\tau}$ is the viscous force, f_{vm} is the virtual mass force, f_B is the Basset force, f_{Saff} is the Saffman force, and f_{Mag} is the Magnus force. Among all these forces, however, $\mathscr{F}_d$, $f_{\nabla p}$, and $f_{\nabla.\tau}$ are the most important ones. The other forces are either ignored or included in some specific cases. Thus, the above equation can be summarized as follows:

$$f_{p,f} = \mathscr{F}_d + f_{\nabla p} + f_{\nabla.\tau}. \tag{122}$$

As discussed earlier, various force models have been developed [406]. But here another popular form of such forces is reviewed, which is known as Koch and Hill model [420–423]. This model is given by:

$$\mathscr{F}_d = \frac{V_p\beta}{\gamma_p}(\mathbf{u} - \mathbf{v}), \tag{123}$$

where V_p denotes particle volume and β is interphase momentum exchange term, defined by:

$$\beta = \frac{18\mu_f\alpha_f^2(1-\alpha_f)}{d_f^2}\left(F_0(1-\alpha_f) + \frac{1}{2}F_3(1-\alpha_f)Re_p\right) \tag{124}$$

where

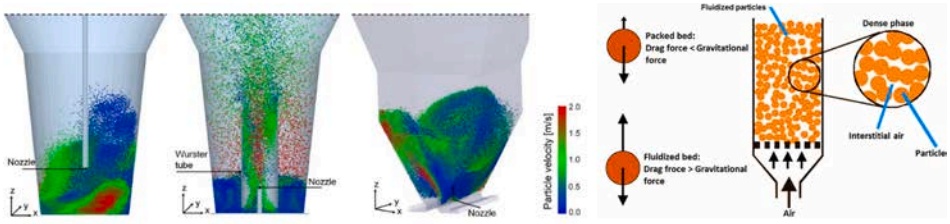

(a) (b) (c) (d)

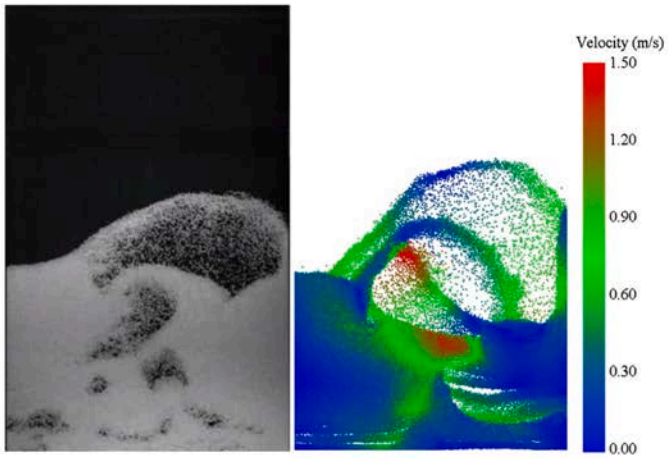

(e)

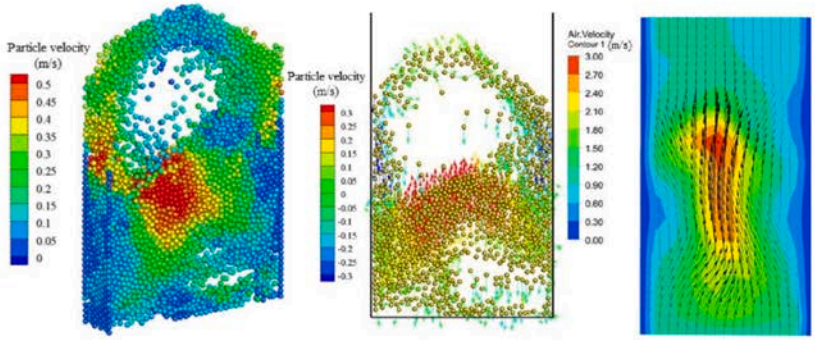

(f)

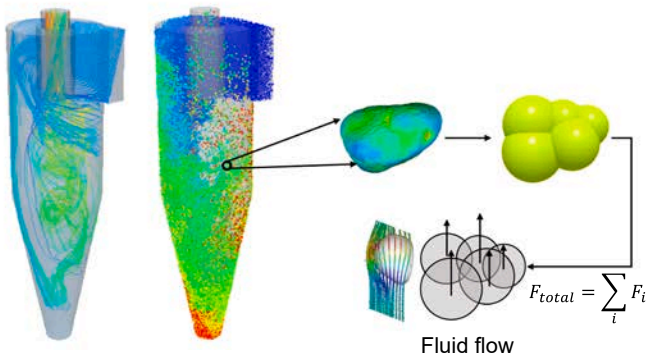

(g)

(caption on next page)

Fig. 51. Demonstration of particle position and velocity for (a) top-spray granulator, (b) the Wurster-coater, and (c) the spouted bed. The colors here represent the velocity [39]. (d) the process using which fluidization, as one of the widely used fluid-particle systems, works [425]. (e) Qualitative comparison of (left) an image of fluidized alumina spheres in the flat fluidized bed with (right) an image of the DEM-CFD simulation with identical particle number at $u = 2 \bullet u_{mf}$ [426]. (f) bubbling effect in a fluidized bed [427]. (g) schematic representation of a common approach in coupling irregular particles using the clump method.

$$Re_p = \frac{\alpha_f \rho_f |\mathbf{u} - \mathbf{v}| d_p}{\mu_f}. \tag{125}$$

Furthermore, functions F_0 and F_3 are given as:

$$F_0(\gamma_p) = \begin{cases} \dfrac{1 + 3\sqrt{\dfrac{(1-\alpha_f)}{2}} + \dfrac{135}{2}(1-\alpha_f)\ln(1-\alpha_f) + 16.14(1-\alpha_f)}{1 + 0.681(1-\alpha_f) - 8.48(1-\alpha_f)^2 + 8.16(1-\alpha_f)^3}, if\,(1-\alpha_f) < 0.4 \\ \dfrac{10(1-\alpha_f)^2}{\alpha_f^3}, if\,(1-\alpha_f) \geq 0.4 \end{cases} \tag{126}$$

$$F_3(1-\alpha_f) = 0.0673 + 0.212(1-\alpha_f) + \frac{0.0232}{\alpha_f^5}. \tag{127}$$

The other two terms, namely $f_{\nabla p}$ and $f_{\nabla .\tau}$ are respectively defined as:

$$f_{\nabla p} = -V_p \nabla p, \tag{128}$$

$$f_{\nabla .\tau} = -V_p \nabla .\tau. \tag{129}$$

Hilton et al. [424] used a coupled CFD/DEM method with individually modeled spray droplets to simulate spray deposition onto solid particles in a fluidized bed spray coating system. The simulation results provided the coating information from the intra-particle level on each individual particle. It was found that the inflow velocity, the spacing between the Wurster insert, and the base and base slope angle have greatly affected the volume deposition and coating quality. With their numerical DEM/CFD method, it is easier to evaluate the optimal settings for the spray coating system compared with the experimental studies; Fig. 51. Fries et al. [39] used coupled DEM-CFD to numerically describe fluid flow, particle motion, and collision dynamics inside a fluidized bed granulator. The results of average particle velocity, average particle–particle and particle–wall collision velocity, and the collision frequency are compared from three different industrial fluidized bed spray granulator configurations, that is, top-spray granulator, Wurster-coater, and spouted bed. The comparison results have been verified by relevant experiments, which showed that the wetting intensity and growth rate of the top-spray granulator are the lowest while the spouted bed has the most intensive gas–liquid-solid contact, and the Wurster-coater achieves the fastest growth rate. More results on the comparison between the computational and experimental methods are shown in Fig. 52. Furthermore, the effect of particle size in irregular and crumpled particles is also studied and the results are compared in Fig. 52(b). As can be seen, changing the particle size can affect the pressure distribution.

Alternatively, DEM can be coupled with LBM [430]. The Lattice Boltzmann Method (LBM) is a computational approach for modeling the mass and velocity field of fluid flow. Numerical simulation of fluid flow is useful for evaluating the hydraulic characteristics of GM. Among various techniques, the LBM is widely accepted due to the ease of implementing boundary conditions and the numerical stability in a wide variety of flow conditions [431]. Kutay et al. [431] used LBM for 2D and 3D environments to represent pore-scale monophasic Newtonian incompressible fluid flow in GM. Three-dimensional geometries of compacted aggregates were generated from the X-ray CT technique and used as input for the LB model. The accuracy of the models was verified by comparing the results with analytical solutions of simple geometries and hydraulic conductivity measurements on the compacted aggregates. A coupled system with DEM and LBM is used for modeling the liquefaction of saturated granular soil [432]. The approach was used to model the response of a saturated soil deposit subjected to low and large-amplitude seismic excitations. Wang et al. [433] developed a 3D coupled bonded particle and LBM (BPLBM) with an immersed moving boundary scheme for fluid–solid interaction. It is then applied to investigate the erosion process of soil particles in granular filters placed within earth dams. Richefeu et al. [434] applied a capillary condensation model simulated by a multiphase Lattice Boltzmann model as a means to generate homogeneous distributions of liquid clusters in 2D granular media. Liquid droplets condense from the vapor phase between and on the grains, and they transform into capillary bonds and liquid clusters as thermodynamic equilibrium is approached. Some results are shown in Fig. 53.

In one of the recent studies, fluid and solid forces are coupled while the effect of morphology is considered [437]. A snapshot of the considered particles with complex shapes is shown in Fig. 54. As can be seen, a variety of particles with complex shapes are considered which are used for a collapse problem in dry and fully-saturated conditions. The results are demonstrated in Fig. 55. The results indicate that the horizontal displacement increase for more regular particles. A similar trend is also observed in the vertical direction but with a smaller intensity. In the fully-saturated system, however, both displacements are hindered.

2.2.8.2. Thermal coupling. Another important physics that has been included in the previously discussed methods and equations is heat [438]. Heat in GM can be produced and transported to other locations through conductions if particles are in contact. This process

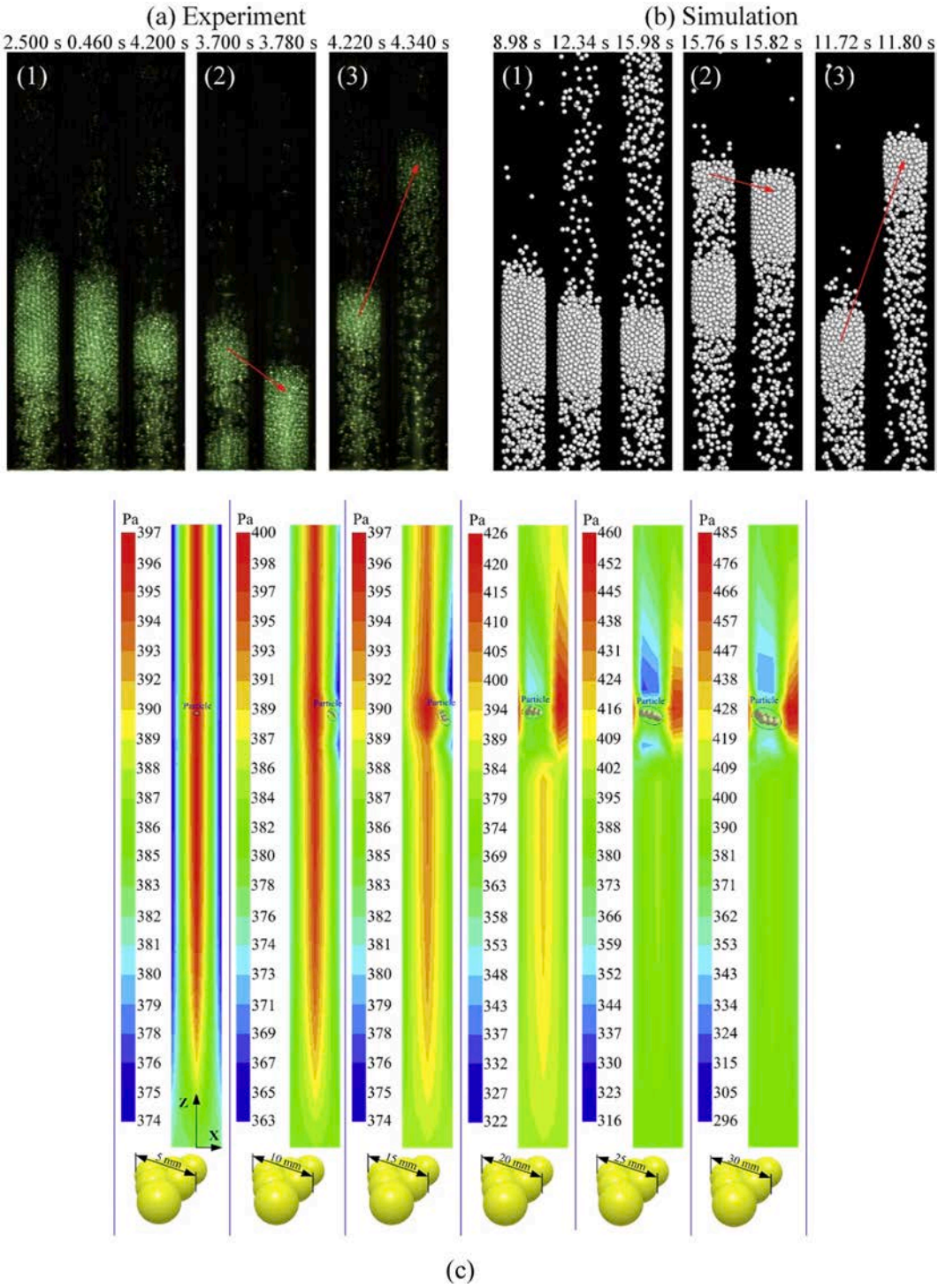

Fig. 52. (a, b) Comparison of plug flow for (1) random length, (2) downward merging, (3) plug collapse in a vertical column of fluid and particles [428]. (c) The effect of particle size on the dynamic pressure of the flow field in the pipe [429].

can be expedited if fluid exists between the particles, which adds another way of heat transfer, namely convection. Furthermore, friction between the particles can be another source of heat. Finally, radiation between the particles' surfaces might also produce heat, which is not very common but can be considered if relevant GM are under consideration. All such heat phenomena are shown in Fig. 56. As can be seen, heat can be transferred in different ways. As an example, drying in porous media is one of those important phenomena found in fluidized beds, rotating drums, and many other locations [439–441]. Aside from these particular applications,

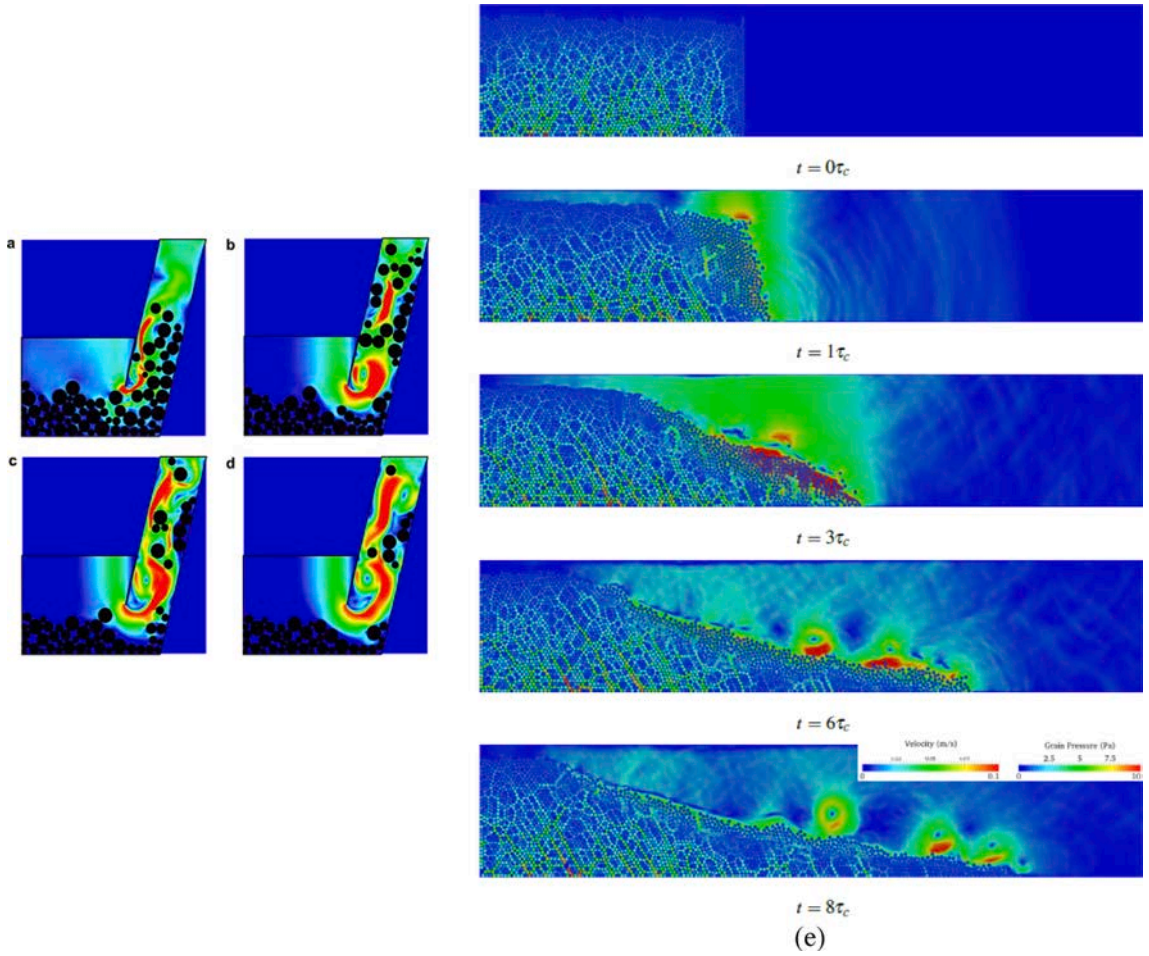

Fig. 53. Total velocity of fluid mixed with particles in four timesteps (a-d) [435], (e) the fluid and particle velocity profiles for a granular column collapse at different times [436].

heat transfer is also relevant to packed GM heat exchangers, catalyst packing, calciners, and many other examples [301,442–447]. This topic has been investigated in GM using DEM as this method can provide detailed information about particles and their heat characteristics. This subject is, however, accompanied by more complexities, such as the temperature- and time-dependent nature of GM, the interactions between the particles, nonlinearity in heat and mass transfer, and complex contact models, which makes the heat transfer problem to be challenging within the DEM framework. As discussed, Eulerian-Eulerian methods are more practical for large systems, but they are not able to provide detailed information about thermal conductivities, stress tensors, and so many other physical properties. Such methods are unable to offer accurate information at the particle level (e.g., temperature distribution on and within particles, local interactions between particles, void space, fluid distribution, …). All such insights are, however, crucial for making an accurate evaluation of the thermal distribution and heat transfer.

Parallel to the Eulerian-Eulerian methods for studying heat transfer, the Eulerian-Lagrangian methods were also developed with a similar purpose, but a different capability. For example, DNS-DEM [448], CFD-DEM [301], and LBM-DEM [449]. Several studies have shown promising results of DEM for heat transfer [450,451]. For example, aside from all the advantages DEM offers, it can also help with an accurate heat transient [442,452–454], but it still can be computationally expensive as the heat transfer equations are solved for each particle individually.

As mentioned, heat in GM can be transferred in different ways. Here, three of them, namely conduction, convection, and radiation, are briefly reviewed. It should be noted that the Biot number $\mathrm{Bi} = h_{gs}d/k_s$ is often used to define the importance of convection and conduction in GM, where k_s is the thermal conductivity, h_s is the convective heat transfer coefficient, and d is a characteristic length [455]. One of the preliminary studies on heat transfer in GM was presented by Batchelor and Brien [456] who offered an analytical equation for two adjacent particles between which heat is transferred through conduction and is valid under limited situations. Later, the elasticity theory was added to this equation to take the contact time and area into account when the particles are moving [457,458]. The provided foundation was used in DEM to take the heat transfer into account [459]. This implementation resulted in unrealistic outcomes since the contact area and time were not modeled accurately. The issue of inaccurate contact area estimation was rectified in separate studies [442,460,461]. Meanwhile, Patil et al. [462] provided the heat produced by collision initially in the DEM,

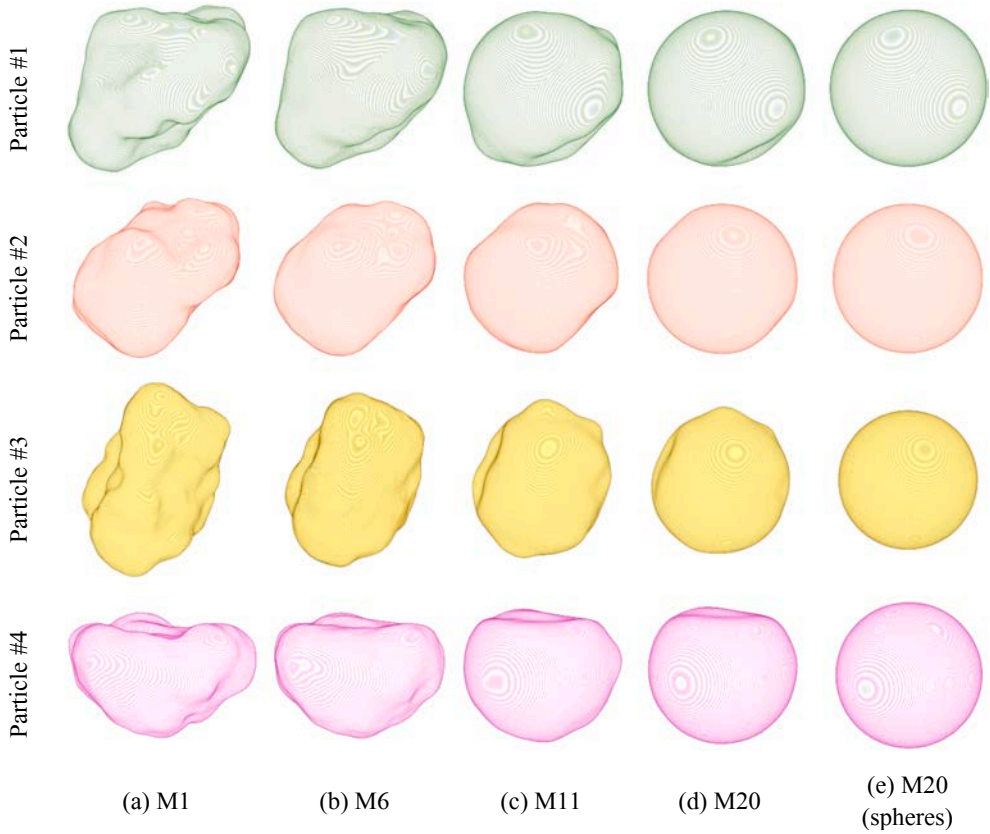

Fig. 54. A set of complex particles starting used for studying the effect of morphology on the dynamic of GM from highly irregular (M1) to spherical particles (M20). These particles are taken directly from the X-ray images without any simplifications [437].

but it fails to address other heat sources (e.g., particle–wall interactions). This condition becomes more complex when a fluid between two particles can affect heat conduction [463,464]. Later, the idea of the Voronoi polyhedron was proposed through two models (A & B), which compute the conduction by taking both the particles and fluid into consideration [465]. This model was further revised, but the foundation remained the same [466–470].

Heat transfer through convection has been studied more extensively compared to other methods. Convection in DEM was implemented based on the water droplet evaporation experiment [471,472], which can vary depending on the solid density in the system. Then, semi-empirical equations were developed for packed pebble GM under different flow settings [473–475]. Later, a correlation function was proposed for pneumatic transport [476]. Subsequently, the effect of particle transverse motion was also added to the previous methods [477,478]. The effect of external force, porosity, coordinate number, and particle size distribution was also studied [479]. A more accurate and resolved version of the above equations was also developed through which the thermal behaviors can be described better [480].

Incorporating radiation, which is the third method of heat transfer in GM, has been found to be more challenging. Generally speaking, one can get a radiation temperature by computing the radioactive intensity of GM-fluid, which is often considered a rough estimation of the temperature [442,481–484]. One other approach to consider the radiation heat transfer is using the view factor solution [467,485–488]. This method is, however, limited in terms of dealing with a blockage, or they are restricted to static systems [489–491], not something we have in dynamic GM. One of the only methods that can be used with a dynamic system, still based on computing the view factor, has recently been presented [492]. Aside from the above models, other studies have also been conducted to deal with GM, in particular those with non-isothermal behaviors. Such GM manifest a distribution of thermal energy inside the particles and surface as well [441,493–495].

For coupling the thermal effects, several parameters should be defined and added to the previously developed equations. Some of these parameters include the initial temperature of the GM, heat capacity, fluid properties and temperature, heat transfer coefficient, and boundary temperature. It should be noted that the previous equations are not changed, but new elements are added to represent the energy in a more comprehensive way. In its basic form, heat transfer for a dry GM, assuming that each particle is described by a temperature, can be described using:

$$m_i c_{p,i} \frac{dT_i}{dt} = \sum Q_i, \tag{130}$$

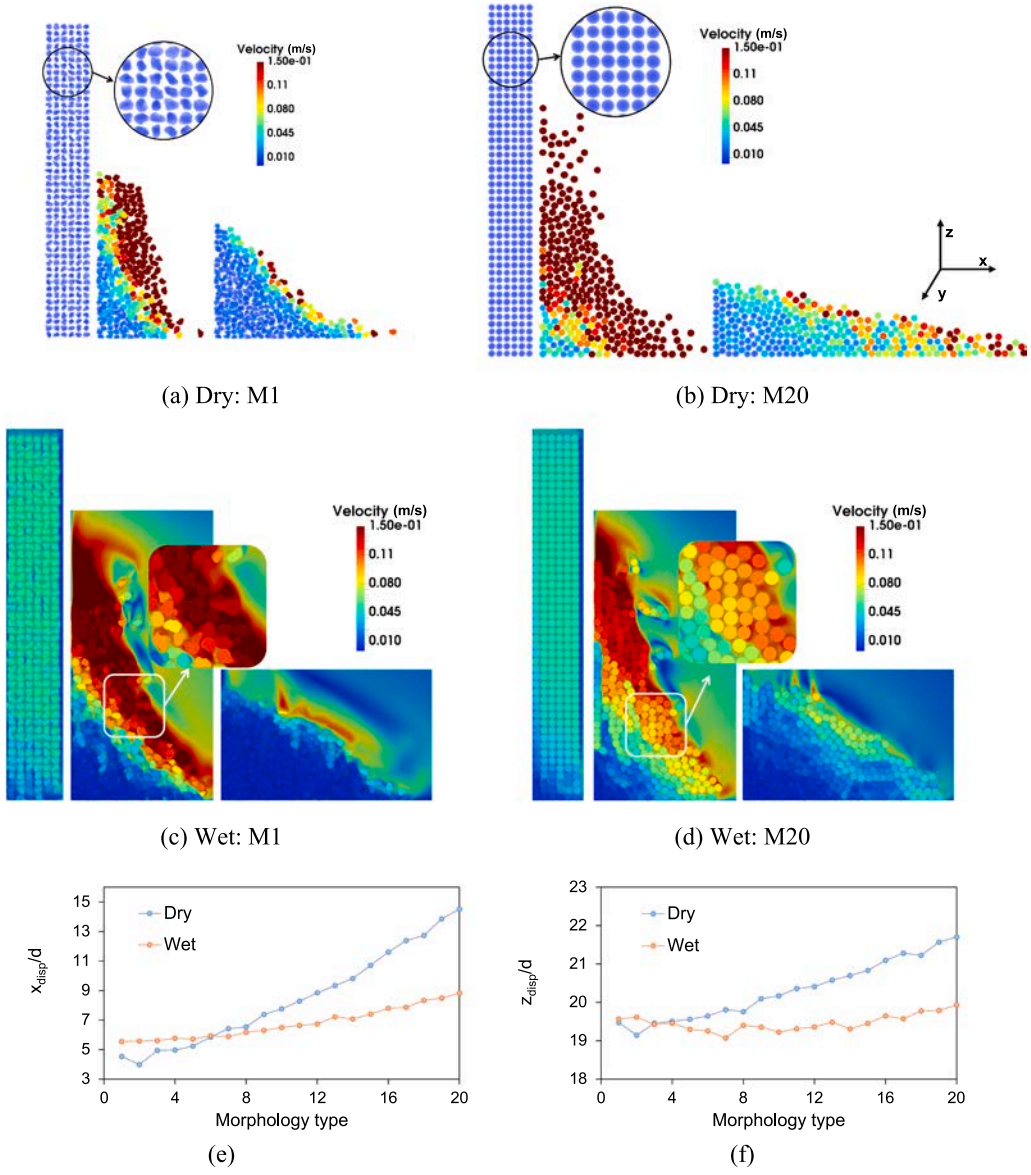

Fig. 55. (a-c) Velocity snapshots of the collapse of irregular (M1) and spherical (M20) particles in both dry and fully-saturated conditions. (e) x-direction (x_{disp}/d) displacement, and (f) z-direction (z_{disp}/d) displacement [437].

where Q_i, m_i, $c_{p,i}$, T_i are the net rate of the transferred heat to particle i by the surrounding particles/fluid/walls/other forms of heat transfer, mass, heat capacity, and temperature of the particle i, respectively. This simple equation should be considered for each individual particle in the system with the initial temperature of $T_i = T_i^0$ and the initial time of 0. Then, the discussed heat transfer mechanisms can be added.

First, the most important way of heat transfer is through the fluid. In this case, the energy equation for a volume can be written as:

$$\frac{\partial(\rho_f \alpha_f E_f)}{\partial t} + \nabla.(\mathbf{u}\alpha_f(\rho_f E_f + p)) = \nabla.\left(\alpha_f k_f^{eff} \nabla T_f\right) + Q_{f,h}, \tag{131}$$

where E_f and T_f are the rate of energy transported by the fluid within the control volume and the temperature of the fluid, respectively. $k_f^{eff} = \sum_{i=1}^{n} k_i^{eff}$ is the effective fluid thermal conductivity, which can be written in form of fluid thermal conductivity k_f [496]:

$$k_{\mathrm{f}}^{\mathrm{eff}} = \frac{1-\sqrt{1-\alpha_f}}{\alpha_f} k_{\mathrm{f}}. \tag{132}$$

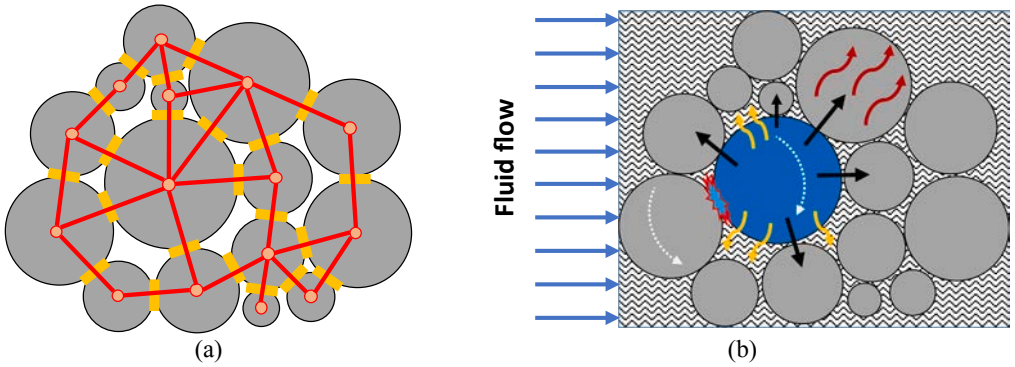

Fig. 56. Demonstration of various ways of heat transfer in GM. (a) conductance in dry conditions, (b) black arrows (conductance), yellow arrows (convection), and red arrows (conduction). The friction between particles is shown using a blue region [296].

E_f is expressed by:

$$E_f = h_f - \frac{p}{\rho_f} + \frac{\mathbf{u}.\mathbf{u}}{2}, \tag{133}$$

where h_f is the specific enthalpy of fluid. By substituting this equation in Eq. (133), we will get:

$$\frac{\partial}{\partial t}\left(\rho_f \alpha_f \left(c_{v,f} T_f + \frac{\mathbf{u}.\mathbf{u}}{2}\right)\right) + \nabla.\left(\mathbf{u}\alpha_f \rho_f \left(c_{p,f} T_f + \frac{\mathbf{u}.\mathbf{u}}{2}\right)\right) = \nabla.\left(\alpha_f k_f^{eff} \nabla T_f\right) + Q_{f,h}, \tag{134}$$

where $c_{v,f}$ and $c_{p,f}$ are the heat capacities of fluid at constant volume and pressure conditions.

Another important element related to heat transfer is for a situation when two particles are in direct contact with each other and hold different temperatures. The amount of transferred heat for particles i and j can be quantified using:

$$Q_{ij,s} = H_C^{ij}\left(T_j - T_i\right), \tag{135}$$

where $H_C^{ij} \in [1\alpha]$ represent contact conductance and it depends on the amount of force exerted on particles and how much the GM is packed. This parameter can be defined as follow based on Hertz's elastic contact theory, which also connects the solid properties (e.g., Young's modulus and Poisson's ratio) to the deformation:

$$H_C^{ij} = 2k_s\left(\frac{3F_n r^*}{4E^*}\right)^{1/3}, \tag{136}$$

where k_s is the thermal conductivity of the solid porous medium, $\frac{1}{r^*} = \frac{1}{r_i} + \frac{1}{r_j}$ and $\frac{1}{E^*} = \frac{1-\nu_i^2}{E_i} + \frac{1-\nu_j^2}{E_j}$ are, respectively, the mean radii of particles and effective Young's modulus for particles i and j. In the later equation, ν represents the Poisson's ratio [476,497].

The convective heat between particle i and the fluid in its vicinity with temperature T_f can be quantified by:

$$Q_{i,f} = h_i A_i\left(T_f - T_i\right), \tag{137}$$

where h_i and A_i are the heat transfer coefficient and surface area of the particle, respectively. The heat transfer coefficient can be calculated using an empirical equation based on Nusselt number Nu_p, which is given by [498]:

$$Nu_p = \left(7 - 10\alpha_f + 5\alpha_f^2\right)\left(1 + 0.7\mathrm{Re}_p^{0.2}\mathrm{Pr}^{0.33}\right) + \left(1.33 - 2.40\alpha_f + 1.20\alpha_f^2\right)\mathrm{Re}_p^{0.7}\mathrm{Pr}^{0.33}, \tag{138}$$

where

$$h = \frac{Nu_p k_f}{d_p}, \mathrm{Re}_p = \frac{\alpha_f \rho_f d_p |\mathbf{u} - \mathbf{v}|}{\mu_f}, \tag{139}$$

and the Prandtl number Pr is defined as:

$$\mathrm{Pr} = \frac{\mu_f c_{p,f}}{k_f}. \tag{140}$$

The above-described heat transfer cases can be used and calculate the thermal model as:

$$mc_p \frac{dT}{dt} = Q_{cond.} + Q_{conv.}. \tag{141}$$

To be more specific, the amount of heat transferred to particle i surrounded by particles ξ can be calculated using:

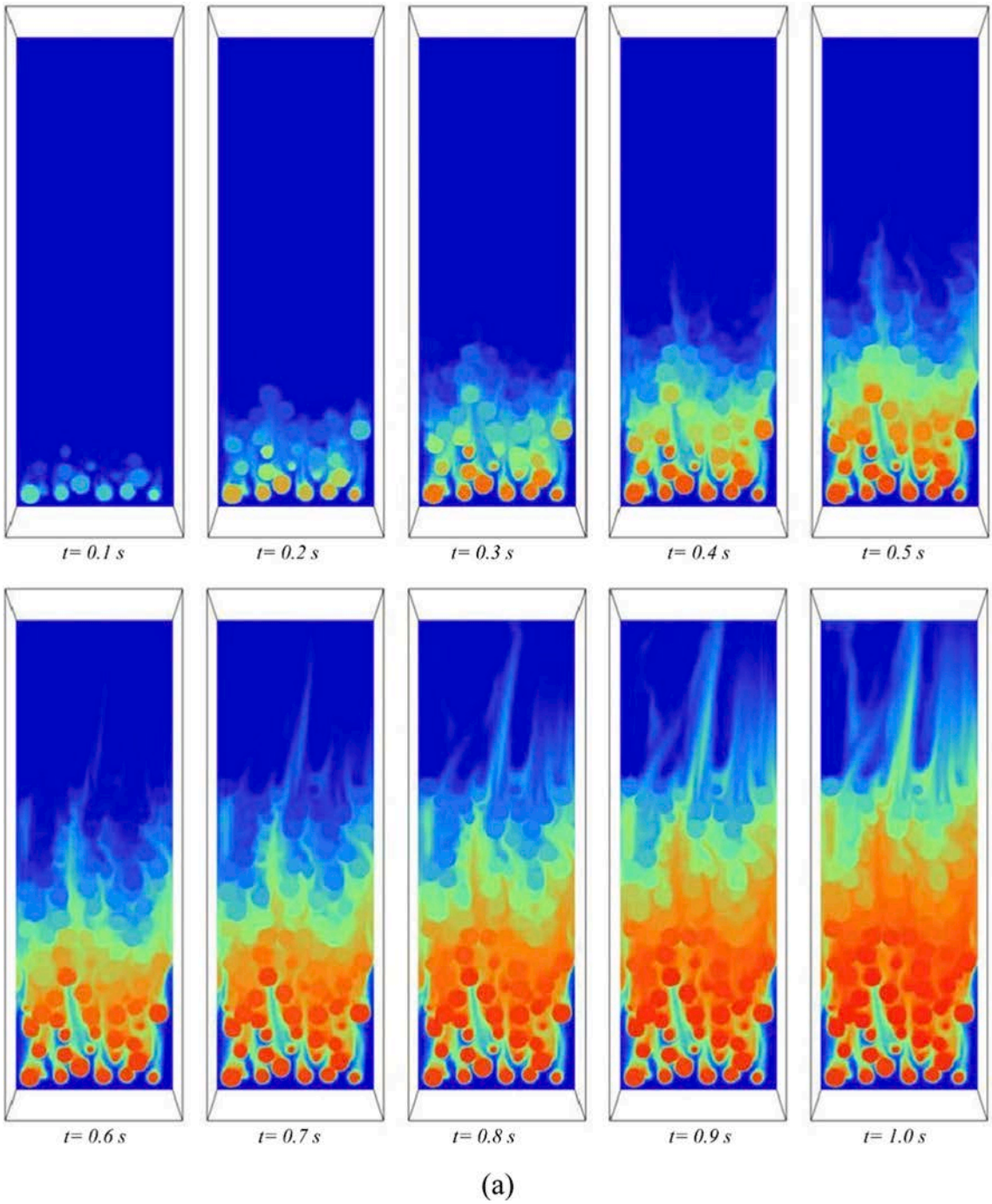

Fig. 57. (a) Temperature evaluation in a 3D GM model [448], (b) Comparison between surface temperature between experimental and computational modeling (CFD-DEM) [494].

$$mc_{p,i}\frac{dT_i}{dt} = \sum_{j=1}^{\xi}\left[H_C^{ij}\Delta T_{ij} + Q_{conv.}^{ij}\right]. \tag{142}$$

The above equation can be eventually incorporated into the mechanical modeling and predict the temperature of particle i after Δt as follow:

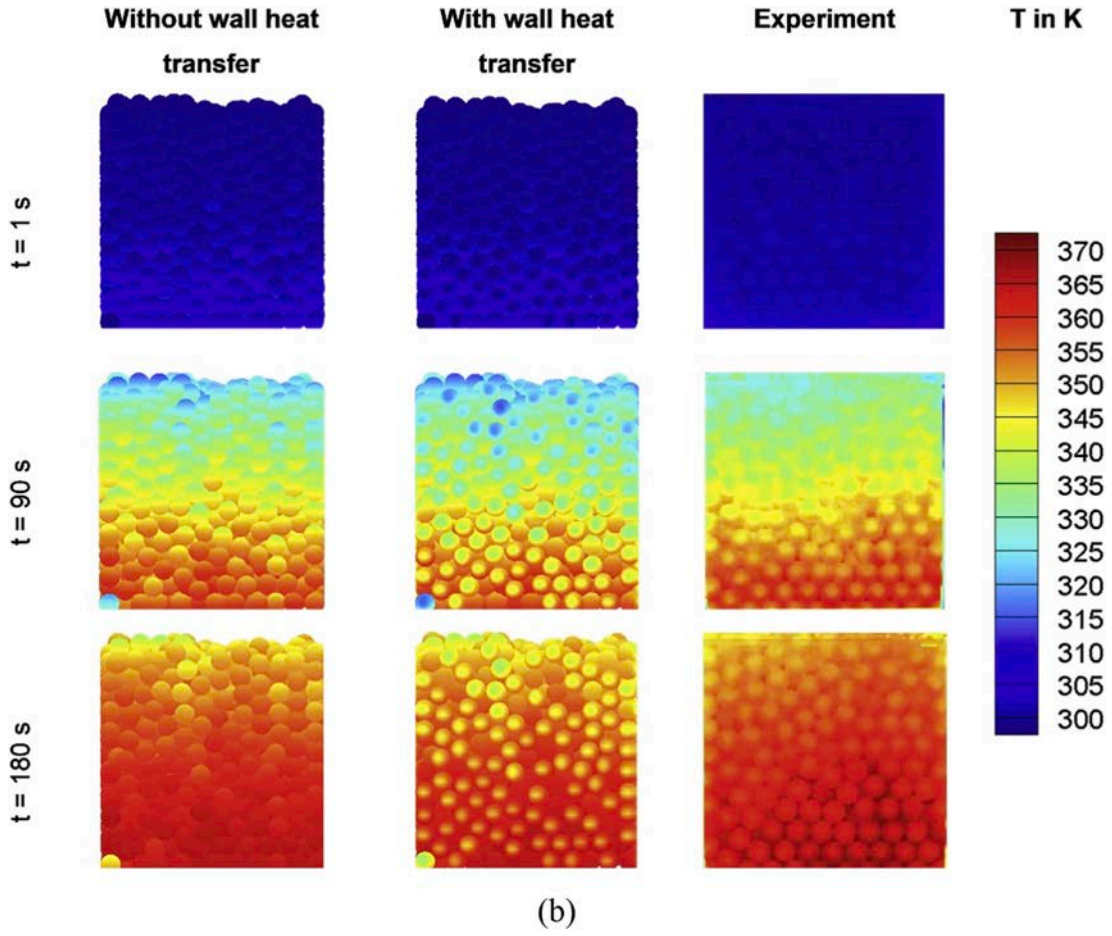

Fig. 57. (*continued*).

$$T_i^{t+\Delta t} = T_i^t + \frac{\Delta t}{mc_{p,i}} \left(\sum_{j=1}^{\xi} \left[H_C^{ij} \Delta T_{ij} + Q_{conv.}^{ij} \right] \right). \tag{143}$$

One of the results produced in the presence of fluid and a granular system is shown in Fig. 57.

Despite all the above-described developments for coupling heat in the modeling of GM, it is still an immature field that requires more research compared to fluid. All such bumpers can be due to the intrinsic complexity of coupling of heat in GM as it depends on both scale and temporal variability. At the moment, the available methods are either developed for a specific scale and GM systems, or they cannot be coupled with other important physics for large and complex models.

2.2.8.3. Chemical coupling. In many of the natural and industrial cases, one can find an active chemical interaction between the particles in GM or with the containing fluid(s). The previously described methods are able to take the momentum and energy equations into account, but they remain limited to considering intra-particle transport phenomena (e.g., reactions and diffusion). In reactive environments, however, such variables are very crucial and control the fate of the modeling [499]. One such example is biomass reactors where various chemical and physical interactions occur [500]; see Fig. 58. In the same figure, another example is provided which shows a combination of heating and chemical reactions in an iron powder as a potential source of sustainable energy resources and climate change. At the particle scale, coupling the transport phenomena with chemical reactions is important since the characteristics of particles, such as morphology, size, void space, thermal properties, chemical properties, and density, can greatly control the temperature and chemical distribution inside the particles as well as their reactivity, and eventually affect the product [501]. Many other parameters, such as the shape of the reactor, pressure, heating, etc. can also affect the performance of such systems [502–505]. It has been shown that when Bi = 0.1–10 (or, particle diameter ~ 100–1000 μm), reaction, conduction, and convection all occur in such systems [506,507]. This multiphysics capability has been implemented in LBM [508–510], but the described complexity and fully multiphysics modeling are not addressed in those studies.

To simulate the above Multiphysics model, one can start with an energy equation, which can be written as:

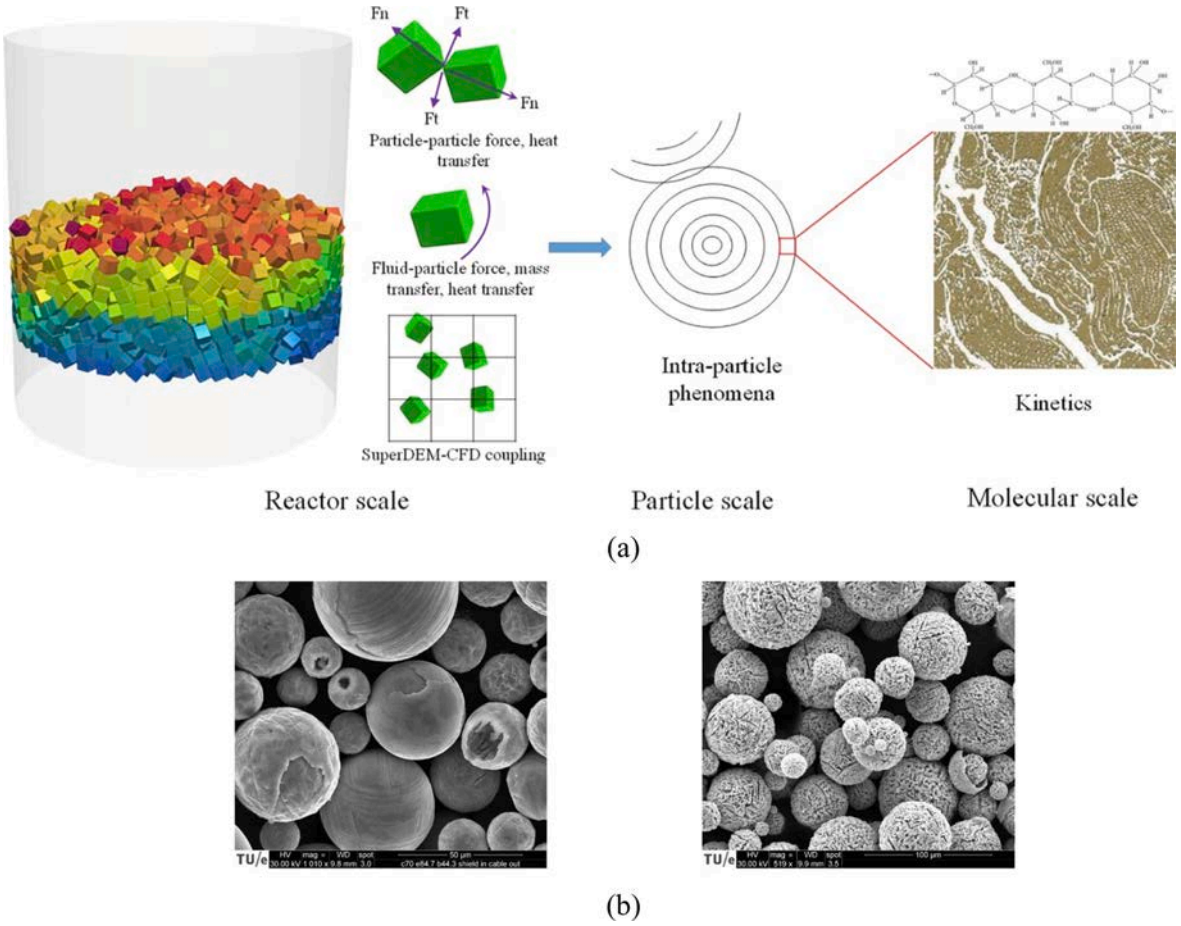

Fig. 58. (a) The multiscale and complex nature of a GM system (here, biomass) [511], (b) iron oxide after combustion (the left image), and Iron after H_2 reduction (the right image) [512].

$$\rho c_p \frac{\partial T}{\partial t} = -\nabla.(-\lambda \nabla T) + \dot{q}, \tag{144}$$

where λ is thermal conductivity and $\dot{q}$ is a volume-specific source term, which can be the reaction energy. This equation can be expanded to represent both the GM and a fluid:

$$\frac{\partial}{\partial t}\left(\sum_{i=1}^{N} \alpha_f C_{f,i} h_{vf,i} MW_i + \rho_s h_{vs}\right) = -\nabla.\left(\sum_{i=1}^{N} \dot{n}_{f,i} h_{vg,i} MW_i - \lambda \frac{\partial T}{\partial r}\right) + \dot{q}, \tag{145}$$

where h_v is the specific enthalpy, MW is the molecular weight, N is the number of fluid species, r is the radius, and $\dot{n}$ is the molar flux.

Since the chemical reactions should be considered, thus, the chemical species should be conserved, which can be described by [492,512]:

$$\frac{\partial}{\partial t} C_{s,i} = s_{s,i} + \dot{p}_{s,i}, \tag{146}$$

where $\dot{p}$ is the phase change rate and s indicates the chemical source term. This equation can be reformed as for the solid whereas a similar one can be written for the fluid phase given $\alpha_s = 1 - \alpha_f$:

$$\frac{\partial}{\partial t}\left(\alpha_s \frac{\overline{\rho}_s}{MW_s}\right) = \sum_{i=1}^{N} s_{s,i} + \sum_{i=1}^{N} \dot{p}_{s,i}. \tag{147}$$

The fluid species can be computed by:

$$\frac{\partial}{\partial t}\left(\alpha_f C_{f,i}\right) = -\nabla.\dot{n}_{f,i} + s_{s,i} + \dot{p}_{s,i}. \tag{148}$$

The fluid flux $\dot{n}_{f,i}$ represents both diffusive and convective flux:

$$\dot{n}_{f,i} = \dot{n}_{f,i}^{\mathrm{DF}} + \dot{n}_{f,i}^{\mathrm{CN}}, \tag{149}$$

where

$$\dot{n}_{f,i}^{\mathrm{DF}} = -\mathscr{D}_e \frac{\partial C_{f,i}}{\partial r}, \tag{150}$$

and,

$$\dot{n}_{f,i}^{\mathrm{CN}} = \frac{C_{f,i}}{C_f}\dot{n}_f \tag{151}$$

such that $\mathscr{D}_e = D\phi/\gamma$ represents the effective diffusion wherein D is the diffusivity of the fluid and γ signifies the tortuosity factor. To achieve the total fluid balance, the sum of the above equations for all fluid species should be computed:

$$\frac{\partial}{\partial t}\left(\alpha_f C_{f,i}\right) = -\nabla.\sum_{i=1}^{N}\dot{n}_{f,i} + \sum_{i=1}^{N} s_{f,i} + \sum_{i=1}^{N}\dot{p}_{f,i}. \tag{152}$$

These equations can be solved numerically and predict the temperature and species concentration along the time and different locations of the GM (i.e., spatial and temporal), which can be achieved by discretizing them first.

The reactivity among particles can be modeled using a mole-based framework with a constant porosity ϕ. The chemical reaction

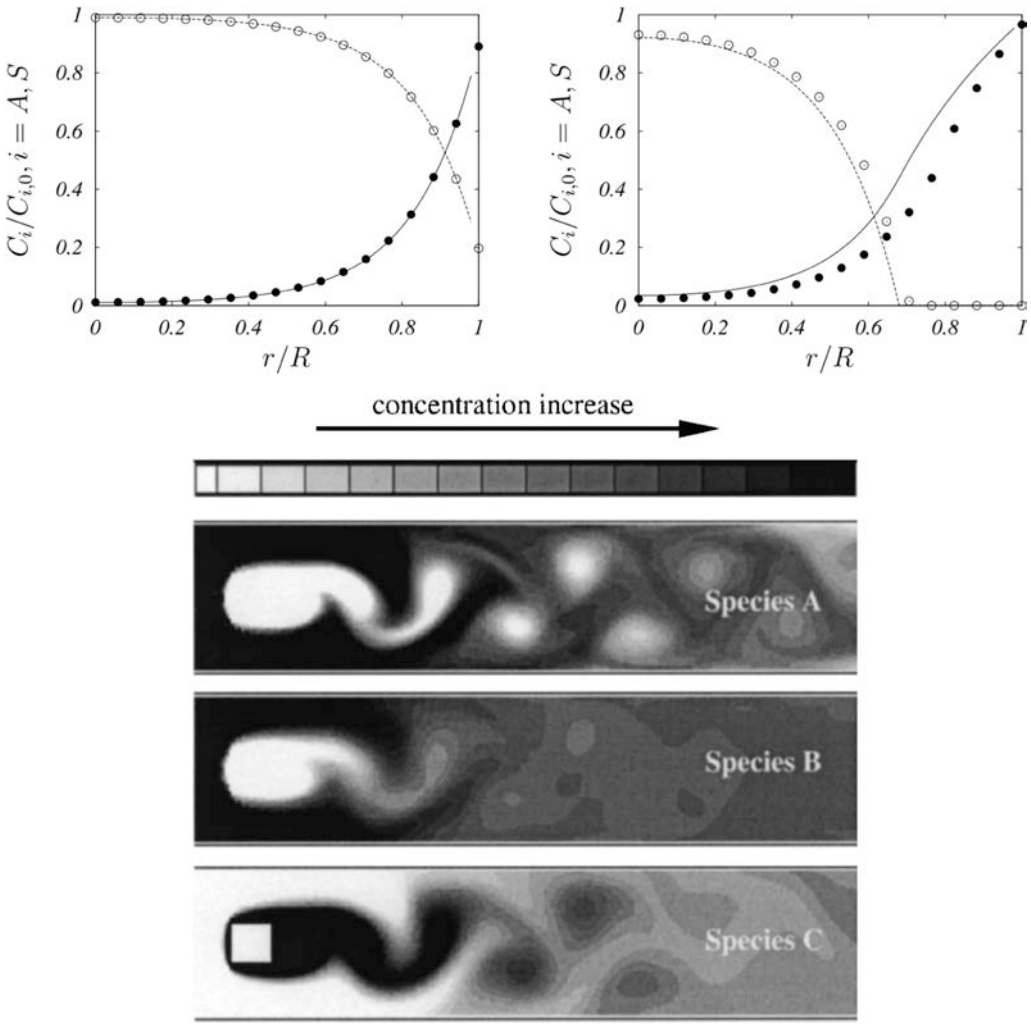

Fig. 59. (Top) Demonstration of solid and fluid concentrations in a Cu particle for (left) early-stage, (right) late-stage in a reactive environment. The curves and dots represent the analytical and numerical results, respectively [515]. (Bottom) The 2D concentration of a reactive fluid was modeled using LBM [508].

here refers to the irreversible reactions in the presence of solid and fluid, which follows the below equation in which solid A interact with fluid B and produce solid C and fluid D:

$$aA(s) + bB(f) \rightarrow cC(s) + dD(f). \tag{153}$$

The mole balance of each species in the porous solid can be described by:

$$\frac{\partial \alpha_s c_i}{\partial t} = -\frac{1}{r^2}\frac{\partial}{\partial r}\left(r^2 \dot{n}_{f,i}\right) + s_i, i = B, D. \tag{154}$$

The mole balance for the solid can be developed similarly, but without considering the flux and just using mola concentration:

$$\frac{\partial c_i}{\partial t} = s_i, i = A, C. \tag{155}$$

The described method and the above equations are applied to a single reaction of Cu oxidation where it is assumed to have an isothermal particle and a first-rate reaction given the fluid species for $2CO + O_2 \rightarrow 2CuO$. [513–515]. These results for both the concentration of solid and fluid inside the particle are shown in Fig. 59 for two different times. Similar results for LBM are also presented in the same figure. It should be noted that this formulation allows one to simulate other important phenomena such as erosion and also swelling. For instance, the swelling can be modeled by gradually changing the radius and making the particles thicker.

3. Other features and topics

There are some applications and specific topics in GM that are not individually and necessarily new concepts, but are interesting subjects that are studied extensively and researchers across different fields are interested in. In most such cases, the previous concepts are still used but more progress is achieved to solve a particular problem. In this section, thus, some of the important topics and applications related to GM are reviewed.

3.1. Micro-Macro bridging

The ways to evaluate the micro and macro deformations of GM are distinguished by considering granular systems as an assembly of individual particles at micro-scale (i.e., particle-scale) or treating them as an equivalent continuum at macro-scale. The macro properties are about porosity, permeability, and the constitutive relationship between stresses and strains. The mechanical characteristics of GM at the macroscale are studied using balance equations aided by the constitutive relations and the imposed boundary conditions. Identifying reliable constitutive equations is probably the most challenging part of these methods. As such, various materials based on the type of the materials, flow regions, and also other conditions are defined. For instance, among many studies, the plasticity and double shearing theories are used for rate-independent deformations of GM [516–518], kinetic theory is used for rapid flow of GM [519,520], and Mohr-Coulomb along with the kinetic theory is used for GM involved with collision and friction [521]. An acceptable and universal continuum theory, which can be applied to different flow conditions, has not yet been derived. On the other hand, at the micro-scale, the physical properties like displacement of individual particles, and force chains generated by contacted particles are investigated, and there is no need of making global assumptions (e.g., constitutive relations, steady-state, uniform constituency) as one should do for continuum methods. These methods, such as DEM, however, are limited to systems with a small number of particles. Thus, several studies have focused on establishing the macro–micro relationships of granular systems based on the characteristics of micro and macro deformations [522–535]. Such studies have investigated three macro–micro relations of granular systems from different angles, that is, micro and macro characterization of internal structure, micro-structural expression of the macro stress tensor in terms of contact forces, and micro-structural expression of the macro strain tensor in terms of relative displacements [536–538]. All such attempts are in the direction of understanding the mechanics of GM, which is providing a relationship between the exerted force on the domain and the resulting deformations. The effect of an external force on GM is expressed by stress, which is a continuum property and can be defined by the Cauchy equations. On the other hand, the deformation of GM can be expressed by strain, as another continuum variable.

One of the classical discussions in micro–macro bridging, which connects the above-mentioned variables (stress and strain), is probably about stress tensor in terms of constitutive relations. This relationship can be written in different forms [539,540]. The idea of the continuum approaches at the macroscale is to consider the domain as a continuous property where the stress and strain can identify the state of the system at any point. Then, the empirical relation between the stress and strain derived from experimental tests is used for large-scale problems. In reality, using such results can be risky as the results might change if the new boundary conditions are just slightly different from the experimental tests. Thus, either more complex constitutive models should be proposed by introducing more parameters, or additional variables, other than the stress and strain. Micromodels of GM, on the other side, aim to help to better find the macroscale properties based on the observations at its scale (e.g., displacements, contact forces, and geometrical characteristics). Thus, the macroscale observations can be made more accurately if such information is used. Eventually, the goal is to establish this relationship between these two distinct scales which is achieved by reproducing the continuum properties using the information generated at the microscale. Such behaviors depend on the fabric/structure (tensor) of the GM as well [541]; see the discussion in the next section.

Constitutive laws make it possible to establish the above-mentioned relationship between stress and strain tensors. As such, the contact forces, displacements, and grain-scale geometry at the microscale can be connected to the stress tensor, strain tensor, and fabric

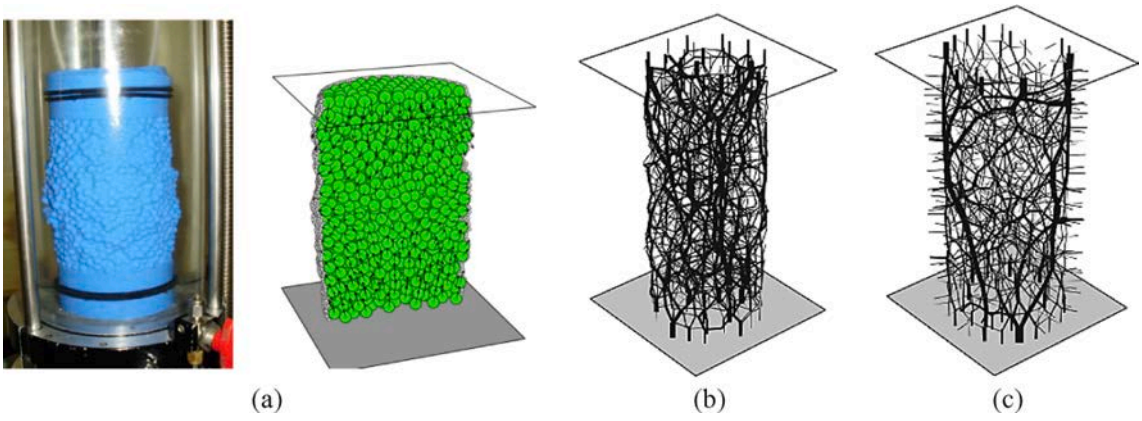

Fig. 60. (a) Demonstration of the experimental and computational triaxial test. As can be seen, the macro-scale behaviors are visible in the experiment while the microscale characteristics can all be observed in the computations. Contact force distributions for (b) flexible and (c) rigid membranes [303].

tensors, respectively. In other words, the mechanical state of GM can be fully and precisely characterized if one has access to the location and geometry of each particle, displacements of each particle (translational and rotational), contact forces, and GM properties. Including such a large number of details may not be necessary and one can identify macroscale state variables through suitable averaging. This micro–macro mapping, while it is known to be controversial due to averaging over scalar/vectorial quantities (e.g., ρ,$\mathbf{u}$, $\boldsymbol{\omega}$), has attracted much attention [522,542–545]. At the same time, considering the aforementioned variables (stress, strain, and fabric tensors) are recognized to be adequate for such a mapping.

In an arbitrary pack of GM of volume V and forces $T_i^1, T_i^2, \cdots, T_i^n$ on each particle at the boundary points $x_i^1, x_i^2, \cdots, x_i^n$, the average stress can be defined by:

$$\sigma_{ij} = \frac{1}{V}\sum_{k=1}^{n} x_i^n T_i^n, \tag{156}$$

which is equivalent to the stress under the same loads and volume in a continuum domain. The above equation also indicates that one can homogenize the microscale responses and, for example, relate particle contact forces to macroscopic stresses. Thus, as noticed, this process filters out the fine-scale information and it necessities that one should pay special attention and caution to the REV selection to avoid any possible under/overestimations [533,535].

Generally, particle-scale simulations are often conducted on a REV (representative elementary volume) and apply different boundary conditions, such as stress–strain, and measure the stress responses through which the stress–strain relationship can be established. At the macro scale, however, such properties are averaged to get the macro-constitutive relations. To shed light on the above complex relations and also provide a detailed insight into such problems, experimental tests have been used. Despite their valuable outcomes, interpreting such results is very difficult at the moment. In fact, the stress–strain responses produced from experimental tests are hardly based on a clear geometry, input, or even a known situation inside the setup. Thus, it is hard to count such tests as REV. Besides, experimental tests regularly provide incomplete information regarding the situation inside the GM and also inter-particle forces. Therefore, one must conduct a very simple experiment or a very sophisticated one to be able to interpret the results and answer some questions on the nature of the observations and where they come from. All such reasons can justify developing more complex and advanced computational modeling that can bridge the scales and also provide more precise information on a small scale.

Ng investigated the micro-macroscopic behaviors of granular systems of bi-disperse ellipsoids, which consisted of larger ellipsoids with an axial length ratio being 1.5 (major axial length to minor axial length) and shorter ellipsoids with an axial length ratio being 1.2 [546]. The granular samples were loaded with three paths of axial extension, triaxial extension, and axial compression condition under various confining pressures. The experimental results showed that critical state lines in the void ratio and mean stress space for the axial and triaxial extension tests are above that of the axial compression tests. It was also found that in the compression tests, there is an excellent relationship between peak shear strength and microscopic descriptors based on the micro-structural tensor of normal contact forces.

Kumar et al. used the discrete element method (DEM) to investigate the micro–macro behavior of granular assemblies characterized by different polydispersities [547]. They focused on the effect of polydispersity on the micro–macro behavior of granular assemblies, which consisted of linearly elastic, frictionless, polydisperse spheres, under purely isotropic loading and unloading, deviatoric (volume conserving), and uniaxial compression paths. Their results showed that scaled pressure, coordination number, and the fraction of rattlers of granular assemblies are systematically dependent on the deformation paths and polydispersity by jamming volume fraction. In a separate study, the authors found that there is a significant effect of boundary conditions on the constitutive behaviors for triaxial tests conducted in a rigid and flexible membrane around the sample when the macroscopic and particle-scale simulations are compared. These results are shown in Fig. 60.

3.2. Critical state

As mentioned frequently in this review paper, the behavior of GM when considered at macroscale can be very different when the behavior of each particle is observed individually. This sharp difference is due to the collective rearrangement characteristics of GM. Based on the contacts between the particles and the boundary conditions, they can adjust to new conditions. There is, however, a situation where the GM does not show any macroscopic/visible change of volume even if it goes under constant shearing. This state is very important and contributes to many constitutive equations for GM [548–553], and was earlier defined as a situation under which the stress and volume tend to be unchanged under an uninterrupted shear strain [554]. As such, extensive research has been conducted to model the critical state and develop a robust mathematical equation to describe this important phenomenon using which the constitutive models can be improved [94,536,555–558].

Aside from the above particular characteristic, the anisotropy of GM is recognized to be an important aspect affecting the behavior of such systems, which can be controlled by the microstructure fabric of GM [559–561]. Two approaches are adopted in GM to include such important information from the anisotropic fabric and microstructure in the constitutive models. One approach is to use the kinematic and mechanical properties of GM at the microscale [524,537,562], which are integrated to find the macroscale stress–strain relation [530,543,563]. Another alternative is to statistically convey the microscale information to the coarser level, namely the macroscale, in which some assumptions on the dependency of stress and strain on the fabric tensor are made [564–570]. These methods, however, require a deep understanding of fabric tensor, its quantification, its development, and its effect on the continuum elements [571].

Before describing the current studies on the critical state, the fabric tensor is defined briefly. Fabric refers to the arrangement of particles under shear stress, gravitational force, or both. The structure of GM, in general, can be divided into solid and void spaces, and the latter group itself can be described by the geometry of the GM and their spatial connections. The topology of GM solid structure, referred to as fabric, was initially characterized using a graph representation [572,573] where two graphs each representing the solid and void spaces were used in 2D. Then, the topology of GM was described using Voronoi-Delaunay tessellation but this method cannot represent the contacts between neighboring particles [528]. These representations can be used to connect the internal solid structure to the stress–strain behaviors and study how changing the structure can affect the final outcomes. In general, contact normal distributions in GM is an internal property that is defined based on how GM is deformed. This parameter can be described based on the contact normal vector **n** using:

$$F_{ij} = \frac{1}{N_c}\sum_{c=1}^{N_c} n_i^c n_j^c, \mathrm{tr}\mathbf{F} = 1, \tag{157}$$

$$G_{ij} = \frac{2}{N_p}\sum_{c=1}^{N_p} n_i^c n_j^c, \mathrm{tr}\mathbf{G} = \frac{2N_c}{N_p}, \tag{158}$$

where N is the total number of contacts, and n_i^c and n_j^c are the contact normal vector components. Here, **F** describes the statistics of the contact directions while G presents extra information regarding the density of contacts. Generally, contact tensor processes involve describing three cases: new contacts (gain), dropped contacts (loss), and those in which the direction of the existing contacts changes (rotation). The second-order F can be expressed using the probability density $E(n)$ of contact distribution:

$$F_{ij} = \iint_{\Omega} E(\mathbf{n}) n_i^c n_j^c d\Omega_s, \tag{159}$$

where $E(n)$ can be defined using the Fourier series [574]:

$$E(\mathbf{n}) = E([03B8], \gamma) = \frac{1}{4\pi}\left[1 + \frac{\alpha}{4}(3\cos 2[03B8] + 1) + 3\beta \sin^2\theta \cos\gamma\right], \tag{160}$$

where the degree of anisotropy is described using α and β (e.g., $\alpha = \beta = 0$ for isotropic GM). Consequently, the fabric tensor can be calculated using:

$$F = \begin{bmatrix} \frac{1}{3} + \frac{2\alpha}{15} & 0 & 0 \\ 0 & \frac{1}{3} - \frac{\alpha}{15} + \frac{2\beta}{5} & 0 \\ 0 & 0 & \frac{1}{3} - \frac{\alpha}{15} - \frac{2\beta}{5} \end{bmatrix}. \tag{161}$$

Additionally, the deviator F_q of F_{ij} can be computed using its principal values:

$$F_q = \frac{1}{\sqrt{2}}\sqrt{(F_1 - F_2)^2 + (F_1 - F_3)^2 + (F_2 - F_3)^2}. \tag{162}$$

As mentioned earlier, the stress tensor can be represented by the contact force and branch vector as follow:

$$\sigma_{ij} = \frac{1}{V}\sum_{c=1}^{N_c} f_i^c l_j^c, \tag{163}$$

where the components of the branch vector and contact force are presented by l_j^c and f_i^c, respectively. Therefore, the mean effective and deviatoric stresses are calculated using:

$$p' = \frac{1}{3}\sigma_{ij} \tag{164}$$

$$q = \sqrt{(2/3)s'_{ij}s'_{ij}}, \tag{165}$$

$$s'_{ij} = \sigma_{ij} - p'\delta_{ij}$$

With the development of accurate computational modeling, such as DEM, this process has accelerated and new insights are provided showing that some other properties, other than volume, can remain unchanged [575]. Most such tests are often conducted on GM samples by applying a constant strain rate in one direction under constant lateral stress where the volumetric strain along with the deviatoric stress is observed. This procedure allows one to examine whether there is a stationary relationship between stress and volume, which is what the critical state is about.

Aside from considering the constant strength and volume, other researchers have also taken into account the effect of fabric anisotropy [576] where the stress and void ratios are provided and it is known as anisotropic critical state theory (ACST) [554,577]. Regardless of the initial anisotropy of the GM and under fixed principal stress, the fabric tensor at the critical state is unique [219]. This general definition leads to the development of further models such that the fabric tensor can be defined differently. For example, it can be based on the void space [577], contact normal [94,555,578], and orientation of particles [94]. In another study, the question of whether all the fabric measurements reach the critical values at the same pace or not was studied [219]. To answer this question, the researchers considered several 2D cases and simulated them using DEM under biaxial stress with different initial void spaces and very distinct fabric anisotropies. Then, the development of the above-mentioned fabric tensors (i.e., particle orientation, contact normal, and void space) was monitored. Their results showed that a unique critical fabric tensor is obtained irrespective of the initial void space and orientation.

3.3. Breakage

Fracturing or breakage in GM is one of the important topics which can control many characteristics in such materials, including flow responses and mechanical properties [579–583]. For example, the strength, dilatancy, porosity, and angularity of GM can be changed sharply when the particle size distribution varies, which is a direct result of producing smaller particles due to breakage [584–587]. Several studies have found that there is a connection between the inception of particle breakage and macroscopic yielding. Therefore, it is essential to improve our understanding of this intricate phenomenon and build more precise plasticity equations for the post-yield step, the stress history of GM, as well as advance more comprehensive constitutive laws. For instance, most, if not all, of the existing constitutive models in GM do not take the effect of particle size distribution into account whereas this distribution constantly changes in mechanically and chemically active environments.

Particle breakage has been studied by considering the effect of various factors, such as composition, morphology, internal stresses, internal forces, crystallography, orientation, and coordinate number. One such study established a link between GM composition and breakage using a survival probability as a function of local tensile strength [588]. The Weibull model has been used extensively in the breakage of GM [586,589–592]. Later, the simultaneous effect of internal stress and coordinate number on fracturing in GM was studied wherein it was shown that the peak tensile stress declines as the coordinate number rises [589,593]. It was found that the probability of fracturing reduces when the coordinate number increases [594]. This finding was later approved using FEM where maximum tensile stress reduces by increasing the coordinate number [595].

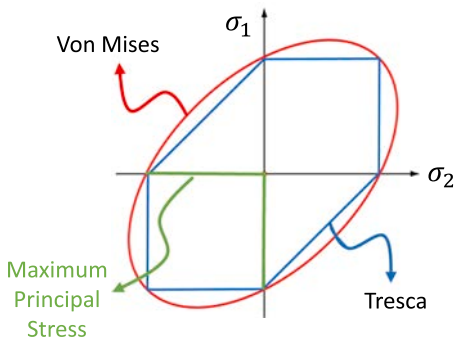

Fig. 61. Demonstration of three yield surfaces reviewed in this paper.

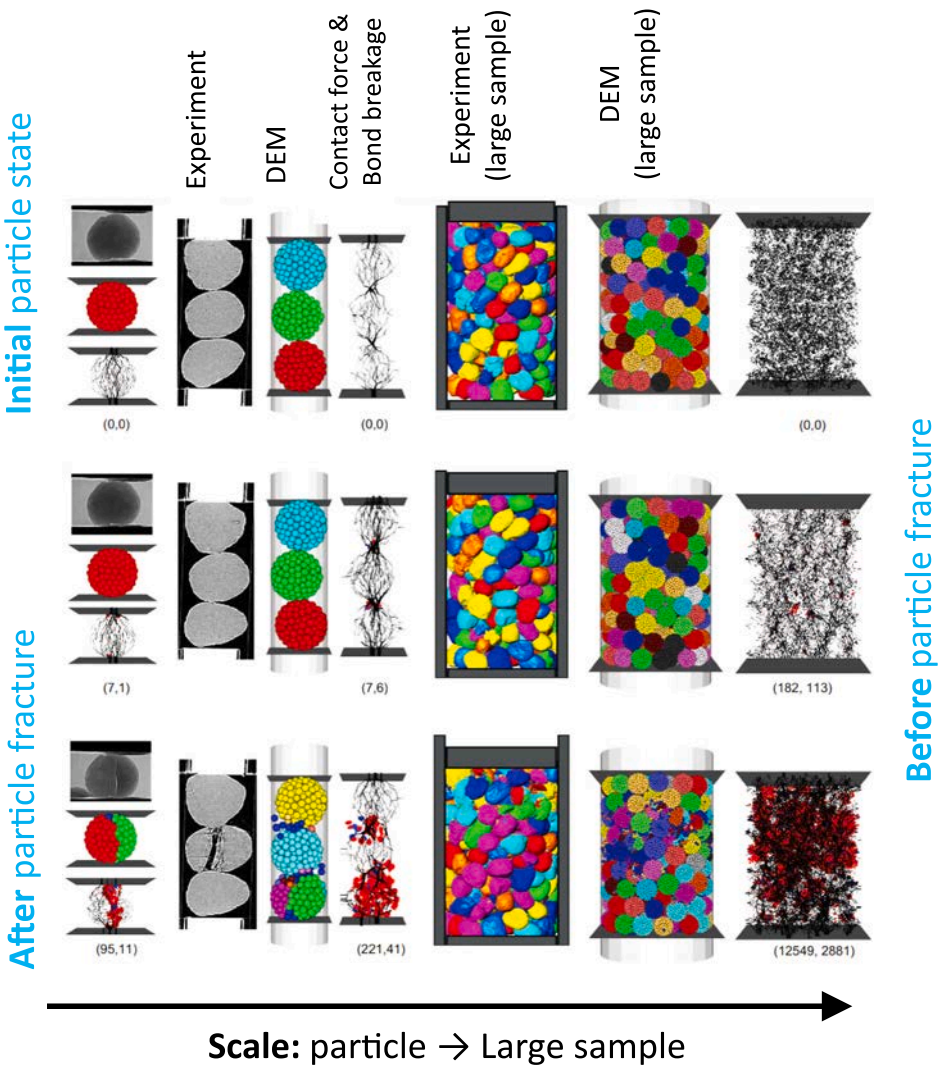

(a)

Fig. 62. (a) Comparison between the experimental data and DEM modeling for fracturing at the scale of single-particle and large samples under different load levels [609]. Note that numbers in parentheses show tensile and shear. (b) the evolution of fracturing a sand GM pack from no loading to maximum loading. The displacements of particles, their rotations, and also small fragments after fracturing are shown [143]. (c) evolution of force chains and fracturing for two force chains using 3D FEM [164]. Here, ε_1 represents the global axial strain.

In a separate study, it was shown that breakage occurs when the maximum contact force meets the threshold strength of particles, which is independent of other contact forces [596]. In a similar fashion, it was observed that a criterion representing the maximum inter-particle force, among major principal stress, maximum force, and mean stress, can reproduce the experimental results [597]. By combining the experimental and computational modeling it was noted that breakage in the particle is correlated with the concentration of the largest internal normal forces [598]. Aside from these studies, various other works have also been done using in-situ experimental modeling (e.g., X-ray) [160,598,599] and FEM [143,164,582,592,595,600,601]. Using FEM is practical when the granular system contains a small number of particles [602]. The FEM-based methods were later enhanced to deal with larger granular systems, but dealing with single particle breakage and the size distribution of particles still remained an issue [603]. Another development was achieved using a hybrid peridynamcis and physics engine, but they still cannot produce complex fracture surfaces [604]. Similarly, DEM has also been used widely through which large particles are broken into smaller fragments [288,599,605,606]. Breakage in DEM is simulated by considering a bond where a particle is fractured as soon as the acting force exceeds the strength of the bond. Furthermore, clumped particles can be used to deal with irregular GM whereas the mass can also be preserved. To accelerate the previously mentioned method, one can replace the target particle with several smaller particles when a certain stress level is met

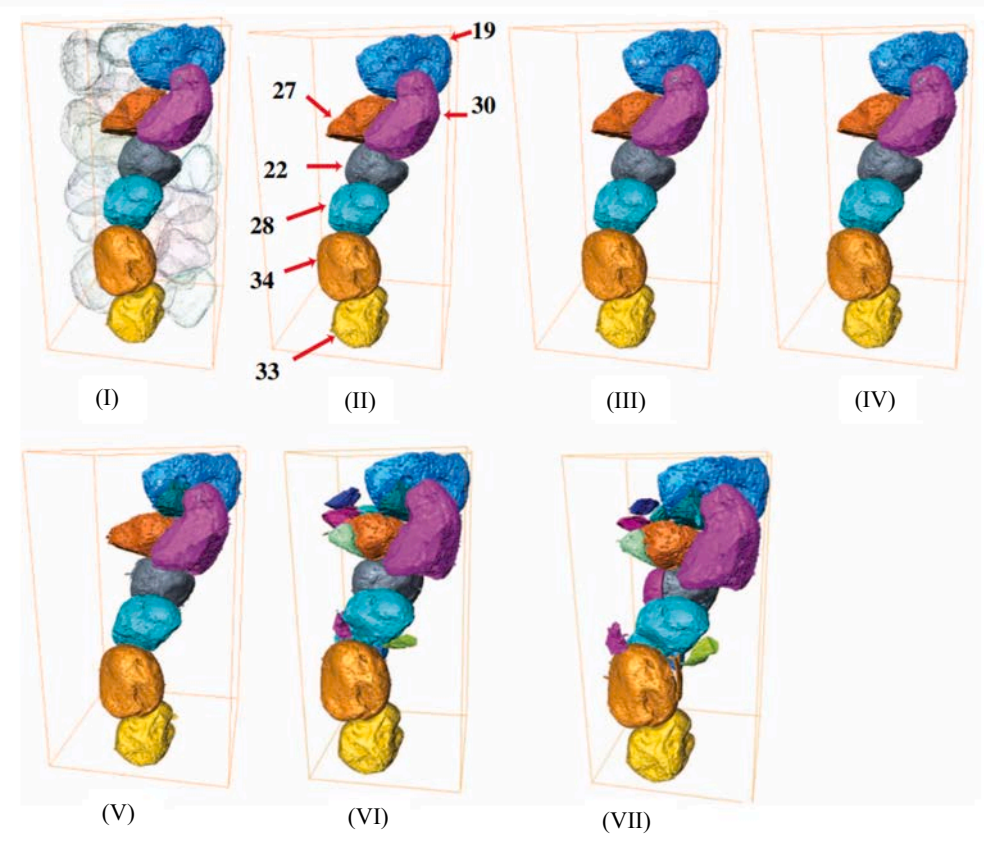

(b)

Fig. 62. (*continued*).

[594,607], but mass conservation becomes challenging here. In the same group of methods, the principal stresses calculated from the average stress inside the particle are calculated based on which a stress-based yield criterion (e.g., the maximum principal stress, von Mises criterion, or the Tresca criterion) is selected [608]. This method has been applied on particles with angular shapes. It should be noted that yield criterion refers to the limit of elasticity in the target GM and is the onset of plastic deformation under any mixture of stresses.

Here, three of the simple and widely used breakage criteria are briefly reviewed. The maximum principal stress standard considers the breakage of a particle with the principal stresses that meets a certain value. Mathematically speaking,

$$\sigma_C^{\max} > \sigma_C = \min\left(\sigma_{p1}, \sigma_{p2}, \sigma_{p3}\right), \tag{166}$$

$$\sigma_T^{\max} > \sigma_T = \max\left(\sigma_{p1}, \sigma_{p2}, \sigma_{p3}\right), \tag{167}$$

where the maximum compressive and tensile stresses are shown by σ_C and σ_T, respectively.

The second criterion, namely the von Mises yield, is defined based on the maximum stress defined using:

$$\sigma_{V\max} > \sigma_V = \sqrt{\frac{1}{2}\left[\left(\sigma_1 - \sigma_2\right)^2 + \left(\sigma_2 - \sigma_3\right)^2 + \left(\sigma_3 - \sigma_1\right)^2\right]}. \tag{168}$$

The Tresca model is specified based on shear stress as follows:

$$\frac{1}{2}\sigma_C^{\max} > \tau = \frac{1}{2}\max(|\sigma_1 - \sigma_2|, |\sigma_2 - \sigma_3|, |\sigma_3 - \sigma_1|), \tag{169}$$

where τ is the maximum shear stress. These criteria are shown graphically in Fig. 61. To illustrate the performances of the discussed methods, some of the results are shown in Fig. 62.

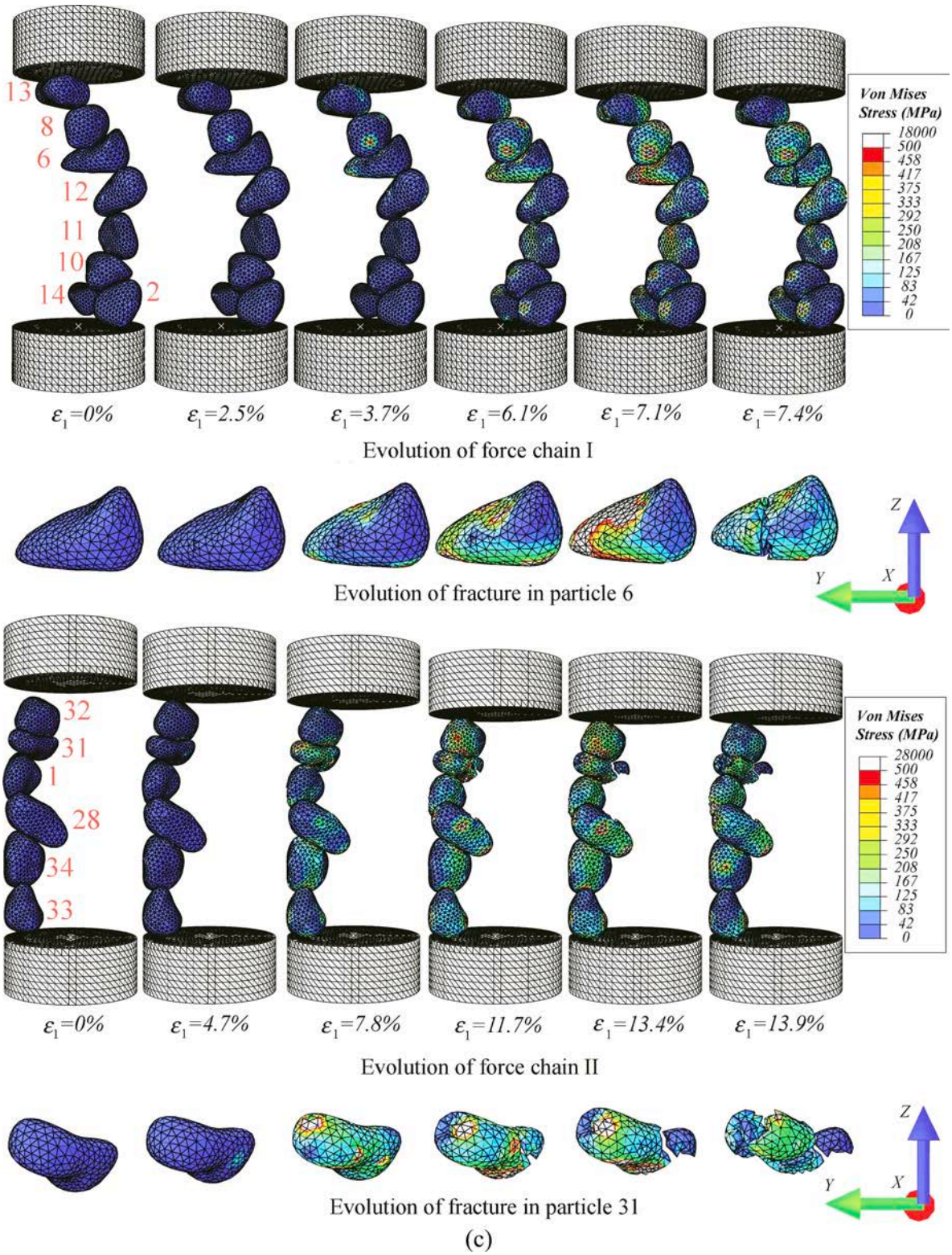

Fig. 62. (*continued*).

3.4. Jamming

Jamming is a very broad mesoscopic physical process that can be found in a variety of materials where the viscosity increases when particle density increases as they flow. Flow and rheology of GM are influenced by the morphology of particles, size distribution, and friction coefficient such that the constitutive relations, packing density, and jamming transition are all affected during this phenomenon. As mentioned earlier, GM can appear as solid, liquid, gas, or all such phases depending on the conditions. Given this complex behavior, three regimes are defined for GM which include inertial (liquid-like), elastic-inertial, and elastic-quasi-static (solid-like) [610–612]. Jamming occurs when GM flow's type goes from a liquid-like to a solid-like behavior [186]. The granular system may unjam if the volume fraction decreases, or an external force can break the yield stress. In a broader sense, jamming is a state where a particular system can support external forces without distorting irreversibly [22]. It is also very difficult to assess if a system of GM is really jammed. Mathematically speaking, the system is called jammed when the system becomes isotopic. To keep this state, there should be non-zero stress, uphold small stress, and shear stress. This is a challenging and interesting problem since the transition is recognized to be nonlinear regarding volume fraction.

GM are always out of the equilibrium conditions in terms of thermodynamics and are only considered to be trapped in a *local* minimum when they appear in the jamming state. As such, they manifest a metastability condition where it can help the characterization of the system using its positional correlations and subsequently the existing forces and contacts among the particle such that the jamming can be varied if a small displacement occurs [613]. Thus, characterizing the particles in terms of stress tensor can provide valuable information at the jamming state [534,614], which can be expressed by:

$$\sigma_{\alpha\beta} = \left(-\frac{1}{2}\right)\sum_{i,j} f_{ij\alpha}(t) r_{ij\beta}(t) \int_0^1 \mathrm{d}s\phi\left(\mathbf{r} - \mathbf{r_i} + s\mathbf{r_{ij}}\right) - \sum_i m_i v'_{i\alpha}(\mathbf{r},t) v'_{i\beta}(\mathbf{r},t)\phi(\mathbf{r} - \mathbf{r}_i), \tag{170}$$

where $V_\alpha(\mathbf{r},t) = v_\alpha(t) - v'_\alpha(t)$ is the local coarse-grained velocity. The collisional/contact stress is shown by the first term on the right side of the equations, which is important for static/slowly growing systems. The second part represents the kinetic/streaming stress which is defined for stiff particles or systems with rapid fluctuations. The density of jammed GM depends on several factors, such as the morphology of particles, friction, deformability, and the dispersity of the system. The above decomposition of stress into contact and kinetic terms highlights the effect of friction and rapid versus slow contacts and also the importance of deformability in jamming. For instance, force chains can be longer in deformable particles with friction [182,615,616], while they can be quite unstable for frictionless GM. The existing fluctuations, thus, requires considering the jamming phenomenon as a collective system, which can be characterized statistically and it itself entails considering a statistically representative volume, the history of the force, and also the heterogeneity of the systems. One of the rationales behind taking into account all the aforementioned factors is the presence of friction, which renders it impossible to characterize GM using coordinates alone, especially when energy dissipation occurs. Hence, incorporating the material's history becomes crucial. Otherwise, one might consider building a statistical model by including the effect of forces to remove the history dependence [614,617–619].

Since the particles in dry GM are all based on repulsive contact forces, thus, the contact network is one of the efficient ways of identifying jamming [620–622]. Similarly, fluid-like behavior starts when the force and torque balance is not satisfied. Therefore, it is very important to consider this phenomenon as a collective system wherein the force chains are considered carefully without which jamming is not constructed. It should be noted that there are some particles in the jamming system, called rattlers, which are in

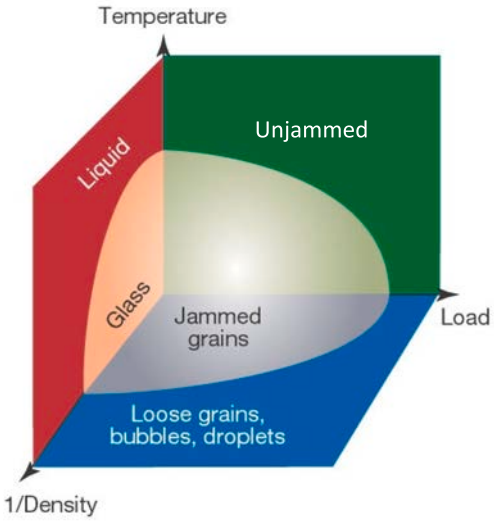

Fig. 63. Liu-Nagel jamming phase diagram (originally from [649] and modified by [650]). As can be seen, jamming exists near the origin. This diagram is developed for glassy systems in which temperature is important while it is not relevant to GM.

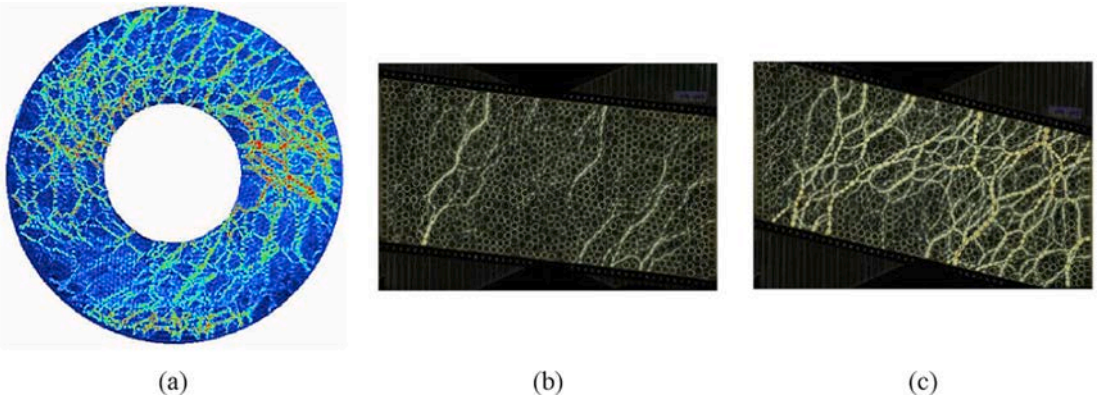

Fig. 64. (a) Force chains demonstration due to shear stress produced by a clockwise rotation which has resulted in force chains along with the rotation [22,651 651]. (b) demonstration of fragile and shear jammed states where the domain is sheared, and it is shown by a different domain's shape. This image shows a fragile state only the strong force chains are constructed in the compression direction, but the image shown in (c), which is for a jammed state, represents a wider distribution of the force chains covering most of the domain [187].

mechanical equilibrium. It also has been shown that increasing the sphericity reduces the average contact between the particles at the jammed state [623]. Thus, one can expect to have a denser packing of particles when a wider size distribution since the void space reduces. Furthermore, a universal theory has also been presented to describe the stress in the jamming state [624,625]. Aside from the shape of particles, friction is also another important parameter that can control jamming [626]. It is reported that jamming volume fraction reduces by increasing the friction coefficient in 2D and 3D spherical shear flows [627,628]. Due to the presence of friction, stress fluctuations become more pronounced as the force chains are produced and eliminated repeatedly. A joint presence of friction and disperse morphology is also investigated in shear flows to evaluate the jamming volume of frictional models using which the stress is linked to morphology [629,630]. A few other methods for identifying the onset of jamming can be found elsewhere [631].

There are two ways of quantifying the heterogeneity: *i*) the distribution of contact forces [182,632–636], and *ii*) spatial characterization of stresses on an ensemble of particles [180,182,185,636,637]. The latter measures can be observed as shear-jammed-frictional GM and characterized partially using two-point correlations and other topology measures to link such observations to macroscopic characteristics [218,638–647]. If the condition of rigidity is considered further, then, aside from the force and torque balance, one must add the Coulomb condition $f_t \leq \mu f_N$ for tangential forces [639,648]. The Liu-Nagel diagram, shown in Fig. 63, illustrates the evolution of jamming in GM.

As can be seen from the diagram shown in Fig. 63, load/shear is an important factor that can be studied more closely. Similar experimental results based on photoelastic discs also demonstrated the jamming, shearing response, and also density dependence which all affect this state [22,651]; see Fig. 64. As can be seen, the direction of the force chains is aligned with the shear stress. The fragile and shear jammed are also demonstrated in the same figure.

Jammed GM systems are usually studied in two states: static (density-driven) and systems under shear stress. The former static state can be thought of as random close packing in physics and materials science when there is no friction between the particles [652–656]. When the temperature is zero, hard spheres only can be found at the jamming point whereas soft spheres can be discovered over a wider range of packing fractions [657,658]. Thus, hard spheres cannot be compressed when they exceed the jamming transition. At the same time, it can be transferred to unjamming phase if the components of the stress tensor are removed, for example, due to the temperature. The problem of jamming transition and separating it from the glass transition for spheres has been studied broadly using

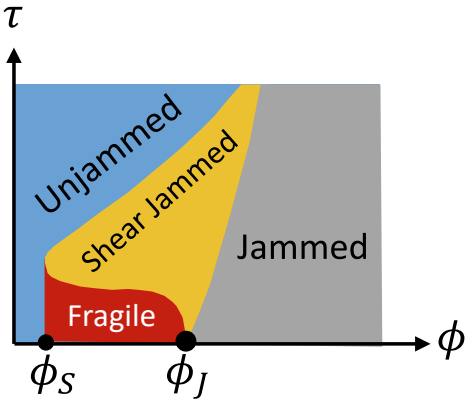

Fig. 65. Demonstration of the shear jamming phase diagram for GM with friction (after [187]).

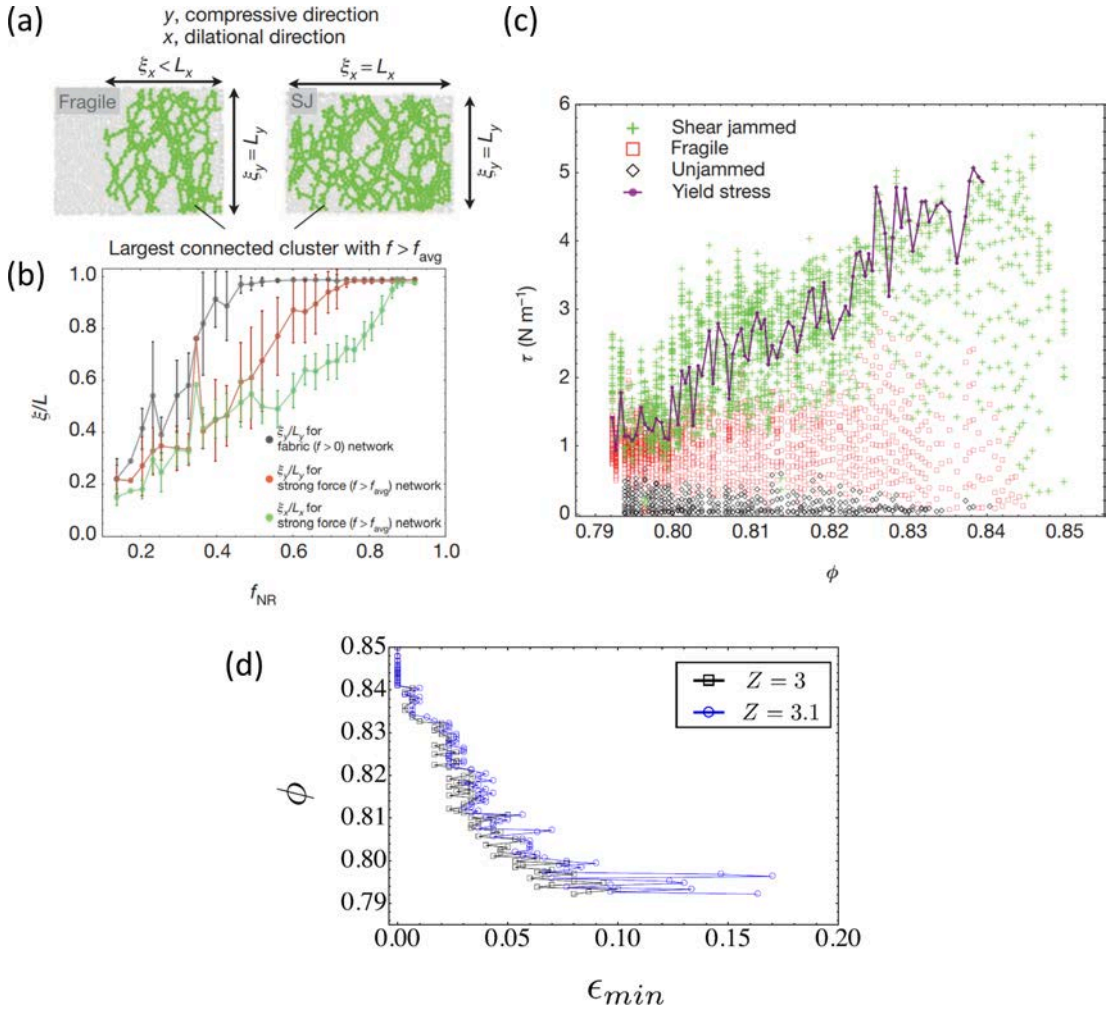

Fig. 66. Experimental results on fragile and jamming in GM. (a) Here, the compressive and dilation occur in Y and X directions, respectively. As can be seen, the force network is distributed in Y direction for the fragile state, but the jammed system shows a distribution in both directions. (b) the ratio of the largest cluster based on the non-rattler fraction function f_{NR}. (c) demonstration of various experiments for different values of ϕ representing distinct states. (d) the minimum amount of required shear strain to produce a shear jammed system for different values of ϕ [22,187].

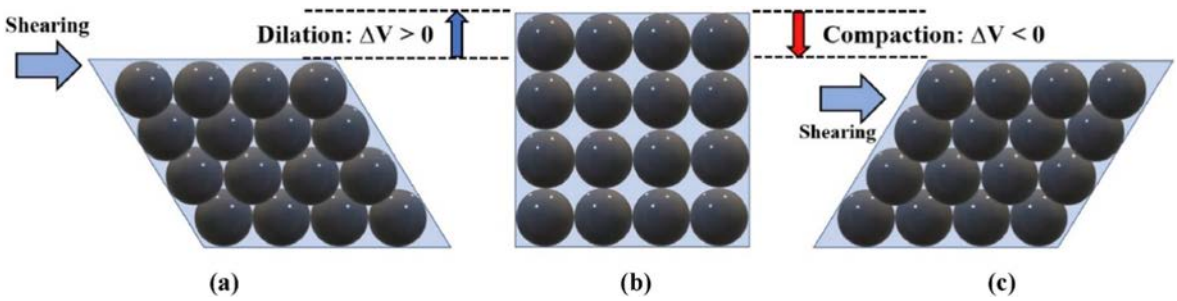

Fig. 67. Demonstration of (Reynolds) dilatancy in GM which causes expanding the samples when it is under shear stress [689].

mean-field methods [659–661]. On the other hand, shear-driven or dynamic jamming are those GM systems wherein friction and stress are important. Thus, one might need to use two networks to analyze such systems, namely contact and force networks which are also related. This group of jamming itself can be studied for both frictionless, in which only normal forces exist, and frictional GM wherein both force and contact are required to characterize the system.

Shear jamming was first observed experimentally using 2D photoelastic disks [187,662,663]. The experiment began without any

external stress and the domain was displaced using a gradually rising shear stress which developed force chains evolving from fragile (very anisotropic) to jammed states. A shear jamming phase diagram was derived, which is shown in Fig. 65. As can be seen, for example, models with packing fractions $\phi_S < \phi < \phi_J$ in jammed systems can have stresses from zero to a large magnitude. Here, the above-mentioned networks are very anisotropic. Furthermore, it can be observed that fragile state is produced with low stresses and its corresponding force chain is distributed in the direction of stress. This chain can only resist external force in the existing direction. By increasing the force further, the system transits to shear jammed wherein the force chains are distributed in both the compressive and dilational directions [22]. More quantitative data from the experimental results are shown in Fig. 66. For instance, the length of networks in the directions of compression and dilations are shown. Besides, the network is distributed mainly in the compression direction for the fragile state while it percolates in both directions when transferred to the jammed state. This experiment was also repeated many times to explore the inception of fragile and shear jammed; see Fig. 66(c). Interestingly, there is a region where all three states can occur for the same packing fraction ϕ. Another important insight is provided in Fig. 66(d) where the relation between the amount of required shear strain for reaching a shear jamming. The shear strain increases, as the packing fraction, limited to ϕ_S. Similar experiment without considering the effect of basal friction is conducted with fluid [189].

Several other sets of experiments have also been conducted about the jamming state in GM. For example, one of the preliminary tests was conducted on randomly packed frictional spheres under gravity to explore how packing fractions vary under different boundary conditions [169]. A similar experiment was conducted with spheres of different types and more versatile compaction methods [664,665]. Later, a few studies reported a series of sedimenting experiments conducted in a solid–fluid domain with a very similar density to eliminate the effect of gravity [666,667]. They also shared the particle–fluid between two cylinders to observe when dilatancy disappears, which has a lot of implications in soil mechanics and critical state characterization as discussed before. This idea was extended to fluidization systems [668–673]. Some of the results produced in fluidized beds were also visualized to better describe the differences [674]. Aside from these experiments, several other studies have been done to investigate the effect of an intruder and force propagation in systems with GM produced using photoelastic materials [675–679].

As mentioned, both the contact and force networks must be analyzed carefully if one aims to understand the jamming. Due to significant fluctuations and dealing with disordered networks, using statistical methods is very important [648,680]. Thus, parallel to the above-discussed extensive experimental tests, various computations have been conducted as well to analyze the force transmission and build a more accurate picture of jamming. One of the investigated topics is the relationship between dilatancy and shear jamming. As previously discussed, particles in GM tend to reorganize to accommodate shear stress which results in expanding the sample [681,682]. It should be noted that researchers have shown that frictionless particles do not demonstrate dilatancy [682,683]. This phenomenon is shown graphically in Fig. 67. Researchers have also studied if frictionless particles can demonstrate shear jamming given that they do not manifest dilatancy and volume change [684,685]. They found that such systems can handle deviatoric stress, but no dilatancy. However, it was clarified that there is a dilatancy but it is very small that cannot be observed macroscopically [547,686,687]. Thus, more research is still needed to understand how friction, and also other physical factors (e.g., thermal), can affect the behavior of GM when they go under shear stress with different boundary conditions [688].

3.5. Segregation

Granular flow is one of the common transport behaviors of GM, which can be found both in natural and industrial applications. During the flow process of non-cohesive materials, they may experience segregation due to differences in the particles' properties. Morphologically, segregation is defined as a non-uniform distribution of particles in the system. Segregation can be found in many systems under gravity [690–692], vibration [693,694], and mixed domains [695]. Some examples of segregation in industrial units include hopper filling/discharge [696–698], the pharmaceutical industry [699], and likewise in natural systems such as debris flow [700]. For example, segregation in industrial processes, and to be more specific, the chemical industry, can affect the hotspot in reactors, and also influence the catalytic packed bed [701,702]. Therefore, it is very important to identify such problems and coordinate them correctly to reduce the cost and time of unit operations.

The properties that affect the segregation process include size, density, surface characteristics, and also the shape of the particles. In an ideal situation with a system of uniform particles, the particle will demonstrate a solid-like behavior. But there is always some degree of heterogeneity in large-scale systems where one cannot control all the above properties and provide a uniform distribution, which eventually results in segregation. Thus, all such properties, individually or collectively, have produced several segregation mechanisms (at least 13). Some of them are percolation [701], convection, fluidization, transport, floatation segregation, and agglomeration. In this review paper, evaluating all such mechanisms is not possible and only a few of the important ones are discussed, namely trajectory, percolation, elutriation, and vibration segregations. These mechanisms are shown graphically in Fig. 68. It should be noted that the following mechanisms can be studied in dry, wet, and fully saturated conditions.

Trajectory segregation: large particles due to their greater mass, and consequently higher kinetic energy, tend to move a larger distance compared to smaller particles before they come to rest. This difference can result in the separation of particles and segregation.

Percolation (Sifting) segregation: Due to gravity and shear stress, and also vibration, smaller particles can fall down and fill the void spaces of larger particles. This separation can produce regions with large and small particles. This type of segregation begins when the particle size ratio is smaller than 0.155 [703]. The higher ratio is described by shear percolation (or kinetic sieving), which is produced using vibration or shear.

Based on the previous studies [703], a non-dimensional percolation velocity is defined by:

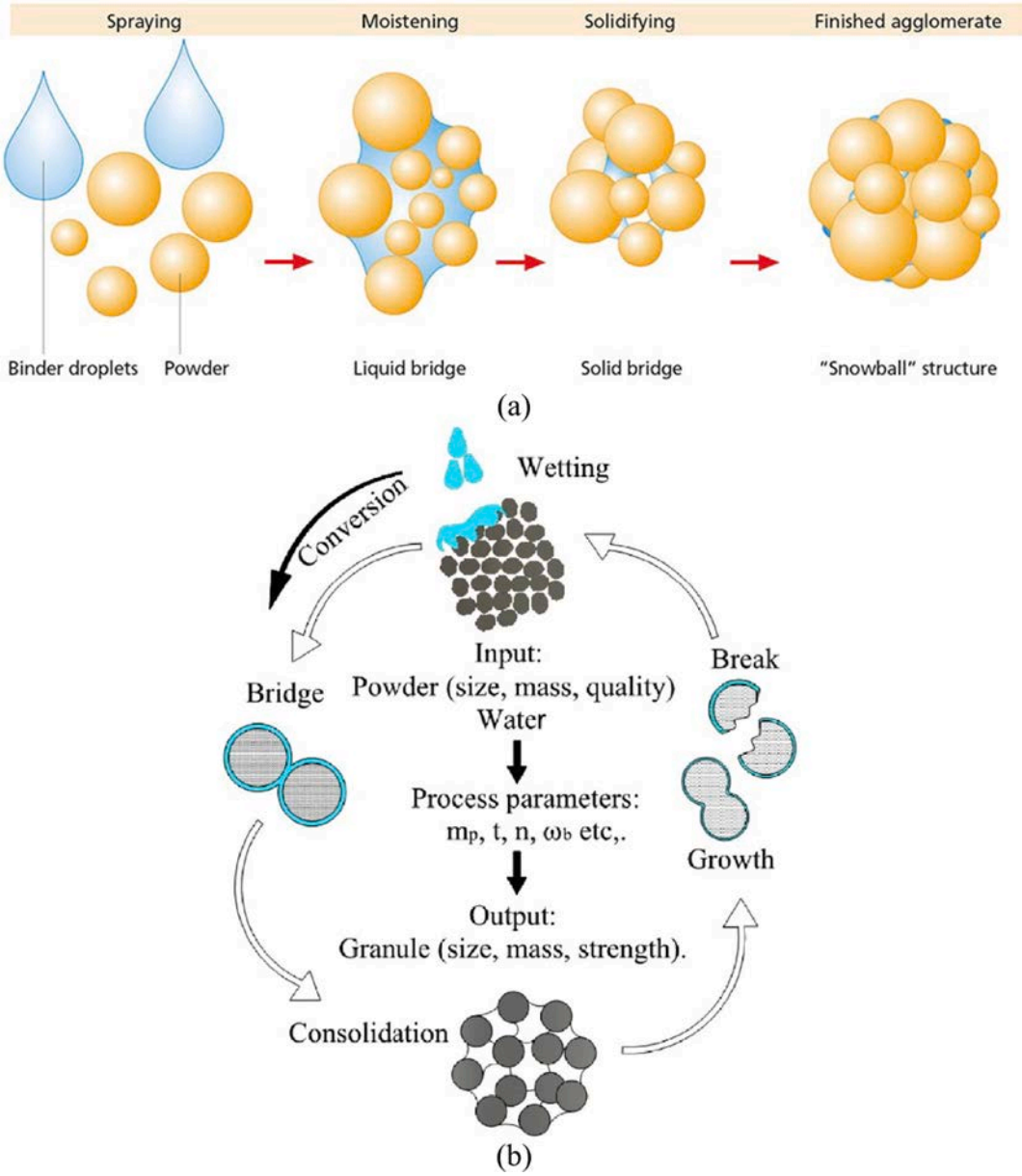

Fig. 68. (a) Agglomeration process from the beginning to final stage [711], (b) the process of adding fluid for agglomerating particles and how a larger one can still be produced after breakage [712].

$$\frac{c}{(2gD)^{1/2}} = f\left(\frac{d}{D}, e, \beta\right), \tag{171}$$

where c is the percolation velocity, d is the diameter of percolating particles, D is the diameter of static particles, e is the coefficient of restitution, and β is the solid fraction. As can be seen, the size of the particles, among the physical properties, is the only important factor. This equation indicates that particles are allowed to move when $d/D \leq 0.155$, which can be accelerated by adding vibration or a shear since β can change.

In a separate study [704,705], the percolation velocity is defined in a more comprehensive way:

$$\frac{c}{YD} = f\left(\frac{d}{D}, Y\left(\frac{D}{g}\right)^{\frac{1}{2}}, \frac{\rho_p}{\rho_b}, \frac{S_p}{S_b}, \frac{\rho_p g D}{E_b}, \frac{\beta}{E_b}, \frac{\mu_p}{\mu_b}\right), \tag{172}$$

where Y is the bulk share rate, S is the shape factor, and subscripts p and b represent the percolating and bulk particles. YD is

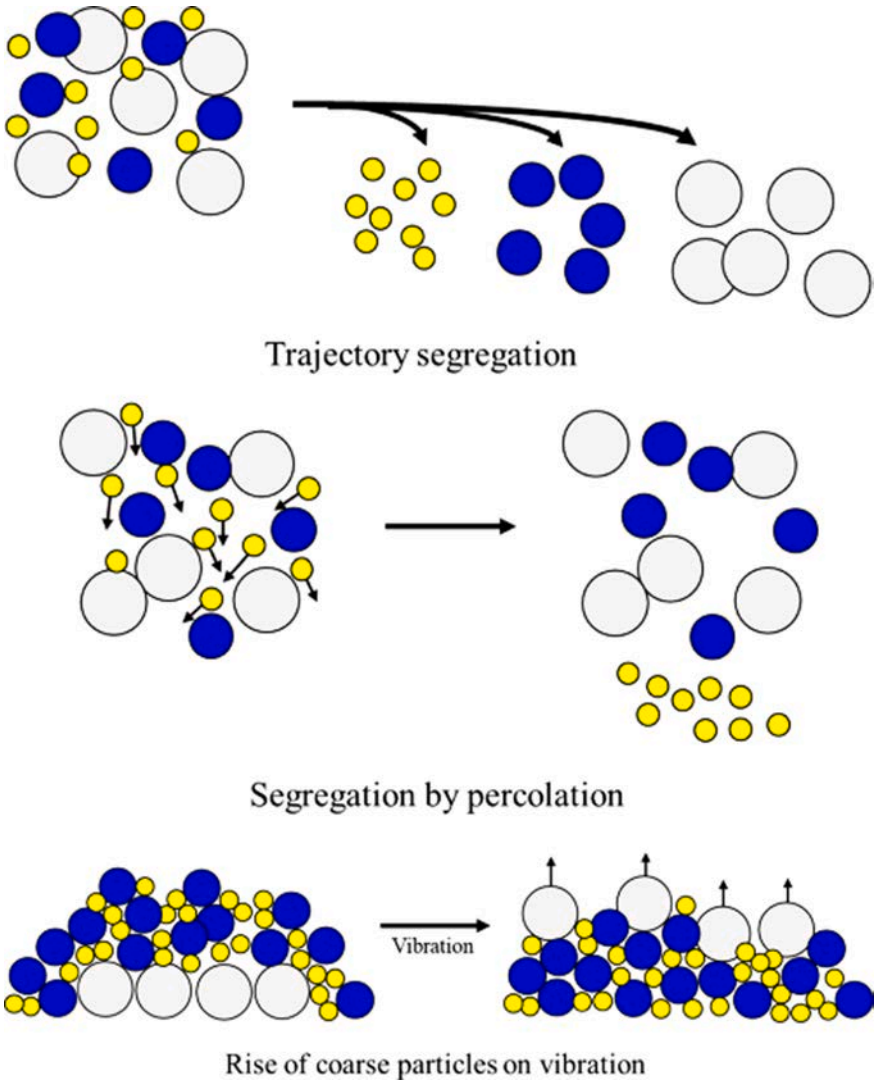

Fig. 69. Some of the frequent segregation mechanisms in GM [718,719].

interpreted as the relative velocity between shear layers, $Y(D/g)$ as the relative velocity to free-fall velocity, $\rho_p gD/E_b$ as the strain of particles, β/E_b as the bulk strain.

Elutriation (Fluidization) segregation: It can occur when a mixture of fine and coarse particles is exposed to a stream of liquid or gas in a direction opposite to the gravity direction.

Rise of coarse particles on vibration: When a collection of particles with different sizes undergoes a vibration, larger particles experience a circulation cycle, similar to the convection of fluids, where larger particles can reach the surface of the domain. This phenomenon is also known as the "Brazil nut effect".

Agglomeration segregation: This type of segregation occurs when very small particles in a mixture of GM form lumps and consequently they build a new system with different mobilities (larger agglomerates produce greater mobility); see Fig. 69.

Particle agglomeration, or granulation, refers to the formation of particle assemblages, which arise from the interaction between particles [706,707]. Particle agglomeration is the process of particle size enlargement, which is commonly used to solve material problems and improve product characteristics. The merits of particle agglomeration involve the following aspects: significant dust reduction, high process efficiency, handling, and transportation improvement, and utilization of waste products. For example, the susceptibility of glass powder being swept up in the airflow results in product loss and skewed formulas while glass agglomeration can overcome these shortcomings, which ensures accurate formulations and high process efficiency. Agglomeration of unsalable limestone fines or wastepaper sludge transforms these wastes into usable products. From a chemical point of view, agglomeration can also occur due to earth alkali (Mg and Ca) [708] and mineral composition [709]. The agglomeration process can enhance flow properties and decrease segregation while the permeability can be improved. The required wetting for connecting the particles can be attained either by a prior binding with a fluid or spraying a fluid during the mixing process. Then, the particles become larger gradually due to

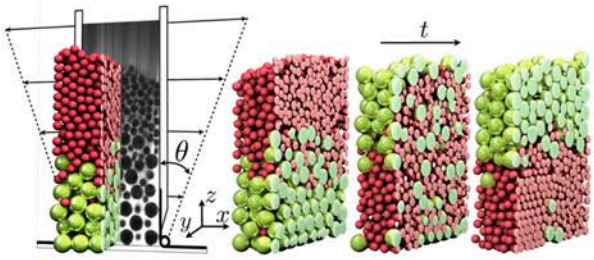

(a)

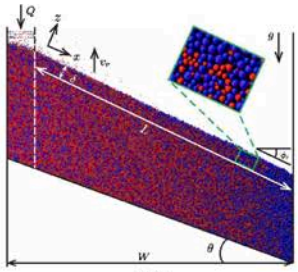

(b)

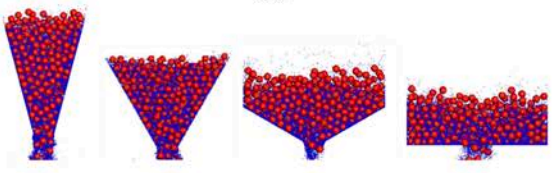

Initial stage

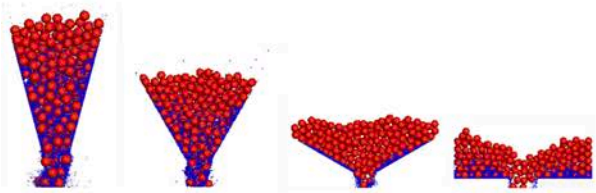

Mass discharged fraction at 40%

(c)

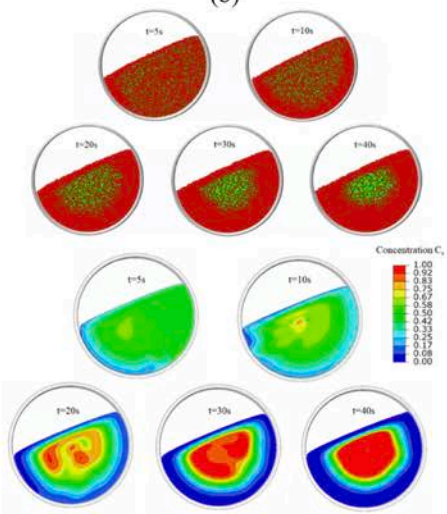

(d)

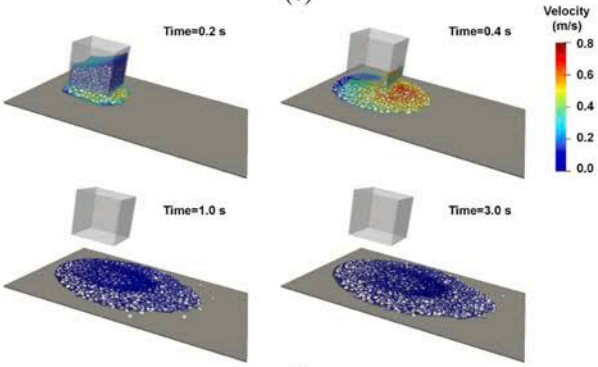

(e)

(f)

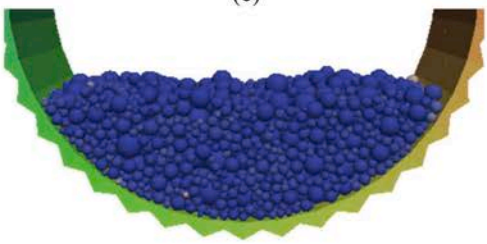

(g)

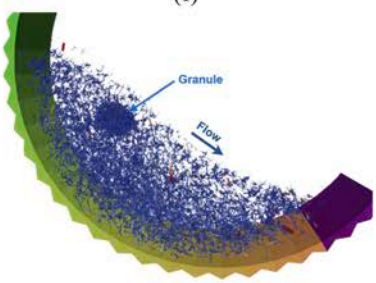

(h)

(caption on next page)

Fig. 70. (a) The effect of a periodic shear on the model shown on the left and the evolution of the pack. As can be seen, larger particles are moving upward [720], (b) quasi-2D segregation in a steady flow for a filling system. As can be seen, larger particles (blue) are moving faster [721] (c) flow pattern in a hopper with different angles [722], (d) comparison between DEM and continuum techniques for modeling of segregation in a rotating drum (the color in the continuum results represents the volumetric concentration of the small/green particles) [723] (e) gravity-driven particle flow in a saturated domain [724], and (f) [725]. (g) the initial stage of particles in a granular bed, (h) force chain once agglomeration occurs [726].

collisional-frictional/capillary-viscous interactions [710]. These particles can be enlarged further or vanish, which is controlled by the amount of available fluid or erosion in the system. One can find many other examples of agglomeration and its applications in different fields, such as powder technology, and the pharmaceutical industry. Agglomeration, on the other hand, can also result in undesirable effects, such as unplanned shutdowns if it is not characterized accurately. The agglomeration is shown in Fig. 68.

The main mechanisms resulting in particle agglomeration can be concluded as the following: *i*) Mechanical interlocking, *ii*) Surface attraction, *iii*) Plastic welding, *iv*) Electrostatic attraction, *v*) Effect of moisture, and *vi*) Temperature fluctuations. When it comes to agglomeration techniques, there are two main categories: pressure agglomeration and non-pressure agglomeration. Aside from all such complexity and variability among the impactful parameters, one can define two broad parameters dominated by the properties of the material (e.g., viscosity, particle size distribution, friction coefficient, …) and the variables related to the mixing methods (e.g., granulator size, speed of rotation, filling rate, fluid volume, slope angle, …). The mixing methods may include fluidized beds and rotating drums. All such parameters should be optimized to tune the agglomeration process and produce products with high density and uniform distribution and optimized strength.

Depending on the scale and required resolution, previously discussed computational methods can be used to simulate the segregation at micro and continuum scales. For example, one can use resolved CFD methods if the characterization of fluid behavior with more detail is necessary. As another example, the concept of segregation is also widely used in geophysical problems, in particular when one deals with natural hazards, such as avalanches, debris flows, and mass flow [713–717]. All such different modeling can also be accomplished experimentally. Some of the results for modeling segregation in dry and wet environments are shown in Fig. 70.

Powders and granular materials are usually intermediates and the final products in many industries ranging from pharmaceutical preparation to manufacturing metallic parts, fertilizers, fodder, ceramic components, and food products [727]. Particle mixing mechanisms have been studied for many decades and are shown to be governed by three major mechanisms namely: convection, shearing, and diffusion [728,729]. Experimental methods for particle mixing under external driving force could be very difficult because of the limitation in such methods to measure particle kinematics and monitoring of collisions accurately at such a scale. Computational methods such as DEM alternatively are valuable tools for carrying out such a task and the capability for millions of particles has even become a reality now due to the increase in computational power. Particle simulators have been applied for simulating the mixing of both cohesive particles and non-cohesive particles in some common industrial mixers such as helical ribbon blade mixers [730], tumbling cylinder mixers [731], tumbling cubic mixers, tumbling double cone mixers, V-blender mixer [732],

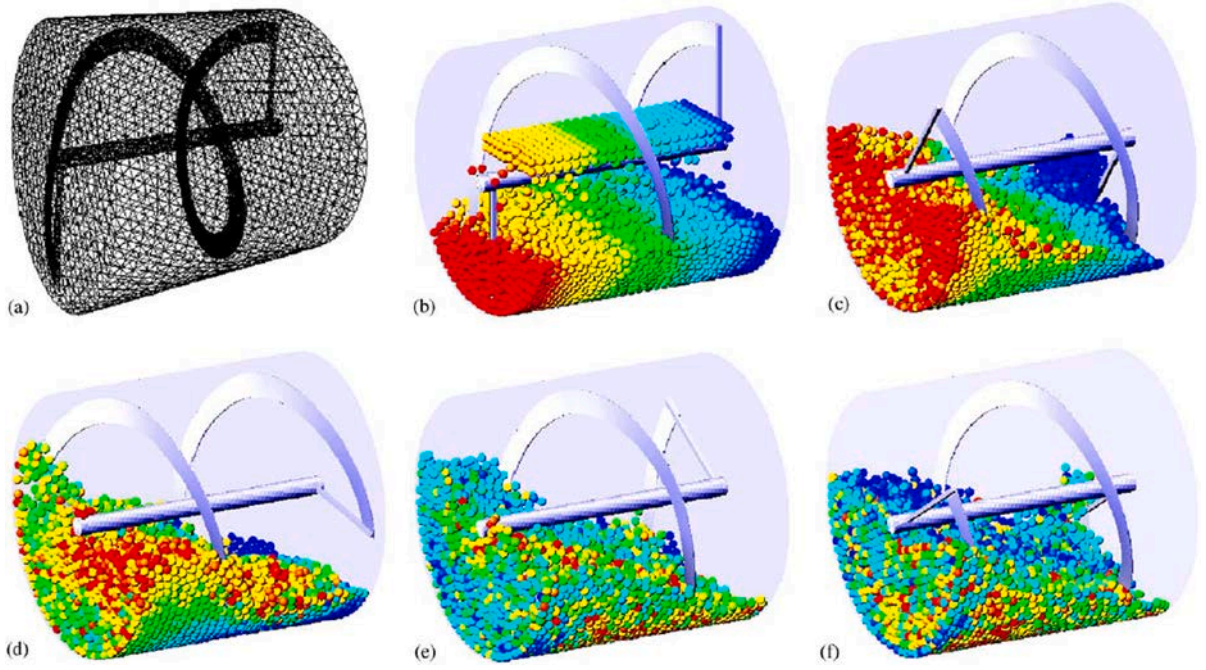

Fig. 71. DEM simulation of the flow of spherical particles in the helical ribbon blender: (a) triangular discretization of the boundary surfaces; (b) filling step at t = 0 s; and (c–f) position of the particles after 1, 2, 5 and 6 s. From [730].

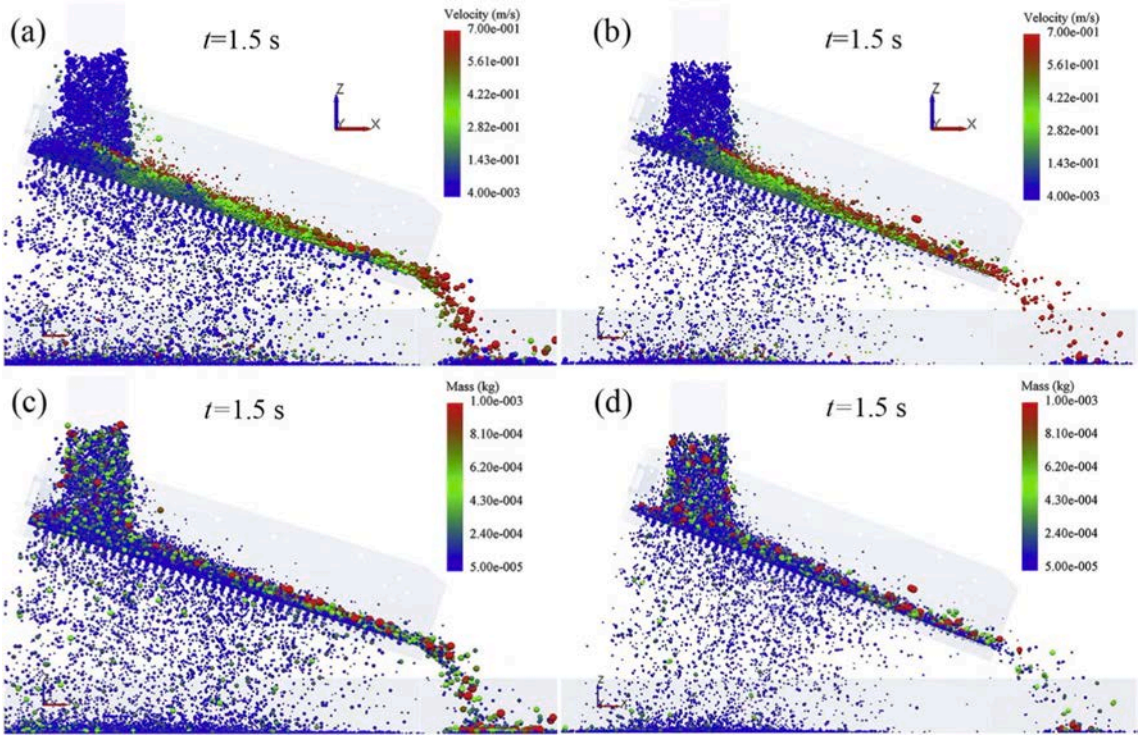

Fig. 72. Snapshots of the screening processes in DEM simulations with the amplitude of 2 mm, vibration frequency of 16 Hz, and inclination of 18° at 1.5 s for. (a), (c) spherical particles, (b), (d) non-spherical particles. (a), (b) are colored by particle velocity (red to blue for high to low speed) and (c), (d) are colored by mass (red to blue for coarse to fine). From [738].

paddle or ploughshare blade mixers, vertical high-speed mixers, rising screw mixers, fluidized bed mixers. Helical mixing can be seen in Fig. 71. The simulation was carried out with the use of 4,096 spherical particles with a diameter of 8-mm. The rotational speed was 40 rpm. It required 15 h of CPU time per revolution on an IBMP690 computer in serial mode (old 2005 paper).

Cleary et al. [733] studied mixing beds of particles with DEM to predict the flow behavior of a peg mixer. A peg mixer is one example of a device that uses an agitator to mix a bed of particles. It is commonly used to reduce residence times and thus equipment dimensions compared to tumbling blenders and bins. This peg mixer had a 300 mm diameter, 600 mm long cylindrical shell. The particles have a coefficient of restitution of 0.3 and a friction coefficient of 0.75. A spring stiffness of 5000 N/m is used. There have also been improvements in the size of particles for mixing simulations that can be carried out. Some of these simulations [732,734,735] involved the mixing of particles in the range of millimeters, and usually, these tend to ignore interparticle forces since the mass of individual particles is much greater. Deng et al [736] used Magnetically assisted impaction mixing (MAIM) using discrete DEM to test the effect of the size of non-magnets on the homogeneity with the radius of non-magnets ranging from approximately 100 μm to 79 μm. They studied the mixing of cohesive particles under magnetically assisted impaction, which includes the cohesive forces based on the JKR model and includes the formation and subsequent mixing of agglomerates. They discovered that smaller magnets and a higher mass ratio of magnets and non-magnets will lead to faster homogeneity of mixing.

Among the separation techniques, the most common method is sieving or screening. Screens are usually used for the separation of particulates into different size fractions. These screens could consist of one or more decks that are fitted with screen panels with arrays of different hole types which are vibrated at high frequencies to generate accelerations that enable the separation of particles flowing over the screen according to size [733]. Screening involves a combination of several variables such as the size distribution of particles, interactions between them, particles and screen surface interaction, and other operational parameters on particle motion which makes it an intricate process [737]. Hence, investigating this screening process would be better suited at the particle scale. Conducting experimental studies, as a result, would be difficult and expensive, especially based on the fact that it is typically difficult to investigate such a screening process at the particle scale using existing experimental techniques [738].

The use of DEM has been used over time for such particle motion studies as well as for several performance-based optimization studies. For example for vibratory screening of rice [739,740]. DEM studies have been implemented by Li et al. [741,742] to investigate the particle motion in the screening process on static meshes or vibrating sieves, in 2D for polydisperse granular systems. Cleary and Sawley [743,744] used DEM to simulate the screening process on a screen surface in the vertical vibration direction based on 3D spherical models. They analyzed the screening mechanism when particles underwent vibration screening. Jahani et al. [745] modified LIGGGHTS, which is a DEM solver, to simulate the effect of several operational parameters on screening both at the industrial and laboratory scale using double-deck banana screens. Dong et al. [746] studied the effects of vibration conditions for coal preparation. A

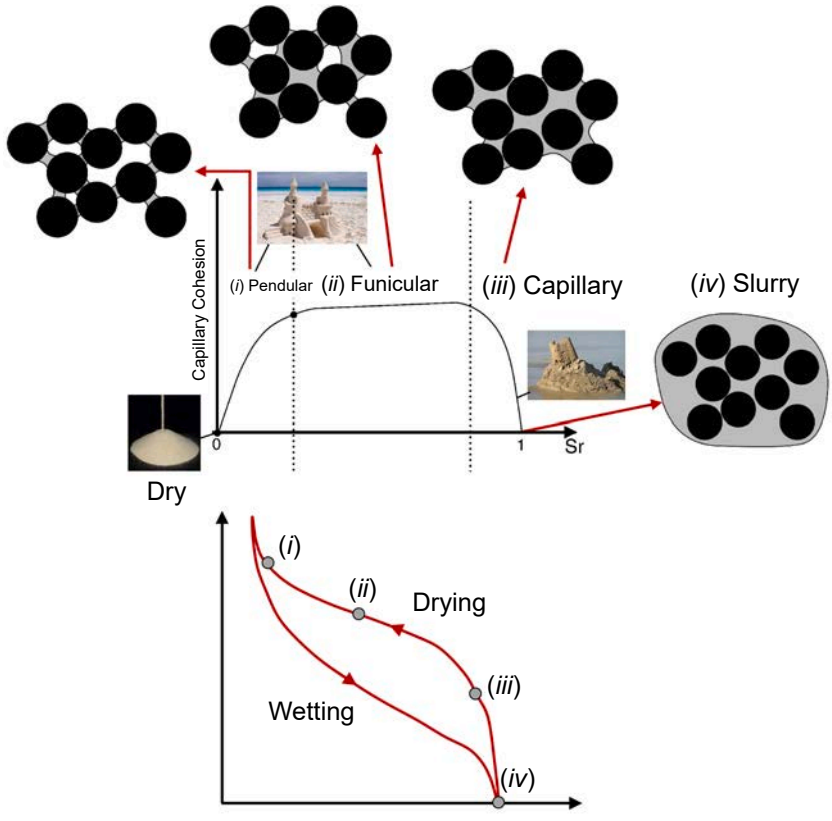

Fig. 73. Schematic representation of different fluid regimes in GM [765,768]. "Sr" represents saturation, and the axes titles are the same for the bottom figure as well.

large-scale demonstration of the use of DEM for a double-layer banana screening process for iron ore was simulated by Cleary et al. [747,748] for a range of accelerations. Screening has also been done circularly vibrating screening model for a combination of both spherical and non-spherical particles [738]. The motion of the particles can be seen at different times in the simulation in Fig. 72.

Coupled models have also been realized for separation processes. SPH and DEM were coupled in a one-way system by Fernandez et al. [749]. SPH was used to model the transport of fine particle slurry over and through the double-deck banana screen then later combined with DEM to simulate the effects of adding a slurry (water and fine material) to coarse particulates on a double-deck banana screen. Li et al. [750] applied CFD-DEM to perform a numerical simulation of material motion on the vibrating screen of the air-and-screen cleaning device. The motion of the discrete particles phase was obtained by DEM while the flow of air was simulated by CFD. The simulation considered the effect of airflow on a vibration screen.

3.6. Unsaturated granular materials

Before starting this section, it should be noted that unsaturated GM refers to those systems where the domain is not fully immersed in a fluid, but fluid exists partially. This type of system is totally different from the previously described models where the domain was occupied with fluid(s). Aside from this note, different forms of cohesive forces can be found in GM, which include van der Waals forces [751], electrostatic forces [752], and capillary forces [753]. Here, the latter force is considered. Most of the GM in the industrial and natural environments are associated with a degree of fluid [26,754–757]. The presence of fluid introduces capillary force caused by fluid pressure and surface tension [758]. This phenomenon enhances the cohesion of GM and, thus, increases the material strength as the capillary force produces an attractive force [759–763]. Characterization of wet GM not only depends on the physical properties of such materials (e.g., morphology, density, particle size distribution, roughness, shear rate, …), but also the fluid properties (e.g., surface tension, viscosity, …). Eventually, a collection of collisional-frictional/capillary-viscous interactions govern the behaviors of wet GM.

This particular case of the non-fully saturated system results in making liquid bridges between particles, which has been characterized and referred to by different names based on the amount of the liquid between the particles [762,764–767]: *i*) **pendular**: the liquid builds bridges between the particles *at the contact points* and cohesive forces are transmitted using the bridges, *ii*) **funicular**: liquid bridges are *around the contact points* and make a thin film around them. In this case, most of the pores are filled with liquid, but there are still some pores left vacant, *iii*) **capillary**: the domain is almost filled with liquid. The surface liquid forms menisci and is

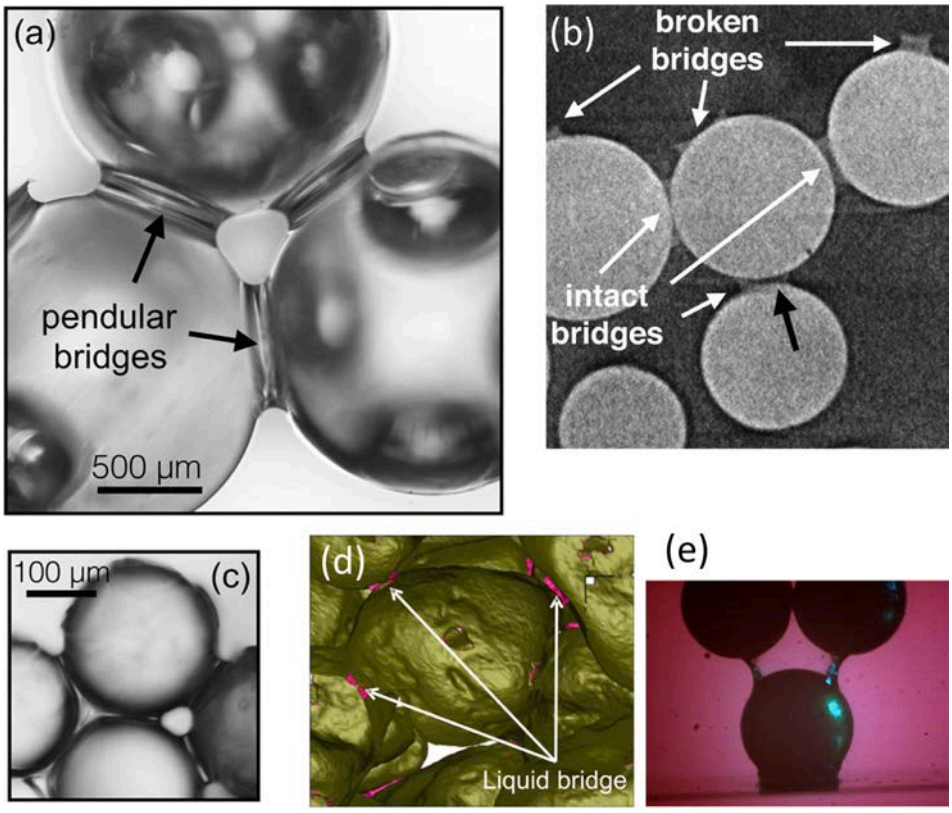

Fig. 74. Experimental observations of thin fluid films around particles for wet GM. (a, b, c) from [797], (d) from [798], and (e) from [765] which shows a funicular regime.

drawn back to the pores as its pressure is lower than the gas/air, and *iv*) **slurry**: the GM is fully saturated in a liquid and the pressure of the liquid is either larger or equal to the air's, which results in no cohesive force. As can be seen, the amount of liquid affects several parameters, such as compressive strength, shear strength, and also the deformation of GM. These cohesive regions are shown in Fig. 73 graphically and it can be noticed that cohesion occurs for the first three cases mentioned above. Thus, their mechanical characteristics will be different. Overall, liquid bridge (pendular), capillary/suction (capillary), or both of such phenomena (funicular) exist in wet GM.

The described capillary bridges are described using their shape and surface geometry, which can be related to the pressure difference between liquid and air and is computed using the Laplace equation. In this equation, the mean curvature of the surface is constant. The results of this equation are also verified experimentally [758,769–774]. This equation links pressure difference to the shape of the surface using which the normal stress balance at the interface is expressed (the tangential stress is ignored as this is the only way a static interface can be made):

$$\begin{aligned}\Delta p &= -\gamma_s \nabla.\mathbf{n} \\ &= -\gamma_s H_f \\ &= \gamma_s \left(\frac{1}{R_1}+\frac{1}{R_2}\right),\end{aligned} \tag{173}$$

where Δp is the Laplace pressure (the difference between the inside and outside pressures), γ_s is the surface tension, H_f is the mean curvature, and R_1 and R_2 are the principal radii of curvature. This relationship, suction, and saturation, is shown in Fig. 73 wherein fluid retention characteristics are not unique and it shows a hysteresis effect when the granular system undergoes drying and wetting [775–777].

The properties of capillary bridges have been studied experimentally [770,778], numerically [770,779–782], and analytically [781]; see Fig. 74. Studying GM in wet environments was started by understanding the pendular liquid bridges between two spherical particles, using either a constant liquid volume [758,759,769,774,783–786] or constant suction [770,779]. They also have been studied with a larger number of particles at the micro-level, such as DEM [95,759,779,782,787–789]. The results indicate that capillary force reduces when the suction increases. At the same time, analytical solutions are also developed in 2D [764,790] and 3D [766,772,791] systems for funicular bridges based on the Young-Laplace law. Such methods are mostly based on the toroidal

approximation where the capillary bridges are presented using a part of a circle [781,785,792,793]. Alternatively, the interface can be presented as an ellipse [786,794,795]. Then, the capillary force can be calculated based on the extracted capillary volume and the separation distance. Despite their realistic assumptions and meaning, such solutions are, however, limited to a small number of particles, and extending them to large systems is challenging. Conducting experimental modeling, at the same time, is very time-demanding, and controlling the boundary conditions and the roughness of particles is difficult [770]. Furthermore, increasing the liquid pressure with constant air pressure is not possible as the liquid may be vaporized [796].

Due to the versatility of DEM and its application for unsaturated conditions, its formulation for such problems is briefly reviewed. Here, it is assumed that a liquid film is covering the particles and, as mentioned earlier, may establish a bridge between them with a neck radius of y_0 and distance of δ_n. The Laplace-Young equation can be written as [799]:

$$\frac{\Delta p}{\sigma}\left(1+y'^2(x)\right)^{3/2}+\frac{1+y'^2(x)}{y(x)}-y''(x)=0, \tag{174}$$

where y coordinate represents the liquid bridge across x-axis.

The final force for a neck radius of y_0 should both the surface tension and the liquid–air pressure difference and can be calculated using:

$$F=2\pi y_0\sigma+\pi y_0^2\Delta p. \tag{175}$$

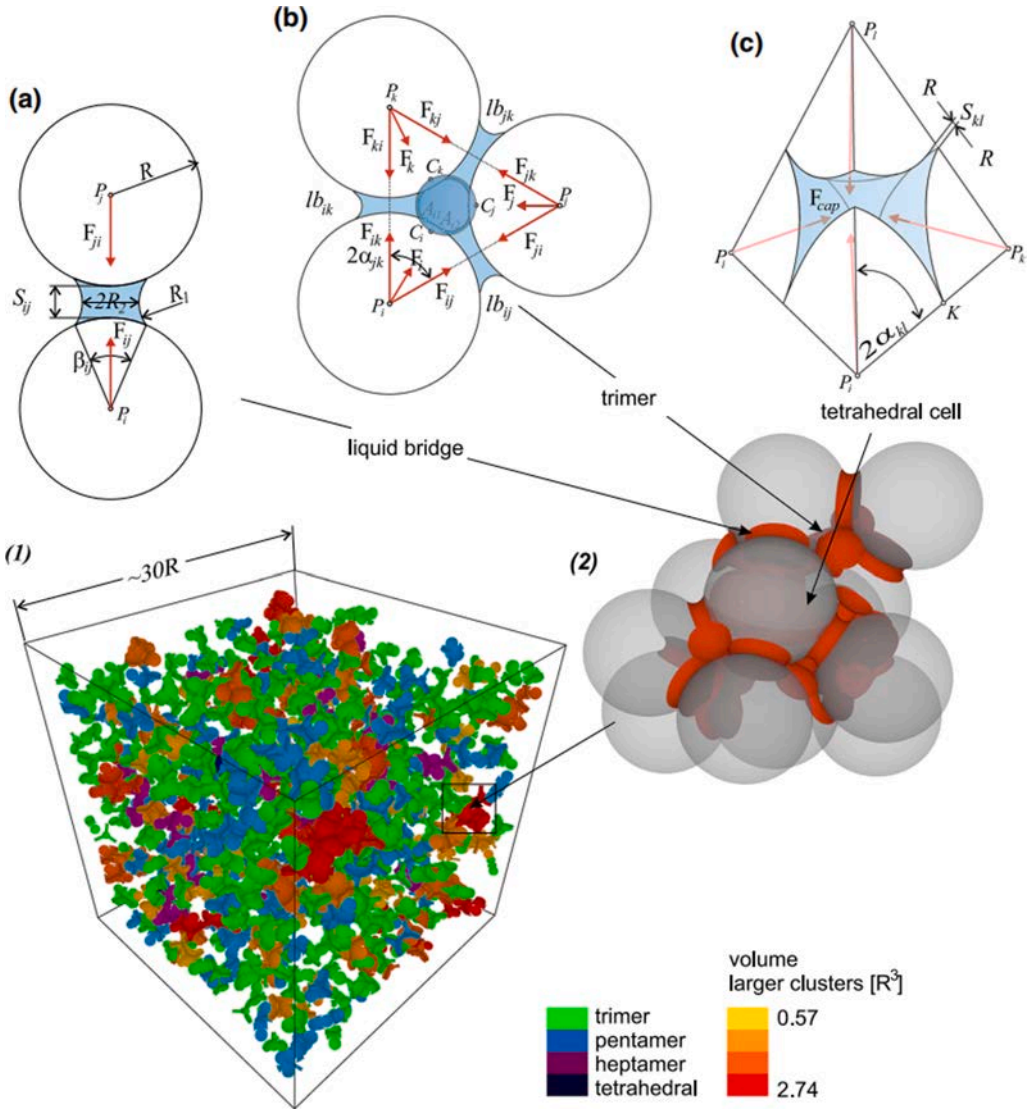

Fig. 75. Fluid representation for a total fluid volume of 3% (1) composed of three structures (a) bridges, (b) trimers, (c) tetrahedral. A zoom-in view of the network in (1) is provided in (2) [801].

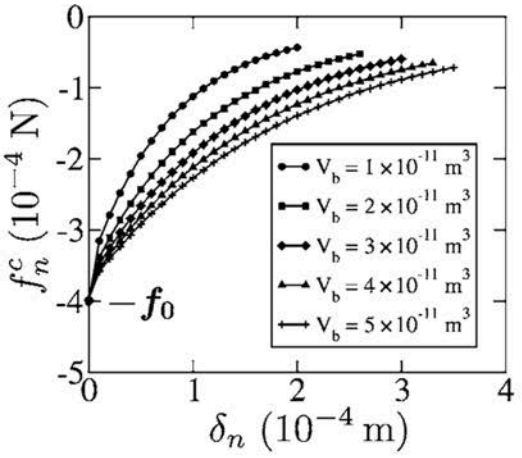

(a)

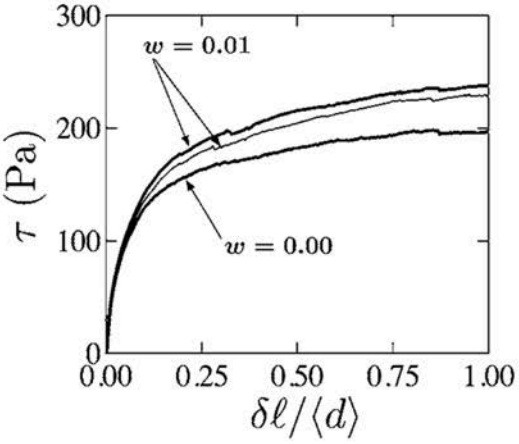

(b)

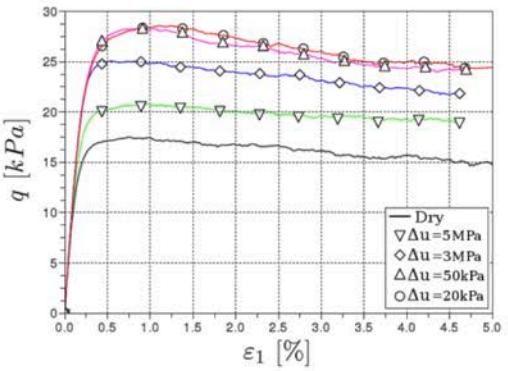

(c)

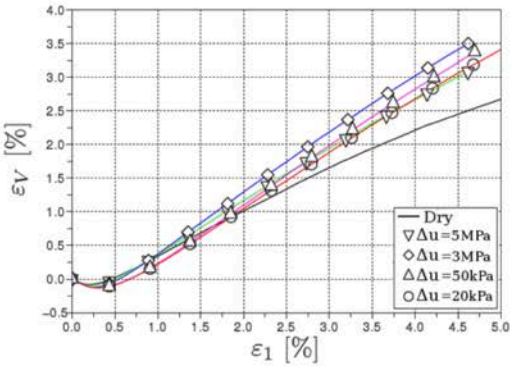

(d)

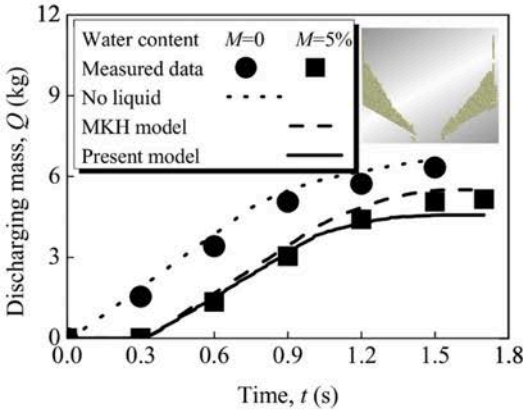

(e)

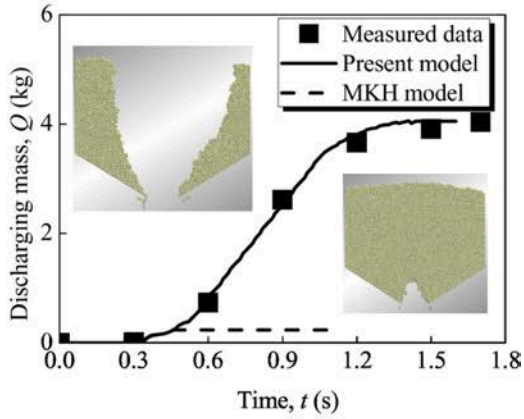

(f)

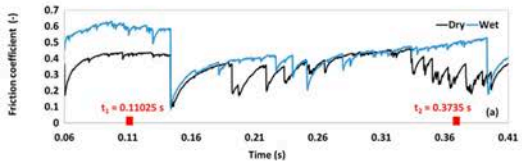

(g)

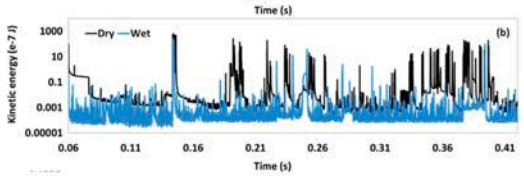

(h)

(caption on next page)

Fig. 76. (a) capillary force f_n^c vs. distance between particles for different volumes of fluid V_b. As can be seen, the largest absolute value f_0 of f_n^c depends on $\sqrt{R_1R_2}$ and weakly on the volume of fluid [787]. (b) the shear stress and shearing distance $\delta\prime/\langle d\rangle$ normalized by the average particle diameter $\langle d\rangle$ for wet and dry samples under a confining stress [787]. (c, d) the effect of different capillary pressure levels on a sample with a confining pressure (10 kPa). The same results for dry samples are also provided to better demonstrate the effect of capillary force. As can be seen, the shear strength is larger for the dry sample. Larger fluid volumes result in a higher deviatoric strength [808]. (e, f) comparison between experimental and computational modeling for discharge mass rate with different fluid contents where (e) is for dry and 5% of fluid and (f) is for 13% of fluid [809]. (g, h) comparison between dry and wet (0.6% pf fluid volume) GM models in terms of bulk friction coefficient (the ratio between shear stress to confining stress) and kinetic energy (both the rotational and translational energies) for s sheared GM in geo-systems [810].

If the above equation is integrated into DEM, it must be expressed explicitly to represent the geometrical properties and physical parameters. Thus, this equation can be rewritten as follows [759,800]:

$$F = \pi\sigma\sqrt{R_1R_2}\left[\mathrm{C} + \exp\left(A + \frac{\delta_n}{R_{\max}} + B\right)\right], \tag{176}$$

where $R_{\max} = \max\{R_1, R_2\}$ and δ_n is the distance between the two particles. A, B, and C are also defined as follows:

$$A = -1.1\left(\frac{V}{R^3}\right)^{-0.53}, \tag{177}$$

$$B = \left(-0.148\ln\left(\frac{V}{R^3}\right) - 0.96\right)\theta^2 - 0.0082\ln\left(\frac{V}{R^3}\right) + 0.48, \tag{178}$$

$$C = 0.0018\ln\left(\frac{V}{R^3}\right) + 0.078, \tag{179}$$

where V is the volume of the bridge and θ is the contact angle.
Given the above definitions, one can also calculate the distance at which the bridges are broken (rupture distance) [786]:

$$d_{rp} = 0.05(1 + 0.5[03B8])\left(V_i + V_j\right)^{1/3}, \tag{180}$$

where V_i and V_j are the volumes of the initial fluid around each particle.

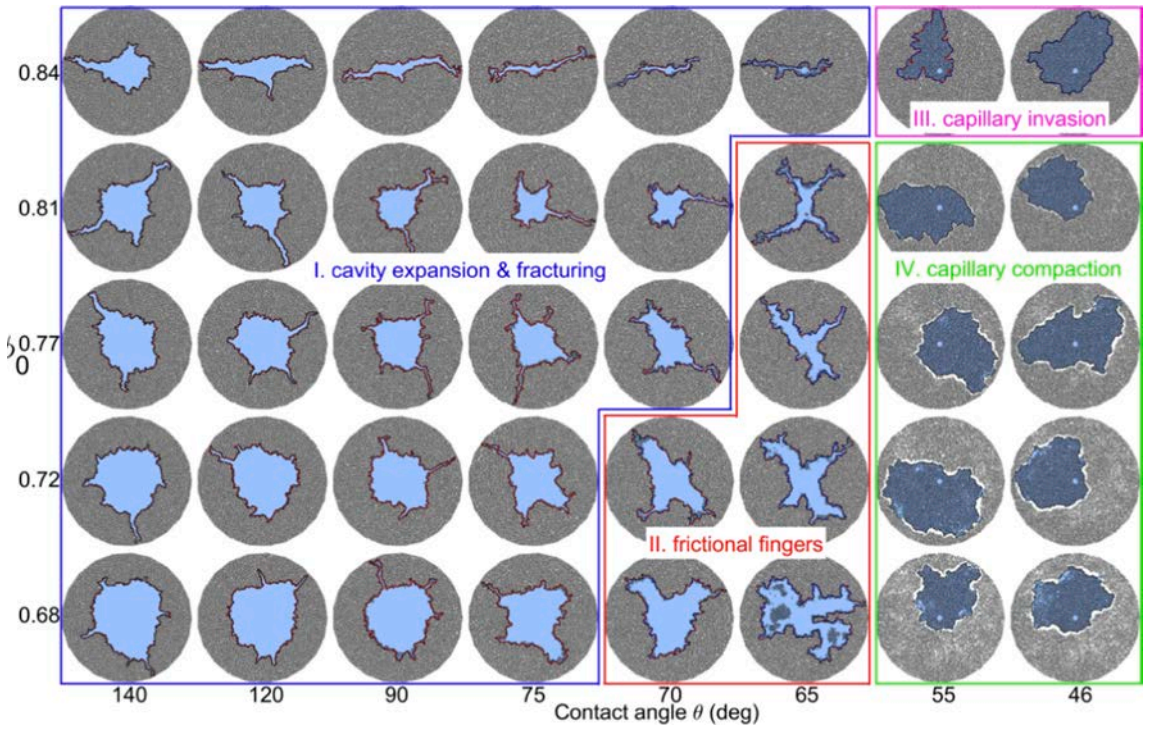

Fig. 77. Testing the effect of wettability (θ) and initial packing density (ϕ_0) on particle displacement along with four distinct morphological regimes produced by the injecting [804].

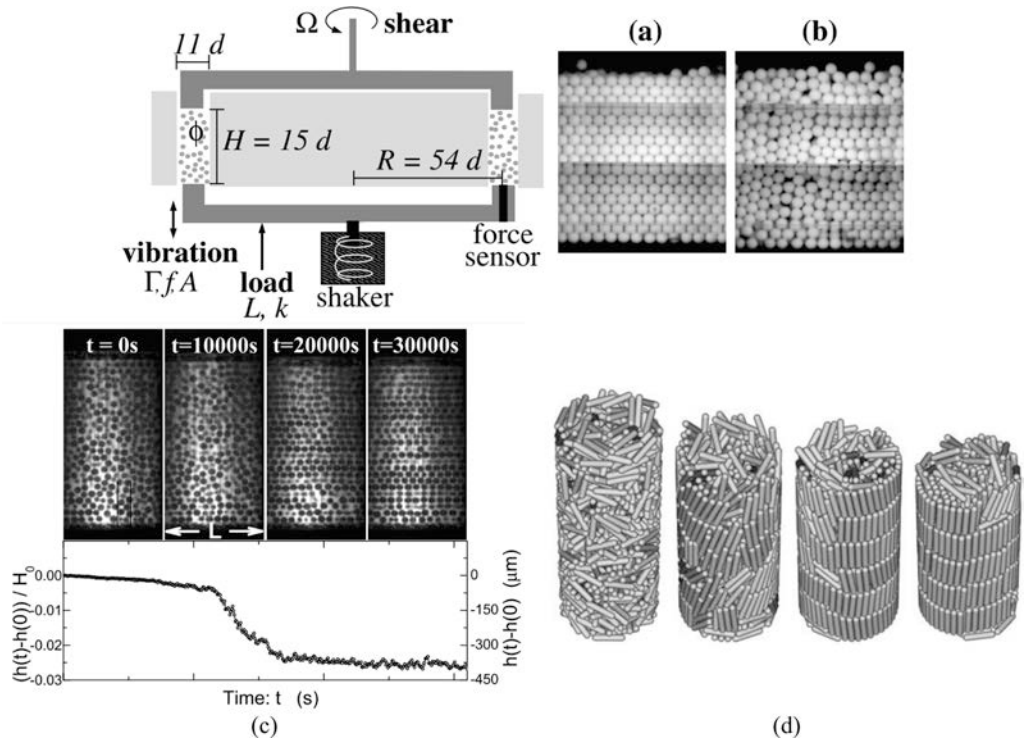

Fig. 78. Demonstration of vibration test for achieving a crystalized/ordered state shown in (a). The initial state is also presented in (b) [822]. (c) The upper image shows how a disordered GM evolves to an ordered system across different timesteps. In the lower image, the fractional volume can be seen, which reduces as time progresses [814]. (d) the process of producing a crystallized GM with time for a spherocylindrical system [91].

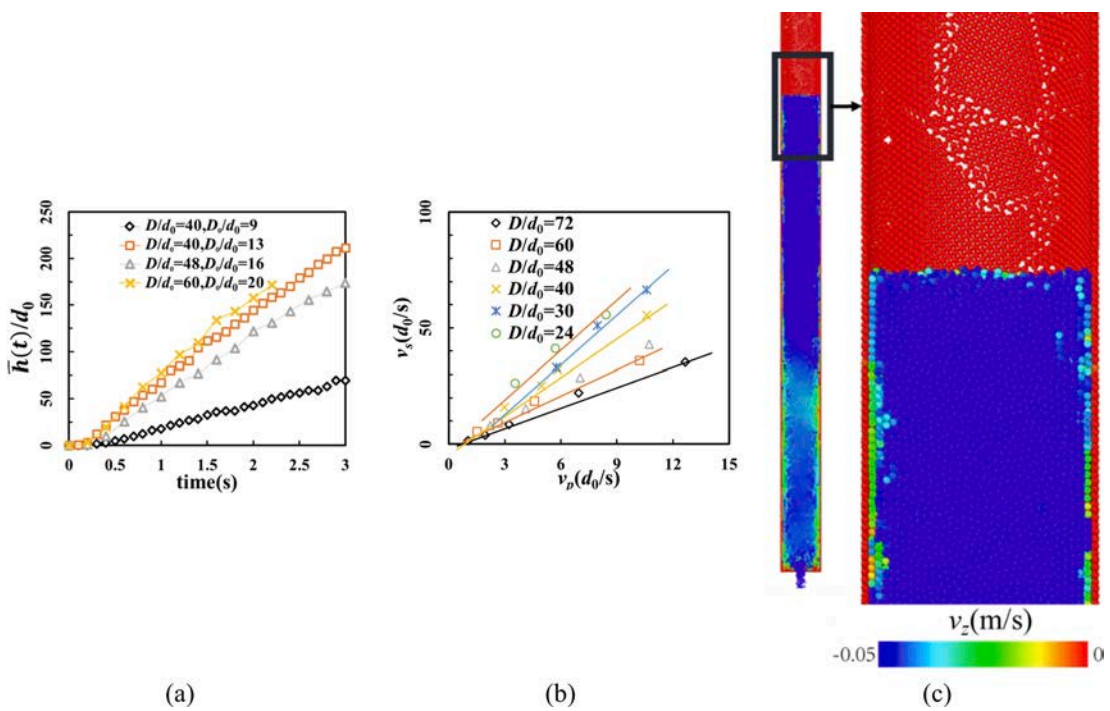

Fig. 79. Computational modeling of crystallization in a cylindrical hopper with a flat bottom. Here, D is the hopper diameter, d is the particle diameter, d_0 is the average of particle diameter, D_0 is the outlet size, and $\bar{h}(t)$ is the sell surface height. Besides, ν_s and ν_p are rate of the shell, and the velocity of potential shell particles, respectively. As can be seen in (a), the averaged surface height is changing linearly with time. There is also a linear relationship between ν_s and ν_p. One of the simulations is shown in (c) where the developed shell at the top of the hopper is visualized [828].

In a separate study [801], the liquid between particles is represented by films [802] on the grain surface and coupled with Contact Dynamics [803] using which the capillary forces produced by the liquid are transferred to particles. Besides, they also studied how macroscopic deformation can affect the liquid distribution at the microscale. The liquid phase is modeled using a Delaunay triangulation which can be interpreted as a pore-throat network where the pore space in each tetrahedral generated by triangulation is considered as pore while its connection with the surrounding pores is considered as throat. Thus, the liquid is represented in three forms of bridges, menisci, and pore bodies. One example is shown in Fig. 75. In this method, the capillary force between two particles is calculated using:

$$\mathbf{F}_{ij} = -\mathbf{F}_{ji} = \mathbf{e}_{ij} \cdot \frac{2\pi R\gamma \cos[03B8]}{1 + 0.5S_{ij}\sqrt{R/\mathrm{V}} + 2.5\delta_{ij}^2 R\Big/V}. \tag{181}$$

When a small amount of liquid is included in the granular system, very distinct behaviors from the dry models are reported. Furthermore, wet GM is also sensitive to many other factors, such as the distance between the particles, water content, etc. For example, the relationship between the capillary force and the distance between the particles for different liquid volumes is shown in Fig. 76. In a separate study, the effect of wettability and capillarity on fluid-induced deformation was studied where four different fluid invasion regimes were identified [804–807]. They also have shown how a fracture in granular systems can be initiated from a jamming state. These results are demonstrated in Fig. 77.

3.7. Crystallization

Crystallization often refers to the process of chemical sedimentation in porous media while this subject is interpreted differently in GM, and it implies the way ordered materials can be produced using shear, vibration, mixing, and flow [811–815]. The internal structure of GM can greatly affect the rheology of such systems and, thus, it is very important to characterize the internal particle

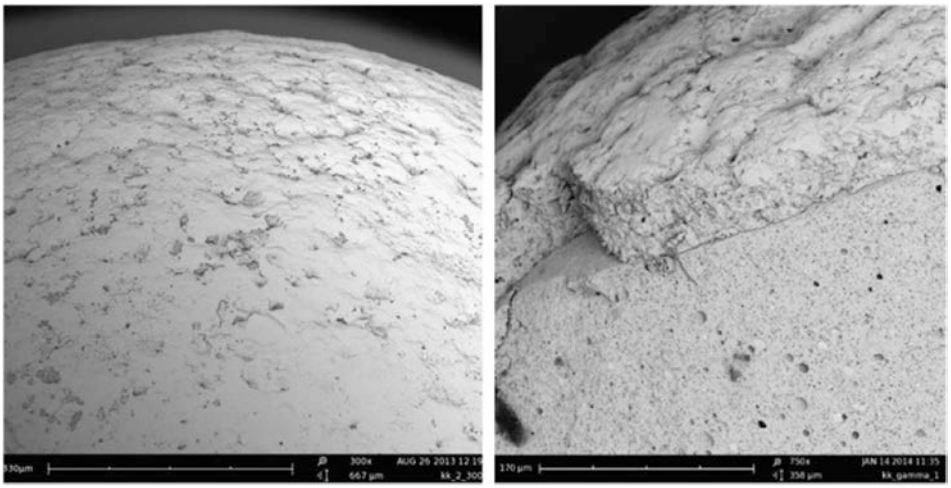

(a)

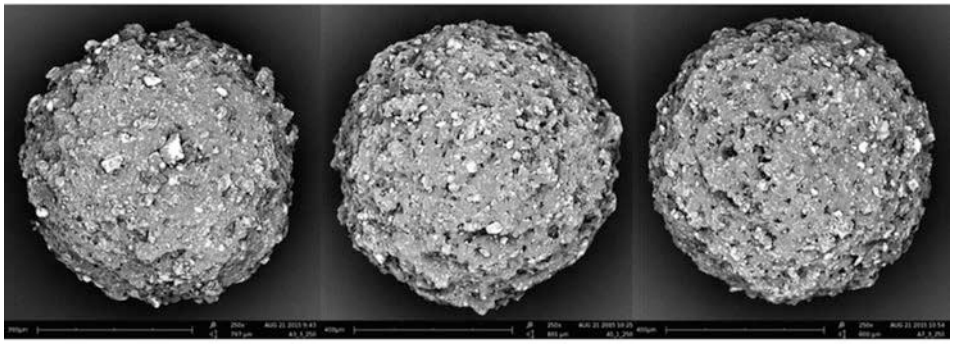

(b)

Fig. 80. (a) SEM image of coating representing the coating layer and its thickness [841], and (b) coating with suspension in a spray fluidized bed [840].

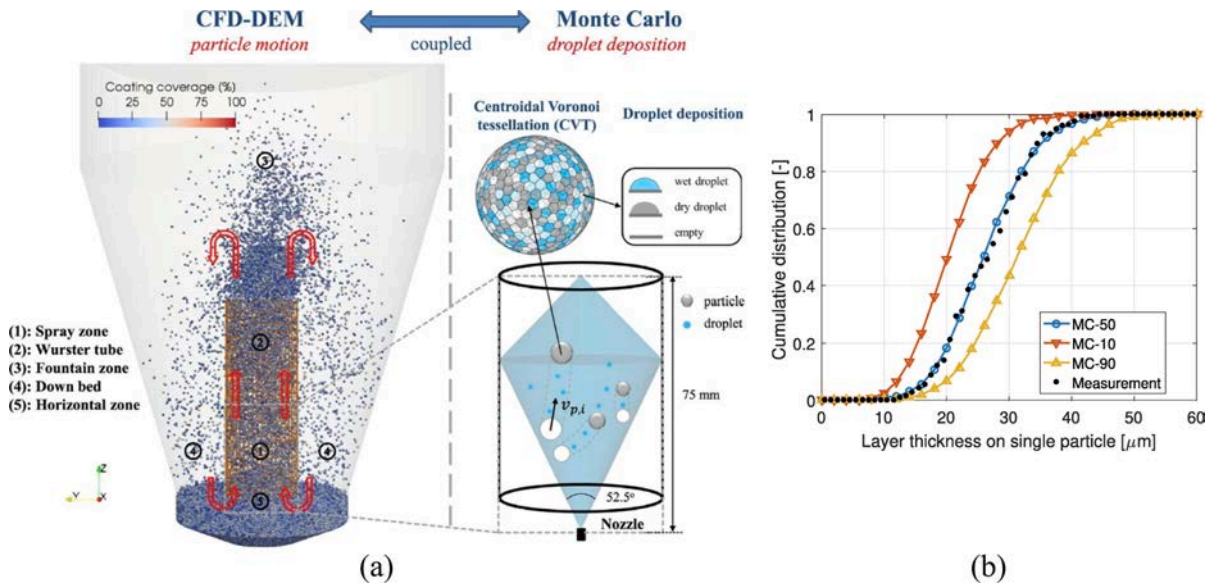

Fig. 81. Coupled CFD-DEM-Monte Carlo simulation for coating of particles in a Wurster fluidized bed, (b) cumulative distributions of thickness on a particle by considering the cohesion force for different property value populations [859].

motion and their arrangements. The order of GM and their alignment has been studied in various cases of shearing, vibration, and twisting in GM [812,813,816–818]. In this process, the shape of particles and also the domain can control the crystallization. For instance, spherocylindrical particles show vertical crystallization. Crystallization of GM due to shearing and vibration has been reported widely by studying the volume fraction and it has been shown that particle–particle friction is an important parameter controlling the ordering degree [814,817,819–822]. One such result is shown in Fig. 78.

Generally, the available studies are conducted both computationally and experimentally. Some of the experimental results are shown in Fig. 79. For example, it has been observed that increasing the roughness of walls in a granular system can boost the thickness of the shear zone around the walls. This observation was made using X-ray and electrical capacitance tomography [823,824]. The modeling of crystallization is similar to the previously described methods for grain-scale techniques, such as DEM and Monte Carlo methods. DEM has also been used to study how the roughness of walls can lead to a transition to crystallization and, consequently, smaller discharge [825–828]. A similar computation was conducted to study the effect of particle frictions on flow rate [829].

3.8. *Particle coating*

The definition of particle coating is that a thin layer of fluid or guest particles is attached to host or core particles [830]. The particle coating process can alter the surface physical/chemical properties and/or functionality of host particles [831]. There are many purposes for particle coating, such as to improve powder flowability, to protect unstable/reactive substances from surroundings (air, oxidation), and to enhance the abrasion resistance or compressibility of host particles. Generally, particle coating techniques are classified into two categories: wet particle coating and solvent-less particle coating [832]. For instance, one must keep the coating thickness very thin while avoiding cracks in pharmaceutical applications.

(i) **Wet particle coating**: Wet particle coating can be divided into the solvent coating and aqueous coating. A typical operation of solvent coating can be achieved as follows: first, coating polymers, pigments, and excipients are dissolved into an organic solvent to form a coating solution; second, the coating solution is sprayed onto the surface of target dosage forms; a smooth and uniform coating filming is finally formed after evaporating the organic solvent. It should be noticed that the disadvantages of toxicity and environmental concerns due to the presence of organic solvents impede the applications of solvent coating. Aqueous coating, which replaces organic solvents with water, is a preferred approach over solvent coating. With water-soluble coating polymers, the operations for the aqueous coating are the same as the organic solvent coating. However, when it comes to water-insoluble coating polymers, the processes are more complicated: first, coating polymers, pigments, and excipients are ground into fine powders, which are further mixed together; second, the mixed fine powders are dispersed into water to form a coating suspension, which is then sprayed onto the surface of target dosage forms; the third, evaporating process is done to form dry particle surface; finally, the mentioned three steps are repeatedly conducted until a homogeneous coating film is formed. Although there are no toxicity or environmental concerns in the aqueous coating, the limitations of evaporation difficulty, higher energy consumption, and inappropriate coating for moisture-sensitive drugs obstruct the wide applications of aqueous coating for modern industries.

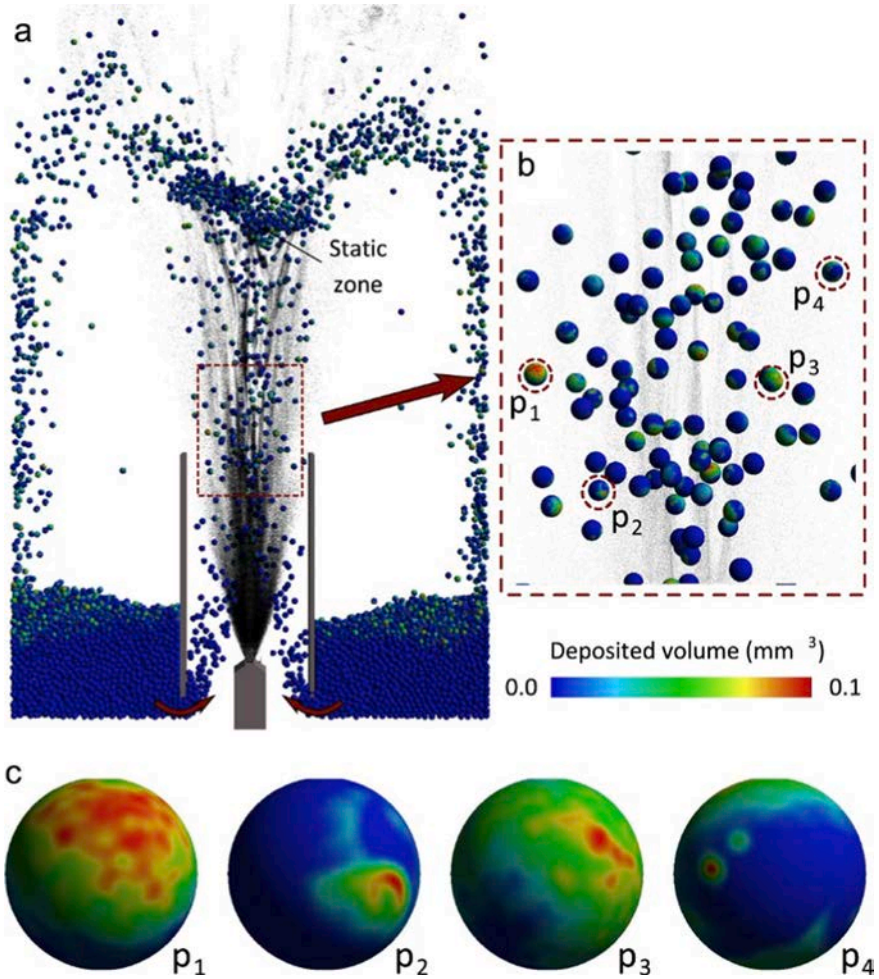

Fig. 82. (a) Particles are individually colored by deposited volume, which is proportional to coating height over the sphere. The spray particles are shown as black points and are not to scale. The three panels show (a) the entire system, (b) a sub-section showing individual particle coating distributions, and (c) coating distributions over four individual particles [424].

(ii) **Solvent-less particle coating:** There are relevant solvent/aqueous coating technologies, such as microencapsulation, fluidized bed coating techniques, solvent evaporation, coacervation, phase separation techniques, spray drying, interfacial polymerization, and pan coating. As mentioned above, the disadvantages of the solvent and aqueous coating are obvious, like high cost, residue and toxicity of organic solvent, high energy consumption, and drug degradation due to involved water. Solvent-less technologies have been developed to overcome the disadvantages associated with the use of solvent/water coatings. There are several modern solvent-less coating methods: photocurable coating, compression coating, hot-melt coating, magnetically assisted impaction coating, powder/dry coating, and supercritical fluid coating.

Particle coating is often achieved using a fluidized bed and rotating drum for large-scale systems [833]. For example, the Wurster fluidized bed is one of the common ways to perform coating in pharmaceutical applications [834–837]. In this method, a gas is injected through the Wurster tube, and the particles are wetted/coated by spraying droplets. The particles are eventually collected when they reach the outer bed region. The drying level of the injected fluid can be adjusted to control the coating process [838,839]. The performance of coating can be examined by evaluating different factors, such as the coating of each individual particle, the overall coating for the system, and the thickness of the coating as well as the porosity and moisture of the coating [840]. One can evaluate these variables using experimental methods like near-infrared and Raman spectroscopy, X-ray, confocal laser scanning microscopy, and also terahertz pulsed imaging. Some of these results are shown in Fig. 80.

In addition to experimental modeling, various computational simulations were also carried out. They are mostly based on CFD-DEM using which the behaviors of fluid and particles can be characterized reasonably and can integrate the effects of heat, mass transfer, the shape of particles (to some degree), and cohesion forces. For example, CFD-DEM is used to study the residence time distributions in different locations of coating systems [426,842–845]. CFD-DEM simulations must be conducted more carefully in the sense that one should consider several factors such that the injected fluid must appear as a droplet. Besides, the induced shear from the

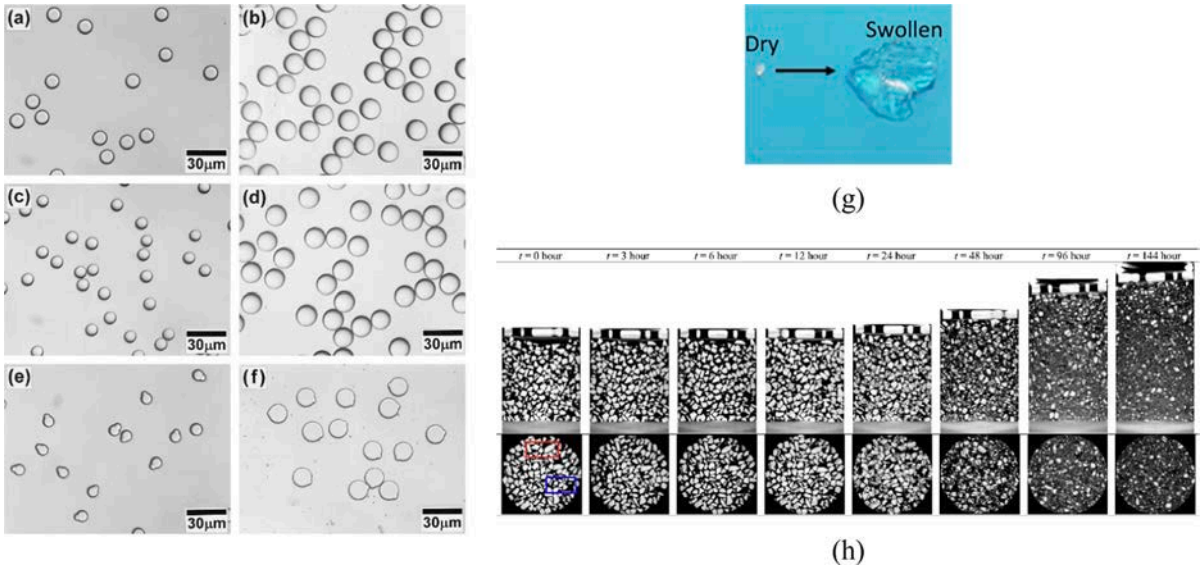

Fig. 83. Monomer-swollen particles swelling after 30 min for different weight percentages (wt%). (a) 0 wt%, (c) 3 wt%, and (e) 3.5 wt% and also similar results after 6 h for (b) 0 wt%, (d) 3 wt%, and (f) 3.5 wt% [871]. (g) sodium polyacrylate particle swelling [872]. (h) swelling mechanism of magnesium oxide granules during hydration [873].

fluid injection, surface tension, aggregation [846,847], breakage [848,849], droplet solidification [847,850], and also the viscosity force of the fluid all should be included [424,830,851–855]. One such method is shown in Fig. 81. In each Monte Carlo loop, one droplet is added to each particle and the new particle diameter is fed to the CFD-DEM solver which passes through another loop, and the updated information will be transferred back to the Monte Carlo model. For this aim, the surface of each particle is divided into smaller regions with a similar area on which the droplets can be placed [856–858]. A similar result of computational modeling for particle coating is shown in Fig. 82.

3.9. Particle swelling

Swelling of porous media, and in particular GM, can be found in natural and industrial fields, such as papers, polymer, biological tissues, clay, and also the food industry [860–864]. Characterization of swelling requires considering both the fluid and solid in the system and how they interact with each other, which can include chemical reactions as well [865,866]. Swelling occurs due to fluid absorption in a solid, which results in expanding the volume of the solid [867]. An example of swelling GM is Super Absorbent Polymers which are composed of long hydrophilic polymer chains that can be banded with water [868]. In these materials, particle size affects the swelling rate, which is often angular at an industrial scale [869]. As such, such particles represent a larger surface-to-volume ratio, and their motion is limited to the irregularity of the shape. A similar example can also be found in geo-materials where due to humidification/drying the particles can swell/shrink [870]. In some cases, this can induce radial (or orthoradial) tensile which increases with time. Swelling in GM has been observed experimentally and simulated computationally. Some of the experimental results are shown in Fig. 83.

Swelling is also studied computationally but not extensively. One of the solutions for implementing the swelling effect is through coupling DEM and a fluid solver, such as Pore Finite Volume (PFV) [868]. In this method, based on the mass of absorbed fluid m_i^f and particle's in its dry condition m_i^s, the absorption ratio $Q_i^{abs}[-]$ is defined for each particle:

$$Q_i^{abs} = \frac{m_i^f + m_i^s}{m_i^s} = \frac{(r_i)^3 \rho_f}{(r_i^0)^3 \rho_s} - \frac{\rho_f}{\rho_s} + 1, \tag{182}$$

where r_i^0 is the radius of the particle in dry conditions. Note that the density of particles can gradually become one of the fluids. It is also assumed that the maximum value of Q_i^{abs} is known and constant, which can be defined experimentally. For their particular application, they assumed that the swelling rate is governed by the diffusion of fluid into the particles:

$$\frac{dQ_i^{abs}}{dt} = \mathrm{K}_i \left(\frac{Q^{max} - Q_i^{abs}}{Q_i^{abs}} \right), \tag{183}$$

$$\mathrm{K}_i = \frac{3Dr_i}{(r_i^0)^3}, \tag{184}$$

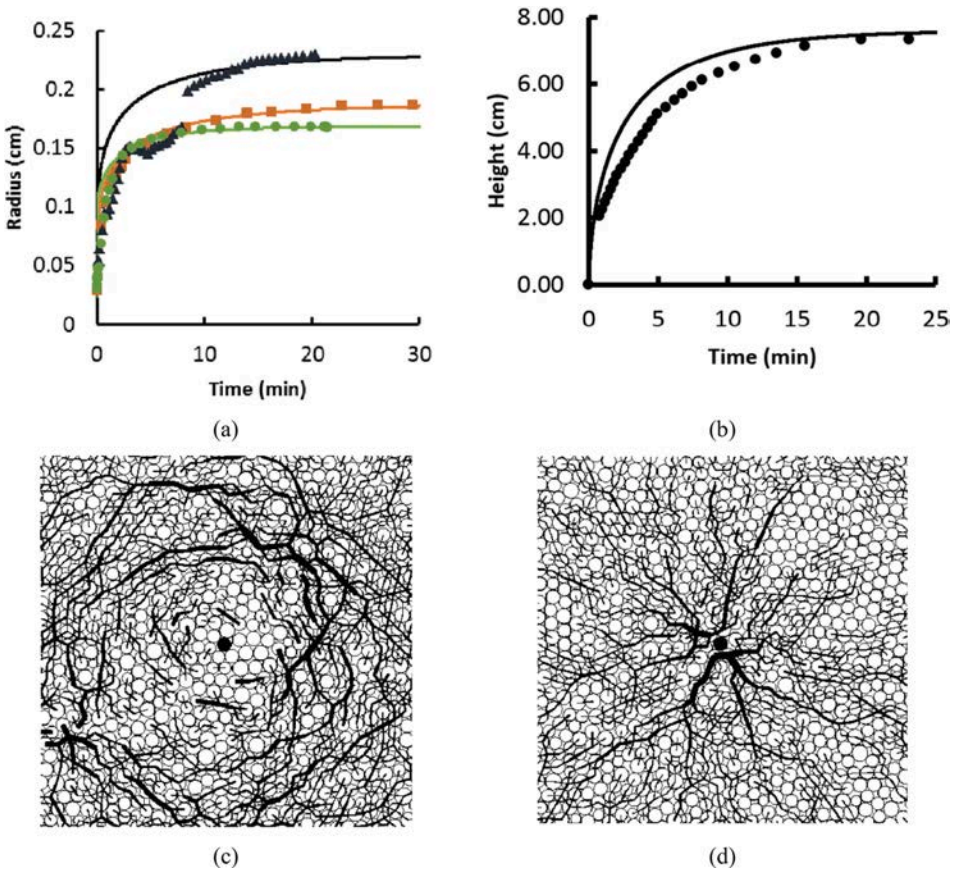

Fig. 84. (a) Particle size evolution for GM with different initial radius sizes. The experimental and computational results are shown in symbols and solid lines, respectively. (b) demonstrating the evolution of sample height [868]. (c) tensile and (d) compression normal forces produced during the swelling of a single particle in an assembly of granular particles [876].

where D is the diffusion coefficient. This equation can be reformed as a derivative of radius based on time:

$$\frac{dr_i}{dt} = \frac{D}{r_i}\frac{\rho_s}{\rho_f}\left(\frac{Q^{max} - Q_i^{abs}(r_i)}{Q_i^{abs}(r_i)}\right). \tag{185}$$

The absorption process is implemented by enlarging the particles size and defining a growth factor as follows:

$$f = \frac{r^{t+\Delta t}}{r^t} = 1 + \frac{\Delta t}{r^t}\frac{dr}{dt}, \tag{186}$$

where $r^{t+\Delta t}$ is the radius at time $t+\Delta t$ and $\frac{dr}{dt} = \frac{r^{t+\Delta t} - r^t}{\Delta t}$. This phenomenon, namely changing the sizes, will result in changing the particle's properties, such as stiffness in both normal and tangential directions. Similarly, the mass and rotational inertia will also change:

$$M_i^{t+\Delta t} = M_i^t . f^3, \tag{187}$$

$$\boldsymbol{I}_i^{t+\Delta t} = \boldsymbol{I}_i^t . f^5. \tag{189}$$

As mentioned, the absorption process can also affect the stiffness, which can be expressed by decreasing the Young's and shear moduli. Thus, the shear modulus of a particle can be written as:

$$G_i = \frac{\beta}{\sqrt[3]{Q_i^{abs}}}, \tag{190}$$

where β is defined using $\left(Q^{abs}, G\right)$. Then, Young's modulus can also be updated:

$$E_i = 2G_i(1+\nu_i). \tag{191}$$

One can couple the above equations with a fluid solver, such as PFV, using which the swelling and other displacements can be

calculated. To do so, a swelling rate can be assigned to each particle. Using the amount of fluid that goes in and out of a pore and also the rate of fluid absorption q_I^{abs}, the change of pore volume, which is a combination of the motion of particles $\frac{dV_I}{dt}\big|_{relmov}$ and swelling $\frac{dV_I}{dt}\big|_{abs}$, can be balanced [874]:

$$\left.\frac{dV_I}{dt}\right|_{relmov} + \left.\frac{dV_I}{dt}\right|_{abs} = \sum_{J=1}^{4} q_{IJ} - q_I^{abs}. \tag{192}$$

Here, the absorption is limited to four surrounding particles. If the density of the fluid is assumed to not change, then, $\frac{dV_I}{dt}\big|_{abs} = -q_I^{abs}$. Thus, the pressure only needs to be solved using:

$$\left.\frac{dV_I}{dt}\right|_{relmov} = \sum_{J=1}^{4} q_{IJ}. \tag{193}$$

As can be seen in Fig. 84, the obtained computational results are in agreement with those produced using experimental modeling. Besides, the swelling effect, manifested by an increase in the radius size, is also demonstrated. Similar results for a 2D model wherein only one particle is swollen are also presented in the same figure. It is also observed that swelling can change the capillary in GM as well [875].

3.10. Cell-Scale biological flows

The fact that red blood cells (RBCs) occupy 45% of the volume of blood determines that blood flow behavior strongly depends on the dynamics of RBCs, such as their deformation and orientation. The dynamics of RBCs is controlled by their rheological properties, such as internal viscosity and cytoskeleton elasticity [877–881]. The viscoelasticity, microenvironment, systemic disturbances as well as dynamic states, such as steady tank-treading, swinging, and unsteady tumbling contribute to the rheological properties [882]. It is therefore interesting to investigate the dynamics of RBCs under various rheological properties and how the dynamics of RBCs affects their rheological properties in turn. An example of the existing cells is shown in Fig. 85. A complex vessel network is also presented in

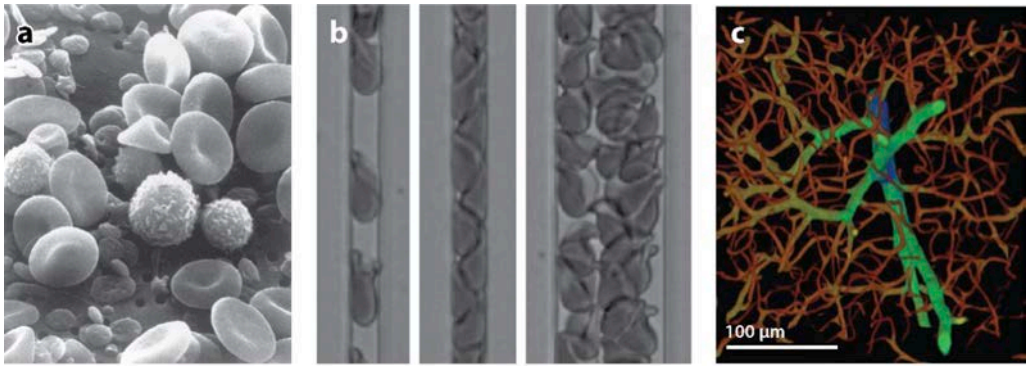

Fig. 85. (a) Red and white blood cells and platelets [883], (b) red blood cells in a microfluidic device [884], and (c) microvasculature scan of a mouse brain [885].

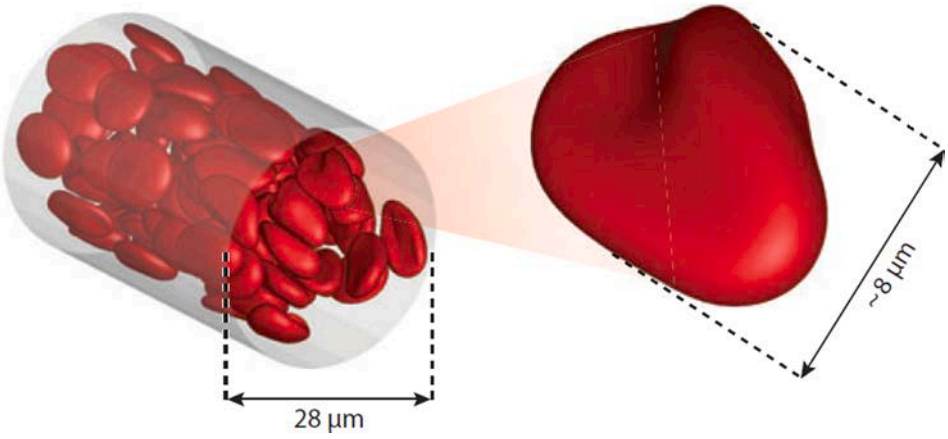

Fig. 86. Demonstration of blood cells along with an approximate size [893].

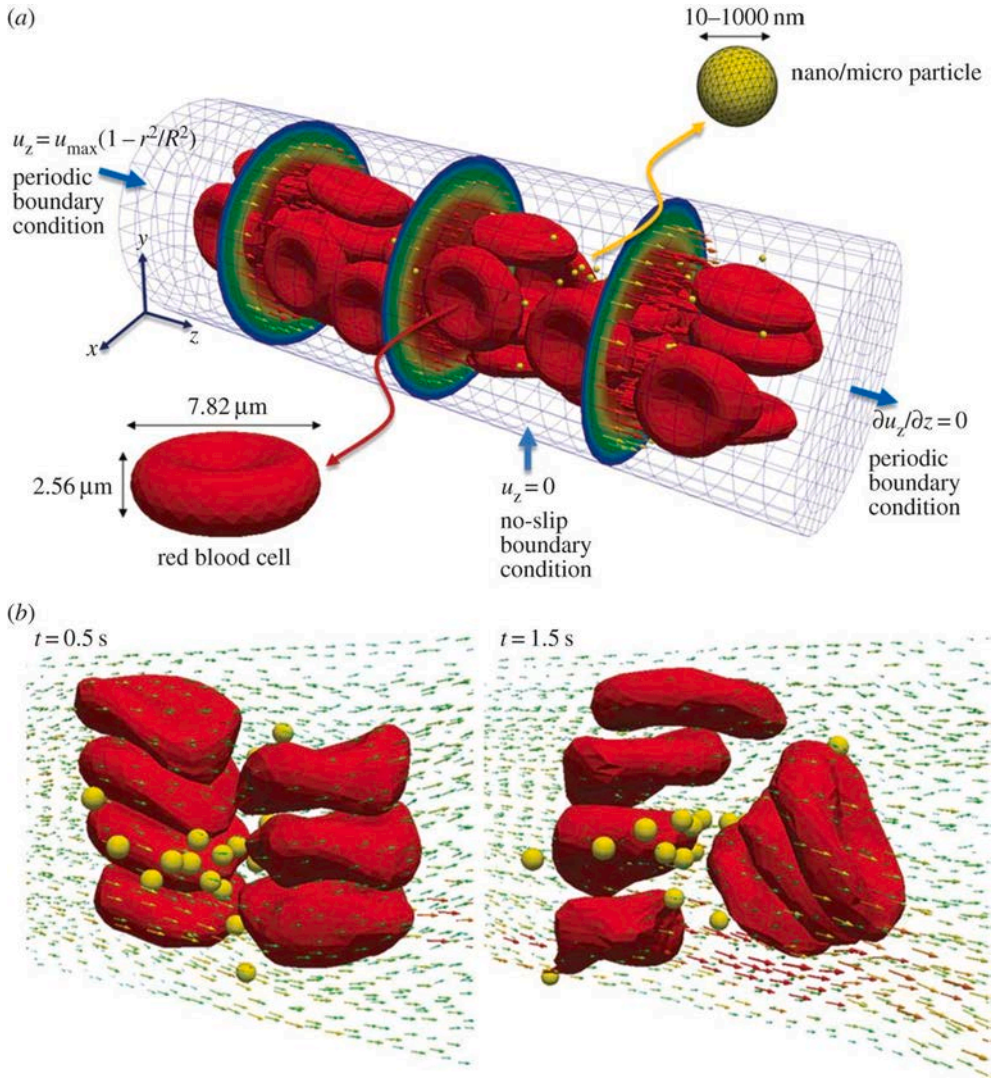

Fig. 87. (a) initial distribution of blood cells along with nanoscale particles, (b) flow distribution around the cells and particles, and how larger cells experience deformation [926].

the same figure. As can be seen, the cells are quite complex and with irregular morphologies.

In addition to experimental works, there are already many numerical studies to simulate the flow behavior of RBCs [886–889]. One example of computational red blood cells is shown in Fig. 86. Skalak et al. computationally simulated the flow behavior of Newtonian blood fluid with the assumption of red cells being axisymmetrically located in a circular tube with no change in their biconcave disk shape. They found that the apparent viscosity was greatly determined by the ratio of the diameter of the red cells to the capillary diameter. The apparent viscosity was linear to low hematocrits while the relationship deviated from the linearity at high hematocrits due to the effect of trapping fluid [890]. Tözeren and Skalak theoretically investigated the steady incompressible suspension flow with elastic spheres through a circular cylindrical tube. They proved that there was little deformation in axisymmetrically distributed elastic spheres in the flow process. With the closely fitting spheres, the flow behavior of the incompressible suspension was strongly controlled by the shear modulus of the elastic spheres and their velocity [891]. Schmid-Schönbein et al. studied the distribution of blood cells with numerical analysis based on a mathematical form consisting of a linear form and Fourier series. The results of network computation showed that the distribution of blood cells would be nonuniform, which was the result of the relation between the cell flux and the nonlinear bulk flow into the daughter's vessels. The alteration of flow distribution simultaneously led to the redistribution of blood cells, which was counteracted by the effect of an additional pressure drop of each blood cell [892].

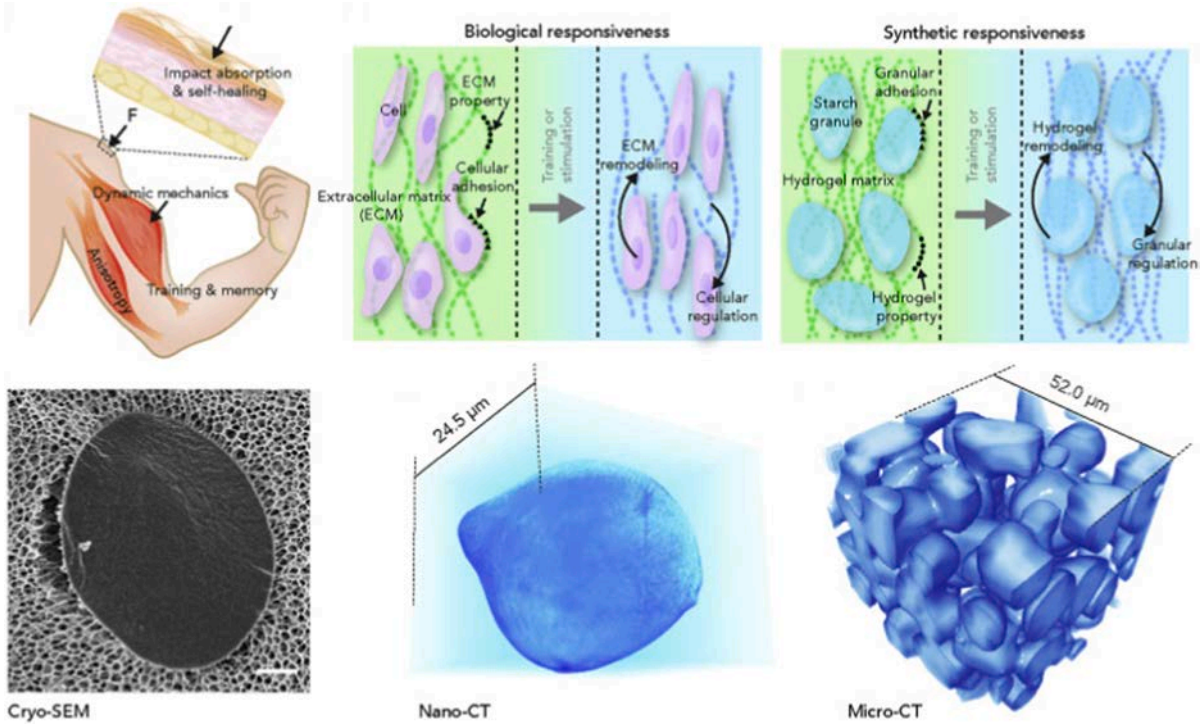

Fig. 88. Granular tissue materials [927].

Using a single method for covering all the possible variations in cell systems is not practical and, thus, one must calibrate and customize methods for specific behaviors. For modeling of the cells, considered as particles, continuum methods [886,894–896] and discrete modeling have been used [889,897–904]. One of the main differences between such granular systems with those that have been reviewed to this point is the expected large deformations of cells. This problem becomes more critical when blood flow is turbulent. Another issue is the fact that the viscoelastic nature of the membrane in the cells requires using some restrictions for time integration [886,905–908]. Furthermore, blood cells move very close to each other and have a very tight interaction, which in some cases may result in aggregation and complex force transmissions. In a more precise way, other important physics, such as thermal fluctuations, the effect of macromolecules, and glycocalyx coating should be included to achieve more accurate and representative simulations. On the fluid/blood flow side, one can use a variety of methods as discussed in the previous sections, such as meshfree methods [904,909–915], mesh-based techniques [886,906,908,916–921], hybrid methods [917,922], and also stochastic methods [889,902,923–925]. An example of cell deformation and translation is shown in Fig. 87.

The concept of GM has recently been used in tissue engineering as well [927]. In one such application, hydrogels, due to their tissue-like characteristics, are used. Biological tissues manifest complex dynamic and multiscale behaviors but mimicking the full functionality of natural tissues in the synthetic samples is difficult. However, hydrogels, as a granular system, can be used to produce a tissue with strain-stiffness behavior, while it shows anisotropy, mechanochemistry, self-healing, and also programmability. The complexity and multiscale nature of these tissues and also their appearance as a granular system are all shown in Fig. 88.

3.11. Colloidal systems

A Colloid is defined as a mixture of a dispersed and insoluble set of particles that are floating in another substance. These complex systems have been studied extensively due to their importance for both scientific and industrial research [928]. These particles can be very different in size when occurred in gas (e.g., aerosols), solid, or liquid [929,930]. In this review paper, however, the focus will be on solid particles dispersed in a liquid wherein understanding the rheological properties to conduct optimized manufacturing is crucial. In terms of scale, the emphasis will be on particles larger than molecular dimension and small enough to observe colloidal forces and thermal variability ($0.1 - 2\mu m$). This range of size can be found in a variety of applications, such as liquid-gel production, proteins in liquid environments [931], drug delivery [932], battery [933], rheological characteristics [934,935], subsurface energy [936], clay sediments [937,938], blood cells and biological systems [880,923,939–941], and nanotechnology [942,943]. An example of a colloidal system in the presence of clogging is shown in Fig. 89.

Various experimental methods, such as scattering methods (X-ray, neutron, and laser) [945–948], pulsed-field-gradient nuclear magnetic resonance [949,950], confocal microscopy [951–954], rheology techniques [930,955–957], and fluorescence recovery after photobleaching, have been used to observe the behaviors of colloidal systems. These methods, as discussed in other sections, cannot provide the dynamics of each individual particle and, thus, interpreting the results is not straightforward. On the other hand,

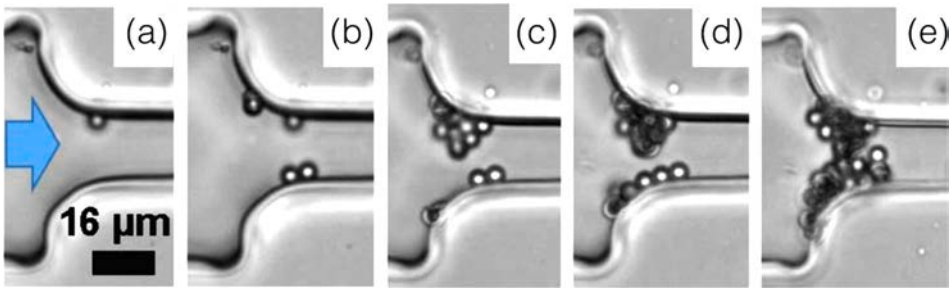

Fig. 89. Colloidal transportation and aggregation resulting in clog formation. The images are recorded at 3, 5, 10, and 36 min [944].

computational methods have been used widely with more detailed information about the behavior of colloidal systems. Most of the utilized methods are similar to those discussed earlier with some additional techniques developed for these problems in the sense that they are either particle-based (Lagrangian) or explicit (the solvent is considered as a separate phase)/implicit (colloid-colloid interactions). For instance, LBM [915,958–960], Eulerian methods [961], FEM, FDM, VOF, and boundary element method have all been used widely for the modeling of such systems [962–966]. It should be noted that the meshless methods (e.g., SPH, FPM, …), as all described before, have not been used extensively for colloidal problems. Among them, however, DEM is used broadly. Aside from these methods, there are various other methods that are popular for modeling colloidal systems. These methods include Fast Lubrication Dynamics (FLD) based on Stokesian dynamics [967–970], multi-particle collision dynamics [971–973], and dissipative particle dynamics [974].

Characterization of colloidal models was studied extensively by Derjahuin and Landau [975], and also Verwey and Overbeek [976], which eventually resulted in the Derjaguin–Landau–Verwey–Overbeek (DLVO) theory. The DLVO theory can explain the colloidal stability using which the colloidal particles and their behaviors can be characterized. This method was later extended to deal with multi-particle systems [977–979]. In this paper, we briefly review the DLVO algorithm within the DEM framework. Given this, Newton's equations of motion for particle i can be presented by:

$$m_i\frac{dv_i}{dt}=\sum_j f_{ij}^{c}+\sum_k f_{ij}^{nc}+f_{ij}^{f-p}+f_{ij}^{g}, \tag{194}$$

$$I_i\frac{d\omega_i}{dt}=\sum_j T_{ij}. \tag{195}$$

where the first equation presents the transitional motion of particle i with the mass of m_i and transitional velocity (v_i), which has contact force (f_{ij}^{c}) with particle j as a collision occurs. Besides, particle i has non-contact force (f_{ij}^{nc}) exerting from particle k, which in this project it refers to DLVO forces as they are considered as non-contact forces. The effect of fluid and gravity are also considered in fluid-particle force (f_{ij}^{f-p}) and gravitational force (f_{ij}^{g}), respectively. In the second equation, the rotational motion of the particle i when it has a collision with particle j is presented. Here, I_i and ω_i are rotational inertia and velocity, respectively. T_{ij} is the torque acting on particle i because of the collision with either wall boundaries or particle j.

The total contact force ($\overrightarrow{f}_{ij}^{c}$) has three components, tangential ($\overrightarrow{f}_{ij}^{t}$), normal force ($\overrightarrow{f}_{ij}^{n}$), and the DLVO forces ($\overrightarrow{f}_{ij}^{DLVO}$):

$$\overrightarrow{f}_{ij}^{c}=\overrightarrow{f}_{ij}^{n}+\overrightarrow{f}_{ij}^{t}+\overrightarrow{f}_{ij}^{DLVO}. \tag{196}$$

To make the above equations suitable for the purpose of calculating the forces and displacements between particles, Hooke's model can be used:

$$\overrightarrow{f}_{ij}^{n}=-\left(k_n\delta\overrightarrow{u}_n+\alpha_n\left(\overrightarrow{v}_{ij}.\overrightarrow{u}_n\right)\overrightarrow{u}_n\right), \tag{197}$$

$$\delta=r_i+r_j-R, \tag{198}$$

where R is the distance between particles' centers. This equation shows the force in the normal direction, where k_n is the normal spring stiffness, δ is particles overlap, $\overrightarrow{u}_n$ is the unit vector of normal force, α_n is normal damping, and $\overrightarrow{v}_{ij}$ is the relative velocity of in-contact particles i and j. Also, the tangential shear force is applied when particles have collisions with each other. To determine the tangential force, the Coulomb friction can be used:

$$\overrightarrow{f}_{ij}^{t}=\min\left\{\left(-k_t\delta+\alpha_t\left(\overrightarrow{v}_{ij}\times\overrightarrow{u}_n\right)\times\overrightarrow{u}_n\right),\mu\left|\overrightarrow{f}_{ij}^{n}\right|\overrightarrow{u}_t\right\}, \tag{199}$$

where k_t is tangential spring's stiffness, α_t and μ are tangential damping and friction coefficients, respectively, and $\overrightarrow{u}_t$ is the unit vector of tangential force.

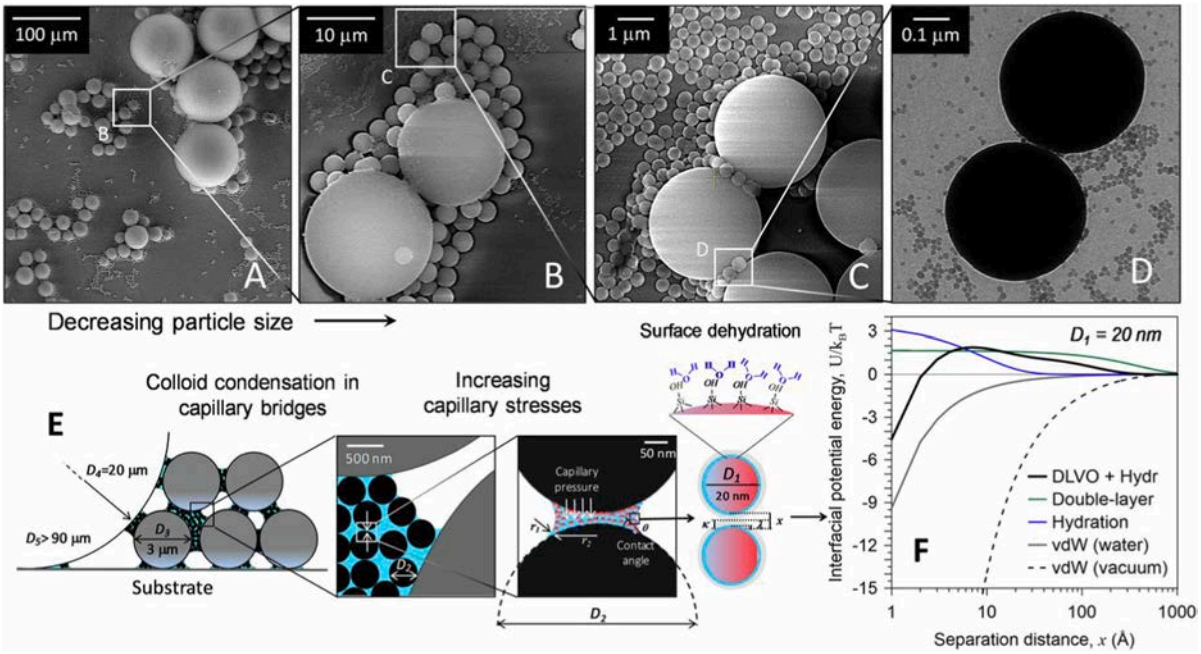

Fig. 90. Multiscale features in a polydisperse colloidal system where a combination of silica particles (90, 20, 3, and 0.4 µm) and silica nanoparticles (20 nm) can be observed (A-D). The effect of the capillary force in keeping the particles together is shown in (E). By dehydrating the surface of particles, the van der Waals (vdW) attraction between particles becomes more pronounced. A comparison of the potential energy for two particles with a size of 20 nm is also shown in (F) [981].

Aside from the above forces, the DLVO forces can be added to those particles that are in contact or close enough ($R \leq r_{cutoff}$). Therefore, the DLVO forces should be considered in both in-contact and non-contact cases. The DLVO forces contain two forces, the van der Waals and the Electric Double Layers, in which the former is an attractive force while the latter is a repulsive force. Formulations for both in-contact and non-contact DLVO forces are the same.

The van der Waals force on particle i is given by [980]:

$$\overrightarrow{f}_{vdW} = -\frac{A\lambda r(\lambda + 22.22h)}{6h^2(\lambda + 11.11h)^2}\widehat{e}_y + \sum_{j=1}^{N} -\frac{A_j\lambda r(\lambda + 22.22h_j)}{6h_j^2(\lambda + 11.11h_j)^2}\widehat{e}_{ij}, \tag{200}$$

where A and A_j are the Hamaker constants for particle–wall and particle–particle, respectively, λ is London retardation wavelength, r is particle radius, and h and h_j are particle–wall and particles i and j separation distance, respectively. Also, $\widehat{e}_y$ is the unit vector which is perpendicular to the wall, and $\widehat{e}_{ij}$ is the normal unit vector between two particles.

Furthermore, the Electric Double Layer (EDL) force on particle i can be calculated using [980]:

$$\overrightarrow{f}_{EDL} = 32\pi\varepsilon\kappa r\left(\frac{kT}{e}\right)^2\left\{2\gamma_p\gamma_w exp(-\kappa h)\widehat{e}_y + {\gamma_p}^2\sum_{j=1}^{N} exp(-\kappa h)\widehat{e}_{ij}\right\}, \tag{201}$$

where

$$\gamma_p = \tanh\left(\frac{\eta e\zeta_p}{4KT}\right), \tag{202}$$

$$\gamma_p = \tanh\left(\frac{\eta e\zeta_w}{4KT}\right), \tag{203}$$

wherein ε is medium's permittivity, kT is the thermal energy, e is the fundamental electronic charge, η is the valency of the symmetric electrolyte, and ζ_p and ζ_w are particle and wall zeta (surface) potentials, respectively. κ (Debye parameter) is the inverse of EDL thickness and is described as:

$$\kappa = \sqrt{\frac{2\eta^2 e^2 n_\infty}{\varepsilon kT}}, \tag{204}$$

where n_∞ is the bulk ionic concentration. An example is shown in Fig. 90 in which different forces in a colloidal system are demonstrated. A comprehensive comparison between various methods for colloidal systems can be found elsewhere [928].

4. Outlook and further discussion

Despite all the discussed topics and progresses, there are many topics in GM that still cannot be explained. One of the future paths that can be followed is extending the application of GM to more problems using which predictive models can be constructed. This progress requires developing multiphysics and realistic models implemented in an efficient framework to make such algorithms feasible and practical. At the same time, the available methods for GM are often developed for a limited class of modeling. For example, the quasi-static condition can only be found in rare and ideal cases. In this review paper, we extensively reviewed the fluid-like and solid-like characteristics of GM, but the gas-like was not discussed greatly due to a lack of development in this field. GM, indeed, can be thought of as gas when the free space is significant. These behaviors are well understood at a small scale, but their statistical modeling still requires more research. One of the interesting features of this particular state is the effect of small perturbation which can cause severe homogenization in the system. Similarly, the effects of fluid in GM are either not fully considered or a significant simplification has been considered. The non-adhesion assumption is one such generalization. Furthermore, granular flows and GM are often found in dense and multiphysics environments, such as hoppers, geo-materials, and batteries, and, thus, including the effect of fluid is critical.

Another important topic that requires more attention is a better connection between the microscopic and macroscopic properties and the existing forces. This connection can be made through the stress tensor. A particle, with complex morphology, represents a very complex force distribution which is averaged to calculate the stress. Thus, this procedure may not represent the original complexity associated with the force distribution. This problem becomes more important when the stress field is estimated using the continuum scale methods. GM, due to their multiscale nature, have been characterized extensively at distinct scales but their connection is what still requires further research and experiment. Probably, understanding the force chain through which the grains are connected to their bulk behaviors, in the presence of the above complexities, can help to better understand such materials. The force chain itself, as a separate topic, is one of the current and future challenges in GM which still requires more research on conducting accurate and time-resolved experiments in 3D. This problem, as mentioned earlier, has been studied using various experimental techniques in 2D systems but they are very different from actual GM samples in 3D. Studying the force chain in 3D can help with stick–slip and intermittent flow, GM flows, identifying hot spots in terms of stress concentration, and how creep flows occur in natural environments. More advanced imaging and data collection equipment need to be developed to provide 3D images at the sub-second resolution if an accurate picture of the force chain is demanded.

Natural and synthetic particles are mostly irregular with a wide range of size distribution as well as different compositions, roughness, and stiffness. Such particles, as discussed, are often considered spherical or multispherical objects. This approach might work for particles with smooth surfaces. This approach does not, however, reproduce the behavior of particles with sharp edges and very angular morphology, which are widely available in nature [437]. Further investigation is required to bring this important physical characteristic into the current computational methods. Some of these methods were reviewed in this paper, but their applications are limited to small granular systems and are often used to inform the constitutive models. One must carefully convey all the contact points, which can be multiple points in irregular morphologies, to the surrounding particles. Their applications can be more complicated and computationally expensive when other important physics (e.g., fluid, heat, …) is deemed to be integrated. More research is also needed when a low volume of fluid is accompanied by irregular particles. Evaluating the capillary forces can be challenging in this case since one must carefully consider the effect of a multiphase fluid system, which results in a three-phase system (particle, fluid, and gas/air).

Many sophisticated experimental methods for observing the behavior of GM in dry and wet conditions and various scales were reviewed. More precise experiments for studying time-lapsed particle tracking and connecting them to macroscopic behaviors are required. For example, we have a clear picture of the breaking of particles, but it will be more informative to continuously follow the particles from the onset of stress buildup and full breakage. By linking this observation to the relevant computational modeling described above one can expect to paint a more accurate picture of force chain, particle morphology, breakage, and other important physics. Such experiments allow us to better understand the flow regimes between quasi-static and rapid flows. In fact, more work is needed to understand the rheophysics of GM and connect the macroscopic behaviors to microscopic complexities. This can be extended to jamming as well. All such experiments, which can be referred to as 4D tests, conducted in multiphysics environments (e.g., THMC) can provide invaluable insight into the GM. Overall, the rich knowledge in GM can be extended to other problems related to climate change and also environmental modelings, such as ice rubbing, ground deformations/earthquakes, and infrastructure management for urban and city environments.

By increasing the resolution of computational and experimental modeling, we will be dealing with large datasets which require advanced data mining techniques to extract meaningful patterns and features from them. Some research has been conducted, for example, to extract the trends and patterns from the contact networks or other physical properties [982–987]. These methods aim to connect the structural topology, mechanics, and solid architecture to provide insights into the physical and mechanical properties. Recently, machine learning and deep-layered models have also been used to estimate the flow and physical properties of complex GM [988–992]. These methods still need further research to deal with complex 3D and dynamic properties. Furthermore, machine learning techniques can be applied to predict the behaviors of GM such as their flowability, jamming transition, and also deformation under different viscous conditions. Such a method can also be used to design GM with specific properties (e.g., strength, and thermal conductivity). Alternatively, one can optimize the processes associated with GM (e.g., packing, mixing, and compaction). Aside from the above future work, machine learning can still be used to analyze the images collected during different experiments and sensor data to dynamically monitor the behaviors of GM in real-time.

In terms of applications, more work is needed to better optimize binder jetting where a powder bed is selectively bonded by a liquid binder in 3D printing. For example, one can develop a more efficient method for tailoring powder packing density so that 3D printing

can be improved with respect to enhancing the quality and reducing the defects. Furthermore, advanced ceramic parts with controlled porosity can be produced for applications in bone implants and filters. In a similar line, novel granular particles with higher strength and thermal conductivity can also be built for 3D printing applications. Eventually, complex metal structures can be produced in binder jetting with higher accuracy for applications such as aerospace and biomedical devices.

Another field that can benefit from GM is additive manufacturing, in particular selective laser sintering/melting (SLS/SLM) where a laser is used to selectively melt or sinter GM to create customized pharmaceuticals with accurate dosages and release rates. GM can also be used to fabricate complex metal parts such as titanium and aluminum or make new composite materials such as ceramic and polymers for electronic and energy applications. In this broad and new field, GM can be used extensively for printing multi-material whereas the current methods are limited to a single type of material. Furthermore, one can explore sustainable and biodegradable materials (e.g., cellulose and lignin) for building new materials. At the same time, new in-situ imaging techniques can be developed for GM in these applications. It should also be noted that we still need more advanced modeling techniques to simulate the interactions between GM and the printing process in particular when complex multiscale printing is used.

GM also plays a significant role in solid-state batteries for making high-energy–density storage systems. GM with tailored morphologies and surface chemistries can be designed to improve interfacial contact and facilitate ion transport. Thus, some techniques developed in GM can potentially be used in this area as well. One example can be integrating the strength of machine learning methods and GM properties and morphologies to predict and screen the performance of solid-state batteries. Furthermore, the reviewed concepts in this paper for large-scale GM can be used to scale-up and manufacture large-scale solid-state batteries with high performance and low cost. As can be seen, many of the concepts and findings in GM can be used directly in such applications.

Declaration of Competing Interest.

The authors declare that they have no known competing financial interests or personal relationships that could have appeared to influence the work reported in this paper.

Declaration of Competing Interest

The authors declare that they have no known competing financial interests or personal relationships that could have appeared to influence the work reported in this paper.

Data availability

No data was used for the research described in the article.

Acknowledgments

The author is grateful to many colleagues, friends, and mentors for the very fruitful discussions over the past years. The author would like to thank his former Ph.D. students, Samuel Fagbemi and Xiaoming Zhang, who helped with this manuscript. This review paper is supported by several projects from the US National Science Foundation (Grant #CMMI-2000966), the National Institutes of Health (NIH, Grant # P20GM103432), the Department of Energy (DOE), and the National Aeronautics and Space Administration (NASA, Grant #80NSSC19M0061).

References

[1] Knowlton TM, Klinzing GE, Yang WC, Carson JW. The importance of storage, transfer, and collection. Chem Eng Progress; (United States) n.d.
[2] Campbell CS. Granular material flows – An overview. Powder Technol 2006;162:208–29. https://doi.org/10.1016/J.POWTEC.2005.12.008.
[3] Jaeger HM, Nagel SR, Behringer RP. Granular solids, liquids, and gases. Rev Mod Phys 1996;68:1259–73. https://doi.org/10.1103/RevModPhys.68.1259.
[4] Duran J. Sands, Powders, and Grains 2000. https://doi.org/10.1007/978-1-4612-0499-2.
[5] Jaeger HM, Liu C, Nagel SR. Relaxation at the Angle of Repose. Phys Rev Lett 1989;62:40. https://doi.org/10.1103/PhysRevLett.62.40.
[6] Duke TAJ, Barker GC, Mehta A. A Monte Carlo Study of Granular Relaxation. EPL (Europhysics Lett 1990;13:19.. https://doi.org/10.1209/0295-5075/13/1/004.
[7] Boguslavskii Y, Drabkin S. The kinetics of powder settlement caused by low level vibration and elastic stresses. Phys A Stat Mech Its Appl 1995;222:75–86. https://doi.org/10.1016/0378-4371(95)00254-5.
[8] Knight JB, Fandrich CG, Lau CN, Jaeger HM, Nagel SR. Density relaxation in a vibrated granular material. Phys Rev E 1995;51:3957. https://doi.org/10.1103/PhysRevE.51.3957.
[9] Laroche C, Douady S, Fauve S. Convective flow of granular masses under vertical vibrations Convective flow of granular masses under vertical vibra-tions. J Phys 1989;50. https://doi.org/10.1051/jphys:019890050070699001.
[10] Douady S, Fauve S, Laroche C. Subharmonic Instabilities and Defects in a Granular Layer under Vertical Vibrations. EPL (Europhysics Lett 1989;8:621.. https://doi.org/10.1209/0295-5075/8/7/007.
[11] Zik O, Stavans J. Self-Diffusion in Granular Flows. EPL (Europhysics Lett 1991;16:255.. https://doi.org/10.1209/0295-5075/16/3/006.
[12] Melo F, Umbanhowar P, Swinney HL. Transition to parametric wave patterns in a vertically oscillated granular layer. Phys Rev Lett 1994;72:172. https://doi.org/10.1103/PhysRevLett.72.172.
[13] Pak HK, Behringer RP. Surface waves in vertically vibrated granular materials. Phys Rev Lett 1993;71:1832. https://doi.org/10.1103/PhysRevLett.71.1832.
[14] Pak HK, Van DE, Behringer RP. Effects of Ambient Gases on Granular Materials under Vertical Vibration. Phys Rev Lett 1995;74:4643. https://doi.org/10.1103/PhysRevLett.74.4643.
[15] Clauss W, Kittel A, Rau U, Parisi J, Peinke J, Huebener RP. Self-Organized Critical Behaviour in the Low-Temperature Impact Ionization Breakdown of p-Ge. EPL (Europhysics Lett 1990;12:423. https://doi.org/10.1209/0295-5075/12/5/008.
[16] Carlson JM, Langer JS, Shaw BE. Dynamics of earthquake faults. Rev Mod Phys 1994;66:657. https://doi.org/10.1103/RevModPhys.66.657.
[17] Dorostkar O, Carmeliet J. Potential Energy as Metric for Understanding Stick-Slip Dynamics in Sheared Granular Fault Gouge: A Coupled CFD–DEM Study. Rock Mech Rock Eng 2018;51:3281–94. https://doi.org/10.1007/s00603-018-1457-6.

[18] G r, al d, s g.. From static to kinetic friction in confined liquid films. Science 1994;263:1741–4. https://doi.org/10.1126/SCIENCE.263.5154.1741.
[19] Radjai F, Evesque P, Bideau D, Roux S. Stick-slip dynamics of a one-dimensional array of particles. Phys Rev E 1995;52:5555. https://doi.org/10.1103/PhysRevE.52.5555.
[20] Sun Q, Wang G, Hu K. Some open problems in granular matter mechanics. Prog Nat Sci 2009;19:523–9. https://doi.org/10.1016/J.PNSC.2008.06.023.
[21] Baule A, Morone F, Herrmann HJ, Makse HA. Edwards statistical mechanics for jammed granular matter. Rev Mod Phys 2018;90:015006. https://doi.org/10.1103/REVMODPHYS.90.015006/FIGURES/25/MEDIUM.
[22] Behringer RP, Chakraborty B. The physics of jamming for granular materials: a review. Reports Prog Phys 2019;82:012601. https://doi.org/10.1088/1361-6633/aadc3c.
[23] Liu AJ, Nagel SR. The jamming transition and the marginally jammed solid. Annu Rev Condens Matter Phys 2010;1:347–69. https://doi.org/10.1146/annurev-conmatphys-070909-104045.
[24] Zhong W, Yu A, Liu X, Tong Z, Zhang H. DEM/CFD-DEM Modelling of Non-spherical Particulate Systems: Theoretical Developments and Applications 2016; vol. 302. https://doi.org/10.1016/J.POWTEC.2016.07.010.
[25] Juanes R, Meng Y, Primkulov BK. Multiphase flow and granular mechanics. Phys Rev Fluids 2020;5:110516. https://doi.org/10.1103/PHYSREVFLUIDS.5.110516/FIGURES/13/MEDIUM.
[26] Mitarai N, Nori F. Wet granular materials. Adv Phys 2006;55:1–45. https://doi.org/10.1080/00018730600626065.
[27] Radjai F, Roux J-N, Daouadji A. Modeling Granular Materials: Century-Long Research across Scales. J Eng Mech 2017;143:04017002. https://doi.org/10.1061/(ASCE)EM.1943-7889.0001196.
[28] Fu Y, Wang L, Tumay TM, Li Q. Quantification and Simulation of Particle Kinematics and Local Strains in Granular Materials Using X-Ray Tomography Imaging and Discrete-Element Method. J Eng Mech 2008:143–54. https://doi.org/10.1061/(ASCE)0733-9399(2008)134.
[29] Oda M. Initial fabrics and their relations to mechanical properties of granular material. Soils Found 1972;12:17–36.
[30] Kanatani K-I. Stereological determination of structural anisotropy. Int J Eng Sci 1984;22:531–46.
[31] Hurley R. Unraveling Force Chains and Failure in Granular Materials | LDRD Annual Report 2017. https://ldrd-annual.llnl.gov/archives/ldrd-annual-2017/earth/17-LW-009 (accessed October 29, 2021).
[32] Gajjar P, Johnson CG, Carr J, Chrispeels K, Gray JMNT, Withers PJ. Size segregation of irregular granular materials captured by time-resolved 3D imaging. Sci Reports 2021.1–6.;2021(111):11. https://doi.org/10.1038/s41598-021-87280-1.
[33] Ketcham RA. Carlson WD. Acquisition, optimization and interpretation of X-ray computed tomographic imagery : applications to the geosciences 2001;27:381–400.
[34] Eastwood DS, Bradley RS, Tariq F, Cooper SJ, Taiwo OO, Gelb J, et al. The application of phase contrast X-ray techniques for imaging Li-ion battery electrodes. Nucl Instruments Methods Phys Res Sect B Beam Interact with Mater Atoms 2014;324:118–23. https://doi.org/10.1016/j.nimb.2013.08.066.
[35] Kashkooli AG, Farhad S, Lee DU, Feng K, Litster S, Babu SK, et al. Multiscale modeling of lithium-ion battery electrodes based on nano-scale X-ray computed tomography. J Power Sources 2016;307:496–509. https://doi.org/10.1016/j.jpowsour.2015.12.134.
[36] Reimann J, Vicente J, Brun E, Ferrero C, Gan Y, Rack A. X-ray tomography investigations of mono-sized sphere packing structures in cylindrical containers. Powder Technol 2017;318:471–83. https://doi.org/10.1016/j.powtec.2017.05.033.
[37] Li T, Lu X, Wang B, Wu Z, Li K, Brett DJL, et al. X-ray tomography-assisted study of a phase inversion process in ceramic hollow fiber systems – Towards practical structural design. J Memb Sci 2017;528:24–33. https://doi.org/10.1016/j.memsci.2017.01.004.
[38] Komini Babu S, Mohamed AI, Whitacre JF, Litster S. Multiple imaging mode X-ray computed tomography for distinguishing active and inactive phases in lithium-ion battery cathodes. J Power Sources 2015;283:314–9. https://doi.org/10.1016/j.jpowsour.2015.02.086.
[39] Fries L, Antonyuk S, Heinrich S, Dopfer D, Palzer S. Collision dynamics in fluidised bed granulators: A DEM-CFD study. Chem Eng Sci 2013;86:108–23. https://doi.org/10.1016/j.ces.2012.06.026.
[40] Alshibli K. Alshibli Archives of Granular Materials n.d. https://alshibli.utk.edu/ (accessed October 29, 2021).
[41] Sasaya T, Sunaguchi N, Hyodo K, Zeniya T, Yuasa T. Multi-pinhole fluorescent x-ray computed tomography for molecular imaging. Sci Rep 2017;7:2–13. https://doi.org/10.1038/s41598-017-05179-2.
[42] De Jonge MD, Vogt S. Hard X-ray fluorescence tomography-an emerging tool for structural visualization. Curr Opin Struct Biol 2010;20:606–14. https://doi.org/10.1016/j.sbi.2010.09.002.
[43] Wildenschild D, Sheppard AP. X-ray imaging and analysis techniques for quantifying pore-scale structure and processes in subsurface porous medium systems. Adv Water Resour 2013;51:217–46.
[44] Lombi E, de Jonge MD, Donner E, Kopittke PM, Howard DL, Kirkham R, et al. Fast X-ray fluorescence microtomography of hydrated biological samples. PLoS One 2011;6:4–8. https://doi.org/10.1371/journal.pone.0020626.
[45] Dewanckele J, Cnudde V, Boone M, Van LD, De WY, Pieters K, et al. Integration of X-ray micro tomography and fluorescence for applications on natural building stones. J Phys Conf Ser 2009;186:12082. https://doi.org/10.1088/1742-6596/186/1/012082.
[46] Laforce B, Masschaele B, Boone MN, Schaubroeck D, Dierick M, Vekemans B, et al. Integrated Three-Dimensional Microanalysis Combining X-Ray Microtomography and X-Ray Fluorescence Methodologies. Anal Chem 2017;89:10617–24. https://doi.org/10.1021/acs.analchem.7b03205.
[47] Pfeiffer S, Florio K, Makowska M, Ferreira Sanchez D, Van Swygenhoven H, Aneziris CG, et al. Iron Oxide Doped Spray Dried Aluminum Oxide Granules for Selective Laser Sintering and Melting of Ceramic Parts. Adv Eng Mater 2019;21:1–14. https://doi.org/10.1002/adem.201801351.
[48] Liu J, Jiang X, Zhang Y, Zhang H, Luo L, Wang X. Size segregation behavior of heavy metals in superfine pulverized coal using synchrotron radiation-induced X-ray fluorescence. Fuel 2016;181:1081–8. https://doi.org/10.1016/j.fuel.2016.04.115.
[49] Pfeiffer S, Makowska M, Florio K, Sanchez DF, Marone F, Zhang X, et al. Selective laser melting of thermal pre-treated METAL oxide doped aluminum oxide granules. Open Ceram 2020;100007. https://doi.org/10.1016/j.oceram.2020.100007.
[50] Miao J, Förster F, Levi O. Equally sloped tomography with oversampling reconstruction. Phys Rev B 2005;72:52103.
[51] Graff CG, Sidky EY. Compressive sensing in medical imaging. Appl Opt 2015;54:C23. https://doi.org/10.1364/ao.54.000c23.
[52] Druckrey AM, Alshibli KA, Al-Raoush RI. 3D characterization of sand particle-to-particle contact and morphology. Comput Geotech 2016;74:26–35. https://doi.org/10.1016/j.compgeo.2015.12.014.
[53] Baruchel J, Buffiere J-Y, Cloetens P, Di Michiel M, Ferrie E, Ludwig W, et al. Advances in synchrotron radiation microtomography. Scr Mater 2006;55:41–6.
[54] Brunke O, Brockdorf K, Drews S, Müller B, Donath T, Herzen J, et al. Comparison between x-ray tube-based and synchrotron radiation-based μCT. Dev. X-ray Tomogr. VI, vol. 7078, International Society for Optics and Photonics; 2008, p. 70780U.
[55] Cnudde V, Boone MNN. High-resolution X-ray computed tomography in geosciences: A review of the current technology and applications. Elsevier 2013;123. https://doi.org/10.1016/j.earscirev.2013.04.003.
[56] Hasan A, Alshibli KA. Experimental assessment of 3D particle-to-particle interaction within sheared sand using synchrotron microtomography. Geotechnique 2010;60:369–79. https://doi.org/10.1680/geot.2010.60.5.369.
[57] Druckrey AM, Alshibli KA, 3D behavior of sand particles using X-ray synchrotron micro-tomography. Geo-Congress,. Geo-characterization Model. Sustain 2014;2014:2814–21.
[58] Betson M, Barker J, Barnes P, Atkinson TIM, Jupe A. Porosity Imaging in Porous Media Using Synchrotron Tomographic. Techniques 2004:203–14.
[59] Hall C, Barnes P, Cockcroft JK, Colston SL, Häusermann D, Jacques SDM, et al. Synchrotron energy-dispersive X-ray diffraction tomography. Nucl Instruments Methods Phys Res Sect B Beam Interact with Mater Atoms 1998;140:253–7.
[60] Al-Raoush RI, Willson CS. A pore-scale investigation of a multiphase porous media system. J Contam Hydrol 2005;77:67–89.
[61] Kim FH, Penumadu D, Hussey DS. Water distribution variation in partially saturated granular materials using neutron imaging. J Geotech Geoenvironmental Eng 2012;138:147–54.
[62] Kim FH, Penumadu D, Gregor J, Kardjilov N, Manke I. High-resolution neutron and X-ray imaging of granular materials. J Geotech Geoenvironmental Eng 2013;139:715–23. https://doi.org/10.1061/(ASCE)GT.1943-5606.0000809.

[63] Ehrichs EE, Jaeger HM, Karczmar GS, Knight JB, Kuperman VY, Nagel SR. Granular convection observed by magnetic resonance imaging. Science (80-) 1995;267:1632–4.
[64] Baldwin CA, Sederman AJ, Mantle MD, Alexander P, Gladden LF. Determination and Characterization of the Structure of a Pore Space from 3D Volume Images. J Colloid Interface Sci 1996;181:79–92. https://doi.org/10.1006/JCIS.1996.0358.
[65] Dijksman JA, Rietz F, Lorincz KA, Van Hecke M, Losert W. Invited Article: Refractive index matched scanning of dense granular materials. Rev Sci Instrum 2012;83. https://doi.org/10.1063/1.3674173.
[66] Altobelli SA, Caprihan A, Fukushima E, Nakagawa M, Givler RC. Multiphase Flow Studies by NMR with Application to Granular Flows in Joint DOE. NSF Work Flow Part Fluids 1991:34–40.
[67] Rao SJ, Bhatia SK, Khakhar DV. Axial transport of granular solids in rotating cylinders. Part 2: Experiments in a non-flow system. Powder Technol 1991;67:153–62.
[68] Nakagawa M. Axial segregation of granular flows in a horizontal rotating cylinder. Chem Eng Sci 1994;49:2540–4.
[69] Altobelli SA, Caprihan A, Cheng HA, Fukushima E, Nakagawa M, Wang LZ. Granular flow studies by NMR. Proc Jt DOE/NSF Work flow Part fluids 1993:233.
[70] Hill KM, Caprihan A, Kakalios J. Bulk segregation in rotated granular material measured by magnetic resonance imaging. Phys Rev Lett 1997;78. https://doi.org/10.1103/PhysRevLett.78.50.
[71] Porion P, Sommier N, Evesque P. Dynamics of mixing and segregation processes of grains in 3d blender by NMR imaging investigation. Europhys Lett 2000;50:319–25.
[72] Stannarius R. Magnetic resonance imaging of granular materials. Rev Sci Instrum 2017;88:051806. https://doi.org/10.1063/1.4983135.
[73] Thompson KE, Willson CS, Zhang W. Quantitative computer reconstruction of particulate materials from microtomography images. Powder Technol 2006;163:169–82.
[74] Al-Raoush R. Microstructure characterization of granular materials. Phys A Stat Mech Its Appl 2007;377:545–58.
[75] Cox MR, Budhu M. A practical approach to grain shape quantification. Eng Geol 2008;96:1–16.
[76] Alshibli KA, Druckrey AM, Al-Raoush RI, Weiskittel T, Lavrik NV. Quantifying morphology of sands using 3D imaging. J Mater Civ Eng 2015;27:4014275.
[77] Ashmawy AK, Sukumaran B, Hoang VV. Evaluating the Influence of Particle Shape on Liquefaction Behavior Using Discrete Element Modeling. Thirteen Int Offshore Polar Eng Conf Int Soc Offshore Polar Eng 2003:2003–5.
[78] Cundall PA, Strack ODL. Development of constitutive laws for soil using the distinct element method. SAE Prepr 1979;1:289–98.
[79] Dubois F, Jean M. The non smooth contact dynamic method: recent LMGC90 software developments and application. Anal Simul Contact Probl, Berlin/Heidelberg: Springer-Verlag 2006:375–8. https://doi.org/10.1007/3-540-31761-9_44.
[80] Tahmasebi P. Packing of discrete and irregular particles. Comput Geotech 2018;100:52–61. https://doi.org/10.1016/j.compgeo.2018.03.011.
[81] Tahmasebi P, Sahimi M. A Stochastic Multiscale Algorithm for Modeling Complex Granular Materials. Granul Matter 2018;20. https://doi.org/10.1007/s10035-018-0816-z.
[82] Tahmasebi P, Sahimi M, Andrade JE. Image-based modeling of granular porous media. Geophys Res Lett 2017;44. https://doi.org/10.1002/2017GL073938.
[83] Cho G-C-G-C-G-C, Dodds J, Santamarina JCC. Particle Shape Effects on Packing Density, Stiffness, and Strength: Natural and Crushed Sands. J Geotech Geoenvironmental Eng 2006;132:591–602. https://doi.org/10.1061/(ASCE)1090-0241(2006)132:5(591).
[84] Sahimi M, Tahmasebi P. Reconstruction, Optimization, and Design of Heterogeneous Materials and Media: Basic Principles, Computational Algorithms, and Applications. Phys Rep 2021. https://doi.org/10.1016/j.physrep.2021.09.003.
[85] Thomas PA, Bray JD. Capturing Nonspherical Shape of Granular Media with Disk Clusters. J Geotech Geoenvironmental Eng 1999;125:169–78. https://doi.org/10.1061/(ASCE)1090-0241(1999)125:3(169).
[86] Salot C, Gotteland P, Villard P. Influence of relative density on granular materials behavior: DEM simulations of triaxial tests. Granul Matter 2009;11:221–36. https://doi.org/10.1007/s10035-009-0138-2.
[87] M. Stahl HK, Stahl M, Konietzky H.. Discrete element simulation of ballast and gravel under special consideration of grain-shape, grain-size and relative density 2011;13:417–28. https://doi.org/10.1007/s10035-010-0239-y.
[88] Katagiri J, Matsushima T, Yamada Y, J. Katagiri TMYY.. Simple shear simulation of 3D irregularly-shaped particles by image-based DEM 2010;12:491–7. https://doi.org/10.1007/s10035-010-0207-6.
[89] Lu M, McDowell GR. The importance of modelling ballast particle shape in the discrete element method. Granul Matter 2006;9:69–80. https://doi.org/10.1007/s10035-006-0021-3.
[90] Jensen RP, Edil TB, Bosscher PJ, Plesha ME, Ben KN. Effect of Particle Shape on Interface Behavior of DEM-Simulated Granular Materials. Int J Geomech 2001;1:1–19. https://doi.org/10.1061/(ASCE)1532-3641(2001)1:1(1).
[91] Pournin L, Weber M, Tsukahara M, Ferrez J-A, Ramaioli M, Liebling TM. Three-dimensional distinct element simulation of spherocylinder crystallization. Granul Matter 2005;7:119–26. https://doi.org/10.1007/s10035-004-0188-4.
[92] Ng T-T. Particle shape effect on macro- and micro-behaviors of monodisperse ellipsoids. Int J Numer Anal Methods Geomech 2009;33:511–27. https://doi.org/10.1002/nag.732.
[93] Azéma E, Radjai F, Saussine G, E. Azema FRGS, Azéma E, Radjai F,, et al. Quasistatic rheology, force transmission and fabric properties of a packing of irregular polyhedral particles. Mech Mater 2009;41:729–41. https://doi.org/10.1016/j.mechmat.2009.01.021.
[94] Fu P, Dafalias YF, P. Fu YD, Fu P, Dafalias YF.. Fabric evolution within shear bands of granular materials and its relation to critical state theory. Int J Numer Anal Methods Geomech 2011;35:1918–48. https://doi.org/10.1002/nag.988.
[95] Azéma E, Radjaï F, Peyroux R, Saussine G, E. Azema FRRPGS. Force transmission in a packing of pentagonal particles 2007;76:011301.
[96] Houlsby GTT. Potential particles: a method for modelling non-circular particles in DEM. Comput Geotech 2009;36:953–9. https://doi.org/10.1016/j.compgeo.2009.03.001.
[97] Birgin EG, Lobato RD, Martínez JM. A nonlinear programming model with implicit variables for packing ellipsoids. J Glob Optim 2016.467–99.;2016(683):68. https://doi.org/10.1007/S10898-016-0483-8.
[98] Yuan Y, VanderWerf K, Shattuck MD, O'Hern CS. Jammed packings of 3D superellipsoids with tunable packing fraction, coordination number, and ordering. Soft Matter 2019;15:9751–61. https://doi.org/10.1039/C9SM01932D.
[99] Zhao S, Matthew Evans T, Zhou X. Random Packing of Tetrahedral Particles Using the Polyhedral and Multi-sphere Discrete Element Method. Springer Proc Phys 2016;188:91–9. https://doi.org/10.1007/978-981-10-1926-5_11.
[100] Tangri H, Guo YY, Curtis JSJS. Packing of cylindrical particles: DEM simulations and experimental measurements. Powder Technol 2017;317:72–82. https://doi.org/10.1016/J.POWTEC.2017.03.058.
[101] Zhuang X, Wang Q, Zhu H. Effective Properties of Composites with Periodic Random Packing of Ellipsoids. Mater 2017, Vol 10, Page 112 2017;10:112. https://doi.org/10.3390/MA10020112.
[102] Podlozhnyuk A, Pirker S, Kloss C. Efficient implementation of superquadric particles in Discrete Element Method within an open-source framework. Comput Part Mech 2016.101–18.;2016(41):4. https://doi.org/10.1007/S40571-016-0131-6.
[103] Cho G-C, Dodds J, Santamarina JC. Closure to "Particle Shape Effects on Packing Density, Stiffness, and Strength: Natural and Crushed Sands" by Gye-Chun Cho, Jake Dodds, and. J Carlos Santamarina J Geotech Geoenvironmental Eng 2007;133:1474. https://doi.org/10.1061/(ASCE)1090-0241(2007)133:11(1474).
[104] Wadell H. Volume, Shape, and Roundness of Rock Particles. J Geol 1932;40:443–51. https://doi.org/10.1086/623964.
[105] Krumbein WC. Measurement and geological significance of shape and roundness of sedimentary particles. J Sediment Res 1941;11:64–72. https://doi.org/10.1306/D42690F3-2B26-11D7-8648000102C1865D.
[106] Powers MC. A new roundness scale for sedimentary particles. J Sediment Res 1953;23:117–9. https://doi.org/10.1306/D4269567-2B26-11D7-8648000102C1865D.

[107] Tillemans H-J, Herrmann HJ. Simulating deformations of granular solids under shear. Phys A Stat Mech Its Appl 1995;217:261–88. https://doi.org/10.1016/0378-4371(95)00111-J.
[108] Galindo-Torres SA, Pedroso DM, S.-A. Galindo-Torres D-MP, Galindo-Torres SA, Pedroso DM. Molecular dynamics simulations of complex-shaped particles using Voronoi-based spheropolyhedra. Phys Rev E 2010;81:061303. https://doi.org/10.1103/PhysRevE.81.061303.
[109] Mollon G, Zhao J. Fourier–Voronoi-based generation of realistic samples for discrete modelling of granular materials. Granul Matter 2012;14:621–38. https://doi.org/10.1007/s10035-012-0356-x.
[110] Bowman ET, Soga K, Drummond W. Particle shape characterisation using Fourier descriptor analysis. Géotechnique 2001;51:545–54. https://doi.org/10.1680/geot.2001.51.6.545.
[111] Garboczi EJ. Three-dimensional mathematical analysis of particle shape using X-ray tomography and spherical harmonics: Application to aggregates used in concrete. Cem Concr Res 2002;32:1621–38. https://doi.org/10.1016/S0008-8846(02)00836-0.
[112] Mollon G, Zhao J. Generating realistic 3D sand particles using Fourier descriptors. Granul Matter 2013;15:95–108. https://doi.org/10.1007/s10035-012-0380-x.
[113] Xu T, Li M. Topological and statistical properties of a constrained Voronoi tessellation. Philos Mag 2009;89:349–74. https://doi.org/10.1080/14786430802647065.
[114] Gross D, Li M. Constructing microstructures of poly- and nanocrystalline materials for numerical modeling and simulation. Appl Phys Lett 2002;80:746–8. https://doi.org/10.1063/1.1432448.
[115] Mollon G, Zhao J. 3D generation of realistic granular samples based on random fields theory and Fourier shape descriptors. Comput Methods Appl Mech Eng 2014;279:46–65. https://doi.org/10.1016/J.CMA.2014.06.022.
[116] Jerves AX, Kawamoto RY, Andrade JE. A geometry-based algorithm for cloning real grains. Granul Matter 2017;19:30. https://doi.org/10.1007/s10035-017-0716-7.
[117] Wadell H. Volume, shape, and roundness of quartz particles. J Geol 1935;43:250–80.
[118] Rechenmacher A, Finno R. Digital Image Correlation to Evaluate Shear Banding in Dilative Sands. Geotech Test J 2004;27:10864. https://doi.org/10.1520/GTJ11263J.
[119] Tahmasebi P, Sahimi M, Kohanpur AH, Valocchi A. Pore-scale simulation of flow of CO2 and brine in reconstructed and actual 3D rock cores. J Pet Sci Eng 2017;155:21–33. https://doi.org/10.1016/j.petrol.2016.12.031.
[120] Hall SA, Bornert M, Desrues J, Pannier Y, Lenoir N, Viggiani G, et al. Discrete and continuum analysis of localised deformation in sand using X-ray μCT and volumetric digital image correlation. Geotechnique 2010;60:315–22.
[121] Alshibli KA, Hasan A. Spatial variation of void ratio and shear band thickness in sand using X-ray computed tomography. Géotechnique 2008;58:249–57. https://doi.org/10.1680/geot.2008.58.4.249.
[122] Andò E, Hall SA, Viggiani G, Desrues J, Bésuelle P. Grain-scale experimental investigation of localised deformation in sand: a discrete particle tracking approach. Acta Geotech 2012;7:1–13. https://doi.org/10.1007/s11440-011-0151-6.
[123] Yeong CLY, Torquato S. Reconstructing random media. Phys Rev E 1998;57:495–506. https://doi.org/10.1103/PhysRevE.57.495.
[124] Tahmasebi P. Accurate modeling and evaluation of microstructures in complex materials. Phys Rev E 2018;97:023307. https://doi.org/10.1103/PhysRevE.97.023307.
[125] Yeong CLYY, Torquato S. Reconstructing random media. II Three-dimensional media from two-dimensional cuts 1998;58:224–33. https://doi.org/10.1103/PhysRevE.58.224.
[126] Jiao Y, Stillinger FH, Torquato S. A superior descriptor of random textures and its predictive capacity. Proc Natl Acad Sci U S A 2009;106:17634–9. https://doi.org/10.1073/pnas.0905919106.
[127] Zachary CE, Torquato S. Improved reconstructions of random media using dilation and erosion processes. Phys Rev E 2011;84:056102. https://doi.org/10.1103/PhysRevE.84.056102.
[128] Guo EY, Chawla N, Jing T, Torquato S, Jiao Y. Accurate modeling and reconstruction of three-dimensional percolating filamentary microstructures from two-dimensional micrographs via dilation-erosion method. Mater Charact 2014;89:33–42. https://doi.org/10.1016/j.matchar.2013.12.011.
[129] Jiao Y, Stillinger FH, Torquato S. Modeling heterogeneous materials via two-point correlation functions. II. Algorithmic details and applications. Phys Rev E 2008;77:031135. https://doi.org/10.1103/PhysRevE.77.031135.
[130] Tahmasebi P, Sahimi M. Cross-correlation function for accurate reconstruction of heterogeneous media. Phys Rev Lett 2013;110:078002. https://doi.org/10.1103/PhysRevLett.110.078002.
[131] Da Pra A, Pontiggia M, Corradi C, Caers J, Tahmasebi P, Constraining 3D sedimentological models to well and seismic using pattern-based multiple-point geostatistics. 77th EAGE Conf. Exhib.. Earth Sci. Energy Environ 2015;2015. https://doi.org/10.3997/2214-4609.201412677.
[132] Tahmasebi P, Sahimi M. Reconstruction of three-dimensional porous media using a single thin section. Phys Rev E - Stat Nonlinear, Soft Matter Phys 2012;85:1–13. https://doi.org/10.1103/PhysRevE.85.066709.
[133] Tahmasebi P, Hezarkhani A, Sahimi M. Multiple-point geostatistical modeling based on the cross-correlation functions. Comput Geosci 2012;16:779–97. https://doi.org/10.1007/s10596-012-9287-1.
[134] Tahmasebi P, Sahimi M, Caers J. MS-CCSIM: Accelerating pattern-based geostatistical simulation of categorical variables using a multi-scale search in fourier space. Comput Geosci 2014;67:75–88. https://doi.org/10.1016/j.cageo.2014.03.009.
[135] Tahmasebi P, Sahimi M. Reconstruction of nonstationary disordered materials and media: Watershed transform and cross-correlation function. Phys Rev E - Stat Physics, Plasmas, Fluids, Relat Interdiscip Top 2015;91:032401. https://doi.org/10.1103/PhysRevE.91.032401.
[136] Dijksman JA, Brodu N, Behringer RP. Refractive index matched scanning and detection of soft particles. Rev Sci Instrum 2017;88:051807. https://doi.org/10.1063/1.4983047.
[137] Vlahinić I, Andò E, Viggiani G, Andrade JE. Towards a more accurate characterization of granular media: extracting quantitative descriptors from tomographic images. Granul Matter 2014;16:9–21. https://doi.org/10.1007/s10035-013-0460-6.
[138] Amon A, Born P, Daniels KE, Dijksman JA, Huang K, Parker D, et al. Preface: Focus on imaging methods in granular physics. Rev Sci Instrum 2017;88. https://doi.org/10.1063/1.4983052.
[139] Cheng X, Lechman JB, Fernandez-Barbero A, Grest GS, Jaeger HM, Karczmar GS, et al. Three-dimensional shear in granular flow. Phys Rev Lett 2006;96. https://doi.org/10.1103/PhysRevLett.96.038001.
[140] Börzsönyi T, Unger T, Szabó B, Wegner S, Angenstein F, Stannarius R. Reflection and exclusion of shear zones in inhomogeneous granular materials. Soft Matter 2011;7:8330–6.
[141] Ren X, Stapf S, Blümich B. Magnetic resonance visualisation of flow and pore structure in packed beds with low aspect ratio. Chem Eng Technol Ind Chem Equipment-Process Eng 2005;28:219–25.
[142] Hall SA, Wright J, Pirling T, Andò E, Hughes DJ, Viggiani G. Can intergranular force transmission be identified in sand? First results of spatially-resolved neutron and X-ray diffraction. Granul Matter 2011;13:251–4.
[143] Cil MB, Alshibli KA, Kenesei P. 3D experimental measurement of lattice strain and fracture behavior of sand particles using synchrotron X-ray diffraction and tomography. J Geotech Geoenvironmental Eng 2017;143:1–18. https://doi.org/10.1061/(ASCE)GT.1943-5606.0001737.
[144] Roscoe KH. The influence of strains in soil mechanics. Geotechnique 1970;20:129–70.
[145] Desrues J. La localisation de la déformation dans les matériaux granulaires 1984.
[146] Colliat-Dangus JL, Desrues J, Foray P. Triaxial testing of granular soil under elevated cell pressure. ASTM International: Adv. triaxial Test. soil rock; 1988.
[147] Desrues J, Chambon R, Mokni M, Mazerolle F. Void ratio evolution inside shear bands in triaxial sand specimens studied by computed tomography 1996;46:529–46. https://doi.org/10.1680/GEOT.1996.46.3.529.
[148] Alshibli KA, Sture S, Costes NC, Frank ML, Lankton MR, Batiste SN, et al. Assessment of localized deformations in sand using X-ray computed tomography. Geotech Test J 2000;23:274–99.

[149] Oda M, Takemura T, Takahashi M. Microstructure in shear band observed by microfocus X-ray computed tomography. Géotechnique 2004;54:539–42.
[150] Matsushima T, Katagiri J, Uesugi K, Nakano T, Tsuchiyama A. Micro X-ray CT at SPring-8 for granular mechanics. Soil Stress. Behav. Meas. Model. Anal.: Springer; 2003. p. 225–34.
[151] Matsushima T, Uesugi K, Nakano T, Tsuchiyama A. Visualization of grain motion inside a triaxial specimen by micro X-ray CT at SPring-8. Adv X-Ray Tomogr Geomaterials 2006:35–52.
[152] Pirling T, Bruno G, Withers PJ. SALSA—A new instrument for strain imaging in engineering materials and components. Mater Sci Eng A 2006;437:139–44.
[153] Wensrich CM, Kisi EH, Luzin V, Garbe U, Kirstein O, Smith AL, et al. Force chains in monodisperse spherical particle assemblies: Three-dimensional measurements using neutrons. Phys Rev E 2014;90:42203. https://doi.org/10.1103/PhysRevE.90.042203.
[154] Alshibli K, Cil MB, Kenesei P, Lienert U. Strain tensor determination of compressed individual silica sand particles using high-energy synchrotron diffraction. Granul Matter 2013;15:517–30. https://doi.org/10.1007/s10035-013-0424-x.
[155] Cil MB, Alshibli K, Kenesei P, Lienert U. Combined high-energy synchrotron X-ray diffraction and computed tomography to characterize constitutive behavior of silica sand. Nucl Instruments Methods Phys Res Sect B Beam Interact with Mater Atoms 2014;324:11–6. https://doi.org/10.1016/j.nimb.2013.08.043.
[156] Hall SA, Wright J. Three-dimensional experimental granular mechanics Géotechnique Lett 2015;5:236–42.
[157] Ganju E, Han F, Prezzi M, Salgado R, Pereira JS. Quantification of displacement and particle crushing around a penetrometer tip. Geosci Front 2019. https://doi.org/10.1016/j.gsf.2019.05.007.
[158] Zhai C, Pagan DC, Hurley RC. In Situ X-ray Tomography and 3D X-ray Diffraction Measurements of Cemented Granular Materials. JOM 2020;72:18–27. https://doi.org/10.1007/s11837-019-03774-4.
[159] Hurley RC, Pagan DC. An in-situ study of stress evolution and fracture growth during compression of concrete. Int J Solids Struct 2019;168:26–40. https://doi.org/10.1016/j.ijsolstr.2019.03.015.
[160] Hurley RC, Lind J, Pagan DC, Akin MC, Herbold EB. In situ grain fracture mechanics during uniaxial compaction of granular solids. J Mech Phys Solids 2018;112:273–90. https://doi.org/10.1016/J.JMPS.2017.12.007.
[161] Frocht MM. Photoelasticity - Google Books. Pergamon Press; 1969.
[162] Cloud GL, Pindera JT. Techniques in infrared photoelasticity. Exp Mech 1968.193–201.;1968(85):8. https://doi.org/10.1007/BF02326275.
[163] Daniels KE, Kollmer JE, Puckett JG, KE Daniels JKJP, Daniels KE, Kollmer JE, et al. Photoelastic force measurements in granular materials. Rev Sci Instrum 2017;88:051808. https://doi.org/10.1063/1.4983049.
[164] Imseeh WH, Alshibli KA. 3D finite element modelling of force transmission and particle fracture of sand. Comput Geotech 2018;94:184–95.
[165] Zhang Y, Behringer R. Pulling an intruder from a granular material: a novel depinning experiment. EPJ Web Conf., vol. 140, EDP Sciences; 2017, p. 03040. https://doi.org/10.1051/EPJCONF/201714003040.
[166] Abed Zadeh A, Barés J, Brzinski TA, Daniels KE, Dijksman J, Docquier N, et al. Enlightening force chains: a review of photoelasticimetry in granular matter. Granul Matter 2019.1–12.;2019(214):21. https://doi.org/10.1007/S10035-019-0942-2.
[167] M Cox DWJBRB, Cox M, Wang D, Barés J, Behringer RP. Self-organized magnetic particles to tune the mechanical behavior of a granular system 2016;115:64003. https://doi.org/10.1209/0295-5075/115/64003.
[168] Blouwolff J, Fraden S. The coordination number of granular cylinders. Europhys Lett 2006;76:1095–101. https://doi.org/10.1209/EPL/I2006-10376-1.
[169] Bernal JD, Mason J. Packing of Spheres: Co-ordination of Randomly Packed Spheres. Nature 1960;188:910–1. https://doi.org/10.1038/188910a0.
[170] Brujić J, Song C, Wang P, Briscoe C, Marty G, Makse HA. Measuring the coordination number and entropy of a 3D jammed emulsion packing by confocal microscopy. Phys Rev Lett 2007;98. https://doi.org/10.1103/PHYSREVLETT.98.248001.
[171] Unger T, Kertész J, Wolf DE. Force indeterminacy in the Jammed state of hard disks. Phys Rev Lett 2005;94. https://doi.org/10.1103/PHYSREVLETT.94.178001.
[172] Silbert LE, Ertaş D, Grest GS, Halsey TC, Levine D. Geometry of frictionless and frictional sphere packings. Phys Rev E - Stat Physics, Plasmas, Fluids, Relat Interdiscip Top 2002;65. https://doi.org/10.1103/PHYSREVE.65.031304.
[173] Wouterse A, Williams SR, Philipse AP. Effect of particle shape on the density and microstructure of random packings. J Phys Condens Matter 2007;19. https://doi.org/10.1088/0953-8984/19/40/406215.
[174] Donev A, Cisse I, Sachs D, Variano EA, Stillinger FH, Connelly R, et al. Improving the Density of Jammed Disordered Packings Using Ellipsoids. Science (80-) 2004;303:990–3. https://doi.org/10.1126/SCIENCE.1093010.
[175] Dally J, Riley W. Experimental stress analysis. 3rd ed. McGraw-Hill; 1991.
[176] Wakabayashi T. Photo-elastic Method for Determination of Stress in Powdered Mass. J Phys Soc Japan 1950;5:383–5. https://doi.org/10.1143/JPSJ.5.383.
[177] Dantu P. Proceedings of the 4th International Conference on Soil Mechanics and Foundation Engineering 1957.
[178] Dantu P. Etude Statistique des Forces Intergranulaires dans un Milieu Pulverulent. Géotechnique 1968;18:50–5. https://doi.org/10.1680/geot.1968.18.1.50.
[179] Clark AH, Kondic L, Behringer RP. Particle Scale Dynamics in Granular Impact. Phys Rev Lett 2012;109:238302. https://doi.org/10.1103/PhysRevLett.109.238302.
[180] Geng J, Reydellet G, Clément E, Behringer RPP. Green's function measurements of force transmission in 2D granular materials. Phys D Nonlinear Phenom 2003;182:274–303. https://doi.org/10.1016/S0167-2789(03)00137-4.
[181] Behringer RP, Howell D, Kondic L, Tennakoon S, Veje C. Predictability and granular materials. Phys D Nonlinear Phenom 1999;133:1–17. https://doi.org/10.1016/S0167-2789(99)00094-9.
[182] Howell D, Behringer RP, Veje C. Stress Fluctuations in a 2D Granular Couette Experiment: A Continuous Transition. Phys Rev Lett 1999;82:5241–4. https://doi.org/10.1103/PhysRevLett.82.5241.
[183] J Barés DWDWTBCORB. Local and global avalanches in a two-dimensional sheared granular medium. Phys Rev E 2017;96:052902.
[184] Abed Zadeh A, Barés J, Socolar JES, Behringer RP. Seismicity in sheared granular matter. Phys Rev E 2019;99.
[185] Geng J, Howell D, Longhi E, Behringer RP, Reydellet G, Vanel L, et al. Footprints in Sand: The Response of a Granular Material to Local Perturbations. Phys Rev Lett 2001;87:035506. https://doi.org/10.1103/PhysRevLett.87.035506.
[186] Majmudar TS, Sperl M, Luding S, Behringer RP. Jamming Transition in Granular Systems. Phys Rev Lett 2007;98:058001. https://doi.org/10.1103/PhysRevLett.98.058001.
[187] Bi D, Zhang J, Chakraborty B, Behringer RP. Jamming by shear. Nature 2011;480:355–8. https://doi.org/10.1038/nature10667.
[188] Wang D, Ren J, Dijksman JA, Zheng H, Behringer RP. Microscopic Origins of Shear Jamming for 2D Frictional Grains. Phys Rev Lett 2018;120:208004. https://doi.org/10.1103/PhysRevLett.120.208004.
[189] Zheng H, Dijksman JA, Behringer RP. Shear jamming in granular experiments without basal friction. EPL 2014;107:34005. https://doi.org/10.1209/0295-5075/107/34005.
[190] Lim MX, Barés J, Zheng H, Behringer RP. Force and Mass Dynamics in Non-Newtonian Suspensions. Phys Rev Lett 2017;119:184501. https://doi.org/10.1103/PhysRevLett.119.184501.
[191] Zheng H, Wang D, Chen DZ, Wang M, Behringer RP. Intruder friction effects on granular impact dynamics. Phys Rev E 2018;98:032904. https://doi.org/10.1103/PhysRevE.98.032904.
[192] Zuriguel I, Mullin T. The role of particle shape on the stress distribution in a sandpile. Proc R Soc A Math Phys Eng Sci 2008;464:99–116. https://doi.org/10.1098/rspa.2007.1899.
[193] Lherminier S, Planet R, Simon G, Vanel L, Ramos O. Revealing the structure of a granular medium through ballistic sound propagation. Phys Rev Lett 2014;113:098001. https://doi.org/10.1103/PhysRevLett.113.098001.
[194] Shukla A. Dynamic photoelastic studies of wave propagation in granular media. Opt Lasers Eng 1991;14:165–84.
[195] Owens ET, Daniels KE. Sound propagation and force chains in granular materials. EPL 2011;94:54005. https://doi.org/10.1209/0295-5075/94/54005.
[196] Huillard G, Noblin X, Rajchenbach J. Propagation of acoustic waves in a one-dimensional array of noncohesive cylinders. Phys Rev E - Stat Nonlinear, Soft Matter Phys 2011;84:016602. https://doi.org/10.1103/PhysRevE.84.016602.

[197] Coulais C, Seguin A, Dauchot O. Shear modulus and dilatancy softening in granular packings above jamming. Phys Rev Lett 2014;113:198001. https://doi.org/10.1103/PhysRevLett.113.198001.
[198] Iikawa N, Bandi MM, Katsuragi H. Sensitivity of Granular Force Chain Orientation to Disorder-Induced Metastable Relaxation. Phys Rev Lett 2016;116:128001. https://doi.org/10.1103/PhysRevLett.116.128001.
[199] Mahabadi N, Jang J. The impact of fluid flow on force chains in granular media. Appl Phys Lett 2017;110:041907. https://doi.org/10.1063/1.4975065.
[200] Barés J, Mora S, Delenne JY, Fourcaud T. Experimental observations of root growth in a controlled photoelastic granular material. EPJ Web Conf 2017;140:14008. https://doi.org/10.1051/epjconf/201714014008.
[201] Wendell DM, Luginbuhl K, Guerrero J, Hosoi AE. Experimental Investigation of Plant Root Growth Through Granular Substrates. Exp Mech 2012;52:945–9. https://doi.org/10.1007/s11340-011-9569-x.
[202] Kolb E, Hartmann C, Genet P. Radial force development during root growth measured by photoelasticity. Plant Soil 2012;360:19–35. https://doi.org/10.1007/s11104-012-1316-2.
[203] Ferguson NM, Laydon D, Nedjati-Gilani G, Imai N, Ainslie K, Baguelin M, et al. Impact of non-pharmaceutical interventions (NPIs) to reduce COVID-19 mortality and healthcare demand. Imperial College COVID-19 Response Team. Imp Coll COVID-19 Response Team 2020:20. https://doi.org/10.25561/77482.
[204] Hayman NW, Ducloué L, Foco KL, Daniels KE. Granular Controls on Periodicity of Stick-Slip Events: Kinematics and Force-Chains in an Experimental Fault. Pure Appl Geophys 2011;168:2239–57. https://doi.org/10.1007/s00024-011-0269-3.
[205] Geller DA, Ecke RE, Dahmen KA, Backhaus S. Stick-slip behavior in a continuum-granular experiment. Phys Rev E 2015;92:060201. https://doi.org/10.1103/PhysRevE.92.060201.
[206] Lherminier S, Planet R, Vehel VLD, Simon G, Vanel L, Måløy KJ, et al. Continuously Sheared Granular Matter Reproduces in Detail Seismicity Laws. Phys Rev Lett 2019:122. https://doi.org/10.1103/PhysRevLett.122.218501.
[207] Lherminier S, Rpgsmmlvor.. A granular experiment approach to earthquakes. Rev Cuba Fís 2016;33:55–8.
[208] Wang Y, Wang Y, Zhang J. Connecting shear localization with the long-range correlated polarized stress fields in granular materials. Nat Commun 2020.1–7.;2020(111):11. https://doi.org/10.1038/s41467-020-18217-x.
[209] Abed Zadeh A, Barés J, Behringer RP. Crackling to periodic dynamics in granular media. Phys Rev E 2019;99:040901. https://doi.org/10.1103/PhysRevE.99.040901.
[210] Farhadi S, Zhu AZ, Behringer RP. Stress Relaxation for Granular Materials near Jamming under Cyclic Compression. Phys Rev Lett 2015;115:188001. https://doi.org/10.1103/PhysRevLett.115.188001.
[211] Iikawa N, Bandi MM, Katsuragi H. Structural evolution of a granular pack under manual tapping. J Phys Soc Japan 2015;84:094401. https://doi.org/10.7566/JPSJ.84.094401.
[212] Zhao Y, Zheng H, Wang D, Wang M, Behringer RP. Particle scale force sensor based on intensity gradient method in granular photoelastic experiments. New J Phys 2019;21:023009. https://doi.org/10.1088/1367-2630/ab05e7.
[213] Andrade JE, Avila CF. Granular element method (GEM): linking inter-particle forces with macroscopic loading. Granul Matter 2012;14:51–61. https://doi.org/10.1007/s10035-011-0298-8.
[214] Hurley R, Marteau E, Ravichandran G, Andrade JE. Extracting inter-particle forces in opaque granular materials: Beyond photoelasticity. J Mech Phys Solids 2014;63:154–66. https://doi.org/10.1016/j.jmps.2013.09.013.
[215] Hurley RC, Hall SA, Andrade JE, Wright J. Quantifying Interparticle Forces and Heterogeneity in 3D Granular Materials. Phys Rev Lett 2016;117:098005. https://doi.org/10.1103/PhysRevLett.117.098005.
[216] Hu Z, Du Y, Luo H, Zhong B, Lu H. Internal deformation measurement and force chain characterization of mason sand under confined compression using incremental digital volume correlation. Exp Mech 2014;54:1575–86.
[217] Bay BK, Smith TS, Fyhrie DP, Saad M. Digital volume correlation: three-dimensional strain mapping using X-ray tomography. Exp Mech 1999;39:217–26.
[218] Peters JF, Muthuswamy M, Wibowo J, Tordesillas A. Characterization of force chains in granular material. Phys Rev E 2005;72:041307. https://doi.org/10.1103/PhysRevE.72.041307.
[219] Wang R, Fu P, Zhang J-M, Dafalias YF. Evolution of Various Fabric Tensors for Granular Media toward the Critical State. J Eng Mech 2017;143:04017117. https://doi.org/10.1061/(ASCE)EM.1943-7889.0001342.
[220] Chen Y, Ma G, Zhou W, Wei D, Zhao Q, Zou Y, et al. An enhanced tool for probing the microscopic behavior of granular materials based on X-ray micro-CT and FDEM. Comput Geotech 2021;132:103974. https://doi.org/10.1016/J.COMPGEO.2020.103974.
[221] Sun Q, Zheng J. Two-dimensional and three-dimensional inherent fabric in cross-anisotropic granular soils. Comput Geotech 2019;116:103197. https://doi.org/10.1016/J.COMPGEO.2019.103197.
[222] Tian J, Liu E, Jiang L, Jiang X, Sun Y, Xu R. Influence of particle shape on the microstructure evolution and the mechanical properties of granular materials. Comptes Rendus Mécanique 2018;346:460–76. https://doi.org/10.1016/J.CRME.2018.03.006.
[223] Druckrey AM. 3D Multi-Scale Behavior of Granular Materials using Experimental and Numerical Techniques 2016:335.
[224] Yang H, Xu WJ, Sun QC, Feng Y. Study on the meso-structure development in direct shear tests of a granular material. Powder Technol 2017;314:129–39. https://doi.org/10.1016/J.POWTEC.2016.12.084.
[225] Viggiani G, Andò E, Jaquet C, Talbot H. Identifying and following particle-to-particle contacts in real granular media: An experimental challenge. AIP Conf. Proc., vol. 1542, American Institute of Physics; 2013, p. 60–5. https://doi.org/10.1063/1.4811868.
[226] Brodu N, Dijksman JA, Behringer RP. Spanning the scales of granular materials through microscopic force imaging. Nat Commun 2015;6:6361. https://doi.org/10.1038/ncomms7361.
[227] Wang Y, Xia C, Cao Y, Kou B, Li J, Xiao X, et al. Fast x-ray micro-tomography imaging study of granular packing under tapping. Dev. X-Ray Tomogr. IX, vol. 9212, International Society for Optics and Photonics; 2014, p. 92120E.
[228] Ahmed S, Klassen TN, Keyes S, Daly M, Jones DL, Mavrogordato M, et al. Imaging the interaction of roots and phosphate fertiliser granules using 4D X-ray tomography 2016:125–34. https://doi.org/10.1007/s11104-015-2425-5.
[229] Kim FH, Penumadu D, Patel P, Xiao X, Garboczi EJ, Moylan SP, et al. Synchrotron 4-dimensional imaging of two-phase flow through porous media 2016;1:2757–61. https://doi.org/10.1557/adv.2016.505.Synchrotron.
[230] Osher S, Fedkiw R. Level Set Methods and Dynamic Implicit Surfaces 2003;153. https://doi.org/10.1007/B98879.
[231] Hirt CW, Nichols BD. Volume of fluid (VOF) method for the dynamics of free boundaries. J Comput Phys 1981;39:201–25. https://doi.org/10.1016/0021-9991(81)90145-5.
[232] Cremonesi M, Franci A, Idelsohn S, Oñate E. A State of the Art Review of the Particle Finite Element Method (PFEM). Arch Comput Methods Eng 2020.1709–35.;2020(275):27. https://doi.org/10.1007/S11831-020-09468-4.
[233] Fritts MJ, Boris JP. The Lagrangian solution of transient problems in hydrodynamics using a triangular mesh. J Comput Phys 1979;31:173–215. https://doi.org/10.1016/0021-9991(79)90069-X.
[234] Bach P, Hassager O. An algorithm for the use of the Lagrangian specification in Newtonian fluid mechanics and applications to free-surface flow. J Fluid Mech 1985;152:173–90. https://doi.org/10.1017/S0022112085000635.
[235] Malcevic I, Ghattas O. Dynamic-mesh finite element method for Lagrangian computational fluid dynamics. Finite Elem Anal Des 2002;38:965–82. https://doi.org/10.1016/S0168-874X(02)00088-4.
[236] Muttin F, Coupez T, Bellet M, Chenot JL. Lagrangian finite-element analysis of time-dependent viscous free-surface flow using an automatic remeshing technique: Application to metal casting flow. Int J Numer Methods Eng 1993;36:2001–15. https://doi.org/10.1002/NME.1620361204.
[237] Radovitzky R, Ortiz M. Lagrangian finite element analysis of newtonian fluid flows. Int J Numer Methods Eng 1998;43:607–19. https://doi.org/10.1002/(SICI)1097-0207(19981030)43:4%3C607::AID-NME399%3E3.0.CO;2-N.
[238] Li S, Liu WK. Meshfree Particle Methods. Berlin, Heidelberg: Springer Berlin Heidelberg; 2004. https://doi.org/10.1007/978-3-540-71471-2.

[239] Donea J, Huerta A, Ponthot J-P, Rodríguez-Ferran A. Arbitrary Lagrangian-Eulerian Methods. Encycl. Comput Mech 2004. https://doi.org/10.1002/0470091355.ECM009.
[240] Idelsohn SR, Oñate E, Del PF. The particle finite element method: a powerful tool to solve incompressible flows with free-surfaces and breaking waves. Int J Numer Methods Eng 2004;61:964–89. https://doi.org/10.1002/NME.1096.
[241] Oñate E, Idelsohn SR, Del PF, Aubry R. The particle finite element method — an overview. Int J Comput Methods 2012;01:267–307. https://doi.org/10.1142/S0219876204000204.
[242] EdelsbrunnerHerbert PM. Three-dimensional alpha shapes ACM Trans Graph 1994;13:43–72. https://doi.org/10.1145/174462.156635.
[243] Koshizuka S, Oka Y. Moving-Particle Semi-Implicit Method for Fragmentation of Incompressible Fluid. Https://DoiOrg/1013182/NSE96-A24205 2017;123:421–34. https://doi.org/10.13182/NSE96-A24205.
[244] Cerquaglia ML, Deliége G, Boman R, Terrapon V, Ponthot J-P. Free-slip boundary conditions for simulating free-surface incompressible flows through the particle finite element method. Int J Numer Methods Eng 2017;110:921–46. https://doi.org/10.1002/NME.5439.
[245] Idelsohn SR, Oñate E, Del Pin F, Calvo N. Fluid–structure interaction using the particle finite element method. Comput Methods Appl Mech Eng 2006;195:2100–23. https://doi.org/10.1016/J.CMA.2005.02.026.
[246] Zhu M, Scott MH. Improved fractional step method for simulating fluid-structure interaction using the PFEM. Int J Numer Methods Eng 2014;99:925–44. https://doi.org/10.1002/NME.4727.
[247] Franci A, de-Pouplana I, Casas G, Celigueta MÁ, González-Usúa J, Oñate E.. PFEM–DEM for particle-laden flows with free surface. Comput Part Mech 2019.101–20.;2019(71):7. https://doi.org/10.1007/S40571-019-00244-1.
[248] Meduri S, Cremonesi M, Perego U. An efficient runtime mesh smoothing technique for 3D explicit Lagrangian free-surface fluid flow simulations. Int J Numer Methods Eng 2019;117:430–52. https://doi.org/10.1002/NME.5962.
[249] Larese A, Rossi R, Oñate E, Idelsohn SR. Validation of the particle finite element method (PFEM) for simulation of free surface flows. Eng Comput (Swansea, Wales) 2008;25:385–425. https://doi.org/10.1108/02644400810874976.
[250] Idelsohn SR, Marti J, Limache A, Oñate E. Unified Lagrangian formulation for elastic solids and incompressible fluids: Application to fluid–structure interaction problems via the PFEM. Comput Methods Appl Mech Eng 2008;197:1762–76. https://doi.org/10.1016/J.CMA.2007.06.004.
[251] Idelsohn SR, Marti J, Souto-Iglesias A, Oñate E. Interaction between an elastic structure and free-surface flows: experimental versus numerical comparisons using the PFEM. Comput Mech 2008.125–32.;2008(431):43. https://doi.org/10.1007/S00466-008-0245-7.
[252] Franci A, Oñate E, Carbonell JM, Chiumenti M. PFEM formulation for thermo-coupled FSI analysis. Application to nuclear core melt accident. Comput Methods Appl Mech Eng 2017;325:711–32. https://doi.org/10.1016/J.CMA.2017.07.028.
[253] Idelsohn S, Mier-Torrecilla M, Oñate E. Multi-fluid flows with the Particle Finite Element Method. Comput Methods Appl Mech Eng 2009;198:2750–67. https://doi.org/10.1016/J.CMA.2009.04.002.
[254] Idelsohn SR, Mier-Torrecilla M, Nigro N, Oñate E. On the analysis of heterogeneous fluids with jumps in the viscosity using a discontinuous pressure field. Comput Mech 2009.115–24.;2009(461):46. https://doi.org/10.1007/S00466-009-0448-6.
[255] Mier-Torrecilla M, Idelsohn SR, Oñate E. Advances in the simulation of multi-fluid flows with the particle finite element method. Application to bubble dynamics. Int J Numer Methods Fluids 2011;67:1516–39. https://doi.org/10.1002/FLD.2429.
[256] Aubry R, Oñate E, Idelsohn SR. Fractional Step Like Schemes for Free Surface Problems with Thermal Coupling Using the Lagrangian PFEM. Comput Mech 2006.294–309.;2006(384):38. https://doi.org/10.1007/S00466-006-0058-5.
[257] Oñate E, Marti J, Ryzhakov P, Rossi R, Idelsohn SR. Analysis of the melting, burning and flame spread of polymers with the Particle Finite Element Method 2016.
[258] Kempel F, Schartel B, Marti JM, Butler KM, Rossi R, Idelsohn SR, et al. Modelling the vertical UL 94 test: competition and collaboration between melt dripping, gasification and combustion. Fire Mater 2015;39:570–84. https://doi.org/10.1002/FAM.2257.
[259] Cremonesi M, Frangi A, Perego U. A Lagrangian finite element approach for the simulation of water-waves induced by landslides. Comput Struct 2011;89:1086–93. https://doi.org/10.1016/J.COMPSTRUC.2010.12.005.
[260] Salazar F, Irazábal J, Larese A, Oñate E. Numerical modelling of landslide-generated waves with the particle finite element method (PFEM) and a non-Newtonian flow model. Int J Numer Anal Methods Geomech 2016;40:809–26. https://doi.org/10.1002/NAG.2428.
[261] Cremonesi M, Ferri F, Perego U. A basal slip model for Lagrangian finite element simulations of 3D landslides. Int J Numer Anal Methods Geomech 2017;41:30–53. https://doi.org/10.1002/NAG.2544.
[262] Oñate E, Franci A, Carbonell JM. A particle finite element method for analysis of industrial forming processes. Comput Mech 2014.85–107.;2014(541):54. https://doi.org/10.1007/S00466-014-1016-2.
[263] Rodríguez JM, Carbonell JM, Cante JC, Oliver J. Continuous chip formation in metal cutting processes using the Particle Finite Element Method (PFEM). Int J Solids Struct 2017;120:81–102. https://doi.org/10.1016/J.IJSOLSTR.2017.04.030.
[264] Rodríguez JM, Jonsén · P, Svoboda · A, Rodríguez BJM, Jonsén P, Svoboda A.. Simulation of metal cutting using the particle finite-element method and a physically based plasticity model. Comp Part Mech 2017;4:35–51. https://doi.org/10.1007/s40571-016-0120-9.
[265] Zhang X, Krabbenhoft K, Pedroso DM, Lyamin AV, Sheng D, da Silva MV, et al. Particle finite element analysis of large deformation and granular flow problems. Comput Geotech 2013;54:133–42. https://doi.org/10.1016/J.COMPGEO.2013.07.001.
[266] Dávalos C, Cante J, Hernández JA, Oliver J. On the numerical modeling of granular material flows via the Particle Finite Element Method (PFEM). Int J Solids Struct 2015;71:99–125. https://doi.org/10.1016/J.IJSOLSTR.2015.06.013.
[267] Cante J, Dávalos C, Hernández JA, Oliver J, Jonsén P, Gustafsson G, et al. PFEM-based modeling of industrial granular flows. Comput Part Mech 2014.47–70.;2014(11):1. https://doi.org/10.1007/S40571-014-0004-9.
[268] Larsson S, Rodríguez Prieto JM, Gustafsson G, Häggblad H-Å, Jonsén P. The particle finite element method for transient granular material flow: modelling and validation. Comput Part Mech 2020.135–55.;2020(81):8. https://doi.org/10.1007/S40571-020-00317-6.
[269] Jin Y-F, Yuan W-H, Yin Z-Y, Cheng Y-M. An edge-based strain smoothing particle finite element method for large deformation problems in geotechnical engineering. Int J Numer Anal Methods Geomech 2020;44:923–41. https://doi.org/10.1002/NAG.3016.
[270] Franci A, Cremonesi M. 3D regularized μ(I)-rheology for granular flows simulation. J Comput Phys 2019;378:257–77. https://doi.org/10.1016/J.JCP.2018.11.011.
[271] Lucy LB. A numerical approach to the testing of the fission hypothesis. Astron J 1977;82:1013–24.
[272] Gingold RA, Monaghan JJ. Smoothed particle hydrodynamics: theory and application to non-spherical stars. Mon Not R Astron Soc 1977;181:375–89.
[273] Monaghan JJ. Smoothed particle hydrodynamics. Annu Rev Astron Astrophys 1992;30:543–74. https://doi.org/10.1887/0750304588/b485b3.
[274] Monaghan JJ. Simulating free surface flows with SPH. J Comput Phys 1994;110:399–406.
[275] Monaghan JJ. Smoothed Particle Hydrodynamics and Its Diverse Applications. Http://DxDoiOrg/101146/Annurev-Fluid-120710-101220 2011;44:323–46. https://doi.org/10.1146/ANNUREV-FLUID-120710-101220.
[276] Violeau D. Fluid mechanics and the SPH method : theory and applications. Oxford University Press; 2012.
[277] Chen W, Qiu T. Numerical Simulations for Large Deformation of Granular Materials Using Smoothed Particle Hydrodynamics Method. Int J Geomech 2012;12:127–35. https://doi.org/10.1061/(ASCE)GM.1943-5622.0000149.
[278] Xu WJ, Dong XY, Ding WT. Analysis of fluid-particle interaction in granular materials using coupled SPH-DEM method. Powder Technol 2019;353:459–72.
[279] Abdelrazek AM, Kimura I, Shimizu Y. Simulation of three-dimensional rapid free-surface granular flow past different types of obstructions using the SPH method 2021. https://doi.org/10.1017/jog.2016.22.
[280] Tayeb R, Mao Y, Zhang Y. Smoothed particle hydrodynamics simulation of granular system under cyclic compressions. Powder Technol 2019;353:84–97. https://doi.org/10.1016/J.POWTEC.2019.04.079.
[281] Wang G, Riaz A, Balachandran B. Smooth particle hydrodynamics studies of wet granular column collapses. Acta Geotech 2019.1205–17.;2019(155):15. https://doi.org/10.1007/S11440-019-00828-4.

[282] Williams JR, Holmes D, Tilke P. Parallel computation particle methods for multi-phase fluid flow with application oil reservoir characterization. Part. Methods: Springer; 2011. p. 113–34.
[283] Bui HH, Fukagawa R, Sako K, Ohno S. Lagrangian meshfree particles method (SPH) for large deformation and failure flows of geomaterial using elastic-plastic soil constitutive model. Int J Numer Anal Methods Geomech 2008;32:1537–70. https://doi.org/10.1002/NAG.688.
[284] Bui HH, Kodikara JK, Bouazza A, Haque A, Ranjith PG. A novel computational approach for large deformation and post-failure analyses of segmental retaining wall systems. Int J Numer Anal Methods Geomech 2014;38:1321–40. https://doi.org/10.1002/NAG.2253.
[285] Ikari H, Gotoh H. SPH-based simulation of granular collapse on an inclined bed. Mech Res Commun 2016;73:12–8. https://doi.org/10.1016/J.MECHRESCOM.2016.01.014.
[286] Nguyen CT, Nguyen CT, Bui HH, Nguyen GD, Fukagawa R. A new SPH-based approach to simulation of granular flows using viscous damping and stress regularisation. Landslides 2016.69–81.;2016(141):14. https://doi.org/10.1007/S10346-016-0681-Y.
[287] Belytschko T, Krongauz Y, Dolbow J, Gerlach C. On the completeness of meshfree particle methods. Int J Numer Methods Eng 1998;43:785–819. https://doi.org/10.1002/(SICI)1097-0207(19981115)43:5.
[288] Cundall PA, Strack ODL. A discrete numerical model for granular assemblies. Géotechnique 1979;29:47–65. https://doi.org/10.1680/geot.1979.29.1.47.
[289] Yeom Ha, Kim J, Hwang C. Application of the Discrete Element Method for Manufacturing Process Simulation in the Pharmaceutical Industry. Pharmaceutics 2019;11:414.. https://doi.org/10.3390/pharmaceutics11080414.
[290] Yan W, Wang B, He H. Research on Damping Mechanism and Parameter Analysis of Particle Damper Based on Energy Theory. J Eng Mech 2020;146:04020054. https://doi.org/10.1061/(ASCE)EM.1943-7889.0001772.
[291] Hertz H. Ueber die Beruhrung fester elastischer Korper. J Reine Angew Math 1882;92:156–71.
[292] Mindlin RD. Elastic spheres in contact under varying oblique forces. J Appl Mech 1953;20:327–44.
[293] Vu-Quoc L, Zhang X. An accurate and efficient tangential force–displacement model for elastic frictional contact in particle-flow simulations. Mech Mater 1999;31:235–69. https://doi.org/10.1016/S0167-6636(98)00064-7.
[294] Di Renzo A, Di Maio FP. Comparison of contact-force models for the simulation of collisions in DEM-based granular flow codes. Chem Eng Sci 2004;59:525–41. https://doi.org/10.1016/j.ces.2003.09.037.
[295] Zhu HP, Zhou ZY, Yang RY, Yu AB. Discrete particle simulation of particulate systems: Theoretical developments. Chem Eng Sci 2007;62:3378–96.
[296] Tahmasebi P, Kamrava S. A pore-scale mathematical modeling of fluid-particle interactions: Thermo-hydro-mechanical coupling. Int J Greenh Gas Control 2019;83:245–55. https://doi.org/10.1016/j.ijggc.2018.12.014.
[297] Ai J, Chen J-F-F, Rotter JM, Ooi JY. Assessment of rolling resistance models in discrete element simulations. Powder Technol 2011;206:269–82. https://doi.org/10.1016/j.powtec.2010.09.030.
[298] Computer VL. “Experiments” on Classical Fluids. I. Thermodynamical Properties of Lennard-Jones Molecules. Phys Rev 1967;159:98.. https://doi.org/10.1103/PhysRev.159.98.
[299] Luding S. Cohesive, frictional powders: contact models for tension. Granul Matter 2008.235–46.;2008(104):10. https://doi.org/10.1007/S10035-008-0099-X.
[300] Wang Y, Alonso-Marroquin F, Xue S, Xie J. Revisiting rolling and sliding in two-dimensional discrete element models. Particuology 2015;18:35–41. https://doi.org/10.1016/J.PARTIC.2014.04.013.
[301] Zhu HP, Zhou ZY, Yang RY, Yu AB. Discrete particle simulation of particulate systems: A review of major applications and findings. Chem Eng Sci 2008;63:5728–70. https://doi.org/10.1016/J.CES.2008.08.006.
[302] Zhao J, Shan T. Coupled CFD–DEM simulation of fluid–particle interaction in geomechanics. Powder Technol 2013;239:248–58. https://doi.org/10.1016/j.powtec.2013.02.003.
[303] Cil MB, Alshibli KA. 3D analysis of kinematic behavior of granular materials in triaxial testing using DEM with flexible membrane boundary 9:287–98.
[304] Zhang X, Tahmasebi P. Micromechanical evaluation of rock and fluid interactions. Int J Greenh Gas Control 2018;76:266–77. https://doi.org/10.1016/J.IJGGC.2018.07.018.
[305] Zhou Y, Shi Z, Zhang Q, Liu W, Peng M, Wu C. 3D DEM investigation on the morphology and structure of landslide dams formed by dry granular flows. Eng Geol 2019;258:105151. https://doi.org/10.1016/j.enggeo.2019.105151.
[306] Zhang X, Tahmasebi P. Effects of Grain Size on Deformation in Porous Media. Transp Porous Media 2019;129:321–41. https://doi.org/10.1007/s11242-019-01291-1.
[307] Mishra BK, Rajamani RK. The discrete element method for the simulation of ball mills. Appl Math Model 1992;16:598–604.
[308] Tsuji Y, Tanaka T, Ishida T. Lagrangian numerical simulation of plug flow of cohesionless particles in a horizontal pipe. Powder Technol 1992;71:239–50. https://doi.org/10.1016/0032-5910(92)88030-L.
[309] Tsuji Y, Kawaguchi T, Tanaka T. Discrete particle simulation of two-dimensional fluidized bed 1993;77:79–87. https://doi.org/10.1016/0032-5910(93)85010-7.
[310] Kazuyoshi I, Masanobu O. Rolling Resistance at Contacts in Simulation of Shear Band Development by DEM. J Eng Mech 1998;124:285–92. https://doi.org/10.1061/(ASCE)0733-9399(1998)124:3(285).
[311] Thornton C. Numerical simulations of deviatoric shear deformation of granular media. Géotechnique 2000;50:43–53. https://doi.org/10.1680/geot.2000.50.1.43.
[312] Scholtès L, Donzé F-V. Modelling progressive failure in fractured rock masses using a 3D discrete element method. Int J Rock Mech Min Sci 2012;52:18–30. https://doi.org/10.1016/j.ijrmms.2012.02.009.
[313] Lim K-W, Andrade JE. Granular element method for three-dimensional discrete element calculations. Int J Numer Anal Methods Geomech 2014;38:167–88. https://doi.org/10.1002/nag.2203.
[314] Kawamoto R, Andò E, Viggiani G, Andrade JE. Level set discrete element method for three-dimensional computations with triaxial case study. J Mech Phys Solids 2016;91:1–13. https://doi.org/10.1016/j.jmps.2016.02.021.
[315] Suchorzewski J, Tejchman J, Nitka M. Discrete element method simulations of fracture in concrete under uniaxial compression based on its real internal structure. Int J Damage Mech 2017;27:578–607. https://doi.org/10.1177/1056789517690915.
[316] Zhao Y, Yang S, Zhang L, Chew JW. Understanding the varying discharge rates of lognormal particle size distributions from a hopper using the Discrete Element Method. Powder Technol 2019;342:356–70. https://doi.org/10.1016/j.powtec.2018.09.080.
[317] Liszka T, Orkisz J. The finite difference method at arbitrary irregular grids and its application in applied mechanics. Comput Struct 1980;11:83–95.
[318] Belytschko T, Lu YY, Gu L. Element-free Galerkin methods. Int J Numer Methods Eng 1994;37:229–56. https://doi.org/10.1002/NME.1620370205.
[319] Jach K, Leliwa-Kopystyński J, Mroczkowski M, Świerczyński R, Wolański P. Free particle modelling of hypervelocity asteroid collisions with the Earth. Planet Space Sci 1994;42:1123–37.
[320] Oñate E, Idelsohn S, Zienkiewicz OC, Taylor RL, Sacco C. A stabilized finite point method for analysis of fluid mechanics problems. Comput Methods Appl Mech Eng 1996;139:315–46.
[321] Monaghan JJ. An introduction to SPH. Comput Phys Commun 1988;48:89–96.
[322] Libersky LD, Petschek AG, Carney TC, Hipp JR, Allahdadi FA. High strain lagrangian hydrodynamics a three-dimensional SPH code for dynamic material response. J Comput Phys 1993;109:67–75.
[323] Johnson GR, Stryk RA, Beissel SR. SPH for high velocity impact computations. Comput Methods Appl Mech Eng 1996;139:347–73.
[324] Randles PW, Libersky LD. Smoothed particle hydrodynamics: Some recent improvements and applications. Comput Methods Appl Mech Eng 1996;139:375–408.
[325] Liu WK, Jun S, Li S, Adee J, Belytschko T. Reproducing kernel particle methods for structural dynamics. Int J Numer Methods Eng 1995;38:1655–79. https://doi.org/10.1002/NME.1620381005.
[326] Chen JS, Pan C, Wu CT, Liu WK. Reproducing Kernel Particle Methods for large deformation analysis of non-linear structures. Comput Methods Appl Mech Eng 1996;139:195–227.

[327] Melenk JM, Babuška I. The partition of unity finite element method: Basic theory and applications. Comput Methods Appl Mech Eng 1996;139:289–314.
[328] Liszka TJ, Duarte CAM, Tworzydlo WW. hp-Meshless cloud method. Comput Methods Appl Mech Eng 1996;139:263–88.
[329] Zienkiewicz OC, Taylor RL, Taylor RL. The finite element method: solid mechanics. Butterworth-heinemann; 2000.
[330] Harlow FH, Welch JE. Numerical Calculation of Time-Dependent Viscous Incompressible Flow of Fluid with Free Surface. Phys Fluids 1965;8:2182. https://doi.org/10.1063/1.1761178.
[331] Burgess D, Sulsky D, Brackbill JU. Mass matrix formulation of the FLIP particle-in-cell method. J Comput Phys 1992;103:1–15.
[332] Sulsky D, Schreyer HL. Axisymmetric form of the material point method with applications to upsetting and Taylor impact problems. Comput Methods Appl Mech Eng 1996;139:409–29.
[333] Więckowski Z. The material point method in large strain engineering problems. Comput Methods Appl Mech Eng 2004;193:4417–38. https://doi.org/10.1016/J.CMA.2004.01.035.
[334] Sulsky D, Chen Z, Schreyer HL. A particle method for history-dependent materials. Comput Methods Appl Mech Eng 1994;118:179–96. https://doi.org/10.1016/0045-7825(94)90112-0.
[335] Coetzee CJ, Basson AH, Vermeer PA. Discrete and continuum modelling of excavator bucket filling. J Terramechanics 2007;44:177–86. https://doi.org/10.1016/J.JTERRA.2006.07.001.
[336] Zhou S, Stormont J, Chen Z. Simulation of geomembrane response to settlement in landfills by using the material point method. Int J Numer Anal Methods Geomech 1999;23:1977–94. https://doi.org/10.1002/(SICI)1096-9853(19991225)23:15.
[337] Abe K, Soga K, Bandara S. Material Point Method for Coupled Hydromechanical Problems. J Geotech Geoenvironmental Eng 2014;140:04013033. https://doi.org/10.1061/(ASCE)GT.1943-5606.0001011.
[338] Sulsky D, Zhou SJ, Schreyer HL. Application of a particle-in-cell method to solid mechanics. Comput Phys Commun 1995;87:236–52. https://doi.org/10.1016/0010-4655(94)00170-7.
[339] Hu W, Chen Z. Model-based simulation of the synergistic effects of blast and fragmentation on a concrete wall using the MPM. Int J Impact Eng 2006;32:2066–96. https://doi.org/10.1016/J.IJIMPENG.2005.05.004.
[340] Guilkey JE, Harman TB, Banerjee B. An Eulerian-Lagrangian approach for simulating explosions of energetic devices. Comput Struct 2007;85:660–74. https://doi.org/10.1016/J.COMPSTRUC.2007.01.031.
[341] Zhang X, Sze KY, Ma S. An explicit material point finite element method for hyper-velocity impact. Int J Numer Methods Eng 2006;66:689–706. https://doi.org/10.1002/NME.1579.
[342] Guilkey JE, Hoying JB, Weiss JA. Computational modeling of multicellular constructs with the material point method. J Biomech 2006;39:2074–86. https://doi.org/10.1016/J.JBIOMECH.2005.06.017.
[343] Bardenhagen SG, Brackbill JU, Sulsky D. The material-point method for granular materials. Comput Methods Appl Mech Eng 2000;187:529–41. https://doi.org/10.1016/S0045-7825(99)00338-2.
[344] Cummins SJ, Brackbill JU. An Implicit Particle-in-Cell Method for Granular Materials. J Comput Phys 2002;180:506–48. https://doi.org/10.1006/JCPH.2002.7101.
[345] Coetzee CJ, Vermeer PA, Basson AH. The modelling of anchors using the material point method. Int J Numer Anal Methods Geomech 2005;29:879–95. https://doi.org/10.1002/NAG.439.
[346] Stomakhin A, Schroeder C, Chai L, Teran J, Selle A. A material point method for snow simulation. ACM Trans Graph 2013;32. https://doi.org/10.1145/2461912.2461948.
[347] Steffen M, Kirby RM, Berzins M. Analysis and reduction of quadrature errors in the material point method (MPM). Int J Numer Methods Eng 2008;76:922–48. https://doi.org/10.1002/NME.2360.
[348] Ionescu I, Guilkey J, Berzins M, Kirby RM, Weiss JA. Computational Simulation of Penetrating Trauma in Biological Soft Tissues Using the Material Point Method. In: et al. JDW, editor. Proceedings, Med. Meets Virtual Real., vol. 13, IOS Press; 2005, p. 213–8.
[349] Patankar NA, Joseph DD. Lagrangian numerical simulation of particulate flows. Int J Multiph Flow 2001;27:1685–706. https://doi.org/10.1016/S0301-9322(01)00025-8.
[350] York AR, Sulsky D, Schreyer HL. Fluid-membrane interaction based on the material point method. Int J Numer Methods Eng 2000;48:901–24. https://doi.org/10.1002/(SICI)1097-0207(20000630)48:6%3C901::AID-NME910%3E3.0.CO;2-T.
[351] Lu H, Daphalapurkar NP, Wang B, Roy S, Komanduri R. Multiscale simulation from atomistic to continuum - Coupling molecular dynamics (MD) with the material point method (MPM). Philos Mag 2006;86:2971–94. https://doi.org/10.1080/14786430600625578.
[352] Li S, Liu WK. Meshfree and particle methods and their applications. Appl Mech Rev 2002;55:1–34. https://doi.org/10.1115/1.1431547.
[353] StomakhinAlexey SchroederCraig, JiangChenfanfu ChaiLawrence, TeranJoseph SelleAndrew. Augmented MPM for phase-change and varied materials. ACM Trans Graph 2014:33. https://doi.org/10.1145/2601097.2601176.
[354] Tran QA, Sołowski W. Generalized Interpolation Material Point Method modelling of large deformation problems including strain-rate effects – Application to penetration and progressive failure problems. Comput Geotech 2019;106:249–65. https://doi.org/10.1016/J.COMPGEO.2018.10.020.
[355] Llano-Serna MA, Farias MM, Pedroso DM. An assessment of the material point method for modelling large scale run-out processes in landslides. Landslides 2015.1057–66.;2015(135):13. https://doi.org/10.1007/S10346-015-0664-4.
[356] de Vaucorbeil A, Nguyen VP, Nguyen-Thanh C. Karamelo: an open source parallel C++ package for the material point method. Comput Part Mech 2020 84 2020;8:767–89. https://doi.org/10.1007/S40571-020-00369-8.
[357] Llano-Serna MA, Farias MM. Numerical, theoretical and experimental validation of the material point method to solve geotechnical engineering problems. Rev Int Métodos Numéricos Para Cálculo y Diseño En Ing 2016;32:110–5. https://doi.org/10.1016/J.RIMNI.2015.02.008.
[358] Wang X, Qiu Y, R. S, Fang Y, Li M, Zhu S-C,, et al. A massively parallel and scalable multi-GPU material point method. ACM Trans Graph 2020:39. https://doi.org/10.1145/3386569.3392442.
[359] Wolper J, Fang Y, Li M, Lu J, Gao M, Jiang C. CD-MPM: Continuum damage material point methods for dynamic fracture animation. ACM Trans Graph 2019:38. https://doi.org/10.1145/3306346.3322949.
[360] Ram D, Gast T, Jiang C, Schroeder C, Stomakhin A, Teran J, et al. A material point method for viscoelastic fluids, foams and sponges. Proc - SCA 2015 14th ACM SIGGRAPH / Eurographics Symp Comput Animat 2015:157–63. https://doi.org/10.1145/2786784.2786798.
[361] Hidalgo RC, Zuriguel I, Maza D, Pagonabarraga I. Role of particle shape on the stress propagation in granular packings. Phys Rev Lett 2009;103:118001. https://doi.org/10.1103/PhysRevLett.103.118001.
[362] Delaney GW, Morrison RD, Sinnott MD, Cummins S, Cleary PW. DEM modelling of non-spherical particle breakage and flow in an industrial scale cone crusher. Miner Eng 2015;74:112–22. https://doi.org/10.1016/j.mineng.2015.01.013.
[363] Njobuenwu DO, Fairweather M. Dynamics of single, non-spherical ellipsoidal particles in a turbulent channel flow. Chem Eng Sci 2015;123:265–82. https://doi.org/10.1016/j.ces.2014.11.024.
[364] Zhou ZY, Pinson D, Zou RP, Yu AB. Discrete particle simulation of gas fluidization of ellipsoidal particles. Chem Eng Sci 2011;66:6128–45. https://doi.org/10.1016/j.ces.2011.08.041.
[365] Xu W, Duan Q, Ma H, Chen W, Chen H. Interfacial effect on physical properties of composite media: Interfacial volume fraction with non-spherical hard-core-soft-shell-structured particles. Sci Rep 2015;5:16003. https://doi.org/10.1038/srep16003.
[366] Williams JR, O'Connor R. Discrete element simulation and the contact problem. Arch Comput Methods Eng 1999;6:279–304. https://doi.org/10.1007/BF02818917.
[367] Kozlowski R, Zheng H, Daniels KE, Socolar JES. Stress propagation in locally loaded packings of disks and pentagons. Soft Matter 2021. https://doi.org/10.1039/d1sm01137e.
[368] Guises R, Xiang J, Latham J-P, Munjiza A. Granular packing: numerical simulation and the characterisation of the effect of particle shape. Granul Matter 2009.281–92.;2009(115):11. https://doi.org/10.1007/S10035-009-0148-0.

[369] Ferellec JF, McDowell GR. A method to model realistic particle shape and inertia in DEM. Granul Matter 2010;12:459–67. https://doi.org/10.1007/s10035-010-0205-8.
[370] Taghavi R. Automatic clump generation based on mid-surface. In: Proceedings, 2nd Int. FLAC/DEM Symp. Melb; 2011. p. 791–7.
[371] Wang L, Park JYJY, Fu Y. Representation of real particles for DEM simulation using X-ray tomography. Constr Build Mater 2007;21:338–46. https://doi.org/10.1016/J.CONBUILDMAT.2005.08.013.
[372] Lai Z. Discrete Element Modeling of the Grading-and Shape-Dependent Behavior of Granular Materials. Clemson University; 2018.
[373] T. Matsushima JKKUATTN. 3D shape characterization and image-based DEM simulation of the Lunar soil simulant FJS-1. J Aerosp Eng 2009;22:15–23. https://doi.org/10.1061/(asce)0893-1321(2009)22:1(15).
[374] Price M, Murariu V, Morrison G. Sphere clump generation and trajectory comparison for real particles. Proc Discret Elem Model 2007 2007..
[375] Garcia X, Latham J-P-J-P, Xiang JS, Harrison JP. A clustered overlapping sphere algorithm to represent real particles in discrete element modelling 2009;vol. 59. https://doi.org/10.1680/geot.8.T.037.
[376] Zheng J, Hryciw RD. A corner preserving algorithm for realistic DEM soil particle generation. Granul Matter 2016.1–18.;2016(184):18. https://doi.org/10.1007/S10035-016-0679-0.
[377] Li T, Peng Y, Zhu Z, Zou S, Yin Z. Discrete Element Method Simulations of the Inter-Particle Contact Parameters for the Mono-Sized Iron Ore Particles. Mater 2017, Vol 10, Page 520 2017;10:520. https://doi.org/10.3390/MA10050520.
[378] Coetzee CJ. Calibration of the discrete element method and the effect of particle shape. Powder Technol 2016;297:50–70. https://doi.org/10.1016/J.POWTEC.2016.04.003.
[379] Psakhie SG, Horie Y, Korostelev SY, Smolin AY, Dmitriev AI, Shilko EV, et al. Method of movable cellular automata as a tool for simulation within the framework of mesomechanics. Russ Phys J 1995.1157–68.;1996(3811):38. https://doi.org/10.1007/BF00559396.
[380] Psakhie SG, Moiseyenko DD, Smolin AY, Shilko EV, Dmitriev AI, Korostelev SY, et al. The features of fracture of heterogeneous materials and frame structures. Potentialities of MCA design. Comput Mater Sci 1999;16:333–43. https://doi.org/10.1016/S0927-0256(99)00076-2.
[381] Psakhie SG, Smolin AY, Tatarintsev EM. Discrete approach to study fracture energy absorption under dynamic loading. Comput Mater Sci 2000;19:179–82. https://doi.org/10.1016/S0927-0256(00)00153-1.
[382] Popov VL, Psakhie SG. Numerical simulation methods in tribology. Tribol Int 2007;40:916–23. https://doi.org/10.1016/J.TRIBOINT.2006.02.020.
[383] Dmitriev AI, Popov VL. Numerical modeling of processes of mass transfer in tribological contacts by the method of movable cellular automata. J Frict Wear 2009.12–6.;2009(301):30. https://doi.org/10.3103/S1068366609010036.
[384] Wang G, Al-Ostaz A, Cheng AHD, Mantena PR. Hybrid lattice particle modeling: Theoretical considerations for a 2D elastic spring network for dynamic fracture simulations. Comput Mater Sci 2009;44:1126–34. https://doi.org/10.1016/J.COMMATSCI.2008.07.032.
[385] Popov VL, Psakhie SG. Theoretical principles of modelling elastoplastic media by moveable cellular automata method. i: Homogenous media. Phys Mesomech 2001;4:16–25.
[386] Psakhie S, Shilko E, Smolin A, Astafurov S, Ovcharenko V. Development of a formalism of movable cellular automaton method for numerical modeling of fracture of heterogeneous elastic-plastic materials. Frat Ed Integrità Strutt 2013;7:26–59. https://doi.org/10.3221/IGF-ESIS.24.04.
[387] Nguyen TK, Combe G, Caillerie D, Desrues J. Modeling of a cohesive granular materials by a multi-scale approach. AIP Conf Proc 2013;1542:1194. https://doi.org/10.1063/1.4812151.
[388] Chu X, Cun Y, Xiu C, Xu Y. Two scale modeling of behaviors of granular structure: Size effects and displacement fluctuations of discrete particle assembly. Struct Eng Mech 2015;55:315–34. https://doi.org/10.12989/sem.2015.55.2.315.
[389] Kaneko K, Terada K, Kyoya T, Kishino Y. Global–local analysis of granular media in quasi-static equilibrium. Int J Solids Struct 2003;40:4043–69. https://doi.org/10.1016/S0020-7683(03)00209-9.
[390] Tsutsumi S, Kaneko K. Constitutive response of idealized granular media under the principal stress axes rotation. Int J Plast 2008;24:1967–89. https://doi.org/10.1016/J.IJPLAS.2008.05.001.
[391] Meier HA, Steinmann P, Kuhl E. Towards multiscale computation of confined granular media–contact forces, stresses and tangent operators. Tech Mech 2008;28:32–42.
[392] Masci J, Meier U, Cireşan D, Schmidhuber J. Stacked convolutional auto-encoders for hierarchical feature extraction. Lect. Notes Comput. Sci. (including Subser. Lect. Notes Artif. Intell. Lect. Notes Bioinformatics), vol. 6791 LNCS, 2011, p. 52–9. https://doi.org/10.1007/978-3-642-21735-7_7.
[393] Liu WK, Karpov EG, Park HS. Nano mechanics and materials : theory, multiscale methods and applications. John Wiley; 2006.
[394] Guo N, Zhao J. A coupled FEM/DEM approach for hierarchical multiscale modelling of granular media. Int J Numer Methods Eng 2014;99:789–818. https://doi.org/10.1002/NME.4702.
[395] Li X, Wang Z, Liang Y, Duan Q. Mixed FEM–Crushable DEM Nested Scheme in Second-Order Computational Homogenization for Granular Materials. Int J Geomech 2016;16:C4016004. https://doi.org/10.1061/(ASCE)GM.1943-5622.0000627.
[396] Li X, Wan K. A bridging scale method for granular materials with discrete particle assembly – Cosserat continuum modeling. Comput Geotech 2011;38:1052–68. https://doi.org/10.1016/J.COMPGEO.2011.07.001.
[397] Munjiza A. The combined finite-discrete element method. wiley 2004. https://doi.org/10.1002/0470020180.
[398] Dang HK, Meguid MA. An efficient finite–discrete element method for quasi-static nonlinear soil–structure interaction problems. Int J Numer Anal Methods Geomech 2013;37:130–49. https://doi.org/10.1002/NAG.1089.
[399] Guo L, Latham JP, Xiang J. Numerical simulation of breakages of concrete armour units using a three-dimensional fracture model in the context of the combined finite-discrete element method. Comput Struct 2015;146:117–42. https://doi.org/10.1016/J.COMPSTRUC.2014.09.001.
[400] Ma G, Chen Y, Yao F, Zhou W, Wang Q. Evolution of particle size and shape towards a steady state: Insights from FDEM simulations of crushable granular materials. Comput Geotech 2019;112:147–58. https://doi.org/10.1016/J.COMPGEO.2019.04.022.
[401] Zhou Q, Xu WJ, Lubbe R. Multi-scale mechanics of sand based on FEM-DEM coupling method. Powder Technol 2021;380:394–407. https://doi.org/10.1016/J.POWTEC.2020.11.006.
[402] Liu X, Gui N, Yang X, Tu J, Jiang S. A DEM-embedded finite element method for simulation of the transient heat conduction process in the pebble bed. Powder Technol 2021;377:607–20. https://doi.org/10.1016/J.POWTEC.2020.09.021.
[403] Andrade JE, Tu X. Multiscale framework for behavior prediction in granular media. Mech Mater 2009;41:652–69. https://doi.org/10.1016/j.mechmat.2008.12.005.
[404] Hu C, Zheng H-K, Qi; Zhang L, Yang; Sheng-Mei, Hu L.. Multiscale Approach and Meso-Macro-Mechanical Analysis of Granular Materials. Int J Geomech 2021. https://doi.org/10.1061/(ASCE)GM.1943-5622.0002047.
[405] Wang J. Continuum theory for dense gas-solid flow: A state-of-the-art review. Chem Eng Sci 2020;215:115428. https://doi.org/10.1016/J.CES.2019.115428.
[406] Gidaspow D. Multiphase flow and fluidization: continuum and kinetic theory descriptions. Academic press; 1994.
[407] Gidaspow D, Jung J, Singh RK. Hydrodynamics of fluidization using kinetic theory: an emerging paradigm: 2002 Flour-Daniel lecture. Powder Technol 2004;148:123–41. https://doi.org/10.1016/J.POWTEC.2004.09.025.
[408] Beetstra R, Van Der Hoef MA, Kuipers JAM. Drag force of intermediate reynolds number flow past mono- And bidisperse arrays of spheres. AIChE J 2007;53:489–501.
[409] Mei R. An approximate expression for the shear lift force on a spherical particle at finite reynolds number. Int J Multiph Flow 1992;18:145–7. https://doi.org/10.1016/0301-9322(92)90012-6.
[410] Sakai M, Koshizuka S. Large-scale discrete element modeling in pneumatic conveying. Chem Eng Sci 2009;64:533–9. https://doi.org/10.1016/J.CES.2008.10.003.
[411] Sakai M, Shibata K, Kawasaki VM, Koshizuka S. Numerical Simulation of a Bubbling Fluidized Bed by the Coarse Grain Modeling of DEM. J Soc Powder Technol Japan 2010;47:17–25. https://doi.org/10.4164/SPTJ.47.17.

[412] Sakai M, Shigeto Y, Sun X, Aoki T, Saito T, Xiong J, et al. Lagrangian-Lagrangian modeling for a solid–liquid flow in a cylindrical tank. Chem Eng J 2012; 200–202:663–72. https://doi.org/10.1016/J.CEJ.2012.06.080.
[413] Glowinski R, Pan TW, Hesla TI, Joseph DD, Glowinski R, Tpthdj.. A distributed Lagrange multiplier/fictitious domain method for particulate flows. Int J Multiph Flow 1999;25:755–94. https://doi.org/10.1016/S0301-9322(98)00048-2.
[414] Gallier S, Lemaire E, Lobry L, Peters F. A fictitious domain approach for the simulation of dense suspensions. J Comput Phys 2014;256:367–87. https://doi.org/10.1016/J.JCP.2013.09.015.
[415] Patankar NA, Singh P, Joseph DD, Glowinski R, Pan T-W. A new formulation of the distributed Lagrange multiplier/fictitious domain method for particulate flows. Int J Multiph Flow 2000;26:1509–24. https://doi.org/10.1016/S0301-9322(99)00100-7.
[416] Patankar NA. A formulation for fast computations of rigid particulate flows. Cent Turbul Res Annu Res Briefs 2001;2001:185–96.
[417] Diaz-Goano C, Minev PD, Nandakumar K. A fictitious domain/finite element method for particulate flows. J Comput Phys 2003;192:105–23. https://doi.org/10.1016/S0021-9991(03)00349-8.
[418] Yu Z, Shao X. A direct-forcing fictitious domain method for particulate flows. J Comput Phys 2007;227:292–314. https://doi.org/10.1016/j.jcp.2007.07.027.
[419] Shirgaonkar AA, MacIver MA, Patankar NA. A new mathematical formulation and fast algorithm for fully resolved simulation of self-propulsion. J Comput Phys 2009;228:2366–90. https://doi.org/10.1016/j.jcp.2008.12.006.
[420] Di Felice R. The voidage function for fluid-particle interaction systems. Int J Multiph Flow 1994;20:153–9. https://doi.org/10.1016/0301-9322(94)90011-6.
[421] Koch DL, Hill RJ. Inertial effects in suspension and porous-media flows. Annu Rev Fluid Mech 2001;33:619–47. https://doi.org/10.1146/annurev.fluid.33.1.619.
[422] Koch DL, Sangani AS. Particle pressure and marginal stability limits for a homogeneous monodisperse gas-fluidized bed: kinetic theory and numerical simulations. J Fluid Mech 1999;400:229–63. https://doi.org/10.1017/S0022112099006485.
[423] van Buijtenen MS, van Dijk WJ, Deen NG, Kuipers JAM, Leadbeater T, Parker DJ. Numerical and experimental study on multiple-spout fluidized beds. Chem Eng Sci 2011;66:2368–76. https://doi.org/10.1016/J.CES.2011.02.055.
[424] Hilton JE, Ying DY, Cleary PW. Modelling spray coating using a combined CFD–DEM and spherical harmonic formulation. Chem Eng Sci 2013;99:141–60. https://doi.org/10.1016/j.ces.2013.05.051.
[425] Naz MY, Sulaiman SA, Shukrullah S, Ghaffar A, Khan Y, Ahmad I. PIV investigations on particle velocity distribution in uniform swirling regime of fluidization. Granul Matter 2017;19:1–7. https://doi.org/10.1007/S10035-017-0727-4/FIGURES/8.
[426] Börner M, Bück A, Tsotsas E. DEM-CFD investigation of particle residence time distribution in top-spray fluidised bed granulation. Chem Eng Sci 2017;161: 187–97. https://doi.org/10.1016/j.ces.2016.12.020.
[427] He Y, Bayly AE, Hassanpour A. Coupling CFD-DEM with dynamic meshing: A new approach for fluid-structure interaction in particle-fluid flows. Powder Technol 2018;325:620–31. https://doi.org/10.1016/J.POWTEC.2017.11.045.
[428] Zhang H, Li T, Huang Z, Kuang S, Yu A. Investigation on vertical plug formation of coarse particles in a non-mechanical feeder by CFD-DEM coupling method. Powder Technol 2018;332:79–89. https://doi.org/10.1016/J.POWTEC.2018.03.055.
[429] Yang D, Xing B, Li J, Wang Y, Hu N, Jiang S. Experiment and simulation analysis of the suspension behavior of large (5–30 mm) nonspherical particles in vertical pneumatic conveying. Powder Technol 2019;354:442–55. https://doi.org/10.1016/J.POWTEC.2019.06.023.
[430] Cook BK, Noble DR, Williams JR. A direct simulation method for particle-fluid systems, vol. 21. Emerald Group Publishing Limited; 2004.
[431] Kutay ME, Aydilek AH, Masad E. Laboratory validation of lattice Boltzmann method for modeling pore-scale flow in granular materials. Comput Geotech 2006; 33:381–95. https://doi.org/10.1016/j.compgeo.2006.08.002.
[432] El Shamy U, Abdelhamid Y. Modeling granular soils liquefaction using coupled lattice Boltzmann method and discrete element method. Soil Dyn Earthq Eng 2014;67:119–32. https://doi.org/10.1016/j.soildyn.2014.09.004.
[433] Wang M, Feng YT, Pande GN, Chan AHC, Zuo WX. Numerical modelling of fluid-induced soil erosion in granular filters using a coupled bonded particle lattice Boltzmann method. Comput Geotech 2017;82:134–43. https://doi.org/10.1016/j.compgeo.2016.10.006.
[434] Richefeu V, Radjai F, Delenne JY. Lattice Boltzmann modelling of liquid distribution in unsaturated granular media. Comput Geotech 2016;80:353–9. https://doi.org/10.1016/j.compgeo.2016.02.017.
[435] Han K, Feng YT, Owen DRJ. Coupled lattice Boltzmann and discrete element modelling of fluid–particle interaction problems. Comput Struct 2007;85:1080–8. https://doi.org/10.1016/J.COMPSTRUC.2006.11.016.
[436] Soundararajan KK. Multi-scale multiphase modelling of granular flows. University of Cambridge; 2015.
[437] Zhang X, Tahmasebi P. Coupling irregular particles and fluid: Complex dynamics of granular flows. Comput Geotech 2022;143:104624. https://doi.org/10.1016/j.compgeo.2021.104624.
[438] Peng Z, Doroodchi E, Moghtaderi B. Heat transfer modelling in Discrete Element Method (DEM)-based simulations of thermal processes: Theory and model development. Pergamon 2020;79. https://doi.org/10.1016/J.PECS.2020.100847.
[439] Li J, Mason DJ. Application of the discrete element modelling in air drying of particulate solids. Http://DxDoiOrg/101081/DRT-120002542 2007;20:255–82. https://doi.org/10.1081/DRT-120002542.
[440] Kharaghani A, Metzger T, Tsotsas E. A proposal for discrete modeling of mechanical effects during drying, combining pore networks with DEM. AIChE J 2011; 57:872–85. https://doi.org/10.1002/AIC.12318.
[441] Sudbrock F, Kruggel-Emden H, Wirtz S, Scherer V. Convective drying of agitated silica gel and beech wood particle beds—experiments and transient DEM-CFD simulations. Dry Technol 2015;33:1808–20. https://doi.org/10.1080/07373937.2015.1026982.
[442] Zhou ZY, Yu AB, Zulli P. A new computational method for studying heat transfer in fluid bed reactors. Powder Technol 2010;197:102–10. https://doi.org/10.1016/J.POWTEC.2009.09.002.
[443] Gerber S, Oevermann M. A two dimensional Euler-Lagrangian model of wood gasification in a charcoal bed – Part I: model description and base scenario. Fuel 2014;115:385–400. https://doi.org/10.1016/J.FUEL.2013.06.049.
[444] Zhu HP, Zhou ZY, Yu AB, Zulli P. Stress fields of solid flow in a model blast furnace. Granul Matter 2009.269–80.;2009(115):11. https://doi.org/10.1007/S10035-008-0123-1.
[445] Krause B, Liedmann B, Wiese J, Wirtz S, Scherer V. Coupled three dimensional DEM–CFD simulation of a lime shaft kiln—Calcination, particle movement and gas phase flow field. Chem Eng Sci 2015;134:834–49. https://doi.org/10.1016/J.CES.2015.06.002.
[446] Hou Q-F, Zhou Z-Y, Yu A-B. Computational Study of the Effects of Material Properties on Heat Transfer in Gas Fluidization. Ind Eng Chem Res 2012;51: 11572–86. https://doi.org/10.1021/IE3015999.
[447] Hou QF, Zhou ZY, Yu AB. Gas–solid flow and heat transfer in fluidized beds with tubes: Effects of material properties and tube array settings. Powder Technol 2016;296:59–71. https://doi.org/10.1016/J.POWTEC.2015.03.028.
[448] Deen NG, Peters EAJF, Padding JT, Kuipers JAM. Review of direct numerical simulation of fluid–particle mass, momentum and heat transfer in dense gas–solid flows. Chem Eng Sci 2014;116:710–24. https://doi.org/10.1016/J.CES.2014.05.039.
[449] Owen DRJ, Leonardi CR, Feng YT. An efficient framework for fluid-structure interaction using the lattice Boltzmann method and immersed moving boundaries. Int J Numer Methods Eng 2011;87:66–95. https://doi.org/10.1002/nme.2985.
[450] Kwapinska M, Saage G, Tsotsas E. Mixing of particles in rotary drums: A comparison of discrete element simulations with experimental results and penetration models for thermal processes. Powder Technol 2006;161:69–78. https://doi.org/10.1016/J.POWTEC.2005.08.038.
[451] Kwapinska M, Saage G, Tsotsas E. Continuous versus discrete modelling of heat transfer to agitated beds. Powder Technol 2008;181:331–42. https://doi.org/10.1016/J.POWTEC.2007.05.025.
[452] Jajcevic D, Siegmann E, Radeke C, Khinast JG. Large-scale CFD–DEM simulations of fluidized granular systems. Chem Eng Sci 2013;98:298–310. https://doi.org/10.1016/J.CES.2013.05.014.
[453] Zhong W, Yu A, Zhou G, Xie J, Zhang H. CFD simulation of dense particulate reaction system: Approaches, recent advances and applications. Chem Eng Sci 2016;140:16–43. https://doi.org/10.1016/J.CES.2015.09.035.

[454] Zhuang YQ, Chen XM, Luo ZH, Xiao J. CFD–DEM modeling of gas–solid flow and catalytic MTO reaction in a fluidized bed reactor. Comput Chem Eng 2014;60:1–16. https://doi.org/10.1016/J.COMPCHEMENG.2013.08.007.
[455] Incropera FP, DeWitt DP. Fundamentals of Heat and Mass Transfer 1996. https://doi.org/10.1016/j.applthermaleng.2011.03.022.
[456] Batchelor GK, O'Brien RW. Thermal or electrical conduction through a granular material. Proc R Soc London A Math Phys Sci 1977;355:313–33. https://doi.org/10.1098/RSPA.1977.0100.
[457] Soo SL. Fluid dynamics of multiphase systems. WALTHAM, MASS, BLAISDELL Publ CO, 1967 524 P, 206 FIG, 8 TAB, 886 REF 1967.
[458] Sun J, Chen MM. A theoretical analysis of heat transfer due to particle impact. Int J Heat Mass Transf 1988;31:969–75. https://doi.org/10.1016/0017-9310(88)90085-3.
[459] Zhou JH, Yu AB, Horio M. Finite element modeling of the transient heat conduction between colliding particles. Chem Eng J 2008;139:510–6. https://doi.org/10.1016/J.CEJ.2007.08.024.
[460] Zhou ZY, Yu AB, Zulli P. Particle scale study of heat transfer in packed and bubbling fluidized beds. AIChE J 2009;55:868–84. https://doi.org/10.1002/AIC.11823.
[461] Morris AB, Pannala S, Ma Z, Hrenya CM. Development of soft-sphere contact models for thermal heat conduction in granular flows. AIChE J 2016;62:4526–35. https://doi.org/10.1002/AIC.15331.
[462] Patil AV, Peters EAJF, Kuipers JAM. Comparison of CFD-DEM heat transfer simulations with infrared/visual measurements. Chem Eng J 2015;277:388–401.
[463] Rong D, Horio M. DEM simulation of char combustion in a fluidized bed. 1999.
[464] Musser JMH. Modeling of heat transfer and reactive chemistry for particles in gas-solid flow utilizing continuum-discrete methodology (CDM). PhD Thesis 2011:West Virginia University. https://doi.org/https://doi.org/10.33915/etd.4760.
[465] Cheng GJ, Yu AB, Zulli P. Evaluation of effective thermal conductivity from the structure of a packed bed. Chem Eng Sci 1999;54:4199–209. https://doi.org/10.1016/S0009-2509(99)00125-6.
[466] Gan J, Zhou Z, Yu A. Particle scale study of heat transfer in packed and fluidized beds of ellipsoidal particles. Chem Eng Sci 2016;144:201–15.
[467] Chen L, Wang C, Moscardini M, Kamlah M, Liu S. A DEM-based heat transfer model for the evaluation of effective thermal conductivity of packed beds filled with stagnant fluid: Thermal contact theory and numerical simulation. Int J Heat Mass Transf 2019;132:331–46.
[468] Vargas WL, McCarthy JJ. Conductivity of granular media with stagnant interstitial fluids via thermal particle dynamics simulation. Int J Heat Mass Transf 2002;45:4847–56. https://doi.org/10.1016/S0017-9310(02)00175-8.
[469] Tsory T, Ben-Jacob N, Brosh T, Levy A. Thermal DEM–CFD modeling and simulation of heat transfer through packed bed. Powder Technol 2013;244:52–60. https://doi.org/10.1016/J.POWTEC.2013.04.013.
[470] Cheng G, Gan J, Xu D, Yu A. Evaluation of effective thermal conductivity in random packed bed: Heat transfer through fluid voids and effect of packing structure. Powder Technol 2020;361:326–36.
[471] Baeyens J, van Gauwbergen D, Vinckier I. Pneumatic drying: the use of large-scale experimental data in a design procedure. Powder Technol 1995;83:139–48.
[472] Feng ZG, Michaelides EE. A numerical study on the transient heat transfer from a sphere at high Reynolds and Peclet numbers. Int J Heat Mass Transf 2000;43:219–29.
[473] Gnielinski V. Formula for calculating the heat and mass transfer in through flow of a fixed bed at medium and large Peclet. Process-Technology 1978;12:63–366.
[474] Gnielinski V. Equations for the calculation of heat and mass transfer during flow through stationary spherical packings at moderate and high Peclet numbers. Int Chem Eng;(United States) 1981;21.
[475] Achenbach E. Heat and flow characteristics of packed beds. Exp Therm Fluid Sci 1995;10:17–27. https://doi.org/10.1016/0894-1777(94)00077-L.
[476] Li J, Mason DJ. A computational investigation of transient heat transfer in pneumatic transport of granular particles. Powder Technol 2000;112:273–82. https://doi.org/10.1016/S0032-5910(00)00302-8.
[477] Li J, Campbell GM, Mujumdar AS. Discrete Modeling and Suggested Measurement of Heat Transfer in Gas-Solids Flows. Http://DxDoiOrg/101081/DRT-120021851 2007;21:979–94. https://doi.org/10.1081/DRT-120021851.
[478] Li J, Mason DJ, Mujumdar AS. A Numerical Study of Heat Transfer Mechanisms in Gas-Solids Flows Through Pipes Using a Coupled CFD and DEM Model. Http://DxDoiOrg/101081/DRT-120025511 2007;21:1839–66. https://doi.org/10.1081/DRT-120025511.
[479] Zhang HW, Zhou Q, Xing HL, Muhlhaus H. A DEM study on the effective thermal conductivity of granular assemblies. Powder Technol 2011;205:172–83. https://doi.org/10.1016/J.POWTEC.2010.09.008.
[480] Oschmann T, Schiemann M, Kruggel-Emden H. Development and verification of a resolved 3D inner particle heat transfer model for the Discrete Element Method (DEM). Powder Technol 2016;291:392–407. https://doi.org/10.1016/J.POWTEC.2015.12.008.
[481] Bellan S, Kodama T, Matsubara K, Gokon N, Cho HS, Inoue K. Thermal performance of a 30 kW fluidized bed reactor for solar gasification: A CFD-DEM study. Chem Eng J 2019:1287–300. https://doi.org/10.1016/j.cej.2018.10.111.
[482] Hou QF, Zhou ZY, Yu AB. Computational study of heat transfer in a bubbling fluidized bed with a horizontal tube. AIChE J 2012;58:1422–34. https://doi.org/10.1002/AIC.12700.
[483] Krause B, Liedmann B, Wiese J, Bucher P, Wirtz S, Piringer H, et al. 3D-DEM-CFD simulation of heat and mass transfer, gas combustion and calcination in an intermittent operating lime shaft kiln. Int J Therm Sci 2017;117:121–35.
[484] Jiang M, Shen Z, Zhou W, Arroyo M, Zhang W. Coupled CFD–DEM method for undrained biaxial shear test of methane hydrate bearing sediments. Granul Matter 2018;20:63. https://doi.org/10.1007/s10035-018-0826-x.
[485] Cheng GJ, Yu AB. Particle scale evaluation of the effective thermal conductivity from the structure of a packed bed: Radiation heat transfer. Ind Eng Chem Res 2013;52:12202–11. https://doi.org/10.1021/IE3033137.
[486] Feingold A, Gupta KG. New analytical approach to the evaluation of configuration factors in radiation from spheres and infinitely long cylinders. J Heat Transfer 1970;92:69–166. https://doi.org/10.1115/1.3449647.
[487] Jones LR. Diffuse radiation view factors between two spheres. J Heat Transfer 1965;87:421–2. https://doi.org/10.1115/1.3689127.
[488] Wu H, Gui N, Yang X, Tu J, Jiang S. Effect of scale on the modeling of radiation heat transfer in packed pebble beds. Int J Heat Mass Transf 2016;101:562–9. https://doi.org/10.1016/j.ijheatmasstransfer.2016.05.090.
[489] Feng YT, Han K. An accurate evaluation of geometric view factors for modelling radiative heat transfer in randomly packed beds of equally sized spheres. Int J Heat Mass Transf 2012;55:6374–83. https://doi.org/10.1016/j.ijheatmasstransfer.2012.06.025.
[490] Maltby JD, Burns PJ. Performance, accuracy, and convergence in a three-dimensional Monte Carlo radiative heat transfer simulation. Numer Heat Transf Part B Fundam 1991;19:191–209. https://doi.org/10.1080/10407799108944963.
[491] Walker T, Xue S-C, Barton GW. Numerical Determination of Radiative View Factors Using Ray Tracing. J Heat Transfer 2010;132:1–6. https://doi.org/10.1115/1.4000974.
[492] Forgber T, Radl S. A novel approach to calculate radiative thermal exchange in coupled particle simulations. Powder Technol 2018;323:24–44. https://doi.org/10.1016/J.POWTEC.2017.09.014.
[493] Baniasadi M, Baniasadi M, Peters B. Coupled CFD-DEM with heat and mass transfer to investigate the melting of a granular packed bed. Chem Eng Sci 2018;178:136–45.
[494] Oschmann T, Kruggel-Emden H. A novel method for the calculation of particle heat conduction and resolved 3D wall heat transfer for the CFD/DEM approach. Powder Technol 2018;338:289–303. https://doi.org/10.1016/j.powtec.2018.07.017.
[495] Gan H, Feng JJ, Hu HH. Simulation of the sedimentation of melting solid particles. Int J Multiph Flow 2003;29:751–69. https://doi.org/10.1016/S0301-9322(03)00035-1.
[496] Syamlal M, Gidaspow D. Hydrodynamics of fluidization: Prediction of wall to bed heat transfer coefficients. AIChE J 1985;31:127–35. https://doi.org/10.1002/AIC.690310115.
[497] Ranz W, Marshall W. Evaporation from drops. Chem Eng Prog 1952;48:173–80.

[498] Gunn DJ. Transfer of heat or mass to particles in fixed and fluidised beds. Int J Heat Mass Transf 1978;21:467–76. https://doi.org/10.1016/0017-9310(78)90080-7.
[499] Dixon AG, Ertan Taskin M, Hugh Stitt E, Nijemeisland M. 3D CFD simulations of steam reforming with resolved intraparticle reaction and gradients. Chem Eng Sci 2007;62:4963–6. https://doi.org/10.1016/J.CES.2006.11.052.
[500] Ciesielski PN, Pecha MB, Bharadwaj VS, Mukarakate C, Leong GJ, Kappes B, et al. Advancing catalytic fast pyrolysis through integrated multiscale modeling and experimentation: Challenges, progress, and perspectives. Wiley Interdiscip Rev Energy Environ 2018;7:e297.
[501] Ciesielski PN, Pecha MB, Lattanzi AM, Bharadwaj VS, Crowley MF, Bu L, et al. Advances in Multiscale Modeling of Lignocellulosic Biomass. ACS Sustain Chem Eng 2020;8:3512–31. https://doi.org/10.1021/ACSSUSCHEMENG.9B07415.
[502] Gao X, Yu J, Li C, Panday R, Xu Y, Li T, et al. Comprehensive experimental investigation on biomass-glass beads binary fluidization: A data set for CFD model validation. AIChE J 2020;66:e16843.
[503] Lu L, Gao X, Shahnam M, Rogers WA. Coarse grained computational fluid dynamic simulation of sands and biomass fluidization with a hybrid drag. AIChE J 2020;66:e16867.
[504] Wang S, Luo K, Fan J. CFD-DEM coupled with thermochemical sub-models for biomass gasification: Validation and sensitivity analysis. Chem Eng Sci 2020;217:115550. https://doi.org/10.1016/J.CES.2020.115550.
[505] Ge W, Wang L, Xu J, Chen F, Zhou G, Lu L, et al. Discrete simulation of granular and particle-fluid flows: from fundamental study to engineering application. Rev Chem Eng 2017;33:551–623. https://doi.org/10.1515/REVCE-2015-0079.
[506] Xiong Q, Kong S-C. High-Resolution Particle-Scale Simulation of Biomass Pyrolysis. ACS Sustain Chem Eng 2016;4:5456–61. https://doi.org/10.1021/ACSSUSCHEMENG.6B01020.
[507] Pecha MB, Garcia-Perez M, Foust TD, Ciesielski PN. Estimation of Heat Transfer Coefficients for Biomass Particles by Direct Numerical Simulation Using Microstructured Particle Models in the Laminar Regime. ACS Sustain Chem Eng 2016;5:1046–53. https://doi.org/10.1021/ACSSUSCHEMENG.6B02341.
[508] Zeiser T, Lammers P, Klemm E, Li YW, Bernsdorf J, Brenner G. CFD-calculation of flow, dispersion and reaction in a catalyst filled tube by the lattice Boltzmann method. Chem Eng Sci 2001;56:1697–704. https://doi.org/10.1016/S0009-2509(00)00398-5.
[509] Freund H, Zeiser T, Huber F, Klemm E, Brenner G, Durst F, et al. Numerical simulations of single phase reacting flows in randomly packed fixed-bed reactors and experimental validation. Chem Eng Sci 2003;58:903–10. https://doi.org/10.1016/S0009-2509(02)00622-X.
[510] Yuen EHL, Sederman AJ, Sani F, Alexander P, Gladden LF. Correlations between local conversion and hydrodynamics in a 3-D fixed-bed esterification process: An MRI and lattice-Boltzmann study. Chem Eng Sci 2003;58:613–9. https://doi.org/10.1016/S0009-2509(02)00586-9.
[511] Gao X, Yu J, Lu L, Rogers WA. Coupling particle scale model and SuperDEM-CFD for multiscale simulation of biomass pyrolysis in a packed bed pyrolyzer. AIChE J 2021;67:e17139.
[512] Hessels CJMC, Tang YY, Buist KAK, Deen NGN. Modeling Iron Oxide Reduction using ParScale 2020.
[513] Wen CY. Noncatalytic Heterogeneous Solid Fluid Reaction Models. Ind Eng Chem 2002;60:34–54. https://doi.org/10.1021/IE50705A007.
[514] Noorman S, Gallucci F, Van Sint AM, Kuipers JAM. A theoretical investigation of CLC in packed beds. Part 1: Particle model. Chem Eng J 2011;167:297–307. https://doi.org/10.1016/J.CEJ.2010.12.068.
[515] Radl S, Forgber T, Aigner A, Kloss C. Parscale-an open-source library for the simulation of intra-particle heat and mass transport processes in coupled simulations. Part. IV Proc. IV Int Conf Part Methods Fundam Appl 2015:117–27.
[516] Oda M, Iwashita K. Mechanics of granular materials: an introduction. CRC Press; 2020.
[517] Powrie W. Soil mechanics : concepts and applications. Spon Press; 2004.
[518] Spencer AJM. A theory of the kinematics of ideal soils under plane strain conditions. J Mech Phys Solids 1964;12:337–51. https://doi.org/10.1016/0022-5096(64)90029-8.
[519] Lun CKK, Savage SB, Jeffrey DJ, Chepurniy N. Kinetic theories for granular flow: inelastic particles in Couette flow and slightly inelastic particles in a general flowfield. J Fluid Mech 1984;140:223–56. https://doi.org/10.1017/S0022112084000586.
[520] Campbell CS. Rapid Granular Flows. Http://DxDoiOrg/101146/AnnurevFl22010190000421 2003;22:57–90. https://doi.org/10.1146/ANNUREV.FL.22.010190.000421.
[521] Johnson PC, Jackson R. Frictional–collisional constitutive relations for granular materials, with application to plane shearing. J Fluid Mech 1987;176:67–93. https://doi.org/10.1017/S0022112087000570.
[522] Cambou B, Dubujet P, Emeriault F, Sidoroff F. Homogenization for granular materials. Eur J Mech A Solids 1995;14:255–76.
[523] Chang CS, Gao J. Kinematic and static hypotheses for constitutive modelling of granulates considering particle rotation. Acta Mech 1996;115:213–29. https://doi.org/10.1007/BF01187439.
[524] Kruyt NP, Rothenburg L. Kinematic and static assumptions for homogenization in micromechanics of granular materials. Mech Mater 2004;36:1157–73. https://doi.org/10.1016/j.mechmat.2002.12.001.
[525] Froiio F, Tomassetti G, Vardoulakis I. Mechanics of granular materials: The discrete and the continuum descriptions juxtaposed. Int J Solids Struct 2006;43:7684–720. https://doi.org/10.1016/j.ijsolstr.2006.03.023.
[526] Goddard JD. From granular matter to generalized continuum. Lect Notes Math 2008;1937:1–22. https://doi.org/10.1007/978-3-540-78277-3_1.
[527] Goddard JD. Microstructural origins of continuum stress fields—a brief history and some unresolved issues 1986:179–208.
[528] Bagi K. Stress and strain in granular assemblies 1996;22:165–77. https://doi.org/10.1016/0167-6636(95)00044-5.
[529] Babic M. Average balance equations for granular materials. Int J Eng Sci 1997;35:523–48. https://doi.org/10.1016/s0020-7225(96)00094-8.
[530] Nemat-Nasser S. A micromechanically-based constitutive model for frictional deformation of granular materials. J Mech Phys Solids 2000;48:1541–63. https://doi.org/10.1016/s0022-5096(99)00089-7.
[531] Lätzel M, Luding S, Herrmann HJJ. From discontinuous models towards a continuum description. Springer 2001:215–30. https://doi.org/10.1007/3-540-44424-6_16.
[532] Bardet JP, Vardoulakis I. Asymmetry of stress in granular media. Int J Solids Struct 2001;38:353–67. https://doi.org/10.1016/S0020-7683(00)00021-4.
[533] Zhu HP, Yu AB. Averaging method of granular materials. Phys Rev E 2002;66:021302. https://doi.org/10.1103/PhysRevE.66.021302.
[534] Ball RC, Blumenfeld R. Stress Field in Granular Systems: Loop Forces and Potential Formulation. Phys Rev Lett 2002;88:115505. https://doi.org/10.1103/PhysRevLett.88.115505.
[535] Ehlers W, Ramm E, Diebels S, D'Addetta GA. From particle ensembles to Cosserat continua: Homogenization of contact forces towards stresses and couple stresses. Int J Solids Struct 2003;40:6681–702. https://doi.org/10.1016/S0020-7683(03)00418-9.
[536] Li X, Yu HS, Li XS. Macro–micro relations in granular mechanics. Int J Solids Struct 2009;46:4331–41. https://doi.org/10.1016/J.IJSOLSTR.2009.08.018.
[537] Roy S, Singh A, Luding S, Weinhart T. Micro–macro transition and simplified contact models for wet granular materials. Comput Part Mech 2015.449–62.;2015(34):3. https://doi.org/10.1007/S40571-015-0061-8.
[538] Born M, Huang K. Dynamical Theory of Crystal Lattices. Clarendon, 1954. Oxford: Clarendon; 1998.
[539] Love AEHA. Treatise of Mathematical Theory of Elasticity. Cambridge Univ Press; 1927.
[540] Voigt W. Theoretische Studien über die Elasticitätverhältnisse der Krystalle. Abhandt Ges Wiss Gött 1887;34:3–52.
[541] Moreno R, Borga M, Smedby Ö. Techniques for Computing Fabric Tensors: A Review. Math Vis 2014:271–92. https://doi.org/10.1007/978-3-642-54301-2_12.
[542] Cambou B, Chaze M, Dedecker F. Change of scale in granular materials. Eur J Mech - A/Solids 2000;19:999–1014. https://doi.org/10.1016/S0997-7538(00)01114-1.
[543] Chang CS, Hicher PY. An elasto-plastic model for granular materials with microstructural consideration. Int J Solids Struct 2005;42:4258–77. https://doi.org/10.1016/J.IJSOLSTR.2004.09.021.
[544] Nicot F, Darve F, RNVO Group. Natural Hazards and Vulnerability of Structures. A multi-scale approach to granular materials. Mech Mater 2005;37:980–1006. https://doi.org/10.1016/J.MECHMAT.2004.11.002.

[545] Christoffersen J, Mehrabadi MM, Nemat-Nasser S. A Micromechanical Description of Granular Material Behavior. J Appl Mech 1981;48:339–44. https://doi.org/10.1115/1.3157619.
[546] Ng TT. Shear strength and micro-descriptors of bidisperse ellipsoids under different loading paths. Mech Mater 2009;41:748–63. https://doi.org/10.1016/J.MECHMAT.2009.01.031.
[547] Kumar N, Imole OI, Magnanimo V, Luding S. Effects of polydispersity on the micro–macro behavior of granular assemblies under different deformation paths. Particuology 2014;12:64–79. https://doi.org/10.1016/j.partic.2013.07.011.
[548] Roscoe KH, Schofield AN, Wroth CP. On the yielding of soils. Geotechnique 1958;8:22–53. https://doi.org/10.1680/GEOT.1958.8.1.22.
[549] Casagrande A. Characteristics of cohesionless soils affecting the stability of slopes and earth fills. J Bost Soc Civ Eng 1936;23:13–32.
[550] Schofield AN, Wroth P. Critical state soil mechanics, vol. 310. McGraw-hill London; 1968.
[551] Been K, Jefferies MG. A state parameter for sands. Geotechnique 1985;35:99–112. https://doi.org/10.1680/GEOT.1985.35.2.99.
[552] Been K, Hachey J, Jefferies MG. The critical state of sands. Geotechnique 1991;41:365–81. https://doi.org/10.1680/GEOT.1991.41.3.365.
[553] Li XS, Dafalias YF. Dissipation consistent fabric tensor definition from DEM to continuum for granular media. J Mech Phys Solids 2015;78:141–53.
[554] Theocharis AI, Vairaktaris E, Dafalias YF, Papadimitriou AG. Necessary and sufficient conditions for reaching and maintaining critical state. Int J Numer Anal Methods Geomech 2019;43:2041–55. https://doi.org/10.1002/NAG.2943.
[555] Guo N, Zhao J. The signature of shear-induced anisotropy in granular media. Comput Geotech 2013;47:1–15. https://doi.org/10.1016/J.COMPGEO.2012.07.002.
[556] Salvatore E, Modoni G, Andò E, Albano M, Viggiani G. Determination of the critical state of granular materials with triaxial tests. Soils Found 2017;57:733–44.
[557] Li XS, Dafalias YF, Wang ZL. State-dependent dilatancy in critical-state constitutive modelling of sand. Can Geotech J 1999;36:599–611. https://doi.org/10.1139/CGJ-36-4-599.
[558] Gao Z, Zhao J, Li XS, Dafalias YF. A critical state sand plasticity model accounting for fabric evolution. Int J Numer Anal Methods Geomech 2014;38:370–90. https://doi.org/10.1002/NAG.2211.
[559] Rothenburg L, Bathurst RJ. Analytical study of induced anisotropy in idealized granular materials. Geotechnique 1989;39:601–14. https://doi.org/10.1680/geot.1989.39.4.601.
[560] Oda M. The Mechanism of Fabric Changes During Compressional Deformation of Sand. Soils Found 1972;12:1–18. https://doi.org/10.3208/SANDF1972.12.1.
[561] Cowin SC. Fabric dependence of an anisotropic strength criterion. Mech Mater 1986;5:251–60. https://doi.org/10.1016/0167-6636(86)90022-0.
[562] Kruyt NP, Rothenburg L. A strain–displacement–fabric relationship for granular materials. Int J Solids Struct 2019;165:14–22. https://doi.org/10.1016/J.IJSOLSTR.2019.01.028.
[563] Chang CS, Yin Z-Y. Micromechanical Modeling for Inherent Anisotropy in Granular Materials. J Eng Mech 2009;136:830–9. https://doi.org/10.1061/(ASCE)EM.1943-7889.0000125.
[564] Dafalias YF, Papadimitriou AG, Li XS. Sand Plasticity Model Accounting for Inherent Fabric Anisotropy. J Eng Mech 2004;130:1319–33. https://doi.org/10.1061/(ASCE)0733-9399(2004)130:11(1319).
[565] Li XS, Dafalias YF. Constitutive Modeling of Inherently Anisotropic Sand Behavior. J Geotech Geoenvironmental Eng 2002;128:868–80. https://doi.org/10.1061/(ASCE)1090-0241(2002)128:10(868).
[566] Oda M. Inherent and induced anisotropy in plasticity theory of granular soils. Mech Mater 1993;16:35–45. https://doi.org/10.1016/0167-6636(93)90025-M.
[567] Tong Z, Fu P, Zhou S, Yannis •, Dafalias F.. Experimental investigation of shear strength of sands with inherent fabric anisotropy. Acta Geotech 2014;9:257–75. https://doi.org/10.1007/s11440-014-0303-6.
[568] Ueda K, Iai S. Constitutive modeling of inherent anisotropy in a strain space multiple mechanism model for granular materials. Int J Numer Anal Methods Geomech 2019;43:708–37. https://doi.org/10.1002/NAG.2883.
[569] Wu W. Rational approach to anisotropy of sand. Int J Numer Anal Methods Geomech 1997;22:921–40. https://doi.org/10.1002/(SICI)1096-9853(199811022:11.
[570] Yao Y, Tian Y, Gao Z. Anisotropic UH model for soils based on a simple transformed stress method. Int J Numer Anal Methods Geomech 2017;41:54–78. https://doi.org/10.1002/NAG.2545.
[571] Zhao CF, Pinzón G, Wiebicke M, Andò E, Kruyt NP, Viggiani G. Evolution of fabric anisotropy of granular soils: x-ray tomography measurements and theoretical modelling. Comput Geotech 2021;133:104046. https://doi.org/10.1016/J.COMPGEO.2021.104046.
[572] Satake M. Constitution of mechanics of granular materials through the graph theory. Proc. US-Japan Semin. Contin. Mech. Stat. Appr. Mech. Granul. Mater.: Sendai; 1978. p. 203–15.
[573] Kuhn MR. Structured deformation in granular materials. Mech Mater 1999;31:407–29. https://doi.org/10.1016/S0167-6636(99)00010-1.
[574] Chang CS. Micromechanical modeling of deformation and failure for granulates with frictional contacts. Mech Mater 1993;16:13–24. https://doi.org/10.1016/0167-6636(93)90023-K.
[575] Drescher A, de Josselin de Jong G.. Photoelastic verification of a mechanical model for the flow of a granular material. J Mech Phys Solids 1972;20:337–40. https://doi.org/10.1016/0022-5096(72)90029-4.
[576] Li XS, Dafalias YF. Anisotropic Critical State Theory: Role of Fabric. J Eng Mech 2011;138:263–75. https://doi.org/10.1061/(ASCE)EM.1943-7889.0000324.
[577] Li X, Li X-S. Micro-Macro Quantification of the Internal Structure of Granular Materials. J Eng Mech 2009;135:641–56. https://doi.org/10.1061/(ASCE)0733-9399(2009)135:7(641).
[578] Yang ZX, Wu Y. Critical State for Anisotropic Granular Materials: A Discrete Element Perspective. Int J Geomech 2017;17:04016054. https://doi.org/10.1061/(ASCE)GM.1943-5622.0000720.
[579] Lee KL, Farhoomand I. Compressibility And Crushing Of Granular Soil In Anisotropic Triaxial Compression. Can Geotech J 1967;4:68–86. https://doi.org/10.1139/T67-012.
[580] Lim WL, McDowell GR. Discrete element modelling of railway ballast. Granul Matter 2005;7:19–29. https://doi.org/10.1007/S10035-004-0189-3.
[581] Omidvar M, Iskander M, Bless S. Response of granular media to rapid penetration. Int J Impact Eng 2014;66:60–82.
[582] Abe S, Mair K. Grain fracture in 3D numerical simulations of granular shear. Geophys Res Lett 2005;32:L05305. https://doi.org/10.1029/2004GL022123.
[583] Anders MH, Laubach SE, Scholz CH. Microfractures: A review. J Struct Geol 2014;69:377–94.
[584] Minh NH, Cheng YP. A DEM investigation of the effect of particle-size distribution on one-dimensional compression. Géotechnique 2015;63:44–53. https://doi.org/10.1680/GEOT.10.P.058.
[585] Kikumoto M, Muir Wood D, Russell A. Particle crushing and deformation behaviour. Soils Found 2010;50:547–63. https://doi.org/10.3208/SANDF.50.547.
[586] McDowell GR, Bolton MD. On the micromechanics of crushable aggregates. Geotechnique 1998;48:667–79. https://doi.org/10.1680/GEOT.1998.48.5.667.
[587] Wood DM, Maeda K. Changing grading of soil: effect on critical states. Acta Geotech 2008;3:3–14. https://doi.org/10.1007/s11440-007-0041-0.
[588] Weibull W. A Statistical Distribution Function of Wide Applicability. J Appl Mech 1951;18:293–7. https://doi.org/10.1115/1.4010337.
[589] McDowell GR, Bolton MD, Robertson D. The fractal crushing of granular materials. J Mech Phys Solids 1996;44:2079–101.
[590] Nakata AFL, Hyde M, Hyodo H, Murata.. A probabilistic approach to sand particle crushing in the triaxial test. Géotechnique 1999;49:567–83. https://doi.org/10.1680/geot.1999.49.5.567.
[591] McDowell GR, Amon A. The application of weibull statistics to the fracture of soil particles. Soils Found 2000;40:133–41. https://doi.org/10.3208/SANDF.40.5_133.
[592] McDowell GR. On the yielding and plastic compression of sand. Soils Found 2002;42:139–45. https://doi.org/10.3208/SANDF.42.139.
[593] Jaeger JC. Failure of rocks under tensile conditions. Int J Rock Mech Min Sci 1967;4:219–27.
[594] Ben-Nun O, Einav I. The role of self-organization during confined comminution of granular materials. Philos Trans R Soc A Math Phys Eng Sci 2010;368:231–47.
[595] Turner AK, Kim FH, Penumadu D, Herbold EB. Meso-scale framework for modeling granular material using computed tomography. Comput Geotech 2016;76:140–6.

[596] Russell A, Wood DM, Kikumoto M. Particle crushing in granular assemblies. AIP Conf Proc 2009;1145:875–8. https://doi.org/10.1063/1.3180069.
[597] De Bono J, McDowell G. Particle breakage criteria in discrete-element modelling. Geotechnique 2016;66:1014–27. https://doi.org/10.1680/JGEOT.15.P.280.
[598] Karatza Z, Andò E, Papanicolopulos SA, Viggiani G, Ooi JY. Evolution of particle breakage studied using x-ray tomography and the discrete element method. EPJ Web Conf 2017;140. https://doi.org/10.1051/EPJCONF/201714007013.
[599] Cil MB, Alshibli KA. 3D evolution of sand fracture under 1D compression. Géotechnique 2014;64:351–64. https://doi.org/10.1680/geot.13.P.119.
[600] Zhang B, Herbold EB, Homel MA, Regueiro RA. Dem particle fracture model 2015.
[601] Iliev PS, Wittel FK, Herrmann HJ. Evolution of fragment size distributions from the crushing of granular materials. Phys Rev E 2019;99:012904. https://doi.org/10.1103/PhysRevE.99.012904.
[602] Potapov AV, Campbell CS. A three-dimensional simulation of brittle solid fracture. Int J Mod Phys C 2011;7(7):717–29. https://doi.org/10.1142/S0129183196000594.
[603] Jiménez-Herrera N, Barrios GKP, Tavares LM. Comparison of breakage models in DEM in simulating impact on particle beds. Adv Powder Technol 2018;29:692–706. https://doi.org/10.1016/J.APT.2017.12.006.
[604] Zhu F, Zhao J. Modeling continuous grain crushing in granular media: A hybrid peridynamics and physics engine approach. Comput Methods Appl Mech Eng 2019;348:334–55. https://doi.org/10.1016/J.CMA.2019.01.017.
[605] Cheng YP, Nakata Y, Bolton MD. Discrete element simulation of crushable soil. Geotechnique 2003;53:633–41. https://doi.org/10.1680/geot.2003.53.7.633.
[606] Wang P, Arson C. Discrete element modeling of shielding and size effects during single particle crushing. Comput Geotech 2016;78:227–36. https://doi.org/10.1016/j.compgeo.2016.04.003.
[607] McDowell GR, de Bono JP. On the micro mechanics of one-dimensional normal compression. Géotechnique 2013;63:895–908. https://doi.org/10.1680/geot.12.P.041.
[608] Harmon JM, Arthur D, Andrade JE. Level set splitting in DEM for modeling breakage mechanics. Comput Methods Appl Mech Eng 2020;365:112961. https://doi.org/10.1016/J.CMA.2020.112961.
[609] Cil MB, Alshibli KA. 3D assessment of fracture of sand particles using discrete element method 2012;2:161–6.
[610] Campbell CS. Granular shear flows at the elastic limit. J Fluid Mech 2002;465:261–91. https://doi.org/10.1017/S002211200200109X.
[611] Campbell CS. Elastic granular flows of ellipsoidal particles. Phys Fluids 2011;23:013306. https://doi.org/10.1063/1.3546037.
[612] Campbell CS. Stress-controlled elastic granular shear flows. J Fluid Mech 2005;539:273–97. https://doi.org/10.1017/S0022112005005616.
[613] Schreck CF, Bertrand T, O'Hern CS, Shattuck MD. Repulsive contact interactions make jammed particulate systems inherently nonharmonic. Phys Rev Lett 2011;107:078301. https://doi.org/10.1103/PhysRevLett.107.078301.
[614] Edwards SF, Oakeshott RBS. Theory of powders. Phys A Stat Mech Its Appl 1989;157:1080–90. https://doi.org/10.1016/0378-4371(89)90034-4.
[615] Radjai F, Jean M, Moreau J-J-J, Roux S. Force Distributions in Dense Two-Dimensional Granular Systems. Phys Rev Lett 1996;77:274–7. https://doi.org/10.1103/PhysRevLett.77.274.
[616] Howell DW, Behringer RP, Veje CT. Fluctuations in granular media. Chaos 1999;9:559–72. https://doi.org/10.1063/1.166430.
[617] Baule A, Makse HA. Fundamental challenges in packing problems: From spherical to non-spherical particles. Soft Matter 2014;10:4423–9. https://doi.org/10.1039/c3sm52783b.
[618] S H, B C. Statistical mechanics framework for static granular matter. Phys Rev E 2009;79:061301. https://doi.org/10.1103/physreve.79.061301.
[619] Bi D, Henkes S, Daniels KE, Chakraborty B. The statistical physics of athermal materials. Annu Rev Condens Matter Phys 2015;6:63–83. https://doi.org/10.1146/annurev-conmatphys-031214-014336.
[620] Moukarzel CF. Isostatic phase transition and instability in stiff granular materials. Phys Rev Lett 1998;81:1634–7. https://doi.org/10.1103/PhysRevLett.81.1634.
[621] Tkachenko AV, Witten TA. Stress propagation through frictionless granular material. Phys Rev E - Stat Physics, Plasmas, Fluids, Relat Interdiscip Top 1999;60:687–96. https://doi.org/10.1103/PhysRevE.60.687.
[622] Wyart M. On the rigidity of amorphous solids. Ann Phys (Paris) 2005;30:1–96. https://doi.org/10.1051/anphys:2006003.
[623] Smith KC, Alam M, Fisher TS. Athermal jamming of soft frictionless Platonic solids. Phys Rev E 2010;82:051304. https://doi.org/10.1103/PhysRevE.82.051304.
[624] Otsuki M, Hayakawa H. Critical behaviors of sheared frictionless granular materials near the jamming transition. Phys Rev E 2009;80:011308. https://doi.org/10.1103/PhysRevE.80.011308.
[625] Otsuki M, Hayakawa H. Universal Scaling for the Jamming Transition. Prog Theor Phys 2009;121:647–55. https://doi.org/10.1143/PTP.121.647.
[626] Song C, Wang P, Makse HA. A phase diagram for jammed matter. Nat 2008.629–32.;2008(4537195):453. https://doi.org/10.1038/nature06981.
[627] Otsuki M, Hayakawa H. Critical scaling near jamming transition for frictional granular particles. Phys Rev E 2011;83:051301. https://doi.org/10.1103/PhysRevE.83.051301.
[628] Ciamarra MP, Pastore R, Nicodemi M, Coniglio A. Jamming phase diagram for frictional particles. Phys Rev E 2011;84:041308. https://doi.org/10.1103/PhysRevE.84.041308.
[629] Chialvo S, Sun J, Sundaresan S. Bridging the rheology of granular flows in three regimes. Phys Rev E - Stat Nonlinear, Soft Matter Phys 2012;85:021305. https://doi.org/10.1103/PhysRevE.85.021305.
[630] Gu Y, Chialvo S, Sundaresan S. Rheology of cohesive granular materials across multiple dense-flow regimes. Phys Rev E - Stat Nonlinear, Soft Matter Phys 2014;90:032206. https://doi.org/10.1103/PhysRevE.90.032206.
[631] Xu M, Zhang Z, Huang X. Identification of jamming transition: a critical appraisal. Granul Matter 2021;23:1–17. https://doi.org/10.1007/s10035-020-01066-2.
[632] Makse HA, Johnson DL, Schwartz LM. Packing of compressible granular materials. Phys Rev Lett 2000;84:4160–3. https://doi.org/10.1103/PhysRevLett.84.4160.
[633] Coppersmith SN, Liu C, h., Majumdar S, Narayan O, Witten TA.. Model for force fluctuations in bead packs. Phys Rev E - Stat Physics, Plasmas, Fluids, Relat Interdiscip Top 1996;53:4673–85. https://doi.org/10.1103/PhysRevE.53.4673.
[634] Radjai F, Wolf DE, Jean M, Moreau JJ. Bimodal character of stress transmission in granular packings. Phys Rev Lett 1998;80:61–4. https://doi.org/10.1103/PhysRevLett.80.61.
[635] O'Hern CS, Silbert LE, Liu AJ, Nagel SR. Jamming at zero temperature and zero applied stress: The epitome of disorder. Phys Rev E 2003;68:011306. https://doi.org/10.1103/PhysRevE.68.011306.
[636] Veje CT, Howell DW, Behringer RP. Kinematics of a two-dimensional granular Couette experiment at the transition to shearing. Phys Rev E 1999;59:739–45. https://doi.org/10.1103/PhysRevE.59.739.
[637] Vanel L, Howell D, Clark D, Behringer RP, Clément E. Memories in sand: Experimental tests of construction history on stress distributions under sandpiles. Phys Rev E - Stat Physics, Plasmas, Fluids, Relat Interdiscip Top 1999;60:R5040. https://doi.org/10.1103/PhysRevE.60.R5040.
[638] Ostojic S, Somfai E, Nienhuis B. Scale invariance and universality of force networks in static granular matter. Nature 2006;439:828–30. https://doi.org/10.1038/nature04549.
[639] Sarkar S, Bi D, Zhang J, Behringer RP, Chakraborty B. Origin of rigidity in dry granular solids. Phys Rev Lett 2013;111:068301. https://doi.org/10.1103/PhysRevLett.111.068301.
[640] Zhou J, Long S, Wang Q, Dinsmore AD. Measurement of Forces Inside a Three-Dimensional Pile of Frictionless Droplets. Science (80-) 2006;312:1631–3. https://doi.org/10.1126/science.1125151.
[641] Tordesillas A, Walker DM, Lin Q. Force cycles and force chains. Phys Rev E - Stat Nonlinear, Soft Matter Phys 2010;81:011302. https://doi.org/10.1103/PhysRevE.81.011302.
[642] Kondic L, Goullet A, O'Hern CS, Kramar M, Mischaikow K, Behringer RP. Topology of force networks in compressed granular media. EPL 2012;97:54001. https://doi.org/10.1209/0295-5075/97/54001.

[643] Tordesillas A, Walker DM, Froyland G, Zhang J, Behringer RP. Transition dynamics and magic-number-like behavior of frictional granular clusters. Phys Rev E - Stat Nonlinear, Soft Matter Phys 2012;86:011306. https://doi.org/10.1103/PhysRevE.86.011306.
[644] Kramar M, Goullet A, Kondic L, Mischaikow K. Persistence of force networks in compressed granular media. Phys Rev E - Stat Nonlinear, Soft Matter Phys 2013;87:042207. https://doi.org/10.1103/PhysRevE.87.042207.
[645] Tordesillas A, Tobin ST, Cil M, Alshibli K, Behringer RP. Network flow model of force transmission in unbonded and bonded granular media. Phys Rev E - Stat Nonlinear, Soft Matter Phys 2015;91:062204. https://doi.org/10.1103/PhysRevE.91.062204.
[646] Kovalcinova L, Goullet A, Kondic L. Scaling properties of force networks for compressed particulate systems. Phys Rev E 2016;93:042903. https://doi.org/10.1103/PhysRevE.93.042903.
[647] Lim MX, Behringer RP. Topology of force networks in granular media under impact. EPL 2017;120:44003. https://doi.org/10.1209/0295-5075/120/44003.
[648] Sarkar S, Chakraborty B. Shear-induced rigidity in athermal materials: A unified statistical framework. Phys Rev E - Stat Nonlinear, Soft Matter Phys 2015;91:042201. https://doi.org/10.1103/PhysRevE.91.042201.
[649] Liu AJ, Nagel SR. Jamming is not just cool any more. Nature 1998;396:21–2. https://doi.org/10.1038/23819.
[650] Trappe V, Prasad V, Cipelletti L, Segre PN, Weitz DA. Jamming phase diagram for attractive particles. Nature 2001;411:772–5. https://doi.org/10.1038/35081021.
[651] Veje CT, Howell DW, Behringer RP, Schöllmann S, Luding S, Herrmann HJ. Fluctuations and flow for granular shearing. Phys. Dry Granul. Media: Springer; 1998. p. 237–42.
[652] Torquato S, Truskett TM, Debenedetti PG. Is random close packing of spheres well defined? Phys Rev Lett 2000;84:2064–7. https://doi.org/10.1103/PhysRevLett.84.2064.
[653] Donev A, Connelly R, Stillinger FH, Torquato S. Underconstrained jammed packings of nonspherical hard particles: Ellipses and ellipsoids. Phys Rev E - Stat Nonlinear, Soft Matter Phys 2007;75:051304. https://doi.org/10.1103/PhysRevE.75.051304.
[654] Kansal AR, Torquato S, Stillinger FH. Diversity of order and densities in jammed hard-particle packings. Phys Rev E - Stat Physics, Plasmas, Fluids, Relat Interdiscip Top 2002;66:8. https://doi.org/10.1103/PhysRevE.66.041109.
[655] Goodrich CP, Liu AJ, Sethna JP. Scaling ansatz for the jamming transition. Proc Natl Acad Sci U S A 2016;113:9745–50. https://doi.org/10.1073/pnas.1601858113.
[656] Silbert LE, Liu AJ, Nagel SR. Vibrations and diverging length scales near the unjamming transition. Phys Rev Lett 2005;95:098301. https://doi.org/10.1103/PhysRevLett.95.098301.
[657] Silbert LE. Jamming of frictional spheres and random loose packing. Soft Matter 2010;6:2918. https://doi.org/10.1039/c001973a.
[658] Kumar N, Luding S. Memory of jamming–multiscale models for soft and granular matter. Granul Matter 2016;18:58–80. https://doi.org/10.1007/s10035-016-0624-2.
[659] Charbonneau P, Corwin EI, Parisi G, Zamponi F. Universal microstructure and mechanical stability of jammed packings. Phys Rev Lett 2012;109:205501. https://doi.org/10.1103/PhysRevLett.109.205501.
[660] Charbonneau P, Ikeda A, Parisi G, Zamponi F. Glass transition and random close packing above three dimensions. Phys Rev Lett 2011;107:185702. https://doi.org/10.1103/PhysRevLett.107.185702.
[661] Parisi G, Zamponi F. Mean-field theory of hard sphere glasses and jamming. Rev Mod Phys 2010;82:789–845. https://doi.org/10.1103/RevModPhys.82.789.
[662] Ren J, Dijksman JA, Behringer RP. Reynolds Pressure and Relaxation in a Sheared Granular System. Phys Rev Lett 2013;110:018302. https://doi.org/10.1103/PhysRevLett.110.018302.
[663] Zhang J, Majmudar TS, Tordesillas A, Behringer RP. Statistical properties of a 2D granular material subjected to cyclic shear. Granul Matter 2010;12:159–72. https://doi.org/10.1007/s10035-010-0170-2.
[664] Scott GD. Packing of spheres: Packing of equal spheres. Nature 1960;188:908–9. https://doi.org/10.1038/188908a0.
[665] Scott GD, Kilgour DM. The density of random close packing of spheres. J Phys D Appl Phys 1969;2:863–6. https://doi.org/10.1088/0022-3727/2/6/311.
[666] Onoda GY, Liniger EG. Random loose packings of uniform spheres and the dilatancy onset. Phys Rev Lett 1990;64:2727–30. https://doi.org/10.1103/PhysRevLett.64.2727.
[667] Nedderman RM. Statics and Kinematics of Granular Materials. Statics Kinemat Granul Mater 1992. https://doi.org/10.1017/CBO9780511600043.
[668] Schröter M, Nägle S, Radin C, Swinney HL. Phase transition in a static granular system. EPL 2007;78:44004. https://doi.org/10.1209/0295-5075/78/44004.
[669] Jerkins M, Schröter M, Swinney HL, Senden TJ, Saadatfar M, Aste T. Onset of Mechanical Stability in Random Packings of Frictional Spheres. Phys Rev Lett 2008;101:018301. https://doi.org/10.1103/PhysRevLett.101.018301.
[670] Schröter M, Goldman DI, Swinney HL. Stationary state volume fluctuations in a granular medium. Phys Rev E - Stat Nonlinear, Soft Matter Phys 2005;71:030301. https://doi.org/10.1103/PhysRevE.71.030301.
[671] Métayer JF, Suntrup DJ, Radin C, Swinney HL, Schröter M. Shearing of frictional sphere packings. EPL 2011;93:64003. https://doi.org/10.1209/0295-5075/93/64003.
[672] Albert I, Sample JG, Morss AJ, Rajagopalan S, Barabási AL, Schiffer P. Granular drag on a discrete object: Shape effects on jamming. Phys Rev E - Stat Physics, Plasmas, Fluids, Relat Interdiscip Top 2001;64:4. https://doi.org/10.1103/PhysRevE.64.061303.
[673] Hill G, Yeung S, Koehler SA. Scaling vertical drag forces in granular media. EPL (Europhysics Lett 2005;72:137.. https://doi.org/10.1209/EPL/I2005-10203-3.
[674] Schröder-Turk GE, Mickel W, Schröter M, Delaney GW, Saadatfar M, Senden TJ, et al. Disordered spherical bead packs are anisotropic. EPL 2010;90:34001. https://doi.org/10.1209/0295-5075/90/34001.
[675] Geng J, Behringer RP. Slow drag in two-dimensional granular media. Phys Rev E - Stat Nonlinear, Soft Matter Phys 2005;71:011302. https://doi.org/10.1103/PhysRevE.71.011302.
[676] Albert I, Tegzes P, Kahng B, Albert R, Sample JG, Pfeifer M, et al. Jamming and fluctuations in granular drag. Phys Rev Lett 2000;84:5122–5. https://doi.org/10.1103/PhysRevLett.84.5122.
[677] Olson Reichhardt CJ, Reichhardt C. Fluctuations, jamming, and yielding for a driven probe particle in disordered disk assemblies. Phys Rev E - Stat Nonlinear, Soft Matter Phys 2010;82:051306. https://doi.org/10.1103/PhysRevE.82.051306.
[678] Candelier R, Dauchot O. Creep Motion of an Intruder within a Granular Glass Close to Jamming. Phys Rev Lett 2009;103:128001. https://doi.org/10.1103/PhysRevLett.103.128001.
[679] Candelier R, Dauchot O. Journey of an intruder through the fluidization and jamming transitions of a dense granular media. Phys Rev E 2010;81:011304. https://doi.org/10.1103/PhysRevE.81.011304.
[680] Sarkar S, Bi D, Zhang J, Ren J, Behringer RP, Chakraborty B. Shear-induced rigidity of frictional particles: Analysis of emergent order in stress space. Phys Rev E 2016;93:042901. https://doi.org/10.1103/PhysRevE.93.042901.
[681] Reynolds O. LVII. On the dilatancy of media composed of rigid particles in contact. With experimental illustrations. London, Edinburgh, Dublin Philos Mag J Sci 1885;20:469–81. https://doi.org/10.1080/14786448508627791.
[682] Peyneau PE, Roux JN. Frictionless bead packs have macroscopic friction, but no dilatancy. Phys Rev E - Stat Nonlinear, Soft Matter Phys 2008;78:011307. https://doi.org/10.1103/PhysRevE.78.011307.
[683] Azéma É, Radjaï F, Roux JN. Internal friction and absence of dilatancy of packings of frictionless polygons. Phys Rev E - Stat Nonlinear, Soft Matter Phys 2015;91:010202. https://doi.org/10.1103/PhysRevE.91.010202.
[684] Bertrand T, Behringer RP, Chakraborty B, O'Hern CS, Shattuck MD. Protocol dependence of the jamming transition. Phys Rev E 2016;93:012901. https://doi.org/10.1103/PhysRevE.93.012901.
[685] Baity-Jesi M, Goodrich CP, Liu AJ, Nagel SR, Sethna JP. Emergent SO(3) Symmetry of the Frictionless Shear Jamming Transition. J Stat Phys 2017;167:735–48. https://doi.org/10.1007/s10955-016-1703-9.
[686] Imole OI, Kumar N, Magnanimo V, Luding S. Hydrostatic and shear behavior of frictionless granular assemblies under different deformation conditions. KONA Powder Part J 2012;30:84–108. https://doi.org/10.14356/kona.2013011.

[687] Vinutha HA, Sastry S. Disentangling the role of structure and friction in shear jamming. Nat Phys 2016;12:578–83. https://doi.org/10.1038/nphys3658.
[688] Rainone C, Urbani P, Yoshino H, Zamponi F. Following the evolution of hard sphere glasses in infinite dimensions under external perturbations: Compression and shear strain. Phys Rev Lett 2015;114:015701. https://doi.org/10.1103/PhysRevLett.114.015701.
[689] Hosseinpoor M, Ouro Koura BI, Yahia A. New methodology to evaluate the Reynolds dilatancy of self-consolidating concrete using 3D image analysis - Coupled effect of characteristics of fine mortar and granular skeleton. Cem Concr Compos 2020;108:103547. https://doi.org/10.1016/j.cemconcomp.2020.103547.
[690] Savage SB, Lun CKK. Particle size segregation in inclined chute flow of dry cohesionless granular solids. J Fluid Mech 1988;189:311–35. https://doi.org/10.1017/S002211208800103X.
[691] Ottino JM, Khakhar DV. Mixing and Segregation of Granular Materials. Annu Rev Fluid Mech 2000;32:55–91. https://doi.org/10.1146/annurev.fluid.32.1.55.
[692] Meier SW, Lueptow RM, Ottino JM. A dynamical systems approach to mixing and segregation of granular materials in tumblers. Adv Phys 2007;56:757–827. https://doi.org/10.1080/00018730701611677.
[693] Rosato A, Strandburg KJ, Prinz F, Swendsen RH. Why the Brazil nuts are on top: Size segregation of particulate matter by shaking. Phys Rev Lett 1987;58:1038–40. https://doi.org/10.1103/PhysRevLett.58.1038.
[694] Knight JB, Jaeger HM, Nagel SR. Vibration-induced size separation in granular media: The convection connection. Phys Rev Lett 1993;70:3728. https://doi.org/10.1103/PhysRevLett.70.3728.
[695] Wu SY, Baeyens J. Segregation by size difference in gas fluidized beds. Powder Technol 1998;98:139–50. https://doi.org/10.1016/S0032-5910(98)00026-6.
[696] Standish N. Studies of size segregation in filling and emptying a hopper. Powder Technol 1985;45:43–56. https://doi.org/10.1016/0032-5910(85)85059-2.
[697] Ketterhagen WR, Curtis JS, Wassgren CR, Kong A, Narayan PJ, Hancock BC. Granular segregation in discharging cylindrical hoppers: A discrete element and experimental study. Chem Eng Sci 2007;62:6423–39.
[698] Xiao H, Fan Y, Jacob KV, Umbanhowar PB, Kodam M, Koch JF, et al. Continuum modeling of granular segregation during hopper discharge. Chem Eng Sci 2019;193:188–204. https://doi.org/10.1016/j.ces.2018.08.039.
[699] Muzzio FJ, Shinbrot T, Glasser BJ. Powder technology in the pharmaceutical industry: The need to catch up fast. Powder Technol 2002;124:1–7.
[700] Gray JMNT, Kokelaar BP. Large particle segregation, transport and accumulation in granular free-surface flows. J Fluid Mech 2010;652:105–37. https://doi.org/10.1017/S002211201000011X.
[701] Scott AM, Bridgwater J. Interparticle Percolation: A Fundamental Solids Mixing Mechanism. Ind Eng Chem Fundam 1975;14:22–7. https://doi.org/10.1021/i160053a004.
[702] Gray JMNT. Particle Segregation in Dense Granular Flows. Annu Rev Fluid Mech 2018;50:407–33. https://doi.org/10.1146/annurev-fluid-122316-045201.
[703] Bridgwater J, Ingram ND. Rate of spontaneous inter-particle percolation. Trans Inst Chem Eng (Institution Chem Eng 1971;49:163–9.
[704] Bridgwater J, MH C, AM S, others.. Interparticle percolation: equipment development and mean percolation velocities. Trans Inst Chem Eng 1978;56:157–67.
[705] Cooke MH, Bridgwater J, Scott AM. Interparticle percolation: lateral and axial diffusion coefficients. Powder Technol 1978;21:183–93. https://doi.org/10.1016/0032-5910(78)80088-6.
[706] Elimelech M, Gregory J, Jia X. Particle deposition and aggregation: measurement, modelling and simulation. Butterworth-Heinemann; 2013.
[707] Ennis BJ, Litster JD. Particle size enlargement. Perry's Chem Eng Handbook 7th Ed McGraw-Hill, New York 1997;20.
[708] Lin CL, Kuo JH, Wey MY, Chang SH, Wang KS. Inhibition and promotion: The effect of earth alkali metals and operating temperature on particle agglomeration/defluidization during incineration in fluidized bed. Powder Technol 2009;189:57–63. https://doi.org/10.1016/j.powtec.2008.06.003.
[709] Lin CL, Wey MY. The effect of mineral compositions of waste and operating conditions on particle agglomeration/defluidization during incineration. Fuel 2004;83:2335–43. https://doi.org/10.1016/j.fuel.2004.06.030.
[710] Ennis BJ, Tardos G, Pfeffer R. A microlevel-based characterization of granulation phenomena. Powder Technol 1991;65:257–72. https://doi.org/10.1016/0032-5910(91)80189-P.
[711] Glatt GmbH - Integrated Process Solutions n.d. https://www.glatt.com/en/ (accessed November 15, 2021).
[712] Raj Kumar SM, Malayalamurthi R. Agglomeration and sizing of rolling particles in the sago sizing mechanism. Powder Technol 2017;320:428–44. https://doi.org/10.1016/j.powtec.2017.07.066.
[713] Hutter K. Geophysical granular and particle-laden flows: Review of the field. Philos. Trans. R. Soc. A Math. Phys. Eng. Sci., vol. 363, The Royal SocietyLondon; 2005, p. 1497–505. https://doi.org/10.1098/rsta.2005.1591.
[714] Johnson CG, Kokelaar BP, Iverson RM, Logan M, Lahusen RG, Gray JMNT. Grain-size segregation and levee formation in geophysical mass flows. J Geophys Res Earth Surf 2012;117:1032. https://doi.org/10.1029/2011JF002185.
[715] Zhou GGD, Cui KFE, Jing L, Zhao T, Song D, Huang Y. Particle Size Segregation in Granular Mass Flows With Different Ambient Fluids. e2020JB019536 J Geophys Res Solid Earth 2020;125. https://doi.org/10.1029/2020JB019536.
[716] Cagnoli B. Granular mass flows and Coulomb's friction in shear cell experiments: Implications for geophysical flows. J Geophys Res 2004;109:4005. https://doi.org/10.1029/2004jf000177.
[717] Palladino DM, Valentine GA. Coarse-tail vertical and lateral grading in pyroclastic flow deposits of the Latera Volcanic Complex (Vulsini, central Italy): origin and implications for flow dynamics. J Volcanol Geotherm Res 1995;69:343–64. https://doi.org/10.1016/0377-0273(95)00036-4.
[718] Kim KM, Bae JH, Park JI, Han JW. Segregation Charging Behavior of Ultra-Fine Iron Ore Briquette in Sinter Feed Bed: DEM Analysis. Met Mater Int 2020;26:1218–25. https://doi.org/10.1007/s12540-019-00415-y.
[719] Williams JC. The segregation of particulate materials. A review Powder Technol 1976;15:245–51. https://doi.org/10.1016/0032-5910(76)80053-8.
[720] Van Der Vaart K, Gajjar P, Epely-Chauvin G, Andreini N, Gray JMNT, Ancey C. Underlying Asymmetry within Particle Size Segregation. Phys Rev Lett 2015;114:238001. https://doi.org/10.1103/PhysRevLett.114.238001.
[721] Gao S, Ottino JM, Umbanhowar PB, Lueptow RM. Modeling granular segregation for overlapping species distributions. Chem Eng Sci 2021;231:116259. https://doi.org/10.1016/j.ces.2020.116259.
[722] Zhang TF, Gan JQ, Yu AB, Pinson D, Zhou ZY. Segregation of granular binary mixtures with large particle size ratios during hopper discharging process. Powder Technol 2020;361:435–45. https://doi.org/10.1016/J.POWTEC.2019.07.010.
[723] Yang LYM, Zheng QJ, Bai L, Yu AB. Continuum modelling of granular segregation by coupling flow rheology and transport equation. Powder Technol 2021;378:371–87. https://doi.org/10.1016/j.powtec.2020.10.010.
[724] Peng C, Zhan L, Wu W, Zhang B. A fully resolved SPH-DEM method for heterogeneous suspensions with arbitrary particle shape. Powder Technol 2021;387:509–26. https://doi.org/10.1016/J.POWTEC.2021.04.044.
[725] Kokelaar BP, Graham RL, Gray JMNT, Vallance JW. Fine-grained linings of leveed channels facilitate runout of granular flows. Earth Planet Sci Lett 2014;385:172–80. https://doi.org/10.1016/j.epsl.2013.10.043.
[726] Trung Vo T, Nezamabadi S, Mutabaruka P, Delenne JY, Izard E, Pellenq R, et al. Agglomeration of wet particles in dense granular flows. Eur Phys J E 2019;42:127. https://doi.org/10.1140/EPJE/I2019-11892-9.
[727] Huang AN, Kuo HP. Developments in the tools for the investigation of mixing in particulate systems - A review. Adv Powder Technol 2014;25:163–73. https://doi.org/10.1016/j.apt.2013.10.007.
[728] Lacey PMC. Developments in the theory of particle mixing. J Appl Chem 2007;4:257–68. https://doi.org/10.1002/jctb.5010040504.
[729] Bridgwater J. Mixing of powders and granular materials by mechanical means—a perspective. Particuology 2012;10:397–427.
[730] Bertrand F, Leclaire L-A, Levecque G. DEM-based models for the mixing of granular materials. Chem Eng Sci 2005;60:2517–31. https://doi.org/10.1016/j.ces.2004.11.048.
[731] Shinbrot T, Alexander A, Muzzio FJ. Spontaneous chaotic granular mixing. Nature 1999;397:675–8. https://doi.org/10.1038/17760.
[732] Lemieux M, Léonard G, Doucet J, Leclaire LA, Viens F, Chaouki J, et al. Large-scale numerical investigation of solids mixing in a V-blender using the discrete element method. Powder Technol 2008;181:205–16. https://doi.org/10.1016/j.powtec.2006.12.009.
[733] Cleary PW, Prakash M, Sinnott MD, Rudman M, Das R. Large scale simulation of industrial, engineering and geophysical flows using particle methods. Part. methods: Springer; 2011. p. 89–111.

[734] Arratia PE, Duong N, Muzzio FJ, Godbole P, Reynolds S. A study of the mixing and segregation mechanisms in the Bohle Tote blender via DEM simulations. Powder Technol 2006;164:50–7.
[735] Lu L-S, Hsiau S-S. Mixing in a vibrated granular bed: Diffusive and convective effects. Powder Technol 2008;184:31–43.
[736] Deng X, Scicolone JV, Davé RN. Discrete element method simulation of cohesive particles mixing under magnetically assisted impaction. Powder Technol 2013;243:96–109. https://doi.org/10.1016/j.powtec.2013.03.043.
[737] Jiang H, Zhao Y, Duan C, Yang X, Liu C, Wu J, et al. Kinematics of variable-amplitude screen and analysis of particle behavior during the process of coal screening. Powder Technol 2017;306:88–95.
[738] Zhao L, Zhao Y, Bao C, Hou Q, Yu A. Optimisation of a circularly vibrating screen based on DEM simulation and Taguchi orthogonal experimental design. Powder Technol 2017;310:307–17.
[739] Meng X, Jia F, Qiu H, Han Y, Zeng Y, Xiao Y, et al. DEM study of white rice separation in an indented cylinder separator. Powder Technol 2019;348:1–12.
[740] Li H, Wang JS, Yuan JB, Yin WQ, Wang ZM, Qian YZ. Analysis of threshed rice mixture separation through vibration screen using discrete element method. Int J Agric Biol Eng 2017;10:231–9. https://doi.org/10.25165/j.ijabe.20171006.2910.
[741] Li J, Webb C, Pandiella SS, Campbell GM. A numerical simulation of separation of crop seeds by screening—effect of particle bed depth. Food Bioprod Process 2002;80:109–17.
[742] Li J, Webb C, Pandiella SS, Campbell GM. Discrete particle motion on sieves—a numerical study using the DEM simulation. Powder Technol 2003;133:190–202.
[743] Cleary PW, Sawley ML. DEM modelling of industrial granular flows: 3D case studies and the effect of particle shape on hopper discharge. Appl Math Model 2002;26:89–111. https://doi.org/10.1016/S0307-904X(01)00050-6.
[744] Cleary PW. DEM simulation of industrial particle flows: case studies of dragline excavators, mixing in tumblers and centrifugal mills. Powder Technol 2000;109:83–104.
[745] Jahani M, Farzanegan A, Noaparast M. Investigation of screening performance of banana screens using LIGGGHTS DEM solver. Powder Technol 2015;283:32–47. https://doi.org/10.1016/j.powtec.2015.05.016.
[746] Dong KJ, Yu AB. Numerical simulation of the particle flow and sieving behaviour on sieve bend/low head screen combination. Miner Eng 2012;31:2–9.
[747] Cleary PW, Sinnott MD, Morrison RD. Separation performance of double deck banana screens–Part 1: Flow and separation for different accelerations. Miner Eng 2009;22:1218–29.
[748] Cleary PW, Sinnott MD, Morrison RD. Separation performance of double deck banana screens–Part 2: Quantitative predictions. Miner Eng 2009;22:1230–44.
[749] Fernandez JW, Cleary PW, Sinnott MD, Morrison RD. Using SPH one-way coupled to DEM to model wet industrial banana screens. Miner Eng 2011;24:741–53.
[750] Li H, Li Y, Gao F, Zhao Z, Xu L. CFD-DEM simulation of material motion in air-and-screen cleaning device. Comput Electron Agric 2012;88:111–9. https://doi.org/10.1016/j.compag.2012.07.006.
[751] Hamaker HC. The London—van der Waals attraction between spherical particles. Physica 1937;4:1058–72. https://doi.org/10.1016/S0031-8914(37)80203-7.
[752] Aranson IS, Blair D, Kalatsky VA, Crabtree GW, Kwok WK, Vinokur VM, et al. Electrostatically Driven Granular Media: Phase Transitions and Coarsening. Phys Rev Lett 2000;84:3306. https://doi.org/10.1103/PhysRevLett.84.3306.
[753] Fisher RA. On the capillary forces in an ideal soil; correction of formulae given by W. B Haines J Agric Sci 1926;16:492–505. https://doi.org/10.1017/S0021859600007838.
[754] Ennis BJ. Agglomeration and size enlargement session summary paper. Powder Technol 1996;88:203–25. https://doi.org/10.1016/S0032-5910(96)03124-5.
[755] Kristensen HG. Particle agglomeration in high shear mixers. Powder Technol 1996;88:197–202. https://doi.org/10.1016/S0032-5910(96)03123-3.
[756] Bika DG, Gentzler M, Michaels JN. Mechanical properties of agglomerates. Powder Technol 2001;117:98–112. https://doi.org/10.1016/S0032-5910(01)00318-7.
[757] Raux PS, Biance AL. Cohesion and agglomeration of wet powders. Phys Rev Fluids 2018;3:014301. https://doi.org/10.1103/PhysRevFluids.3.014301.
[758] Willett CD, Adams MJ, Johnson SA, Seville JPK. Capillary bridges between two spherical bodies. Langmuir 2000;16:9396–405.
[759] Soulié F, Cherblanc F, El Youssoufi MS, Saix C. Influence of liquid bridges on the mechanical behaviour of polydisperse granular materials. Int J Numer Anal Methods Geomech 2006;30:213–28. https://doi.org/10.1002/NAG.476.
[760] Richefeu V, El Youssoufi MS, Azéma E, Radjaï F. Force transmission in dry and wet granular media. Powder Technol 2009;190:258–63. https://doi.org/10.1016/j.powtec.2008.04.069.
[761] Scholtès L, Chareyre B, Nicot F, Darve F. Micromechanics of granular materials with capillary effects. Int J Eng Sci 2009;47:64–75. https://doi.org/10.1016/j.ijengsci.2008.07.002.
[762] Delenne J-Y, Richefeu V, Radjai F. Liquid clustering and capillary pressure in granular media. J Fluid Mech 2015;762:R5. https://doi.org/10.1017/jfm.2014.676.
[763] Pouragha M, Wan R, Duriez J, Sultan NH. Statistical analysis of stress transmission in wet granular materials. Int J Numer Anal Methods Geomech 2018;42:1935–56.
[764] Urso MED, Lawrence CJ, Adams MJ. Pendular, Funicular, and Capillary Bridges: Results for Two Dimensions. J Colloid Interface Sci 1999;220:42–56. https://doi.org/10.1006/jcis.1999.6512.
[765] Wang J-P-P, Gallo E, François B, Gabrieli F, Lambert P. Capillary force and rupture of funicular liquid bridges between three spherical bodies. Powder Technol 2017;305:89–98.
[766] Murase K, Mochida T, Sagawa Y, Sugama H. Estimation on the strength of a liquid bridge adhered to three spheres. Adv Powder Technol 2008;19:349–67. https://doi.org/10.1163/156855208X314949.
[767] Lievano D, Velankar S, McCarthy JJ. The rupture force of liquid bridges in two and three particle systems. Powder Technol 2017;313:18–26. https://doi.org/10.1016/j.powtec.2017.02.053.
[768] Vo TT. Modeling the rheology of wet granular materials. Université Montpellier 2019.
[769] Rabinovich YI, Esayanur MS, Moudgil BM. Capillary forces between two spheres with a fixed volume liquid bridge: Theory and experiment. Langmuir 2005;21:10992–7. https://doi.org/10.1021/LA0517639.
[770] Gras JP, Delenne JY, El Youssoufi MS. Study of capillary interaction between two grains: A new experimental device with suction control. Granul Matter 2013;15:49–56. https://doi.org/10.1007/S10035-012-0388-2.
[771] Nguyen HNG, Millet O, Gagneux G. Exact calculation of axisymmetric capillary bridge properties between two unequal-sized spherical particles. Math Mech Solids 2019;24:2767–84. https://doi.org/10.1177/1081286518787842.
[772] Gagneux G, Millet O. An analytical framework for evaluating the cohesion effects of coalescence between capillary bridges. Granul Matter 2016;18. https://doi.org/10.1007/S10035-016-0613-5.
[773] Gagneux G, Millet O, Mielniczuk B, El Youssoufi MS. Theoretical and experimental study of pendular regime in unsaturated granular media. Eur J Environ Civ Eng 2017;21:840–53. https://doi.org/10.1080/19648189.2016.1167782.
[774] Mason G, Clark WC. Liquid bridges between spheres. Chem Eng Sci 1965;20:859–66. https://doi.org/10.1016/0009-2509(65)80082-3.
[775] van Genuchten MT. A Closed-form Equation for Predicting the Hydraulic Conductivity of Unsaturated Soils. Soil Sci Soc Am J 1980;44:892–8.
[776] Fredlund DG, Xing A, Fredlund MD, Barbour SL. The relationship of the unsaturated soil shear strength to the soil-water characteristic curve. Can Geotech J 1996;33:440–8.
[777] Wheeler SJ, Sharma RS, Buisson MSR. Coupling of hydraulic hysteresis and stress-strain behaviour in unsaturated soils. Geotechnique 2003;53:41–54. https://doi.org/10.1680/geot.2003.53.1.41.
[778] Scheel M, Seemann R, Brinkmann M, Di Michiel M, Sheppard A, Breidenbach B, et al. Morphological clues to wet granular pile stability. Nat Mater 2008.189–93.;2008(73):7. https://doi.org/10.1038/nmat2117.
[779] Scholtès L, Hicher PY, Nicot F, Chareyre B, Darve F. On the capillary stress tensor in wet granular materials. Int J Numer Anal Methods Geomech 2009;33:1289–313. https://doi.org/10.1002/NAG.767.

[780] Duriez J, Wan R. Contact angle mechanical influence in wet granular soils. Acta Geotech 2017;12:67–83. https://doi.org/10.1007/S11440-016-0500-6.
[781] Nazemi AH, Majnooni-Heris A. A mathematical model for the interactions between non-identical rough spheres, liquid bridge and liquid vapor. J Colloid Interface Sci 2012;369:402–10. https://doi.org/10.1016/j.jcis.2011.11.051.
[782] Gras JP, Delenne JY, Soulié F, El Youssoufi MS. DEM and experimental analysis of the water retention curve in polydisperse granular media. Powder Technol 2011;208:296–300. https://doi.org/10.1016/j.powtec.2010.08.019.
[783] Hotta K, Takeda K, Iinoya K. The capillary binding force of a liquid bridge. Powder Technol 1974;10:231–42. https://doi.org/10.1016/0032-5910(74)85047-3.
[784] Lambert P, Chau A, Delchambre A, Régnier S. Comparison between two capillary forces models. Langmuir 2008;24:3157–63. https://doi.org/10.1021/LA7036444.
[785] Harireche O, Faramarzi A, Alani AM. A toroidal approximation of capillary forces in polydisperse granular assemblies. Granul Matter 2013;15:573–81. https://doi.org/10.1007/S10035-013-0425-9.
[786] Lian G, Thornton C, Adams MJ. A Theoretical Study of the Liquid Bridge Forces between Two Rigid Spherical Bodies. J Colloid Interface Sci 1993;161:138–47. https://doi.org/10.1006/jcis.1993.1452.
[787] Richefeu V, El Youssoufi MS, Radjaï F. Shear strength properties of wet granular materials. Phys Rev E - Stat Nonlinear, Soft Matter Phys 2006;73. https://doi.org/10.1103/PHYSREVE.73.051304.
[788] Gabrieli F, Lambert P, Cola S, Calvetti F. Micromechanical modelling of erosion due to evaporation in a partially wet granular slope. Int J Numer Anal Methods Geomech 2012;36:918–43. https://doi.org/10.1002/NAG.1038.
[789] Wang JP, Li X, Yu HS. A micro–macro investigation of the capillary strengthening effect in wet granular materials. Acta Geotech 2018;13:513–33.
[790] Urso MED, Lawrence CJCJ, Adams MJ. A two-dimensional study of the rupture of funicular liquid bridges. Chem Eng Sci 2002;57:677–92. https://doi.org/10.1016/S0009-2509(01)00418-3.
[791] Murase K, Mochida T, Sugama H. Experimental and numerical studies on liquid bridge formed among three spheres. Granul Matter 2004;6:111–9. https://doi.org/10.1007/S10035-004-0168-8.
[792] Molenkamp F, Nazemi AH. Interactions between two rough spheres, water bridge and water vapour. Géotechnique 2003;53:255–64. https://doi.org/10.1680/geot.2003.53.2.255.
[793] Lechman J, Lu N. Capillary Force and Water Retention between Two Uneven-Sized Particles. J Eng Mech 2008;134:374–84. https://doi.org/10.1061/(ASCE)0733-9399(2008)134:5(374).
[794] Kruyt NP, Millet O. An analytical theory for the capillary bridge force between spheres. J Fluid Mech 2017;812:129–51. https://doi.org/10.1017/JFM.2016.790.
[795] Zhao CF, Kruyt NP, Millet O. Capillary bridge force between non-perfectly wettable spherical particles: An analytical theory for the pendular regime. Powder Technol 2018;339:827–37. https://doi.org/10.1016/j.powtec.2018.08.062.
[796] Fredlund DG. Unsaturated Soil Mechanics in Engineering Practice. J Geotech Geoenvironmental Eng 2006;132:286–321. https://doi.org/10.1061/(ASCE)1090-0241(2006)132:3(286).
[797] Hemmerle A, Schröter M, Goehring L. A cohesive granular material with tunable elasticity. Sci Rep 2016;6:1–11. https://doi.org/10.1038/srep35650.
[798] Lukyanov AV, Mitkin VV, Theofanous TG, Baines M. Capillary transport in particulate porous media at low levels of saturation. J Appl Phys 2019;125:185301. https://doi.org/10.1063/1.5086869.
[799] Soulié F, El Youssoufi MS, Cherblanc F, Saix C. Capillary cohesion and mechanical strength of polydisperse granular materials. Eur Phys J E 2006;21:349–57. https://doi.org/10.1140/EPJE/I2006-10076-2.
[800] Mikami T, Kamiya H, Horio M. Numerical simulation of cohesive powder behavior in a fluidized bed. Chem Eng Sci 1998;53:1927–40. https://doi.org/10.1016/S0009-2509(97)00325-4.
[801] Melnikov K, Wittel FK, Herrmann HJ. Micro-mechanical failure analysis of wet granular matter. Acta Geotech 2016;11:539–48. https://doi.org/10.1007/s11440-016-0465-5.
[802] Melnikov K, Mani R, Wittel FK, Thielmann M, Herrmann HJ. Grain-scale modeling of arbitrary fluid saturation in random packings. Phys Rev E - Stat Nonlinear, Soft Matter Phys 2015;92:022206. https://doi.org/10.1103/PhysRevE.92.022206.
[803] Brendel L, Unger T, Wolf DE. Contact Dynamics for Beginners. Phys Granul Media, Wiley 2004:325–43. https://doi.org/10.1002/352760362X.ch14.
[804] Meng Y, Primkulov BK, Yang Z, Kwok CY, Juanes R. Jamming transition and emergence of fracturing in wet granular media. Phys Rev Res 2012:2. https://doi.org/10.1103/PhysRevResearch.2.022012.
[805] Zhao B, MacMinn CW, Juanes R. Wettability control on multiphase flow in patterned microfluidics. Proc Natl Acad Sci 2016;113:10251–6. https://doi.org/10.1073/PNAS.1603387113.
[806] Davydzenka T, Fagbemi S, Tahmasebi P. Coupled fine-scale modeling of the wettability effects: Deformation and fracturing. Phys Fluids 2020;32:083308. https://doi.org/10.1063/5.0018455.
[807] Davydzenka T, Fagbemi S, Tahmasebi P. Wettability control on deformation: Coupled multiphase fluid and granular systems. Phys Rev E 2020;102:013301. https://doi.org/10.1103/PhysRevE.102.013301.
[808] Scholtes L, Chareyre B, Nicot F, Darve F. Discrete modelling of capillary mechanisms in multi-phase granular media. C - Comput Model Eng Sci 2009;52:297–318. https://doi.org/10.3970/cmes.2009.052.297.
[809] Xiao F, Jing J, Kuang S, Yang L, Yu A. Capillary forces on wet particles with a liquid bridge transition from convex to concave. Powder Technol 2020;363:59–73. https://doi.org/10.1016/J.POWTEC.2020.01.020.
[810] Dorostkar O, Guyer RA, Johnson PA, Marone C, Carmeliet J. Cohesion-Induced Stabilization in Stick-Slip Dynamics of Weakly Wet, Sheared Granular Fault Gouge. J Geophys Res Solid Earth 2018;123:2115–26. https://doi.org/10.1002/2017JB015171.
[811] Dux C, Versmold H. Light diffraction from shear ordered colloidal dispersions. Phys Rev Lett 1997;78:1811–4. https://doi.org/10.1103/PhysRevLett.78.1811.
[812] Asencio K, Acevedo M, Zuriguel I, Maza D. Experimental Study of Ordering of Hard Cubes by Shearing. Phys Rev Lett 2017;119:228002. https://doi.org/10.1103/PhysRevLett.119.228002.
[813] Lee J, Jiang Z, Wang J, Sandy AR, Narayanan S, Lin XM. Unraveling the Role of Order-to-Disorder Transition in Shear Thickening Suspensions. Phys Rev Lett 2018;120:5. https://doi.org/10.1103/PhysRevLett.120.028002.
[814] Tsai JC, Voth GA, Gollub JP. Internal Granular Dynamics, Shear-Induced Crystallization, and Compaction Steps. Phys Rev Lett 2003;91:064301. https://doi.org/10.1103/PhysRevLett.91.064301.
[815] Saadatfar M, Takeuchi H, Robins V, Francois N, Hiraoka Y. Pore configuration landscape of granular crystallization. Nat Commun 2017.1–11.;2017(81):8. https://doi.org/10.1038/ncomms15082.
[816] Carvente O, Ruiz-Suárez JC. Crystallization of confined non-Brownian spheres by vibrational annealing. Phys Rev Lett 2005;95:018001. https://doi.org/10.1103/PhysRevLett.95.018001.
[817] Panaitescu A, Reddy KA, Kudrolli A. Nucleation and crystal growth in sheared granular sphere packings. Phys Rev Lett 2012;108:108001. https://doi.org/10.1103/PhysRevLett.108.108001.
[818] Silbert LE, Grest GS, Plimpton SJ, Levine D. Boundary effects and self-organization in dense granular flows. Phys Fluids 2002;14:2637–46. https://doi.org/10.1063/1.1487379.
[819] Alam M, Luding S. First normal stress difference and crystallization in a dense sheared granular fluid. Phys Fluids 2003;15:2298–312. https://doi.org/10.1063/1.1587723.
[820] Reis PM, Ingale RA, Shattuck MD. Crystallization of a quasi-two-dimensional granular fluid. Phys Rev Lett 2006;96:258001. https://doi.org/10.1103/PhysRevLett.96.258001.
[821] Shinde DP, Mehta A, Barker GC. Shaking-induced crystallization of dense sphere packings. Phys Rev E - Stat Nonlinear, Soft Matter Phys 2014;89:6. https://doi.org/10.1103/PhysRevE.89.022204.

[822] Daniels KE, Behringer RP. Hysteresis and competition between disorder and crystallization in sheared and vibrated granular flow. Phys Rev Lett 2005;94:168001. https://doi.org/10.1103/PhysRevLett.94.168001.
[823] Grudzień K, Niedostatkiewicz M, Adrien J, Tejchman J, Maire E. Quantitative estimation of volume changes of granular materials during silo flow using X-ray tomography. Chem Eng Process Process Intensif 2011;50:59–67. https://doi.org/10.1016/j.cep.2010.11.008.
[824] Niedostatkiewicz M, Tejchman J, Grudzień K, Chaniecki Z. Application of ECT to solid concentration measurements during granular flow in a rectangular model silo. Chem Eng Res Des 2010;88:1037–48. https://doi.org/10.1016/j.cherd.2010.01.034.
[825] González-Montellano C, Ayuga F, Ooi JY. Discrete element modelling of grain flow in a planar silo: Influence of simulation parameters. Granul Matter 2011;13:149–58. https://doi.org/10.1007/s10035-010-0204-9.
[826] Sukumaran B, Ashmawy AK. Influence of inherent particle characteristics on hopper flow rate. Powder Technol 2003;138:46–50. https://doi.org/10.1016/j.powtec.2003.08.039.
[827] Tian T, Su J, Zhan J, Geng S, Xu G, Liu X. Discrete and continuum modeling of granular flow in silo discharge. Particuology 2018;36:127–38. https://doi.org/10.1016/j.partic.2017.04.001.
[828] Zhang S, Lin P, Wang M, Wan J, feng, Peng Y, Yang L,, et al. Flow-induced surface crystallization of granular particles in cylindrical confinement. Sci Rep 2021;11:1–11. https://doi.org/10.1038/s41598-021-92136-9.
[829] Vidyapati V, Subramaniam S. Granular flow in silo discharge: Discrete element method simulations and model assessment. Ind Eng Chem Res 2013;52:13171–82. https://doi.org/10.1021/ie303598e.
[830] Suzzi D, Radl S, Khinast JG. Local analysis of the tablet coating process: Impact of operation conditions on film quality. Chem Eng Sci 2010;65:5699–715. https://doi.org/10.1016/j.ces.2010.07.007.
[831] Pfeffer R, Dave RN, Wei D, Ramlakhan M. Synthesis of engineered particulates with tailored properties using dry particle coating. Powder Technol 2001;117:40–67. https://doi.org/10.1016/S0032-5910(01)00314-X.
[832] Chavda VP, Soniwala MM, Chavda JR. Particle coating: from conventional to advanced. Int J Pharm Med Al Res 2013;1:1–17.
[833] Turton R. Challenges in the modeling and prediction of coating of pharmaceutical dosage forms. Powder Technol 2008;181:186–94. https://doi.org/10.1016/j.powtec.2006.12.006.
[834] Rajniak P, Stepanek F, Dhanasekharan K, Fan R, Mancinelli C, Chern RT. A combined experimental and computational study of wet granulation in a Wurster fluid bed granulator. Powder Technol 2009;189:190–201. https://doi.org/10.1016/j.powtec.2008.04.027.
[835] Heinrich S, Dosta M, Antonyuk S. Multiscale Analysis of a Coating Process in a Wurster Fluidized Bed Apparatus. Adv Chem Eng 2015;46:83–135. https://doi.org/10.1016/bs.ache.2015.10.012.
[836] Hampel N, Bück A, Peglow M, Tsotsas E. Continuous pellet coating in a Wurster fluidized bed process. Chem Eng Sci 2013;86:87–98. https://doi.org/10.1016/j.ces.2012.05.034.
[837] Müller D, Bück A, Tsotsas E. Influence of separation properties and processing strategies on product characteristics in continuous fluidized bed spray granulation. Powder Technol 2019;342:572–84. https://doi.org/10.1016/j.powtec.2018.10.024.
[838] Peglow M, Antonyuk S, Jacob M, Palzer S, Heinrich S, Tsotsas E. Particle Formulation in Spray Fluidized Beds. Mod Dry Technol 2011;3:295–378. https://doi.org/10.1002/9783527631667.CH7.
[839] Bück A, Neugebauer C, Meyer K, Palis S, Diez E, Kienle A, et al. Influence of operation parameters on process stability in continuous fluidised bed layering with external product classification. Powder Technol 2016;300:37–45. https://doi.org/10.1016/j.powtec.2016.03.019.
[840] Schmidt M, Bück A, Tsotsas E. Shell porosity in spray fluidized bed coating with suspensions. Adv Powder Technol 2017;28:2921–8. https://doi.org/10.1016/j.apt.2017.08.020.
[841] Sondej F, Bück A, Koslowsky K, Bachmann P, Jacob M, Tsotsas E. Investigation of coating layer morphology by micro-computed X-ray tomography. Powder Technol 2015;273:165–75. https://doi.org/10.1016/j.powtec.2014.12.050.
[842] Fries L, Antonyuk S, Heinrich S, Palzer S. DEM–CFD modeling of a fluidized bed spray granulator. Chem Eng Sci 2011;66:2340–55. https://doi.org/10.1016/j.ces.2011.02.038.
[843] Li L, Remmelgas J, van Wachem BGM, von Corswant C, Johansson M, Folestad S, et al. Residence time distributions of different size particles in the spray zone of a Wurster fluid bed studied using DEM-CFD. Powder Technol 2015;280:124–34. https://doi.org/10.1016/j.powtec.2015.04.031.
[844] Kulju T, Paavola M, Spittka H, Keiski RL, Juuso E, Leiviskä K, et al. Modeling continuous high-shear wet granulation with DEM-PB. Chem Eng Sci 2016;142:190–200. https://doi.org/10.1016/j.ces.2015.11.032.
[845] Jiang Z, Bück A, Tsotsas E. CFD–DEM study of residence time, droplet deposition, and collision velocity for a binary particle mixture in a Wurster fluidized bed coater. Dry Technol 2018;36:638–50. https://doi.org/10.1080/07373937.2017.1319852.
[846] Terrazas-Velarde Korina K, Peglow M, Tsotsas E. Kinetics of fluidized bed spray agglomeration for compact and porous particles. Chem Eng Sci 2011;66:1866–78. https://doi.org/10.1016/j.ces.2011.01.037.
[847] Rieck C, Bück A, Tsotsas E. Monte Carlo modeling of fluidized bed coating and layering processes. AIChE J 2016;62:2670–80. https://doi.org/10.1002/AIC.15237.
[848] Zhao H, Maisels A, Matsoukas T, Zheng C. Analysis of four Monte Carlo methods for the solution of population balances in dispersed systems. Powder Technol 2007;173:38–50. https://doi.org/10.1016/j.powtec.2006.12.010.
[849] Zhang W, You C. Numerical approach to predict particle breakage in dense flows by coupling multiphase particle-in-cell and Monte Carlo methods. Powder Technol 2015;283:128–36. https://doi.org/10.1016/j.powtec.2015.05.025.
[850] Freireich B, Wassgren C. Intra-particle coating variability: Analysis and Monte-Carlo simulations. Chem Eng Sci 2010;65:1117–24. https://doi.org/10.1016/j.ces.2009.09.066.
[851] Hede PD, Bach P, Jensen AD. Two-fluid spray atomisation and pneumatic nozzles for fluid bed coating/agglomeration purposes: A review. Chem Eng Sci 2008;63:3821–42. https://doi.org/10.1016/j.ces.2008.04.014.
[852] Poozesh S, Setiawan N, Akafuah NK, Saito K, Marsac PJ. Assessment of predictive models for characterizing the atomization process in a spray dryer's bi-fluid nozzle. Chem Eng Sci 2018;180:42–51. https://doi.org/10.1016/j.ces.2018.01.033.
[853] Jiang X, Siamas GA, Jagus K, Karayiannis TG. Physical modelling and advanced simulations of gas-liquid two-phase jet flows in atomization and sprays. Prog Energy Combust Sci 2010;36:131–67. https://doi.org/10.1016/j.pecs.2009.09.002.
[854] Luo K, Shao C, Chai M, Fan J. Level set method for atomization and evaporation simulations. Prog Energy Combust Sci 2019;73:65–94. https://doi.org/10.1016/j.pecs.2019.03.001.
[855] Kieckhefen P, Lichtenegger T, Pietsch S, Pirker S, Heinrich S. Simulation of spray coating in a spouted bed using recurrence CFD. Particuology 2019;42:92–103. https://doi.org/10.1016/j.partic.2018.01.008.
[856] Rioboo R, Marengo M, Tropea C. Time evolution of liquid drop impact onto solid, dry surfaces. Exp Fluids 2002;33:112–24. https://doi.org/10.1007/S00348-002-0431-X.
[857] Du Q, Faber V, Gunzburger M. Centroidal Voronoi tessellations: Applications and algorithms. SIAM Rev 1999;41:637–76. https://doi.org/10.1137/S0036144599352836.
[858] Koay CG. Analytically exact spiral scheme for generating uniformly distributed points on the unit sphere. J Comput Sci 2011;2:88–91. https://doi.org/10.1016/j.jocs.2010.12.003.
[859] Jiang Z, Rieck C, Bück A, Tsotsas E. Modeling of inter- and intra-particle coating uniformity in a Wurster fluidized bed by a coupled CFD-DEM-Monte Carlo approach. Chem Eng Sci 2020;211:115289. https://doi.org/10.1016/J.CES.2019.115289.
[860] Diersch HJG, Clausnitzer V, Myrnyy V, Rosati R, Schmidt M, Beruda H, et al. Modeling Unsaturated Flow in Absorbent Swelling Porous Media: Part 2. Numerical Simulation Transp Porous Media 2011;86:753–76. https://doi.org/10.1007/s11242-010-9650-4.
[861] Diersch HJG, Clausnitzer V, Myrnyy V, Rosati R, Schmidt M, Beruda H, et al. Modeling unsaturated flow in absorbent swelling porous media: Part 1. theory. Transp Porous Media 2010;83:437–64. https://doi.org/10.1007/s11242-009-9454-6.

[862] Romero E, Della Vecchia G, Jommi C. An insight into the water retention properties of compacted clayey soils. Geotechnique 2011;61:313–28. https://doi.org/10.1680/GEOT.2011.61.4.313.
[863] Takhar PS. Unsaturated fluid transport in swelling poroviscoelastic biopolymers. Chem Eng Sci 2014;109:98–110. https://doi.org/10.1016/j.ces.2014.01.016.
[864] Murad MA, Cushman JH. Multiscale flow and deformation in hydrophilic swelling porous media. Int J Eng Sci 1996;34:313–38. https://doi.org/10.1016/0020-7225(95)00057-7.
[865] Huyghe JM, Janssen JD. Quadriphasic mechanics of swelling incompressible porous media. Int J Eng Sci 1997;35:793–802. https://doi.org/10.1016/s0020-7225(96)00119-x.
[866] Malakpoor K, Kaasschieter EF, Huyghe JM. Mathematical modelling and numerical solution of swelling of cartilaginous tissues. Part I: Modelling of incompressible charged porous media. Math Model Numer Anal 2007;41:661–78. https://doi.org/10.1051/M2AN:2007036.
[867] Louf JF, Lu NB, O'Connell MG, Cho HJ, Datta SS. Under pressure: Hydrogel swelling in a granular medium. Sci Adv 2021;7. https://doi.org/10.1126/sciadv.abd2711.
[868] Sweijen T, Chareyre B, Hassanizadeh SM, Karadimitriou NK. Grain-scale modelling of swelling granular materials; application to super absorbent polymers. Powder Technol 2017;318:411–22.
[869] Graham AT, Wilson LR. Commercial processes for the manufacture of superabsorbent polymers. Mod. superabsorbent Polym. Technol.: Wiley; 1998. p. 69–114.
[870] Mitchell JK, Soga K. Fundamentals of soil behavior. John Wiley & Sons; 2005.
[871] Kim JW, Do ShK. Monodisperse micron-sized polystyrene particles by seeded polymerization: Effect of seed crosslinking on monomer swelling and particle morphology. Polymer (Guildf) 2000;41:6181–8. https://doi.org/10.1016/S0032-3861(99)00846-0.
[872] Mahon R, Balogun Y, Oluyemi G, Njuguna J. Swelling performance of sodium polyacrylate and poly(acrylamide-co-acrylic acid) potassium salt. SN Appl Sci 2020;2:1–15. https://doi.org/10.1007/S42452-019-1874-5/TABLES/4.
[873] Park S, Ma J, Yun TS, Jeon S, Byeun Y, Kang D, et al. Pore-scale swelling mechanism of magnesium oxide granules during hydration. Constr Build Mater 2020;251:119101. https://doi.org/10.1016/J.CONBUILDMAT.2020.119101.
[874] Catalano E, Chareyre B, Barthélémy E. Pore-scale modeling of fluid-particles interaction and emerging poromechanical effects. Int J Numer Anal Methods Geomech 2014;38:51–71.
[875] Sweijen T, Nikooee E, Hassanizadeh SM, Chareyre B. The Effects of Swelling and Porosity Change on Capillarity: DEM Coupled with a Pore-Unit Assembly Method. Transp Porous Media 2016;113:207–26. https://doi.org/10.1007/S11242-016-0689-8/FIGURES/9.
[876] El Youssoufi MS, Delenne JY, Radjai F. Self-stresses and crack formation by particle swelling in cohesive granular media. Phys Rev E - Stat Nonlinear, Soft Matter Phys 2005;71:051307. https://doi.org/10.1103/PHYSREVE.71.051307/FIGURES/6/MEDIUM.
[877] Chien S. Red Cell Deformability and its Relevance to Blood Flow. Annu Rev Physiol 1987;49:177–92. https://doi.org/10.1146/annurev.ph.49.030187.001141.
[878] Tomaiuolo G, Lanotte L, D'Apolito R, Cassinese A, Guido S. Microconfined flow behavior of red blood cells. Med Eng Phys 2016;38:11–6. https://doi.org/10.1016/j.medengphy.2015.05.007.
[879] Kamm RD. Cellular fluid mechanics. Annu Rev Fluid Mech 2002;34:211–32. https://doi.org/10.1146/annurev.fluid.34.082401.165302.
[880] Popel AS, Johnson PC. Microcirculation and hemorheology. Annu Rev Fluid Mech 2005;37:43–69. https://doi.org/10.1146/annurev.fluid.37.042604.133933.
[881] Pries AR, Secomb TW, Gaehtgens P, Gross JF. Blood flow in microvascular networks. Experiments and simulation Circ Res 1990;67:826–34. https://doi.org/10.1161/01.RES.67.4.826.
[882] Dupire J, Socol M, Viallat A. Full dynamics of a red blood cell in shear flow. Proc Natl Acad Sci U S A 2012;109:20808–13. https://doi.org/10.1073/pnas.1210236109.
[883] Wetzel B, Schaefer H. Scanning electron microscope image of blood cells. Natl Cancer Institute Https//Visualsonline Cancer Gov/Details Cfm 1982.
[884] Burns JM, Yang X, Forouzan O, Sosa JM, Shevkoplyas SS. Artificial microvascular network: A new tool for measuring rheologic properties of stored red blood cells. Transfusion 2012;52:1010–23. https://doi.org/10.1111/j.1537-2995.2011.03418.x.
[885] Mayerich D, Kwon J, Sung C, Abbott L, Keyser J, Choe Y. Fast macro-scale transmission imaging of microvascular networks using KESM. Biomed Opt Express 2011;2:2888. https://doi.org/10.1364/boe.2.002888.
[886] Pozrikidis C. Numerical simulation of the flow-induced deformation of red blood cells. Ann Biomed Eng 2003;31:1194–205. https://doi.org/10.1114/1.1617985.
[887] Liu Y, Liu WK. Rheology of red blood cell aggregation by computer simulation. J Comput Phys 2006;220:139–54. https://doi.org/10.1016/J.JCP.2006.05.010.
[888] Secomb TW, Styp-Rekowska B, Pries AR. Two-dimensional simulation of red blood cell deformation and lateral migration in microvessels. Ann Biomed Eng 2007;35:755–65. https://doi.org/10.1007/s10439-007-9275-0.
[889] Fedosov DA, Caswell B, Karniadakis GE. A multiscale red blood cell model with accurate mechanics, rheology, dynamics. Biophys J 2010;98:2215–25. https://doi.org/10.1016/j.bpj.2010.02.002.
[890] Skalak R, Chen PH, Chien S. Effect of hematocrit and rouleaux on apparent viscosity in capillaries. Biorheology 1972;9:67–82. https://doi.org/10.3233/BIR-1972-9204.
[891] Tözeren H, Skalak R. The steady flow of closely fitting incompressible elastic spheres in a tube. J Fluid Mech 1978;87:1–16. https://doi.org/10.1017/S002211207800289X.
[892] Schmid-Schönbein GW, Skalak R, Usami S, Chien S. Cell distribution in capillary networks. Microvasc Res 1980;19:18–44. https://doi.org/10.1016/0026-2862(80)90082-5.
[893] Freund JB. Numerical Simulation of Flowing Blood Cells. Annu Rev Fluid Mech 2014;46:67–95. https://doi.org/10.1146/annurev-fluid-010313-141349.
[894] Nans A, Mohandas N, Stokes DL. Native ultrastructure of the red cell cytoskeleton by cryo-electron tomography. Biophys J 2011;101:2341–50. https://doi.org/10.1016/j.bpj.2011.09.050.
[895] Skalak R, Tozeren A, Zarda RP, Chien S. Strain Energy Function of Red Blood Cell Membranes. Biophys J 1973;13:245–64. https://doi.org/10.1016/S0006-3495(73)85983-1.
[896] Mills JP, Qie L, Dao M, Lim CT, Suresh S. Nonlinear elastic and viscoelastic deformation of the human red blood cell with optical tweezers. Mech Chem Biosyst 2004;1:169–80. https://doi.org/10.3970/mcb.2004.001.169.
[897] Suresh S. Mechanical response of human red blood cells in health and disease: Some structure-property-function relationships. J Mater Res 2006;21:1871–7. https://doi.org/10.1557/jmr.2006.0260.
[898] Boal DH, Seifert U, Zilker A. Dual network model for red blood cell membranes. Phys Rev Lett 1992;69:3405–8. https://doi.org/10.1103/PhysRevLett.69.3405.
[899] Discher DE, Mohandas N, Evans EA. Molecular maps of red cell deformation: Hidden elasticity and in situ connectivity. Science (80-) 1994;266:1032–5. https://doi.org/10.1126/science.7973655.
[900] Discher DE, Boal DH, Boey SK. Simulations of the erythrocyte cytoskeleton at large deformation. II Micropipette aspiration Biophys J 1998;75:1584–97. https://doi.org/10.1016/S0006-3495(98)74076-7.
[901] Waugh R, Evans EA. Thermoelasticity of red blood cell membrane. Biophys J 1979;26:115–31. https://doi.org/10.1016/S0006-3495(79)85239-X.
[902] Pivkin IV, Karniadakis GE. Accurate coarse-grained modeling of red blood cells. Phys Rev Lett 2008;101:118105. https://doi.org/10.1103/PhysRevLett.101.118105.
[903] Abkarian M, Faivre M, Horton R, Smistrup K, Best-Popescu CA, Stone HA. Cellular-scale hydrodynamics. Biomed Mater 2008;3:034011. https://doi.org/10.1088/1748-6041/3/3/034011.
[904] Reasor DA, Clausen JR, Aidun CK. Coupling the lattice-Boltzmann and spectrin-link methods for the direct numerical simulation of cellular blood flow. Int J Numer Methods Fluids 2012;68:767–81. https://doi.org/10.1002/fld.2534.
[905] Dimitrakopoulos P. Interfacial dynamics in Stokes flow via a three-dimensional fully-implicit interfacial spectral boundary element algorithm. J Comput Phys 2007;225:408–26. https://doi.org/10.1016/j.jcp.2006.12.004.

[906] Veerapaneni SK, Rahimian A, Biros G, Zorin D. A fast algorithm for simulating vesicle flows in three dimensions. J Comput Phys 2011;230:5610–34. https://doi.org/10.1016/j.jcp.2011.03.045.
[907] Freund JB. Leukocyte margination in a model microvessel. Phys Fluids 2007;19:023301. https://doi.org/10.1063/1.2472479.
[908] Zhao H, Isfahani AHG, Olson LN, Freund JB. A spectral boundary integral method for flowing blood cells. J Comput Phys 2010;229:3726–44. https://doi.org/10.1016/j.jcp.2010.01.024.
[909] Nguyen NQ, Ladd AJC. Lubrication corrections for lattice-Boltzmann simulations of particle suspensions. Phys Rev E - Stat Physics, Plasmas, Fluids, Relat Interdiscip Top 2002;66:12. https://doi.org/10.1103/PhysRevE.66.046708.
[910] Ding EJ, Aidun CK. Extension of the Lattice-Boltzmann Method for Direct Simulation of Suspended Particles Near Contact. J Stat Phys 2003;112:685–708. https://doi.org/10.1023/A:1023880126272.
[911] Leveque RJ, Li Z. Immersed interface methods for Stokes flow with elastic boundaries or surface tension. SIAM J Sci Comput 1997;18:709–35. https://doi.org/10.1137/S1064827595282532.
[912] Vigmostad SC, Udaykumar HS, Lu J, Chandran KB. Fluid-structure interaction methods in biological flows with special emphasis on heart valve dynamics. Int j Numer Method Biomed Eng 2010;26:435–70. https://doi.org/10.1002/cnm.1340.
[913] Macmeccan RM, Clausen JR, Neitzel GP, Aidun CK. Simulating deformable particle suspensions using a coupled lattice-Boltzmann and finite-element method. J Fluid Mech 2009;618:13–39. https://doi.org/10.1017/S0022112008004011.
[914] Sun C, Munn LL. Lattice-Boltzmann simulation of blood flow in digitized vessel networks. Comput Math with Appl 2008;55:1594–600. https://doi.org/10.1016/j.camwa.2007.08.019.
[915] Aidun CK, Clausen JR. Lattice-Boltzmann Method for Complex Flows. Annu Rev Fluid Mech 2010;42:439–72. https://doi.org/10.1146/annurev-fluid-121108-145519.
[916] Muldowney GP, Higdon JJL. A spectral boundary element approach to three-dimensional Stokes flow. J Fluid Mech 1995;298:167–92. https://doi.org/10.1017/S0022112095003260.
[917] Hockney RW, Eastwood JW. Computer Simulation Using Particles. A Hilger 1988. https://doi.org/10.1887/0852743920.
[918] Sierou A, Brady JF. Accelerated Stokesian Dynamics simulations. J Fluid Mech 2001;448:115–46. https://doi.org/10.1017/s0022112001005912.
[919] Rahimian A, Lashuk I, Veerapaneni SK, Chandramowlishwaran A, Malhotra D, Moon L, et al. Petascale direct numerical simulation of blood flow on 200K cores and heterogeneous architectures. 2010 ACM/IEEE Int. Conf. High Perform. Comput. Networking, Storage Anal. SC 2010, 2010. https://doi.org/10.1109/SC.2010.42.
[920] Selmi H, Elasmi L, Ghigliotti G, Misbah C. Boundary integral and fast multipole method for two dimensional vesicle sets in poiseuille flow. Discret Contin Dyn Syst - Ser B 2011;15:1065–76. https://doi.org/10.3934/dcdsb.2011.15.1065.
[921] Lambert CG, Darden TA, Board JA. A multipole-based algorithm for efficient calculation of forces and potentials in macroscopic periodic assemblies of particles. J Comput Phys 1996;126:274–85. https://doi.org/10.1006/jcph.1996.0137.
[922] Kumar A, Graham MD. Accelerated boundary integral method for multiphase flow in non-periodic geometries. J Comput Phys 2012;231:6682–713. https://doi.org/10.1016/j.jcp.2012.05.035.
[923] Noguchi H, Gompper G. Shape transitions of fluid vesicles and red blood cells in capillary flows. Proc Natl Acad Sci U S A 2005;102:14159–64. https://doi.org/10.1073/pnas.0504243102.
[924] Fedosov DA, Noguchi H, Gompper G. Multiscale modeling of blood flow: From single cells to blood rheology. Biomech Model Mechanobiol 2014;13:239–58. https://doi.org/10.1007/s10237-013-0497-9.
[925] Koumoutsakos P. Multiscale flow simulations using particles. Annu Rev Fluid Mech 2005;37:457–87. https://doi.org/10.1146/annurev.fluid.37.061903.175753.
[926] Li Y, Lian Y, Zhang LT, Aldousari SM, Hedia HS, Asiri SA, et al. Cell and nanoparticle transport in tumour microvasculature: The role of size, shape and surface functionality of nanoparticles. Interface. Focus 2016:6. https://doi.org/10.1098/rsfs.2015.0086.
[927] Fang Y, Han E, Zhang XX, Jiang Y, Lin Y, Shi J, et al. Dynamic and Programmable Cellular-Scale Granules Enable Tissue-like Materials. Matter 2020;2:948–64. https://doi.org/10.1016/j.matt.2020.01.008.
[928] Bolintineanu DS, Grest GS, Lechman JB, Pierce F, Plimpton SJ, Schunk PR. Particle dynamics modeling methods for colloid suspensions. Comput Part Mech 2014;1:321–56.
[929] Matijević E. Principles of colloid and surface chemistry. J Colloid Interface Sci 1979;70:399. https://doi.org/10.1016/0021-9797(79)90045-6.
[930] Lawrence asc.. Book Reviews. Nature 1953;171:142. https://doi.org/10.1038/171142a0.
[931] Schmid G. Clusters and Colloids. Wiley 1994. https://doi.org/10.1002/9783527616077.
[932] Mitragotri S, Lahann J. Physical approaches to biomaterial design. Nat Mater 2009;8:15–23. https://doi.org/10.1038/nmat2344.
[933] Zhang X, Shyy W, Marie SA. Numerical Simulation of Intercalation-Induced Stress in Li-Ion Battery Electrode Particles. J Electrochem Soc 2007;154:A910. https://doi.org/10.1149/1.2759840/XML.
[934] Cohu O, Magnin A. Rheometry of paints with regard to roll coating process. J Rheol (N Y N Y) 1998;39:767. https://doi.org/10.1122/1.550656.
[935] Brennan JG. Colloids in food. Food Chem 1983;11:228–9. https://doi.org/10.1016/0308-8146(83)90109-7.
[936] Mack JC, Smith JE. In-Depth Colloidal Dispersion Gels Improve Oil Recovery Efficiency. EOR, SPE 1994. https://doi.org/10.2118/27780-MS.
[937] Dijkstra M, Hansen JP, Madden PA. Gelation of a Clay Colloid Suspension. Phys Rev Lett 1995;75:2236. https://doi.org/10.1103/PhysRevLett.75.2236.
[938] Harward ME. An Introduction to Clay Colloid Chemistry. For clay technologists, geologists, and soil scientists. H. van Olphen. Interscience (Wiley), New York, 1963. xvi + 301 pp. Illus. $10. Science (80-) 1964;143:1023–4. https://doi.org/10.1126/science.143.3610.1023-a.
[939] Clausen JR, Reasor DA, Aidun CK. The rheology and microstructure of concentrated non-colloidal suspensions of deformable capsules. J Fluid Mech 2011;685:202–34. https://doi.org/10.1017/jfm.2011.307.
[940] Goldsmith HL, Bell DN, Braovac S, Steinberg A, McIntosh F. Physical and chemical effects of red cells in the shear-induced aggregation of human platelets. Biophys J 1995;69:1584–95. https://doi.org/10.1016/S0006-3495(95)80031-7.
[941] Earl DJ, Pooley CM, Ryder JF, Bredberg I, Yeomans JM. Modeling microscopic swimmers at low Reynolds number. J Chem Phys 2007;126:064703. https://doi.org/10.1063/1.2434160.
[942] Donnet J-B, Chand Bansal R. Mechanical Properties of Carbon Fibers. Carbon Fibers, vol. 63, CRC Press; 1998, p. 321–80. https://doi.org/10.1201/9781482285390-11.
[943] Thompson RB, Ginzburg VV, Matsen MW, Balazs AC. Predicting the mesophases of copolymer-nanoparticle composites Science (80-) 2001;292:2469–72. https://doi.org/10.1126/science.1060585.
[944] Dersoir B, de Saint Vincent MR, Abkarian M, Tabuteau H. Clogging of a single pore by colloidal particles. Microfluid Nanofluidics 2015.953–61.;2015(194):19. https://doi.org/10.1007/S10404-015-1624-Y.
[945] Carpenter DK. Dynamic Light Scattering with Applications to Chemistry, Biology, and Physics (Berne, Bruce J.; Pecora, Robert). J Chem Educ 1977;54:A430. https://doi.org/10.1021/ed054pa430.1.
[946] Doty P, Steiner RF. Light scattering and spectrophotometry of colloidal solutions. J Chem Phys 1950;18:1211–20. https://doi.org/10.1063/1.1747913.
[947] Van Megen W, Underwood SM. Dynamic-light-scattering study of glasses of hard colloidal spheres. Phys Rev E 1993;47:248–61. https://doi.org/10.1103/PhysRevE.47.248.
[948] Pusey PN, Tough RJA. Langevin approach to the dynamics of interacting brownian particles. J Phys A Math Gen 1982;15:1291–308. https://doi.org/10.1088/0305-4470/15/4/030.
[949] Söderman O, Stilbs P. NMR studies of complex surfactant systems. Prog Nucl Magn Reson Spectrosc 1994;26:445–82. https://doi.org/10.1016/0079-6565(94)80013-8.
[950] Momot KI, Kuchel PW. PFG NMR diffusion experiments for complex systems. Concepts Magn Reson Part A Bridg Educ Res 2006;28:249–69. https://doi.org/10.1002/CMR.A.20056/FORMAT/PDF.

[951] Weeks ER, Crocker JC, Levitt AC, Schofield A, Weitz DA. Three-dimensional direct imaging of structural relaxation near the colloidal glass transition. Science (80-) 2000;287:627–31. https://doi.org/10.1126/science.287.5453.627.
[952] Prasad V, Semwogerere D, Weeks ER. Confocal microscopy of colloids. J Phys Condens Matter 2007;19:4152–9. https://doi.org/10.1088/0953-8984/19/11/113102.
[953] Crocker JC, Grier DG. Methods of Digital Video Microscopy for Colloidal Studies. J Colloid Interface Sci 1996;179:298–310. https://doi.org/10.1006/jcis.1996.0217.
[954] Cheng X, McCoy JH, Israelachvili JN, Cohen I. X Cheng JMJIIC. Imaging the microscopic structure of shear thinning and thickening colloidal suspensions. Science (80-) 2011;333:1276–9. https://doi.org/10.1126/SCIENCE.1207032/SUPPL_FILE/CHENG_SOM.PDF.
[955] Fuchs M, Cates ME. Theory of Nonlinear Rheology and Yielding of Dense Colloidal Suspensions. Phys Rev Lett 2002;89:248304. https://doi.org/10.1103/PhysRevLett.89.248304.
[956] Mewis J, Wagner NJ. Colloidal suspension rheology 2011;vol. 9780521515. https://doi.org/10.1017/CBO9780511977978.
[957] Russel WB. Review of the Role of Colloidal Forces in the Rheology of Suspensions. J Rheol (N Y N Y) 1980;24:287–317. https://doi.org/10.1122/1.549564.
[958] Chen S, Doolen GD. Lattice boltzmann method for fluid flows. Annu Rev Fluid Mech 1998;30:329–64. https://doi.org/10.1146/annurev.fluid.30.1.329.
[959] Dünweg B, Ladd AJC. Lattice Boltzmann Simulations of Soft Matter Systems. Adv Polym Sci 2009;221:89–166. https://doi.org/10.1007/978-3-540-87706-6_2.
[960] Ladd AJC, Verberg R. Lattice-Boltzmann simulations of particle-fluid suspensions. J Stat Phys 2001;104:1191–251. https://doi.org/10.1023/A:1010414013942.
[961] Enwald H, Peirano E, Almstedt AE. Eulerian two-phase flow theory applied to fluidization. Int J Multiph Flow 1996;22:21–66. https://doi.org/10.1016/s0301-9322(96)90004-x.
[962] Esmaeeli A, Tryggvason G. Direct numerical simulations of bubbly flows Part 2. Moderate Reynolds number arrays. J Fluid Mech 1999;385:325–58. https://doi.org/10.1017/S0022112099004310.
[963] Fujita M, Yamaguchi Y. Development of three-dimensional structure formation simulator of colloidal nanoparticles during drying. J Chem Eng Japan 2006;39:83–9. https://doi.org/10.1252/jcej.39.83.
[964] Koike O, Ohta S, Fujita M, Yamaguchi Y. Simulation model of concentrated colloidal rod-like nanoparticles. Jpn J Appl Phys 2008;47:8124–30. https://doi.org/10.1143/JJAP.47.8124.
[965] Hu HH. Direct simulation of flows of solid-liquid mixtures. Int J Multiph Flow 1996;22:335–52. https://doi.org/10.1016/0301-9322(95)00068-2.
[966] Lechman JB, Nemer MB, Noble DR. Toward application of conformal decomposition finite elements to non-colloidal particle suspensions. Int J Numer Methods Fluids 2012;68:1409–21. https://doi.org/10.1002/fld.3638.
[967] Kumar A, Higdon JJL. Origins of the anomalous stress behavior in charged colloidal suspensions under shear. Phys Rev E - Stat Nonlinear, Soft Matter Phys 2010;82:051401. https://doi.org/10.1103/PhysRevE.82.051401.
[968] Bossis G, Brady JF. Dynamic simulation of sheared suspensions. I General method J Chem Phys 1984;80:5141–54. https://doi.org/10.1063/1.446585.
[969] Brady JF, Bossis G. The rheology of concentrated suspensions of spheres in simple shear flow by numerical simulation. J Fluid Mech 1985;155:105. https://doi.org/10.1017/S0022112085001732.
[970] Brady JF, Bossis G. Stokesian Dynamics. Annu Rev Fluid Mech 1988;20:111–57. https://doi.org/10.1146/annurev.fl.20.010188.000551.
[971] Hecht M, Harting J, Ihle T, Herrmann HJ. Simulation of claylike colloids. Phys Rev E - Stat Nonlinear, Soft Matter Phys 2005;72:408. https://doi.org/10.1103/PhysRevE.72.011408.
[972] Noguchi H, Gompper G. Transport coefficients of off-lattice mesoscale-hydrodynamics simulation techniques. Phys Rev E - Stat Nonlinear, Soft Matter Phys 2008;78:706. https://doi.org/10.1103/PhysRevE.78.016706.
[973] Padding JT, Louis AA. Hydrodynamic interactions and Brownian forces in colloidal suspensions: Coarse-graining over time and length scales. Phys Rev E - Stat Nonlinear, Soft Matter Phys 2006;74:402. https://doi.org/10.1103/PhysRevE.74.031402.
[974] Hoogerbrugge PJ, Koelman JMVA. Simulating microscopic hydrodynamic phenomena with dissipative particle dynamics. EPL 1992;19:155–60. https://doi.org/10.1209/0295-5075/19/3/001.
[975] Derjaguin B, Landau L. Theory of the stability of strongly charged lyophobic sols and of the adhesion of strongly charged particles in solutions of electrolytes. Prog Surf Sci 1993;43:30–59. https://doi.org/10.1016/0079-6816(93)90013-L.
[976] Verwey EJW. Theory of the Stability of Lyophobic Colloids. J Phys Colloid Chem 2002;51:631–6. https://doi.org/10.1021/J150453A001.
[977] Mazo RM. On the theory of brownian motion. III. Two-body distribution function. J Stat Phys 1969;1:559–62. https://doi.org/10.1007/BF01024130.
[978] Deutch JM, Oppenheim I. Molecular Theory of Brownian Motion for Several Particles. J Chem Phys 2003;54:3547. https://doi.org/10.1063/1.1675379.
[979] Chandrasekhar S. Stochastic Problems in Physics and Astronomy. Rev Mod Phys 1943;15:1. https://doi.org/10.1103/RevModPhys.15.1.
[980] Adamczyk Z, Siwek B, Szyk L. Flow-Induced Surface Blocking Effects in Adsorption of Colloid Particles. J Colloid Interface Sci 1995;174:130–41. https://doi.org/10.1006/JCIS.1995.1374.
[981] Seiphoori A, Ma X, guang, Arratia PE, Jerolmack DJ.. Formation of stable aggregates by fluid-assembled solid bridges. Proc Natl Acad Sci U S A 2020;117:3375–81. https://doi.org/10.1073/PNAS.1913855117/VIDEO-10.
[982] Arévalo R, Zuriguel I, Maza D. Topology of the force network in the jamming transition of an isotropically compressed granular packing. Phys Rev E - Stat Nonlinear, Soft Matter Phys 2010;81:041302. https://doi.org/10.1103/PhysRevE.81.041302.
[983] Walker DM, Tordesillas A. Topological evolution in dense granular materials: A complex networks perspective. Int J Solids Struct 2010;47:624–39. https://doi.org/10.1016/j.ijsolstr.2009.10.025.
[984] Tordesillas A, O'Sullivan P, Walker DM, Paramitha.. Évolution de connectivitÉ fonctionnelle des rÉseaux de contact et de chaines de force. Comptes Rendus - Mec 2010;338:556–69. https://doi.org/10.1016/j.crme.2010.09.004.
[985] Bassett DS, Owens ET, Daniels KE, Porter MA. Influence of network topology on sound propagation in granular materials. Phys Rev E - Stat Nonlinear, Soft Matter Phys 2012;86:041306. https://doi.org/10.1103/PHYSREVE.86.041306/FIGURES/9/MEDIUM.
[986] Walker DM, Tordesillas A, Pucilowski S, Lin Q, Rechenmacher AL, Abedi S. Analysis of grain-scale measurements of sand using kinematical complex networks. Int J Bifurc Chaos 2012;22:1230042. https://doi.org/10.1142/S021812741230042X.
[987] Tordesillas A, Walker DM, Andò E, Viggiani G. Revisiting localized deformation in sand with complex systems. Proc R Soc A Math Phys. Eng Sci 2013;469. https://doi.org/10.1098/rspa.2012.0606.
[988] Kamrava S, Sahimi M, Tahmasebi P. Simulating fluid flow in complex porous materials by integrating the governing equations with deep-layered machines. Nat Comput Mater 2021;7:1–9. https://doi.org/10.1038/s41524-021-00598-2.
[989] Kamrava S, Tahmasebi P, Sahimi M. Linking morphology of porous media to their macroscopic permeability by deep learning. Transp Porous Media 2020;131:427–48. https://doi.org/10.1007/s11242-019-01352-5.
[990] Kamrava S, Tahmasebi P, Sahimi M. Physics- and image-based prediction of fluid flow and transport in complex porous membranes and materials by deep learning. J Memb Sci 2021;622:119050. https://doi.org/10.1016/j.memsci.2021.119050.
[991] Cang R, Xu Y, Chen S, Liu Y, Jiao Y, Ren MY. Microstructure representation and reconstruction of heterogeneous materials via deep belief network for computational material design. J Mech Des Trans ASME 2017;139. https://doi.org/10.1115/1.4036649.
[992] Karimpouli S, Tahmasebi P. Segmentation of digital rock images using deep convolutional autoencoder networks. Comput Geosci 2019;126:142–50. https://doi.org/10.1016/j.cageo.2019.02.003.